UNIVERSITÀ
DEGLI STUDI
DI PADOVA

Sede Amministrativa: Università degli Studi di Padova

Dipartimento di Ingegneria Industriale

DOTTORATO DI RICERCA IN INGEGNERIA CHIMICA, DEI MATERIALI E MECCANICA
CICLO XVIII

A STUDY OF RAPID MOULD TEMPERATURE VARIATION INFLUENCE ON MORPHOLOGY AND APPEARANCE OF INJECTION MOULDED PARTS

Direttore della Scuola: Ch.mo Prof. Paolo Colombo
Coordinatore: Ch.mo Prof. Enrico Savio
Supervisore: Ch.mo Prof. Giovanni Lucchetta

Dottorando: Luca Crema

Alla mia famiglia

SOMMARIO

La tecnologia di riscaldamento e raffreddamento rapido dello stampo (RHCM) è ampliamente utilizzata per realizzare componenti senza difetti superficiali e con elevato gloss. Grazie ai numerosi vantaggi quali la riduzione della pressione di iniezione, l'aumento della qualità superficiale del componente stampato e la possibilità di controllare la temperatura stampo, questa tecnologia sta diventando una soluzione interessante per stampare parti in parete sottile. Tuttavia, la variazione di temperatura dello stampo aumenta sostanzialmente il tempo ciclo diminuendo la produttività. Sviluppare soluzioni e tecnologie per la variazione rapida della temperatura dello stampo è tecnicamente difficile a causa dei vincoli del processo di stampaggio ad iniezione. In questo lavoro è stato sviluppato uno stampo equipaggiato con inserti porosi di geometria definita per aumentare lo scambio termico tra l'acqua e la cavità stampo. A tal fine, un modello numerico accurato dello stampo è stato sviluppato e successivamente validato sperimentalmente. I risultati mostrano un sostanziale incremento del coefficiente globale di conduzione termica rispetto alle attuali tecnologie per la variazione rapida della temperatura stampo. Un ulteriore studio sperimentale fu focalizzato sull'influenza della tecnologia RHCM sulla microstruttura e sulle proprietà meccaniche di componenti stampati in polipropilene caricato con fibra lunga. Una tomografia computerizzata è stata utilizzata per consentire una diretta osservazione dell'orientazione delle fibre mentre una procedura innovativa è stata impiegata per misurare la lunghezza residua delle fibre. Analisi di trazione statica e di resistenza a fatica sono state svolte per caratterizzare i provini stampati con tecnologia convenzionale e con un processo RHCM. L'utilizzo di una elevata temperatura stampo risultò in una minore orientazione delle fibre mentre la lunghezza delle residua delle stesse fu incrementata. Per quanto riguarda le proprietà meccaniche, impiegare una tecnologia RHCM garantisce un aumento della resistenza a trazione per componenti a parete sottile, mentre sia le proprietà statiche che quelle dinamiche sono diminuite per parti di grosso spessore. L'influenza della temperatura stampo nello stampaggio ad iniezione di preforme a spessore sottile in PET è stata oltretutto investigata sperimentalmente. Un aumento della temperatura stampo risultò in una sostanziale diminuzione della pressione di iniezione senza superare il limite di cristallizzazione imposto dal sub-seguente processo di soffiaggio. Un ultimo scopo del lavoro riguarda l'utilizzo di una tecnologia RHCM per controllare la temperatura stampo ed il tempo di ricottura durante lo stampaggio ad iniezione di parti in PLA. L'analisi mostrò

un'interessante dipendenza dalla temperatura stampo con il grado di cristallizzazione e conseguentemente con le proprietà meccaniche.

ABSTRACT

Rapid Heating Cycle Molding (RHCM) is a widely used technology for manufacturing high gloss components without visible surface defects. Due to the several improvements such as the injection pressure reduction, the increasing on molded parts quality and the possibility to control the mold temperature, this technology is becoming an interesting solution for injection molding of thin wall components with engineering polymers. The elevated mold temperature, however, substantially increases the cycle time, thus lowering the productivity to a great extent. Development of capable techniques for rapidly heating and cooling a mold with a relatively large mass is technically challenging because of the constraints set by the injection molding process. In this work a porous mold insert with a regular deterministic geometry was developed and optimized through a numerical simulations to increase heat exchange between water and the cavity surface. An accurate mold numerical model was developed and experimentally validated. The results showed a substantial increase of the global coefficient of thermal conduction compared to the existing technologies for the rapid variation of the mold cavity temperature. A further experimental study was focused on the RHCM influence on microstructure and mechanical properties of long glass fiber reinforced polypropylene. X-ray computed tomography (CT) was employed to allow a direct observation of the fibers orientation and image analysis was used to measure the residual fibers length distribution. Tensile strength and fatigue analysis were performed in order to characterize the injection molded specimens, with a CIM and RHCM technologies, from static and dynamic point of view. The using of an high mold temperature resulted in a lower fiber orientation while the residual fiber length was enhanced. Concerning mechanical properties, the employment of a RHCM technology ensure an increasing of the tensile strength for thin wall components while both static and dynamic properties are decreased for thick parts. The mold temperature influence on injection molding of PET thin wall bottle preforms was also numerically investigated. The increasing in mold temperature resulted in a substantial decreasing of injection pressure without overcoming the limit of crystallization degree imposed by the subsequent blow molding process. A final aim of this work regarded the employment of a RHCM technology in order to control the mold temperature and the annealing phase during the injection molding of parts made with PLA. The analysis showed an interesting capability of adjusting the mold temperature in order to control the material crystallization degree and consequently its mechanical properties.

ACKNOWLEDGMENTS

Firt of all, I would like to acknowledge the "Department of Industrial engineering" for having funded the scholarship of my PhD. Thanks to the professor Giovanni Lucchetta, who has guided me over my entire PhD course. I would like to thank all the people of the Te.Si laboratory for the enjoyable time spent together. I thank all my friends for the fun times and their friendship. A special thanks is devoted to my mother, my brother and my sister for supporting me during these years, you have always been a point of reference and an example to follow. I would like to remember also people that loved me but that unfortunately cannot longer stand by my side; hoping that they are proud of me, I will dedicate to them this thesis.

L. C.

CONTENTS

0.1 Industrial problem xx
0.2 The aim of this work xxiii
0.3 Outline xxiv

I BACKGROUND AND LITERATURE REVIEW 1

1 INTRODUCTION OF RAPID HEAT CYCLE MOULDING TECHNOLOGY 3
1.1 Process principe 4
1.2 Heat transfer process in injection moulding 6
1.3 RHCM applications and benefits 6
1.3.1 Minimizing weld lines 7
1.4 Mould design for rapid thermal cycling 15
1.4.1 Constituent elements 16
1.4.2 Mould with scaffolded structures 17
1.4.3 Multilayer mould 18
1.5 Mould surface heating methods 19
1.5.1 Electrical resistive heating 19
1.5.2 Induction heating 20
1.5.3 High-frequency proximity heating 22
1.5.4 Dielectric heating 22
1.5.5 Thermoelectric heating 23
1.5.6 Radiation heating 23
1.5.7 Contact heating 24
1.5.8 Convective heating 27
1.5.9 RHCM technology summary 31

2 INJECTION MOLDING OF FIBER REINFORCED MATERIALS 33
2.1 Mechanical properties of fiber reinforced materials . . 33
2.1.1 Fiber degradation 38
2.1.2 Fiber orientation 45
2.2 Fatigue behaviour of fiber reinforced materials 48

3 INJECTION MOLDING OF CRYSTALLINE MATERIALS 67
3.1 Injection molding of PET thin wall bottles preforms . . 67
3.2 Producing of PLA components: crystallization and mechanical performances 69

II AN INNOVATIVE SOLUTION FOR POROUS INSERTS REALIZATION 73

4 AN INNOVATIVE SOLUTION FOR POROUS INSERTS REALIZATION 75
4.1 Mold with metal foam 75
4.2 Objectives definition 78
4.3 Porous inserts with a labyrinth geometry 78

4.3.1 Formulation of the idea . . . 78
4.3.2 Design strategy definition . . . 80
4.3.3 First phase: porous inserts geometry optimization and mold designing . . . 81
4.3.4 Second phase: detailed fluid-dynamic model generation . . . 85
4.3.5 Mold structural verification . . . 92
4.4 Mold manufacturing and fluid-dynamic model validation 95
4.4.1 Materials and methods . . . 95
4.4.2 Model validation . . . 96
4.5 Discussions . . . 98

iii STUDYING OF THE RAPID HEAT CYCLE MOLDING INFLUENCE ON APPEARANCE AND MECHANICAL PROPERTIES OF FIBER REINFORCED MATERIALS 101

5 RHCM INFLUENCE ON SURFACE APPEARANCE FOR LGFP 103
5.1 material and methods . . . 103
5.2 Experimental apparatus and measuring system . . . 104
5.3 Results and discussions . . . 105

6 RHCM INFLUENCE ON MORPHOLOGY AND TENSILE STRENGTH OF LGFP 109
6.1 material and methods . . . 110
6.2 Mechanical test setup . . . 110
6.3 System computed microtomography . . . 110
6.4 Residual fiber length measurement procedure . . . 112
6.4.1 Traditional procedure for measuring the residual fibers length . . . 112
6.4.2 Innovative procedure for measuring the residual fibers length . . . 114
6.5 Design of Experiments . . . 118
6.6 Residual fiber length analysis . . . 120
6.7 Fiber orientation analysis . . . 122
6.7.1 A qualitative analysis of fiber orientation . . . 123
6.7.2 A quantitative analysis of fiber orientation . . . 129
6.8 Tensile strength results . . . 131
6.9 discussions . . . 133

7 RHCM INFLUENCE ON FATIGUE RESISTANCE OF FIBER REINFORCED POLYMER MATERIALS 135
7.1 Experimental plan . . . 135
7.2 Results and discussions . . . 136
7.2.1 Fatigue resistance analysis . . . 136
7.2.2 Fractional fatigue test . . . 137

iv STUDYING OF THE RAPID HEAT CYCLE MOLDING INFLUENCE ON CRYSTALLINE MATERIALS 143

8 INJECTION MOLDING OF PET BOTTLE PREFORMS WITH A RHCM TECHNOLOGY 145

8.1 Materials and methods . . . 146
8.1.1 Mold equipment . . . 146
8.1.2 Material characterization . . . 146
8.1.3 software calibration . . . 147
8.1.4 Numerical simulation of PET preforms with a RHCM technology . . . 150
8.2 Results and discussions . . . 151
9 RHCM INFLUENCE ON PLA CRYSTALLINITY AND HARDNESS 155
9.1 Experiments . . . 155
9.1.1 sample preparation . . . 155
9.1.2 Differential scanning calorimetry . . . 156
9.1.3 Shore hardness test . . . 157
9.2 Analysis of results . . . 158
9.2.1 DSC Data . . . 158
9.2.2 Hardness test . . . 158
9.3 discussions . . . 161
V CONCLUSIONS 163
10 CONCLUSIONS 165
BIBLIOGRAPHY 169

Figure 0.1	Comparison between a fiber reinforced component injection molded with a CIM (on the left) and a RHCM process (on the right)	xxi
Figure 0.2	Example of preforms with different thickness-length ratio	xxii
Figure 0.3	Example of products injection molded with PLA	xxiii
Figure 0.4	Thesis outline	xxv
Figure 1.1	Comparison of the changes of the mould temperature in RHCM and CIM processes	5
Figure 1.2	Schematic of heat transfer process in injection moulding	6
Figure 1.3	Structure of opposite flow weld line	8
Figure 1.4	Weld line depth varying mold temperature for:(a) ABS/PMMA normal and high gloss, ABS (b) PP (c) PS	8
Figure 1.5	Weld line width varying mold temperature for:(a) ABS/PMMA/nano $CaCO_3$ (b) PP 30% LGF	9
Figure 1.6	RHCM application on (a) flow marks (b) jetting marks	9
Figure 1.7	Example of micro-features replicated (a) by conventional injection molding and (b) employing the RHCM system	10
Figure 1.8	Mold temperature influence on gloss for:(a) ABS and ABS/PMMA (b) PP (c) PS	11
Figure 1.9	Effect of process parameters on gloss for:(a) ABS/PMMA/nano $CaCO_3$ (b) PP 30% LGF	12
Figure 1.10	The negligible influence of mold temperature on PS	13
Figure 1.11	Injection molding of PEEK at high temperature (RocTool)	13
Figure 1.12	Illustration of the formation mechanism of the concave warpage in RHCM	14
Figure 1.13	The TV front shells produced with different packing pressures in RHCM	15
Figure 1.14	Schematic heating and cooling response at the mold surface	17
Figure 1.15	Example of a 3D printed scaffolded structure	18
Figure 1.16	An electrical resistive heating with low-frequency electrical current	20
Figure 1.17	A schematic setup of mould rapid heating by electrical resistive film (Thermoceramix system)	20

Figure 1.18 A schematic setup for induction heating of mould inserts 21
Figure 1.19 A schematic setup for induction heating with internal coils (3iTech system developed by Roctool) 21
Figure 1.20 Principle of high-frequency proximity heating 22
Figure 1.21 Infrared heating system 24
Figure 1.22 Schematic of the infrared heating system assembled on the mould 25
Figure 1.23 The basic composition of ULPAC cavity and core block 26
Figure 1.24 Thermal behaviour of the metal surface layer in varying (a) its thickness and (b) the thickness of the insulation layer 26
Figure 1.25 Composition and structure of RHCM systems with steam heating 27
Figure 1.26 An example of RHCM mould with conformal cooling channels 28
Figure 1.27 The schematic cavity structure of a typical electric-heating mould 29
Figure 1.28 Schematic view of the BFMOLD TM technology principle 30
Figure 1.29 Mold with the alluminum foam inserts 30
Figure 1.30 Mold temperature response: (a) temperature profiles (b) temperature distribution 31
Figure 1.31 RHCM technology summary 32
Figure 2.1 Residual fiber length versus fibre content . . . 34
Figure 2.2 Tensile Young's modulus versus fibre content . 35
Figure 2.3 Tensile strength versus fibre content 35
Figure 2.4 Notched Izod impact versus fibre content . . . 35
Figure 2.5 Notched Charpy impact versus fibre content . 36
Figure 2.6 Normalized mechanical properties versus fibre content 37
Figure 2.7 Modelling of mechanical performance 37
Figure 2.8 Effect of feedstock fiber length on the tensile strength of composite 39
Figure 2.9 Effect of feedstock fiber length on the tensile modulus of composite 39
Figure 2.10 Fiber length distribution (number-average fiber length) for molding filling of center-gated disk 41
Figure 2.11 Shear rate distribution (number-average fiber length) for molding filling of center-gated disk 41
Figure 2.12 Contours of weight-average fiber length Lw versus position in the mold cavity 44
Figure 2.13 Experimental and predicted average fiber lengths 45

Figure 2.14 Layering configuration of an injection molded plate 46
Figure 2.15 Measured and predicted FOD with the RSC model (a) and the ARD-RSC model (b) 48
Figure 2.16 Tensile stress–strain curves for dfferent specimen orientations 50
Figure 2.17 S–N curves for different specimen orientations; bright symbols indicate test interrupted at 10^6 cycles (run-outs) 51
Figure 2.18 Cyclic creep: stress–strain cycles; percent numbers indicate the stage of specimen life at which the full cycles have been recorded, with reference to the number of cycles to failure. 52
Figure 2.19 Cyclic creep: maximum and minimum strain variation with number of cycles (specimen orientation $\theta = 0\ ^\circ$; test conditions $\sigma_{max} = 40$ MPa, $N_f > 10^6$) 53
Figure 2.20 SEM micrographs of the fracture surface of a specimen oriented at $0\ ^\circ$ showing the presence of micro-brittle and micro-ductile areas 54
Figure 2.21 Interpolation of the tensile strength values by the Tsai–Hill criterion 54
Figure 2.22 Interpolation of the fatigue strength values by the Tsai–Hill criterion 56
Figure 2.23 Normalized S–N data with superimposed S–N curve of ISO 527 standard specimens 56
Figure 2.24 Mechanical energy density per cycle vs number of cycles for different test frequencies . . . 57
Figure 2.25 Characteristic hysteresis loops measured during the fatigue tests 58
Figure 2.26 Mechanical energy density per cycle versus the number of cycles for tested materials 58
Figure 2.27 S-N curves for the longitudinal and transersal directions 59
Figure 2.28 S-N curves normalized for the longitudinal and transersal directions 60
Figure 2.29 S-N curves for the longitudinal and transersal directions, varying the testing frequency 60
Figure 2.30 Energy loss tested at different frequencies, varying the testing frequency 61
Figure 2.31 Fracture surface of the tensile specimen 62
Figure 2.32 A comparison of the fatigue behavior of LFT with unreinforced PP 62
Figure 2.33 Temperature rise in PP and LFT tested at 10 MPa and 20 Hz 63

Figure 2.34 Skin–shell–transition–core microstructure formation of PA66/GF30 observed by lCT technique 64
Figure 2.35 Evolution of normalized dynamic modulus ($E_N = E_0$), maximum strain (ϵ_{max}) and mean temperature ($T_{max} - T_{room}$) 65
Figure 3.1 Variation of the enthalpy of cold crystallization, $\triangle H_c$ and peak temperature, T_C with the mold temperature, T_w 69
Figure 4.1 Schematic structure of the RHCM mould with metallic foams 76
Figure 4.2 Titanium scaffolds following experimental testing and corresponding FEA results 77
Figure 4.3 Aluminum foam inserts: comparison of the temperature history between experimental data and simulation results 77
Figure 4.4 Labyrinth porous inserts generation 79
Figure 4.5 Geometry of a single metal sheet 80
Figure 4.6 solids meshing for CFD simulation 82
Figure 4.7 The RHCM mold assembly 82
Figure 4.8 Solid domain considered in the first simulations campaign 83
Figure 4.9 Model boundary conditions 83
Figure 4.10 Simulation response surface 85
Figure 4.11 Meshing of the detailed CFD model 88
Figure 4.12 Model utilized to determine the pressure drop 89
Figure 4.13 Boundary conditions for the transient simulation 91
Figure 4.14 Mold section temperature distribution after 0.1 seconds(a) after 2 seconds (b) after 6 seconds (c) and after 10 seconds (d) 92
Figure 4.15 Heating profiles obtained for a cavity central point (red), for the average temperature of the cavity mold (blu) and for the thermocouple point (green) 93
Figure 4.16 Mold cavity pressure profile 94
Figure 4.17 Mechanical simulation stress results 94
Figure 4.18 Mechanical simulation deformation results . . 95
Figure 4.19 (a) Thermoregulator system (b) Pneumatic valves system 96
Figure 4.20 (a) Thermocouple placed in the mold water inlet (b) Thermocouple placed in the mold cavity 96
Figure 4.21 Comparison between the inlet water temperature using long channels (red line) or short channels (blue line) 97
Figure 4.22 Numerical and experimental comparison between the heating profiles 98
Figure 4.23 Heating profiles for different water temperatures 99

Figure 5.1 Optical microscope Sensofar 104
Figure 5.2 Normal probability plot of the standardized effects 105
Figure 5.3 Main effects plot: (a) Mold temperature (b) Packing pressure (c) Injection Rate 106
Figure 5.4 Interaction plots: (a) Mold temperature-Injection rate (b) Packing pressure-Injection Rate (c) Mold temperature-Packing pressure 106
Figure 5.5 Surface topography for the specimens molded with a mold temperature of 70 $^{\circ}C$(a) and 110 $^{\circ}C$ (b) 107
Figure 6.1 Technical drawing of the plate with a thickness of 1 mm 111
Figure 6.2 Thermocouple position for checking the mold cavity temperature 112
Figure 6.3 CT System Nikon Metrology XTEK MCT225 . 113
Figure 6.4 The utilized oven for burning the polymer matrix 115
Figure 6.5 Sample obtained from the specimen before and after pyrolysis 115
Figure 6.6 Grid placed above the scanner glass 116
Figure 6.7 (a) Image acquired with the high resolution scanner (b) Fibers recognition with ctFire (b) . 117
Figure 6.8 The molded specimen 120
Figure 6.9 Influence of injection molding parameters on residual fibers length: main effects 121
Figure 6.10 Influence of injection molding parameters on residual fibers length: Interaction plots 123
Figure 6.11 Portion of the specimen scanned with micro-tomography 124
Figure 6.12 Different fiber distribution by layering the specimen through the thickness: skin layer (a), shell layer (b), core layer (c) 124
Figure 6.13 The specimen fixed on the micro-ct rotating table 125
Figure 6.14 FOD through the sample thickness for the specimen molded at injection speed of 10mm/s . . 126
Figure 6.15 FOD through the sample thickness for the specimen molded at injection speed of 100 mm/s . 127
Figure 6.16 Shear rate profile in function of the specimen thickness 128
Figure 6.17 FOD distribution through the samples 128
Figure 6.18 Specimen central section subdivision for those ones with a thickness of 4 mm 130
Figure 6.19 Specimen central section subdivision for those ones with a thickness of 1 mm 130
Figure 6.20 FOD distribution contour plot 130

Figure 6.21 Influence of mold temperature and cavity thickness on fiber orientation 131
Figure 6.22 Tensile strength: main effects 132
Figure 6.23 Tensile strength: interaction plot 133
Figure 6.24 (a) Fibers orientation, (b) Mold temperature, (c) Tensile strength 134
Figure 7.1 S-N curve 137
Figure 7.2 Variation of the UTS with the mold temperature 138
Figure 7.3 Mastercurve enclosing all fatigue data normalized by the UTS 138
Figure 7.4 Specimen plastic elongation evolution during the fatigue life 139
Figure 7.5 Micro-voids variation during the fatigue test . 141
Figure 8.1 Mold Equipment 146
Figure 8.2 Pressure acquisition system 147
Figure 8.3 Cross model parameters 148
Figure 8.4 Material modellation with a Cross-WLF model 148
Figure 8.5 Thermal characterization of PET 149
Figure 8.6 An example of an acquired injection pressure profile with a mold temperature of 30 $^{\circ}C$, an injection speed of 70 mm/s and the specimen thickness of 1mm 150
Figure 8.7 Physical and virtual measurement of the short shot length 151
Figure 8.8 Channels simulation model (a) and the simulated heating phase (b) 151
Figure 8.9 Model calibration response surface 152
Figure 8.10 Model calibration response surface 153
Figure 9.1 Thermal cycle for the PLA specimens injection molding 156
Figure 9.2 The mold for injection molding of PLA 157
Figure 9.3 DSC scans of the sample cut in the middle of the specimens annealed with a mold temperature of 100$^{\circ}C$(a), 120$^{\circ}C$ (b) and 140$^{\circ}C$ (c) . . . 159
Figure 9.4 The crystallization degree trend varying the mold temperature and the annealing time . . . 160
Figure 9.5 The samples hardness trend varying the mold temperature and the annealing time 160

Figure 9.6 The crystals analysis with the polarized optical microscope 162

LIST OF TABLES

Table 2.1 Mean values ($\pm$ standard deviation) of the tensile properties of PA6 GF30 specimens extracted from plates at dfferent orientations 50
Table 2.2 Values of the fatigue strength coeffient σ_f and the fatigue strength exponent b of PA6 GF30 specimens extracted from plates at different orientations 51
Table 2.3 Tsai-Hill parameters 55
Table 2.4 Tsai-Hill parameters for the fatigue Tsai-Hill formula 55
Table 2.5 Tensile properties of LFT 59
Table 4.1 Model boundary conditions 84
Table 4.2 Model initial conditions 84
Table 4.3 Maximum cavity temperature ($^{\circ}C$) after 2 seconds varying the inserts geometry parameters 85
Table 4.4 Domains properties 87
Table 4.5 Model boundary conditions for the transient simulation 90
Table 4.6 Injection molding simulation parameters . . . 93
Table 5.1 Design of experiments 104
Table 6.1 Design of experiments 119
Table 6.2 Design of experiments 119
Table 6.3 CT acquisition parameters 124
Table 6.4 Specimens thickness and layers percentage distribution 127
Table 6.5 Specimens porosity at different molding conditions 129
Table 7.1 Design of experiments 136
Table 7.2 Fatigue curves fitting parameters 137
Table 8.1 Design of experiments 149
Table 8.2 Injection molding parameters 152
Table 9.1 Injection molding parameters 156
Table 9.2 Shore hardness instrument specifications . . . 157

INTRODUCTION

Plastics injection molding is one of the most widely used processing technologies in the plastic industry. With the development of modern industries, more comprehensive and strict functional requirements are requested for plastic parts. The mold temperature control technique adopted in conventional injection molding is the continuous cooling method, in which the coolant is circulated in the cooling channels at constant temperature to cool the mold and the polymer melt. As a result, a solidified layer, occurring at the wall of the cavity, greatly increases the flow resistance and decreases the mold-filling ability of the polymer melt. Due to this issue, the injection molding defects such as weld line, sink mark, and short shot cannot be avoided with this conventional technique. Molding micro features with high aspect ratio is a critical issue for a conventional molding process (CIM) because the higher the feature surface-volume ratio the faster the polymer solidification. Concerning the branch of fiber reinforced thermoplastic molding, the poor surface aesthetic of the product molded by CIM process significantly limits its application where the surface appearance is fundamental. For those reasons, a novel injection molding technology is proposed: the so-called Rapid Heat Cycle Molding (RHCM) or Varioterm Injection Molding (VIM). In RHCM, before the melt injection, the mold is firstly heated to a preset temperature then, during filling it is kept at high temperature and at the end it is cooled to allow the solidification of the polymer melt. For amorphous polymers, the cavity surface is usually heated up to a temperature that is $10^{\circ}C$ higher than the polymer glass transition temperature (Tg). A large number of innovative approaches for rapidly heating the mold cavity have been developed in recent years. This innovative methods still have many shortcomings to be applied in mass production. Despite of its industrial relevance, there are several aspects of this novel process that need to be understood completely in particular regarding the injection molding of fiber reinforced and crystalline materials. In this Ph.D. thesis, an innovative heating and cooling system was developed replacing the traditional cooling channel with a porous insert placed behind the mold cavity surface and geometrically optimized through numerical simulation. The optimization was carried out developing a series of thermal and mechanical simulations with the aim of defining the most suitable inserts geometry to maximize the thermal exchange without impairing the mold integrity. A testing mold was made with the aim of validating the numerical simulations and characterizing the RHCM influence on the surface quality and mechanical properties of fiber re-

inforced polypropylene molded parts. A deep analysis has been carried out in order to completely understand the influence of a RHCM technology on composite and crystalline materials.

0.1 INDUSTRIAL PROBLEM

There is a growing market for thinner plastic parts. Nowadays, the part thickness of cellular phone components, laptop and notebook computer components, and similar telecommunication items has already reached 1 mm or less. This trend is partially caused by the increasing demand for product portability and material savings as well as high mechanical strength, close dimensional tolerances, high shape accuracy, low residual stress, good appearance and excellent surface texture. Molding thin wall parts the main difficulty is the fact that the ratio of frozen layer thickness to part thickness during filling will drastically increase with the decrease of part thickness. The problem is even enhanced when the frozen layer thickness and the part thickness are comparable in fact the frozen skin of each side is approximately 0.25mm thick regardless of the nominal wall thickness of the part. To solve this problem , resin suppliers recommend using higher injection speed and melt temperature, however, this leads to a rapid increasing of the local shear stress and the injection pressure which consequently could cause the deformation of the mold structure. Two competing factors influence the injection pressure in conventional injection molding process. On one hand, increase of injection rate results in increase of shear stresses and therefore increase of the injection pressure. On the other hand, increase of injection rate reduces solidification during filling, thus resulting in increase of the effective flow thickness. The combined effects give rise to a critical injection rate, Qc , which allow the lowest injection pressure. The critical injection rate depends on the part thickness. As the part thickness decreases, Qc shifts to the region with faster injection rates. The typical filling time corresponding to Qc for standard parts (thickness above 2mm) is several seconds, while for thin wall parts (thickness less than 1 mm) it drops to a few tenths of a second. In contrast, isothermal filling does not experience solidification, and therefore the injection pressure increases monotonically as the injection rate increases. In injection molding of fiber reinforced polymers, the achievement of an high aesthetical appearance with a CIM process is possible by adopting an high injection speed. However, this processing condition results in increase of shear stress which is the main factor influencing the fibers breakage during the filling phase. Especially stiffness and impact strength are related to the length of the reinforcement, which is negatively affected by breakage during processing. RHCM has been recently employed to enhance the molded parts surface appearance. The rapid heating and cooling of a mold

cavity surface can greatly mitigate or even eliminate critical surface defects, such as flow marks, weld lines and poor surface finish due to the appearance of glass fibers . In particular, it has been detected as increasing the mold temperature the fiber reinforced molded parts surface roughness decrease (Figure 0.1). A further RHCM technology benefit is the higher flow length achievable comparing with the CIM technology for an injection molding process at the same injection pressure. This is an important aspect considering that the melt viscosity is increased by the presence of the fibers which hinder the polymer flow. Therefore, the employment of a RHCM technology for injection mold fiber reinforced materials could lead to the decreasing of the injection speed, taking advantage of the longer achievable flow length and the better surface quality, in order to increase the residual fiber length and consequently the mechanical properties of the molded composites.

Figure 0.1: Comparison between a fiber reinforced component injection molded with a CIM (on the left) and a RHCM process (on the right)

Besides the fiber reinforced materials issue, also the industry of packaging promotes more and more a reduction in the parts thickness. This is also done in the production of bottles by encouraging the use of preforms with a thickness becoming thinner with the origin of several problems related to the process. First of all, if the cooling rate is too high, the material solidifies before to complete the filling of the cavity. For preforms with high length-to-thickness ratio it is necessary to increase the injection speed causing the increasing of the cavity pressure, and consequently the material degradation. A rapid heat cycle molding solution could be the solution for these problems in fact, by increasing the mold temperature, greater flow lengths with the same injection pressure are achievable.

Figure 0.2: Example of preforms with different thickness-length ratio

Therefore, the possibility of heating the mold cavity surface before the injection phase can heavily solve the filling problems. Ideally, the rapid control of the mold temperature could be interesting not only for decreasing the injection pressure or improving the molded part appearance, but even for improving mechanical properties by thermally changing the material morphology. For example, an increase in overall crystallinity could lead to the improvements in stiffness, strength, heat deflection temperature, and chemical resistance of crystalline materials. However, the crystallization for polymers like PLA hardly takes place under conventional injection molding conditions where the cooling rate is too high for promoting the crystals nucleation. In this case a strict control of the mold temperature by using a RHCM technology could be an interesting solution for setting a favorable mold temperature for the crystals nucleation as well as control the material cooling rate in order to promote the crystals growing.

Among all available heat generation technologies, the simplest approach to thermally cycle the cavity surface temperature consists in circulating alternatively hot and cool water in the mold cooling channels. The utilization of water as operative fluid simplifies the whole system and it permits to reduce the initial investment and the operating costs. Conformal channels are used to ensure a high thermal exchange and a uniform temperature along the mold cavity. A further solution regards the development of a modular mold where inserts made of open-cell aluminum foam in order to allow high thermal diffusivity and high area to volume ratios for heat transfer. However, some disadvantages such as low stiffness and high purchase costs have limited the usage of this solution therefore, further studies are needed for developing a reliable and industrially interesting solution.

Figure 0.3: Example of products injection molded with PLA

0.2 THE AIM OF THIS WORK

The present work comes from a project of the Department of Industrial Engineering (DII) at the University of Padova. Part of this research work has been carried out within a collaborative research activity program carried out between the DII and the Polymer Competence Center of Leoben (PCCL), University of Leoben. The first purpose of this study is the development of a new solution to rapidly control the mold temperature. A further aim regards the the identification of the best process conditions that can be used to maximize the mechanical properties and surface appearance of fiber reinforced component. A final task will regard the usage of RHCM technology for improving the filling behavior as well as the mechanical properties of injection molded crystalline materials. The analysis was structured in the following points:

- An innovative RHCM system was developed replacing the traditional cooling channel with a porous insert placed behind the mold cavity surface and geometrically optimized through numerical simulation. The optimization was carried out developing a series of thermal and mechanical simulations with the aim of defining the most suitable inserts geometry to maximize the thermal exchange without impairing the mold integrity. The purpose of this study was to overcome the limitations of the available technologies concerning the cycle time and the mold temperature uniformity. A testing mold was made with the aim of validating the numerical simulations.
- An experimental analysis was carried out to understand the mold temperature, injection rate and packing pressure effects on surface topography of fiber reinforced injection molding components. A Design of Experiments analysis (DOE) was developed to experimentally study the influence of the injection mold-

ing process parameters on residual fiber length, fiber morphology and mechanical properties. A new methodology was developed for measuring the residual fibers length. The procedure involved the using of a professional scanner and a specific software able to automatically measure the fibers length. Conversely, the internal molded part morphology was investigated with an X-ray tomography system which allowed the reconstruction of the internal part micro-structure without impairing the material integrity.

- Tensile tests were conducted to investigate the influence of processing parameters on the specimens ultimate tensile stress. The results were interpreted by analyzing the correlation between residual fibers length and fibers orientation with the mechanical results.

- Fatigue tests were conducted to investigate the influence of mold temperature and part thickness on the fatigue behavior of fiber-reinforced material. A fatigue fractioned test was also carried out in order to evaluate the influence of porosity on the molded specimens fatigue resistance.

- A numerical approach was considered for studying the RHCM technology influence on injection pressure and crystallization degree of PET thin wall bottle preforms. The purpose of this task consisted in taking advantage of the high mold temperature for reducing the injection pressure, without increase the final part crystallinity above the allowed limit.

- A RHCM technology was involved in order to promote the PLA crystallization directly inside of the mold. The mold temperature and the annealing time were varied in order to investigate their influence on material crystallization and surface hardness.

0.3 OUTLINE

In Figure 0.4 it is shown the outline of this thesis connecting the RHCM capabilities with the industrial problems and consequently the researches activities carried out in this work.

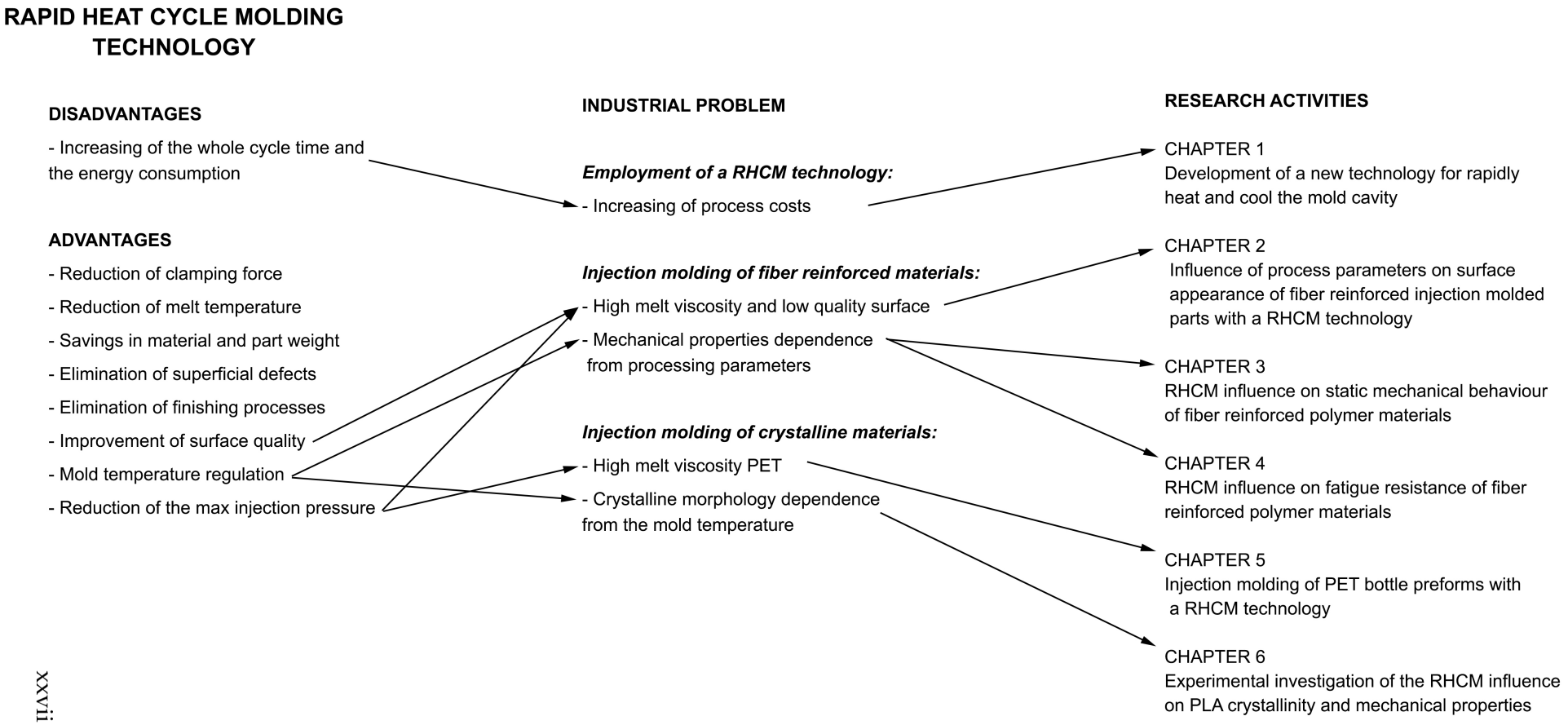

Figure 0.4: Thesis outline

Part I

BACKGROUND AND LITERATURE REVIEW

1

INTRODUCTION OF RAPID HEAT CYCLE MOULDING TECHNOLOGY

Injection moulding is one of the most widely used processing technologies in the plastics industry. In conventional injection moulding (CIM), polymer melt is injected into a closed cavity, held under pressure to compensate for thermal shrinkage until the gate freezes, and then ejected out of the cavity after the part has sufficiently cooled. A constant mould temperature is widely used in conventional injection moulding practice. The mould temperature is controlled by pumping fluid with constant temperature through the cooling channels of the mould and adjusting the rate and the temperature of the coolant. The standard injection moulding process suffers from problems caused by the large temperature difference between the mould and the incoming polymer. Upon contact with the mould surface, the polymer melt starts to solidify, almost instantaneously, at the mould surface. Because of this frozen layer, it is difficult to fill a part with a large length/thickness ratio. The premature freezing problem during the filling stage also results in weak weld lines because of the lack of molecular diffusion between the joining melt fronts. More important, the frozen outer layer deteriorates the optical and mechanical properties of the moulded part. The molecular orientations in the skin result in distributed birefringence and residual stresses, of which the latter is the primary driver for part warpage and dimensional instability. Often, the injection pressure in thin-wall moulding exceeds 100 MPa, a thousand times higher than the atmospheric pressure, resulting in high shear rates approaching $10^4 s^{-1}$. Most of the aforementioned part defects may be alleviated or eliminated if an elevated mould temperature close to or even above the polymer transition temperature is used. This elevated mould temperature, however, substantially increases the cycle time, thus lowering the productivity to a reat extent. The ideal moulding condition is to have a hot mould during the filling stage and a cold mould during the cooling stage. In reality, a single mould is used in injection moulding; therefore, means for rapid temperature change of the same mould are required to approximate this ideal moulding condition. Despite the advantages of the differential mould temperature setup, an injection mould typically presents a large thermal mass and is difficult to heat and cool rapidly within the normal injection moulding cycle. Furthermore, any modified mould should possess similar mechanical performance as a standard mould. Some early study demonstrated the capability of improving the part quality but in a rather impractical way since it in-

volved time-consuming heating and cooling of a large portion of the mould system. The number of studies on mould rapid heating and cooling has increased in recent years, especially after the 1990*s*. The primary driver comes from the growing need of precision parts, optical parts, and parts with microfeatures in the electronics and biomedical industries. Without an elevated mould temperature during the filling stage, it is difficult to mould a thin and long part without short shots, a precision part with minimal residual stress and thus acceptable warpage and dimensional stability and an optical part with a low level of birefringence. Recent works focused on selectively heating only the surface portion of the mould. Development of capable techniques for rapidly heating and cooling the mould surface portion is a difficult task because of the constraints and the endurance limits of the materials used for the mould. At present, rapidly heating and cooling a large surface area mould remains a major challenge in the polymer moulding industry. This chapter presents an overview on the state of the art in mould rapid heating and cooling, aiming at explaining the working mechanisms and providing an unbiased account of the pros and cons of existing processes and techniques. Successful applications of existing processes are described and potential improvements to these processes are highlighted.

1.1 PROCESS PRINCIPE

The mould temperature control strategy of RHCM is quite different from that of CIM. CIM process consists of plastication of the polymer pellets in barrel, filling and packing of the resin melt in mould cavity, solidification of the shaped resin melt, and mould opening to eject out the moulded part. In RHCM, the mould is circularly heated and cooled and so the cavity surface temperature fluctuates significantly. As the temperature of the cavity surface reaches the designated value, generally 10°C higher than Tg of the polymer, the resin melt in the barrel is injected into the cavity. When the thermal couple detects that the mould cavity surface has been heated up to the required temperature, the variothermal mould temperature control system sends a signal to the moulding machine immediately for melt injection. After filling and packing, the mould is cooled down quickly to solidify the shaped resin. Once the cavity surface temperature lowers to the required temperature, usually 10°C lower than the heat deflection temperature of the polymer, the moulding machine is given a signal to open the mould and the moulded part is ejected out. Then, the mould is reheated for the next moulding cycle. Figure 1.1 shows the comparison of the changes of the mould temperature during RCHM and CIM processes.

As most of the shell plastic parts just fulfill the requirement of a good outer surface appearance, only one side of the mould, usually

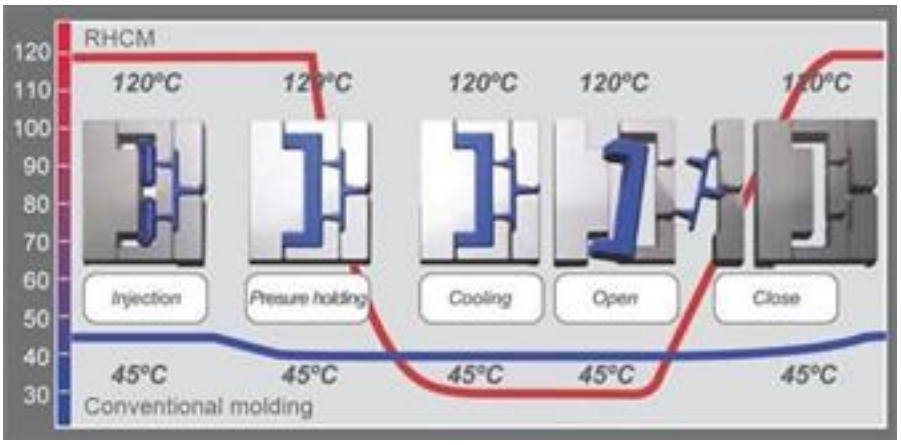

Figure 1.1: Comparison of the changes of the mould temperature in RHCM and CIM processes

the cavity side, needs to be heated. According to the temperature feedback of a thermal couple, the variothermal mould temperature control system can coordinate the activities of the heating system, cooling system, and the moulding machine to achieve a continuous RHCM process. The cycle time is one of the most important factors to be considered because it affects the production efficiency. In RCHM we expect to decrease the moulding cycle time by determining a reasonable starting time of the heating process to fully use ejecting time and mould closing time to heat the moulds. The heating process can start once the moulds are opened and the moulded part separates from the mould cavity. In this condition, the mould are heated during mould-opening, ejecting and taking out the part, and mould closing. The whole moulding cycle time, t cycle , can be expressed as:

$$t_{cycle} = t_{filling} + t_{packing} + t_{cooling} + max(t_{opening} + t_{ejection} + t_{closing}), t_{heating} \tag{1.1}$$

where $t_{filling}$, $t_{packing}$, $t_{cooling}$, $t_{opening}$, $t_{ejecting}$, $t_{closing}$, and $t_{heating}$ denote the filling time, packing time, cooling time, mould-opening time, ejecting time, mould-closing time, and heating time, respectively. max($t_{opening}$ + $t_{ejecting}$ + $t_{closing}$), $t_{heating}$) represents the maximum between the $t_{heating}$ and the sum of $t_{opening}$, $t_{ejecting}$, $t_{closing}$. However, if both the surfaces parts sides are required to have good aesthetics, the surfaces of the mould cavity and core sides all need to be heated. For this case, the heating process of the cavity and core can be started once the part is ejected out from the mould. The heating process of the cavity and core is performed simultaneously with the operations of ejecting and mould closing. In this condition, the whole moulding cycle time can be expressed as:

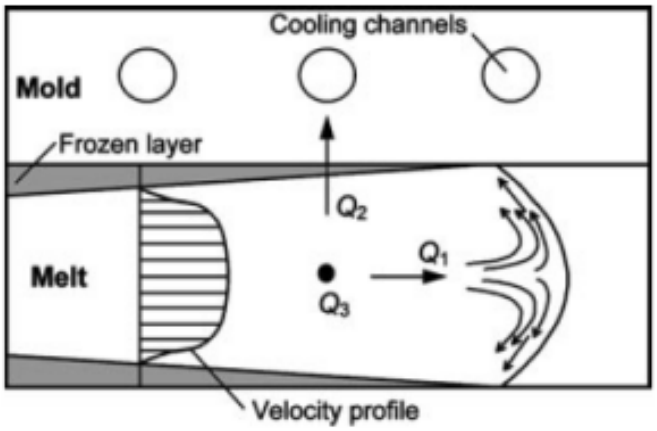

Figure 1.2: Schematic of heat transfer process in injection moulding

$$t_{cycle} = t_{filling} + t_{packing} + t_{cooling} + t_{opening} + max(t_{ejection} + t_{closing}), t_{heating} \tag{1.2}$$

1.2 HEAT TRANSFER PROCESS IN INJECTION MOULDING

There are three contributions to the heat in the thermoplastic melt during the injection stage: Q_1, convected heat from the melt; Q_2 , heat conducted to the mold; and Q_3, heat generation inside the thermoplastic. These contributions are quantitatively represented in the following equation:

$$\delta * c_p(\frac{\partial T}{\partial t} + v * \nabla T) = \nabla * (k\nabla T) + (\alpha\sigma : \dot{\gamma} + \dot{s}) \tag{1.3}$$

where δ is density, c_p is specific heat, k is thermal conductivity, T is temperature, t is time, v is a velocity vector, σ is a total stress tensor, $\dot{\gamma}$ is a strain rate tensor, α is the fraction of deformation energy converted into heat, and $\dot{s}$ is a heat generation source from a non deformation field. In Equation 1.3, $\delta c_p v\nabla T$ represents the convective energy, that is, Q_1; $\nabla(k\nabla T)$ corresponds to the conduction loss to the mold, that is, Q_2 ; and $(\alpha\sigma : \dot{\gamma} + \dot{s})$ represents the total heat generation source, that is, Q_3. In Q_3 , $\alpha\sigma : \dot{\gamma}$ denotes the heat generation due to permanent deformation, and in the filling stage, it is viscous heating, that is, $\eta\ \gamma^2$, where γ is the equivalent strain rate. Figure 1.2 schematically illustrates the heat transfer process in thermoplastic injection moulding.

1.3 RHCM APPLICATIONS AND BENEFITS

With a rapidly heated mould surface during the filling stage, the frozen layer is reduced, or even eliminated, if the mould surface tem-

perature exceeds the polymer freezing or vitrification temperature. This reduction in freezing has a profound effect on the quality of the moulded part. In particular, flow induced molecular orientations are reduced, allowing the molding of a more isotropic part. The resulting part exhibits a lower level of birefringence, reduced residual stresses, better optical properties, and improved dimensional accuracy and stability. The fluidity of the polymer is also increased, resulting in a longer flow path, better replication of surface topography and microstructures, and stronger weld lines. In addition, with active mould heating and cooling during the entire moulding cycle, the thermal history of the polymer can be controlled so as to optimize its structure and morphology. This appears to be useful for polymers, particularly for those in which structural formation is sensitive to thermal changes within the normal time scale in injection moulding.

1.3.1 *Minimizing weld lines*

Weld lines are formed during the filling stage when two or more melt fronts come in contact with each other. Weld lines represent a potential source of weakness in moulded parts. The low mechanical properties in weld lines are considered to be caused by several factors such as poor intermolecular entanglement across the weld line, molecular orientation induced by fountain flow, and the stress concentration effect of surface V-notch etc. This is a particular concern for parts subjected to dynamic loads. It is generally believed that the weld line strength increases as the temperature and pressure at the weld increases.

The contribution of the skin layer reduction combined with the less material viscosity in proximity of the weld line allow, during the packing phase, the complete filling of the small groove as shown in Figure 1.3 [1]. An high mold temperature ensures the hiding of the weld line for human eyes as well as optical microscope. The groove reduction is obtained for amorphous,crystalline and nano-filled materials, however the weld line behaviour is less understandable for fiber reinforced materials (Figure 1.4,Figure 1.5), where the weld line reduction can be achieved only within a small range of mold temperature[1, 2]. As far as the weld line resistance is concerned, a deep analysis is carried out by Wang et al.[3]. The author have tested six different materials, in particular PS, PP, ABS, blend ABS/PMMA, ABS/PMMA/nano-clay and fiber reinforced PP. A suitable mold was made for realizing tensile and IZOD impact specimens, with and without weld line. The analysis was carried out in order to study the mold temperature influence on mechanical properties. The analysis of results showed that the weld line directly influenced mechanical properties and the variation was function of the material used. The static resistance was only partially influenced by the weld line except

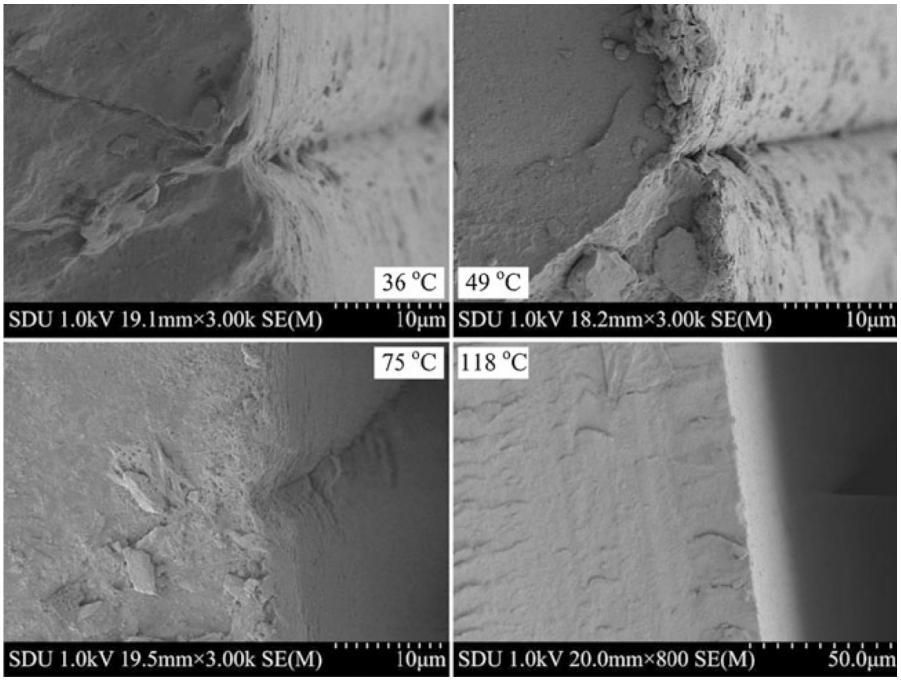

Figure 1.3: Structure of opposite flow weld line

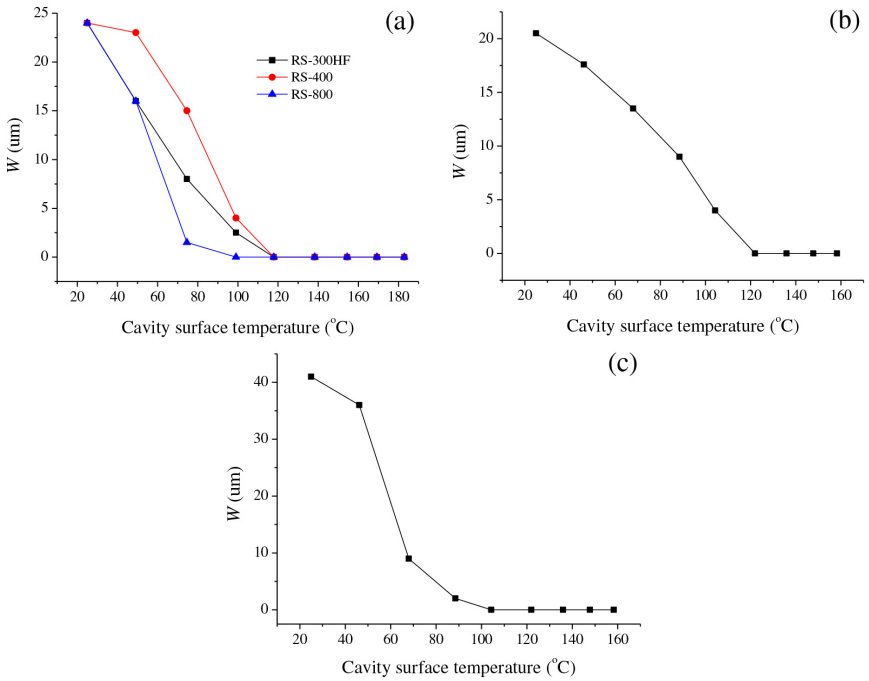

Figure 1.4: Weld line depth varying mold temperature for:(a) ABS/PMMA normal and high gloss, ABS (b) PP (c) PS

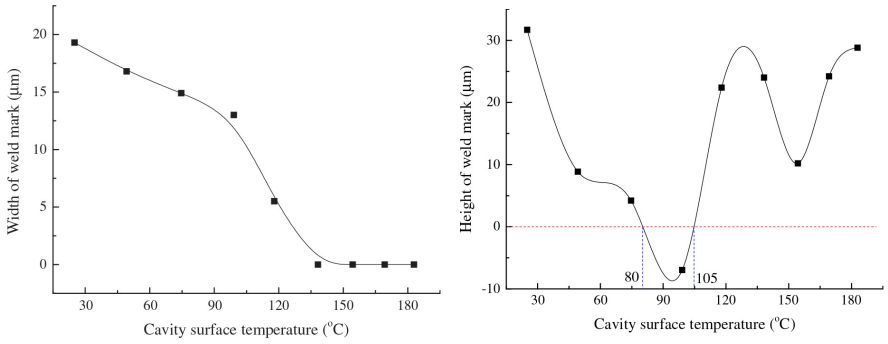

Figure 1.5: Weld line width varying mold temperature for:(a) ABS/PMMA/-nano $CaCO_3$ (b) PP 30% LGF

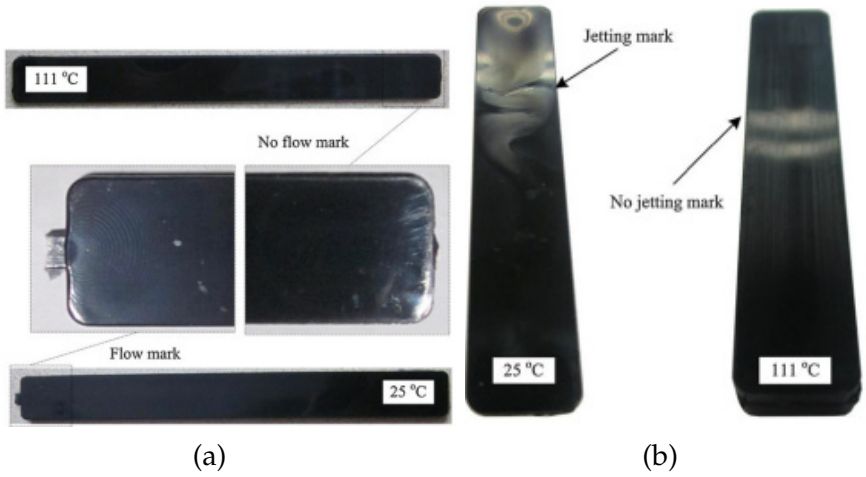

Figure 1.6: RHCM application on (a) flow marks (b) jetting marks

for the fiber reinforced polypropylene which pointed out a reduction of static resistance up to 60%. The main reduction was seen injection molding at high mold temperature. Conversely, for the impact resistance test, the weld line caused a reduction of $30 - 50\%$ for all the investigated materials. The impact resistance was slightly higher for the specimens injection molded at high mold temperature.

JETTING MARKS AND FLOW MARKS REDUCTION Considering that the jetting marks phenomenon is caused by the gate geometry and position and the injection velocity, it is not possible to completely solve this problem by increasing the mold temperature. However, using the RHCM technology it is possible to release the surface stress deleting any defects which could appear on the surface [4]. Figure 1.6 shows that an high mold temperature hides jetting marks and flow marks as well.

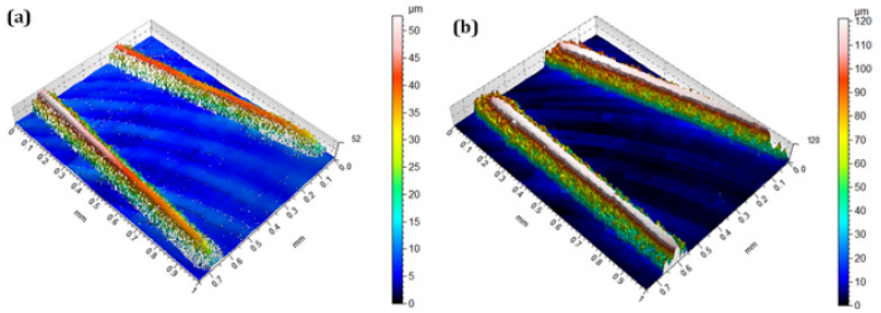

Figure 1.7: Example of micro-features replicated (a) by conventional injection molding and (b) employing the RHCM system

MICROFEATURES REPLICATION As already advanced in the previous chapters, the controlling of mold temperature is important in biomedical field where, for particular applications, it is required the replication of micro features with high aspect ratio. Reducing the melt material freezing it is possible to keep the injected melt at low viscosity ensuring the filling of the micro cavities during the packing phase. The replicability is considerably increased as reported by Lucchetta et al. [5] (Figure 1.7).

AESTHETIC APPLICATIONS In injection molding, the achievement of components with high aesthetic quality is difficult in fact, for many applications, subsequent finishing operations such as coating or painting were necessary. The increasing in importance of aesthetic components is becoming critical especially in automotive field. One of the main institutes which work about this topic is the Chalmers University of Technology of Goteborg in Sweden. There, in collaboration with Volvo, many studies were developed concerning the influence of process parameters on gloss surface and micro features replication. Pisciotti et al. [6], investigated the effects of mold temperature, injection velocity and packing pressure on respectively rough and polished surfaces. The material investigated was polypropylene charged with pigments. The results underlined that injection velocity was the main parameter and it affects the surface appearance, increasing the gloss for the mold with low roughness, while the injection velocity effect was the opposite in case of rough surfaces. In this test, the mold temperature effect was negligible due to the limited investigated range. Indeed, the maximum mold temperature was set to $60°C$. From this point of view, other research activities pointed out the benefits obtained using high mold temperature. Dawkins et al. [7], for example, highlighted that the main parameters affecting gloss were mold temperature, melt temperature, injection speed and packing pressure. In Oliveira et al. [8], similar conclusions were drawn, even though in this case, increasing the mold temperature a higher gloss surface was obtained both for polished and rough surfaces. The

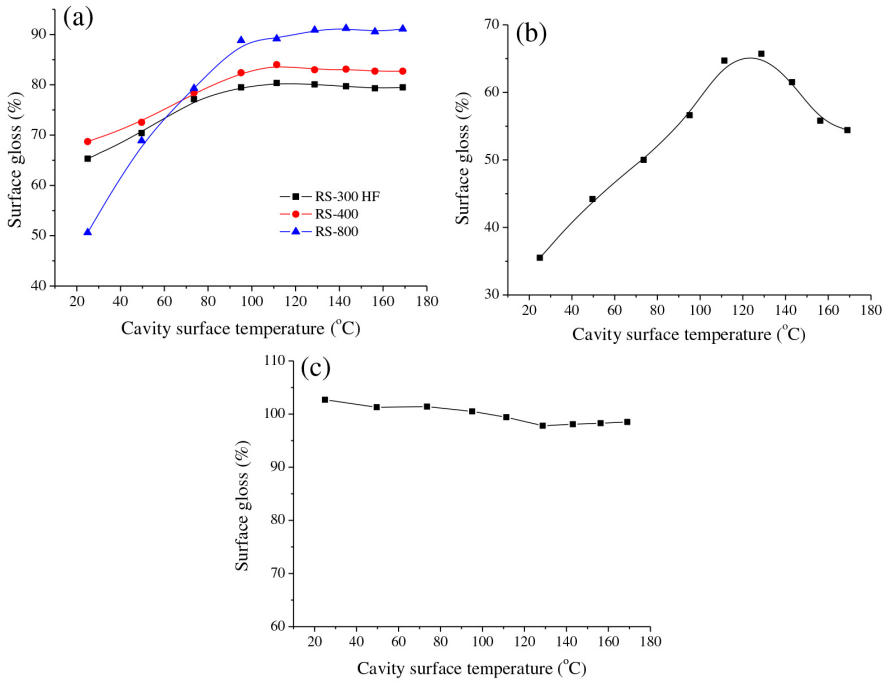

Figure 1.8: Mold temperature influence on gloss for:(a) ABS and ABS/PMMA (b) PP (c) PS

development of varioterm technologies allowed the possibility of controlling precisely the brightness and the surface roughness on the molded part surface.

Wang et al. [1, 2], in particular, have carried out several studies concerning the mold temperature influence on surface appearance of injection molded parts with RHCM, both with polished and rough cavity surfaces. The author adopted a white light interferometer to characterize the surface topography and a glossmeter for measuring gloss. Blends of ABS/PMMA, ABS, PP and PS have been investigated, as well as reinforced materials such as ABS/PMMA nanofilled and fiber reinforced PP.

Except for the PS, all the investigated materials have shown an increasing of gloss associated with a decreasing of roughness surface, as visible in Figure 1.8and Figure 1.9. It is interesting to note that there is a mold temperature threshold above that roughness surface and gloss stabilize. Therefore, it is worth considering a mold temperature value which is close to this limit in order to take advantage of the RHCM technology but still ensuring a small cycle time. Concerning the PS, which is a 100% amorphous material, the influence of mold temperature on roughness surface and gloss is almost negligible. This behavior can be understood considering the phenomenon of rough surface formation on a polished mold cavity, which is governed by the material heterogeneity. Indeed, the increasing of surface roughness is due by the nano-clay surfacing in the nano-charged ma-

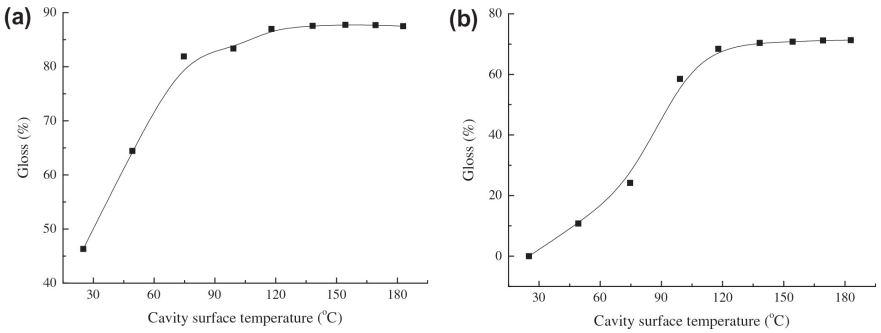

(a) (b)

Figure 1.9: Effect of process parameters on gloss for:(a) ABS/PMMA/nano $CaCO_3$ (b) PP 30% LGF

terials, the exposition of butadiene particles in the ABS and the differential shrinkage on macroscopic scale for semi-crystalline materials and blends. The PS is homogeneous therefore it does not show this phenomenon as visible in the images below (Figure 1.10) acquired with a white light interferometer.

LEAD TIME REDUCTION AND ENVIRONMENT IMPACT The results just reported are very interesting. The possibility of obtaining high gloss, directly by injection molding, open new horizons in terms of lead time reduction and simplification of the technologic cycle of high level components. In general, the benefits due to the usage of a RHCM technology can justify the purchase of a Varioterm system. In particular, producing an end product it is possible to save money regarding the equipment, the manpower, the management cost, the disposal costs and the warehouse costs connected with the finishing operation. The market lead time is also decreased, which is very important for electronics of consumption products. The elimination of these operations, the painting phase in particular, results also in an environment friendly way to produce components and to dispose them after their life.

INJECTION MOLDING OF HIGH PERFORMANCE MATERIALS There are polymer materials with high performances that historically are considered difficult to injection mold, due to their high melt temperature, up to $400°C$. For example, the PEEK material has been successfully injection molded by Roc Tool (leader in the field of injection molding) with a mold temperature of above $300°C$ in order to completely fill the mold cavity and to obtain an aesthetic surface. Therefore, this technology enables the injection molding of materials with an high ratio between mechanical properties and density ensuring a good appearance.

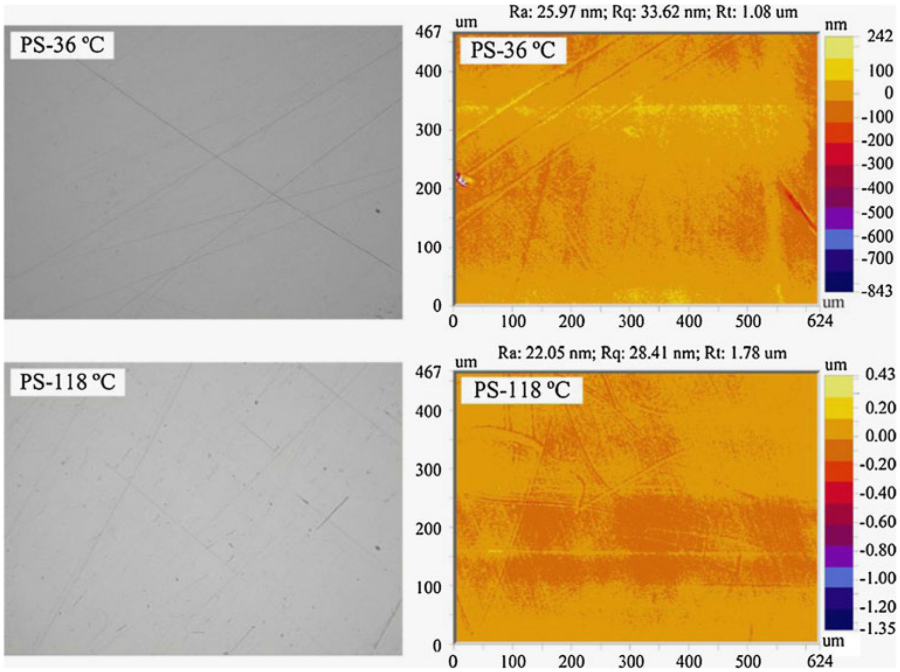

Figure 1.10: The negligible influence of mold temperature on PS

Figure 1.11: Injection molding of PEEK at high temperature (RocTool)

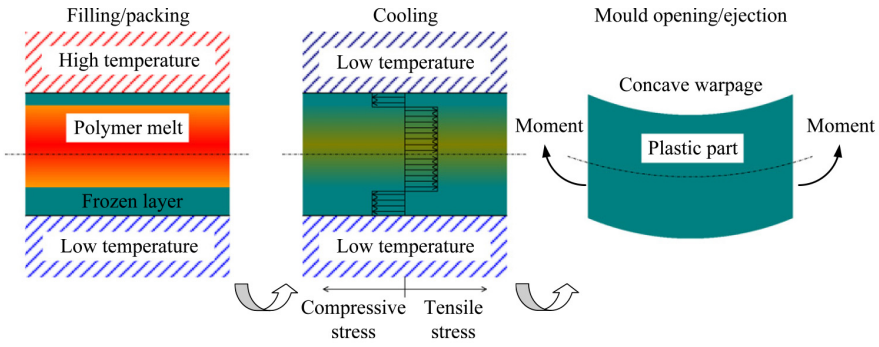

Figure 1.12: Illustration of the formation mechanism of the concave warpage in RHCM

RHCM TECHNOLOGY DISADVANTAGES As often happen in engineering, besides the benefits of a technology there are also some disadvantages. In this case, the problems can be solved through a suitable design of the mold and the process. A first issue, concerning the injection molding with high mold temperature, is due to the low material viscosity during the injection phase. It is known that during the mold life, the closure surfaces are subjected to wearing which can lead to the formation of a flash between the half molds. With a RHCM technology, it is predictable that this phenomenon occurs for less cycles considering the low material viscosity and the thermal mold fatigue. This is a further problematic since the high thermal gradients lead to fast expansion and contraction of the mold which induces the mold thermal fatigue.. Many issues have to be taken into account using a new technology as RHCM, the know-how acquisition, the system setup, the personal training and the employees safety is fundamental. Indeed, the heating of the mold can involve for example high frequency current, electromagnetic fields, hot water or steam and many other systems potentially dangerous for the operators safety. From the process parameters point of view, the warpage phenomenon has been investigated since it could be enhanced by using a Varioterm technology. This behavior has been studied by Wang et al. [9] where a process parameter optimization was carried out to minimize the warpage of a TV frame. Here, the goal was the achievement of an aesthetic surface only in one side of the injection molded part. For this aim, a RHCM technology was involved to rapidly heat the mold surface on one mold half, therefore the thermic asymmetric distribution induced leaded to an unbalancing of the melt flow due to the different thermal exchange between the polymer melt and respectively the hot and the cold mold surfaces (Figure 1.12). Here, the differential freezing of the melt through the thickness leads to a an internal stress which causes the warpage of the molded part. It is clear that the warpage phenomenon occurs in the conventional process as well, but in this case it is magnified.

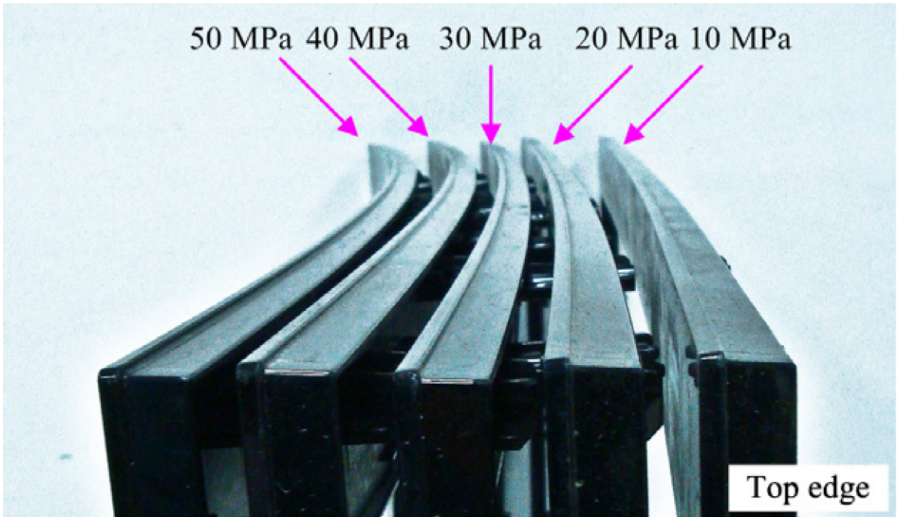

Figure 1.13: The TV front shells produced with different packing pressures in RHCM

Conversely, from the study has emerged the possibility of aging on packing pressure and packing time in order to minimize the part warpage (Figure 1.13).

To conclude, thanks to the development of reliable software of injection molding simulation, it is possible to predict the warpage amount during the design phase checking also the possibility of thermally control both the half molds in order to ensure a symmetric freezing of the part.

1.4 MOULD DESIGN FOR RAPID THERMAL CYCLING

The difficulty in designing a rapidly heatable and coolable mold arises from several specific functional requirements that a productive mold must satisfy. The typical injection pressure ranges from 10 MPa to more than 100 MPa. The high cavity pressure could cause a significant deformation of the mold cavity. If soft organic materials are involved for insulation purposes, appropriate design schemes must be utilized to minimize the amount of mold deflection. The mold must be mechanically capable of supporting an extremely high injection pressure and a large clamping force. This is important when stiff but brittle materials are used. The mold should have a low thermal mass and exhibit a low inertia to variation of thermal loads [10]. Cycle time is as important as part quality in mass production and is directly related to the manufacturing cost. Even if the formidably high heating energy could be made affordable, it would still be difficult to cool a large thermal mass within the normal cycle time. Finally, thermomechanical durability during thermal cycling is critical in mass production of plastic parts. The design of a rapidly heatable and coolable molding system must be considered carefully and must

be economically and practically feasible. For a system with different materials used for insulation and heating purposes, the thermal mismatching problem could greatly reduce the life of the mold.

1.4.1 *Constituent elements*

An industrial process or machine can be decomposed into its constituent elements. These elements can then be recombined in a systematic way into either innovative solutions. In accordance with Yao et al. [11], four constituent elements are needed for a rapidly heatable and coolable mould:

- low thermal mass;
- a stiff, strong, and durable mould;
- a mold heating system;
- a mold cooling system.

Conventionally, mould cooling is achieved with fluid coolants, usually water and less frequently air or other fluid media. Although, in theory, cooling can be achieved by other mechanisms. But these methods are expensive and less effective than conventional water cooling. Compared with heating, cooling can be performed at a lower rate because, during cooling, the injection moulding machine needs additional time for plasticating a new shot for the next cycle. Therefore, the thermal gradient developed in the cooling stage is lower than that in the heating stage and the mechanical requirements are almost solely designed for the heating means. In most studies [10, 12, 13], on mold rapid heating and cooling, although heating was carried out unconventionally, cooling was performed in the conventional way. Therefore, studies with unconventional cooling systems are uncommon.

MOLD WITH LOW THERMAL MASS For RHCM, the required heating and cooling time of the mould mostly depends on the mass of the cavity/core to be heated and cooled. A mould with a low thermal mass exhibits a low thermal inertia and can be rapidly heated and cooled. As shown in Figure 1.14, the thermal performance of a rapidly heatable and coolable mould to three thermal rates: the initial heating rate, the secant heating rate and the initial cooling rate. Previous investigations [12, 14, 15] showed that a mould with a low thermal mass can deliver a rapid temperature rise of $100°C/s$ with a heating power of the order of $100W/cm^2$. Since the heat used during heating needs to be removed during cooling, the low thermal mass is also critical for energy saving.

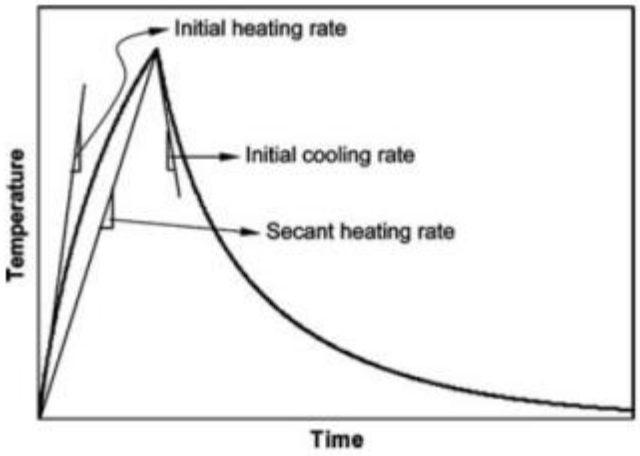

Figure 1.14: Schematic heating and cooling response at the mold surface

The thermal mass, M, can be defined as the product of mass and specific heat, as given in Equation 1.4:

$$M = \delta * V * c_p \tag{1.4}$$

where V is the volume of the mass. Three basic building blocks for a low thermal mass are revealed from Equation 1.4, that are density, specific heat and volume. The density and specific heat for most materials, including metals, ceramics, and polymers, is about 310^6 $J/(m^3K)$. Density and specific heat are intrinsic material properties that cannot be modified. The first two building blocks are not variable in practice. To reduce the thermal mass, the volume of the material being heated should be reduced. However, the extent of volume reduction is limited by some mould design constraints, particularly the required structural stiffness [16].

1.4.2 *Mould with scaffolded structures*

In the porous material building block, the mould comprises a significant percentage of voids. The actual volume of the mass is much smaller than the apparent volume of the mould. Technical approaches to this building block include scaffolded structures [17, 18]. Xu et al. [16] designed a scaffolded mould with beams as supporting elements arranged in a three-dimensional pattern, resulting in a fully open-pore mould insert. In general, to create such a mould, free-form additive manufacturing techniques are needed (e.g., selective laser sintering and three-dimensional printing). Figure 1.15 shows a demo insert with cooling channels and truss support made by $3D$ printing process. For a scaffolded mould, structural issues, particularly on the stiffness of the mould, need to be addressed in the design.

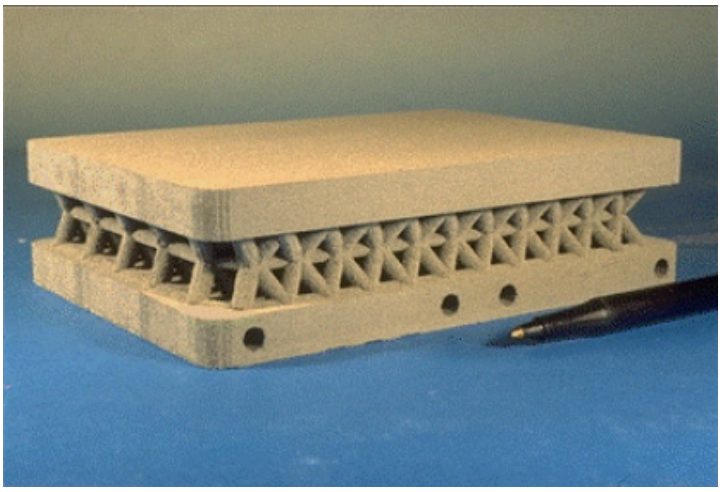

Figure 1.15: Example of a 3D printed scaffolded structure

This can be accomplished by a computer-aided structural analysis. In the case of simple internal hollow geometries combined machining and fusion techniques may be used. Yao et al. [15] created a thin plate with rectangular pockets on one side and welded this side to a thick mould base. The conformal pockets or channels placed near the mould surface create an opportunity for rapid cooling by passing a cooling medium in these spaces during the cooling stage [18, 19]. Recently, Chen et al. [20] more quantitatively investigated the use of pulsed cooling for enhancing the thermal performance, proven to be effective even for a more conventional mould design. Anyway, for structures of this configuration, a detailed mechanical analysis have to be carried out in order to completely understand their static and dynamic resistance [21].

1.4.3 *Multilayer mould*

In an insulated mass building block, a thermal insulation is sandwiched between the bulk mould base and the cavity surface portion, resulting in a multilayer mould design [12, 14, 22–28]. In this case, different materials are used in the mould. Because the thermal and mechanical properties are different between a typical conductor and an insulator, the main challenge arises from the high interfacial shear stress between the layers generated during the heating and cooling stages. Yao and Kim [14] simulated the thermal stress developed in a multilayer mould with a steel base, a metallic coating layer and an oxide insulation layer. Although most reported multiplayer moulds suffered from serious durability issues, the approach was found to be useful during passive heating [29]. Innovative technologies have been developed for creating many layers of thin materials near the surface, allowing gradual variation of properties between layers [30].

Similar techniques may be developed to improve the durability of a multilayer injection mould. Orthotropic materials have been used for mould rapid heating applications. In particular, Yao and Kim [31] used pyrolytic graphite with orthotropic properties produced in a chemical vapor deposition (CVD) process. The material exhibited a factor of 200 in thermal conductivity difference and a factor of 1200 in electrical resistivity difference, and can be heated and cooled rapidly with a thermal rate over $100^{\circ}C/s$. Although graphite is not a desired mould material, this approach could be extended to a more durable material.

1.5 MOULD SURFACE HEATING METHODS

The only two mechanisms relevant to mould rapid heating are heat generation and heat conduction. Among all possible internal heat generation mechanisms, electrical resistive heating is the most used mechanism for mould rapid heating. Electrical resistive heating can be accomplished by passing direct or alternating current in a thin electrical conductive layer or by skin effects from a high-frequency electromagnetic field. Two useful technical approaches for implementing this skin effect are induction heating and proximity heating. If the mould material is an insulator exhibiting reasonable dielectric loss, it may be heated by high-frequency dielectric heating, including microwave heating. Heat generation using the Peltier effect has also been reported in mould heating, although the thermal rate was slow. The technical aspects for each technology will be described in detail in the following sections.

1.5.1 *Electrical resistive heating*

In electrical resistive heating, the heat is generated according to Joule's first law. For safety reasons, low voltage and high current are typically desired. Most good resistive heating materials either are brittle or require a specific geometry (e.g., resistive wires). In the case of mould rapid heating, a metallic heating layer is desired. However, metals are excellent electrical conductors and therefore high resistance is difficult to obtain unless the geometry is long and thin. A schematic setup of mould rapid heating by low frequency electrical resistive heating is illustrated in Figure 1.16.

Flexible, thin-film heaters are available commercially, typically made of a zigzag thin-film metallic pattern to increase the resistance, sandwiched between two insulation layers. For this method, an insulation layer is needed beneath the thin resistive heating layer (Figure 1.17). However, any tiny scratch on the surface could result in a catastrophic failure due to nonuniform heating and local stress generated. Furthermore, the contact resistance at any connecting junctions could be

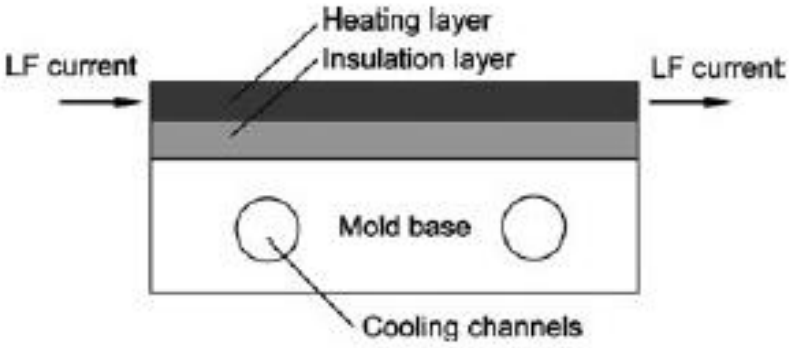

Figure 1.16: An electrical resistive heating with low-frequency electrical current

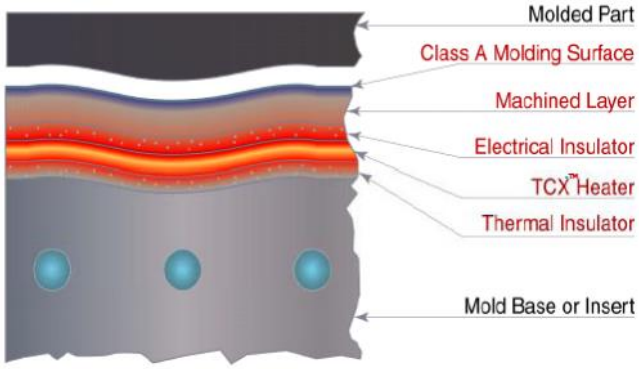

Figure 1.17: A schematic setup of mould rapid heating by electrical resistive film (Thermoceramix system)

significant, resulting in an additional failure mode. Significant efforts in multilayer resistive heating was directed to identify a identify stiff, strong, and durable materials with relatively high resistivity [22].

1.5.2 *Induction heating*

Induction heating is the process of heating an electrically conducting object (usually a metal) by electromagnetic induction, where eddy currents are generated within the metal and resistance leads to Joule heating of the metal. An induction heater consists of an electromagnet, through which a high-frequency alternating current is passed. Induction heating is an efficient means to heat the mould surface in a non-contact procedure. Chen et al. [32] applied induction heating to improve the surface appearance of weldlines. Kim et al. [33] used induction heating in a procedure that rapidly raises the surface temperature of a nickel stamp with nanoscale-grating structures. Park et al. [34] improved the mouldability of micro-features by applying high-frequency induction heating. This study applies induction heat-

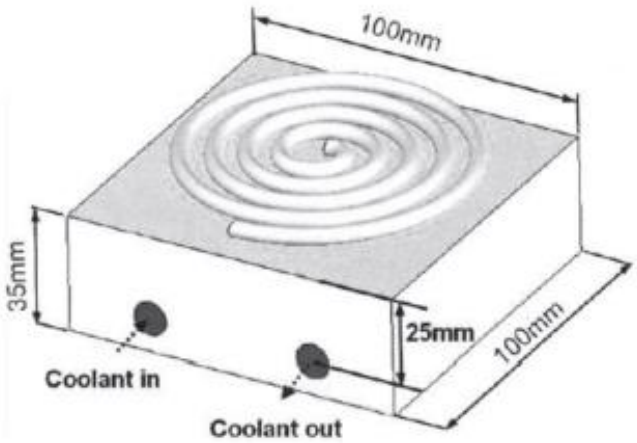

Figure 1.18: A schematic setup for induction heating of mould inserts

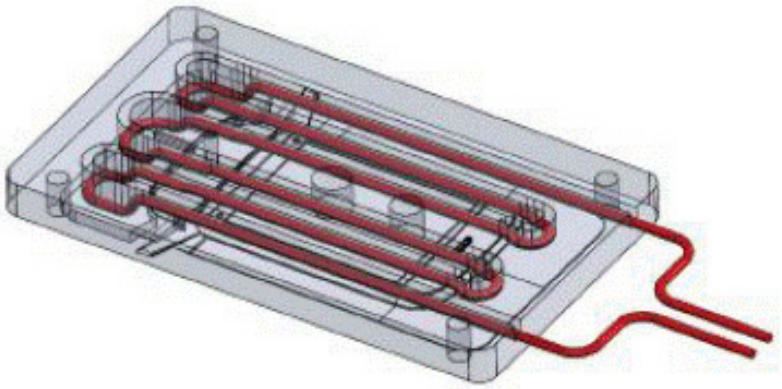

Figure 1.19: A schematic setup for induction heating with internal coils (3iTech system developed by Roctool)

ing to the elimination of weld lines in an injection-moulded mobile phone cover. A schematic setup of a induction heating system with an external elliptic coil is shown in Figure 1.18.

One benefit of this method, therefore, is that the electrical insulation right beneath the mould surface is not needed. But its use in mould surface heating requires solutions to several problems, including coil design, system operations, and parameter control. In general, direct embedment of the coil inside the mould is difficult and the common practice is to use a separate external coil. For this reason, the reported experiments were limited to mould preheating before the mould closes. Concerning the effectiveness of the internal coils solution for induction heating cannot be assessed at this moment because of the lack of experimental data reported.

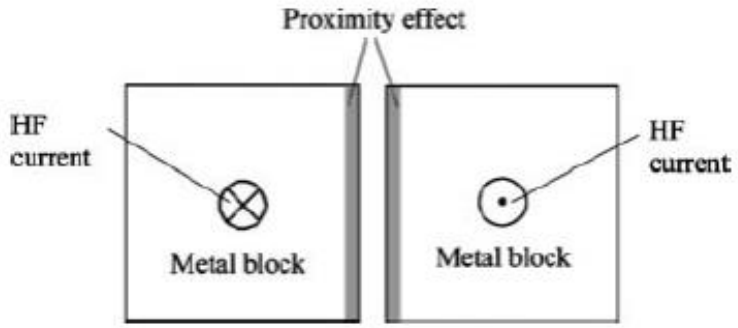

Figure 1.20: Principle of high-frequency proximity heating

1.5.3 *High-frequency proximity heating*

Another high-frequency resistive heating method is proximity heating [15]. The principle of this method is based on the proximity effect [35] between a pair of conductive blocks facing each other with a small gap in between and forming a high- frequency electric circuit, as shown in Figure 1.20. The high-frequency current flows at the inner sides of the facing pair, heating the mould surface portion. The proximity heating method does not need the presence of an electrical insulation layer beneath the mould surface. The main benefit of proximity mould heating over inductive mould heating is that the separate electrical coil is eliminated. This facilitates active heating to be performed even when the mould is closed. However, mould surfaces with complex shapes are difficult to heat.

1.5.4 *Dielectric heating*

Dielectric heating, also known as high-frequency heating, is the process in which a high-frequency alternating electric field, or radio wave or microwave electromagnetic radiation heats a dielectric material. The use of dielectric heating for mould rapid heating requires that the mould be a dielectric material and an electrical insulator. This method has limited applications in mould heating, and more often it is used for heating the polymer [36]. Dielectric heating of the polymer can be combined with induction heating for enhancing the mould heating performance [37]. In the case in which the mould is also made of a dielectric material, both the mould and the polymer can be actively heated by the high-frequency energy [38]. It should be noted that most polymers are poor electromagnetic absorbers. Therefore, either a high power source or easily excitable additives are needed for the practical use of dielectric heating of the moulding polymer.

1.5.5 *Thermoelectric heating*

Thermoelectric cooling is based on the Peltier effect to create a heat flux between the junction of two different types of materials. A Peltier heater is a solid-state active heat pump which transfers heat from one side of the device to the other side against the temperature gradient with consumption of electrical energy. The direction of heat transfer can be reversed by switching the polarity of the power supply. Sequential heating and cooling can be performed by a single thermoelectric device. Kim and Wadhwa [10] used commercially thermoelectric devices for mould heating. The major limitation of such a thermoelectric heating device is that the heat generated on one junction is rapidly conducted to the other junction because of the small space involved and the moulding heating and cooling rate with thermoelectric heating is rather slow. Whiteside et al. [39] showed that the Peltier device did not have the power to adequately control the temperature of the cavity.

1.5.6 *Radiation heating*

The radiation heating building block implements a radiation boundary condition in the heat transfer process. The energy is transmitted from a remote body in a noncontact manner in the form of rays and waves. The use of radiation for mould rapid heating has been exclusively focused on infrared heating [40–46]. As is generally known, radiation energy propagating in a radiation absorbent is exponentially absorbed and attenuated. Its relation is described by Lambed-Beer's law.

$$I = I_0 exp(-\beta x) \tag{1.5}$$

Absorbed radiation energy is converted into thermal energy, and then the absorbent temperature is increased. The extent of the radiation heating depends on the radiation Background study and literature review absorption coefficient that is a function of the material components and radiation wavelength. A characteristic point of the proposing technique is its non-contact, volumetric heating and good controllability for the heating extent. One part of the mould wall must be transparent to introduce the radiation energy from the outside of the mould blocks. Thus the moulded polymer is directly heated by radiation energy, and the temperature of the moulded polymer is easily controlled by radiation intensity. Many polymer materials have several absorption bands for infrared radiation. Rapid thermal processing using radiation heat transfer is a widely used technique in semiconductor manufacturing processes such as chemical vapor deposition (CVD) on silicon substrates. Because of vacuum environment in the CVD chamber, radiation is a more efficient heat

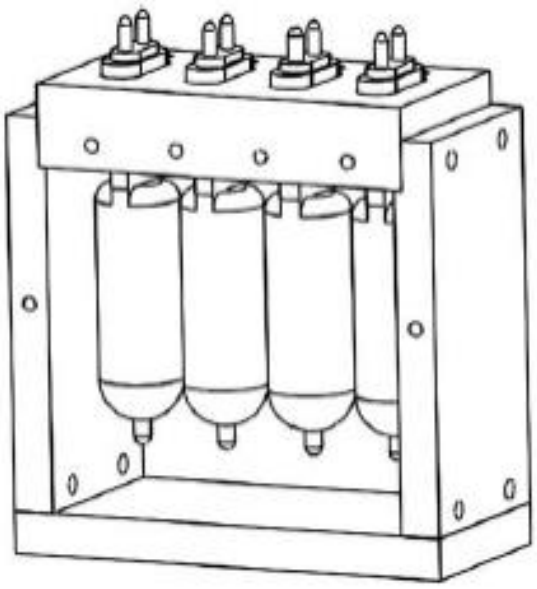

Figure 1.21: Infrared heating system

transfer mode to heat the silicon substrates rapidly. The short wavelength halogen lamps are used as the infrared source. The silicon substrate is insulated by quartz pillars and the temperature of silicon substrate can be raised from $300^{\circ}K$ to $1300^{\circ}K$ in 10s. Some researchers have studied the temperature control of the RTPCVD system. In injection moulding, multiple infrared lamps can be assembled on a lamp holder and used as a single external device that can be moved in and out of the space between the two mould plates [43–45]. A flat reflector with scattered lamps is shown in Figure 1.21.

With the modification of the infrared rapid surface heating technique for injection moulding, e.g., increase power of bulbs, focus the energy at the area of mould insert and lower the mould temperature, the cycle time can be kept within an affordable period of time. One difficulty in infrared heating is to achieve uniform heating temperature across the mould surface. Commercial optical analysis software can be used to simulate the infrared absorption of the mould surface for the first stage of analysis and to optimize the lamp pattern. Infrared lamps can be installed inside the mould plates in addition to external infrared sources [42]. In this case, infrared heat is available when the mould is closed, allowing active heating during the entire mould cycle. A schematic setup of a infrared heating system with external infrared lamps is shown in Figure 1.22.

1.5.7 *Contact heating*

In contact heating or conduction heating, a low temperature body is conductively heated by contacting with a high-temperature body. Lit-

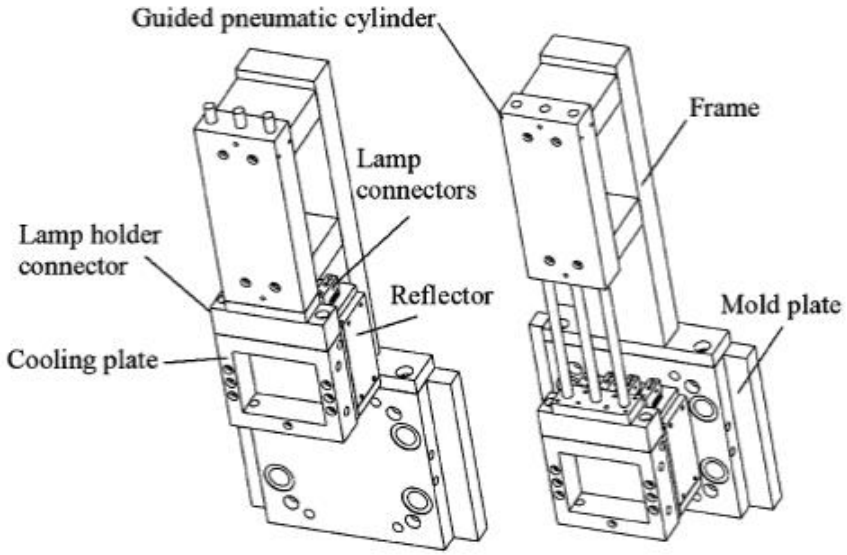

Figure 1.22: Schematic of the infrared heating system assembled on the mould

tle effort has been reported in mould rapid heating using contact heating [47]. Stumpf and Schulte [48] disclosed a mould design in which a thin inner region of the mould adjacent to a hollow mould cavity is conductively heated by a more bulky outer region maintained at a higher temperature. After moulding, the thin inner mould region together with the moulded part is cooled independent of the outer region. Yao et al.[47] experimentally investigated the use of two stations, one hot and the other cold, for rapidly heating and cooling flat shell moulds. They reported that aluminum shell moulds with a thickness of $1.4mm$ could be rapidly heated from room temperature to $200^{\circ}C$ in about 3s with a hot station at $250^{\circ}C$. The use of contact heating between solid bodies for mould rapid heating is constrained by several physical limits of the heat conduction process. Since heat conduction is a diffusion process, penetration of heat into a thick section is a slow process. For complex shell geometry, additional concerns are on the uniform contact between the contacting bodies. For these reasons, contact heating is suitable for thin shell moulds with simple geometries and high thermal conductivity. Passive heating of the mould surface by the incoming polymer melt may be considered as one special case of contact heating. In this case, the major mechanism for heat transfer is also heat conduction. A practical solution is to incorporate an insulation layer at the mould surface, as exemplified in the literature [23, 49]. If a metallic surface is needed, as in compact disk moulding and micro moulding, a separate metallic stamp with microstructures can be placed over the insulation layer and heated by passive heating. In general, the mould surface temperature rise due to passive heating is moderate; however, a proper use of this effect

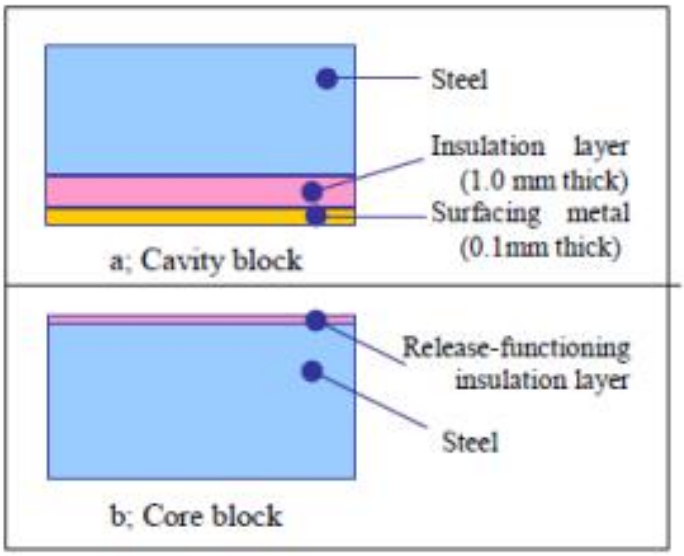

Figure 1.23: The basic composition of ULPAC cavity and core block

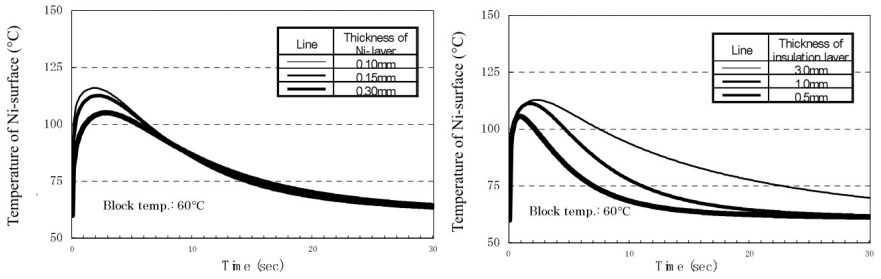

(a) (b)

Figure 1.24: Thermal behaviour of the metal surface layer in varying (a) its thickness and (b) the thickness of the insulation layer

can result in a significant delay of the frozen layer formation, thus improving the moulding quality. Iwami et al. [50] developed an injection mould system with an insulated thin metal cavity surface and a release-functioning core surface, as shown in Figure 1.23. Immediately after mould-filling under a low pressure such as one third of that in conventional moulding, the cavity surface rapidly increases in temperature to develop wettability and adhering, while the resin on the core side is released and migrates toward cavity side to compensate the surface shrinkage. Before deciding a proper ULPAC-cavity block, simulations for the thermal behaviour of ABS melt and metal surface was performed under variable parameters using a simulation software Figure 1.23.

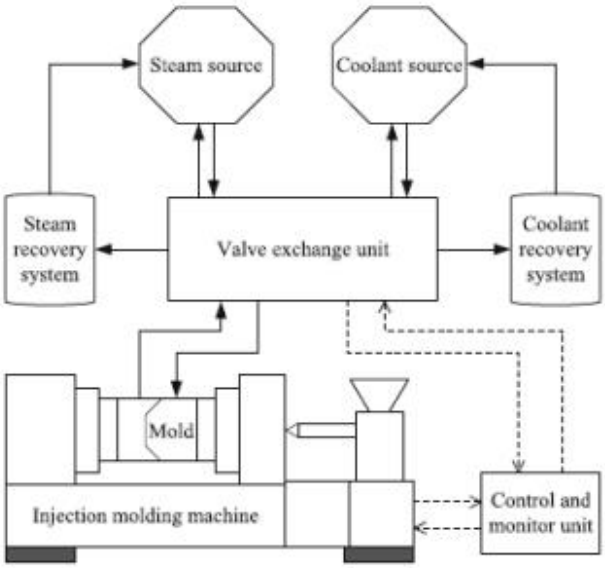

Figure 1.25: Composition and structure of RHCM systems with steam heating

1.5.8 *Convective heating*

The convective medium (oil, liquid or heated gas) imposes a convective heat flux at the fluid–solid interface. The heated fluid may be circulated inside the mould or directly introduced to the mould surface from the mould cavity. The internal convective heating method is the most common method of controlling mould temperature in the traditional injection moulding industry. Some earlier efforts in mould rapid heating and the earlier version of the variotherm mould heating process [51] were based on this method. In internal convective heating, heated oil has been the most widely used heating medium. But the reported heating response in these systems was quite slow, typically needing more than several minutes to achieve a $100^{\circ}C$ change of temperature. In order to overcome the limited heating temperature of oil, hot air and steam can be used. In particular, the steam heating method has recently generated some interest in the industry. An example of an RHCM system with steam heating is illustrated in Figure 1.25. It consists of a steam system, a coolant system, a valve exchange unit, a control and monitoring unit, an injection moulding machine, a steam-heating mould.

Conventional machining like CNC drilling can be used to make straight channels. But this technology doesn't allow producing complicated channels in three-dimension, especially close to the wall of the mould. An alternative method that provides a cooling system that conforms' to the shape of the part in the core, cavity or both has been proposed. This method utilises a contour-like channel, constructed

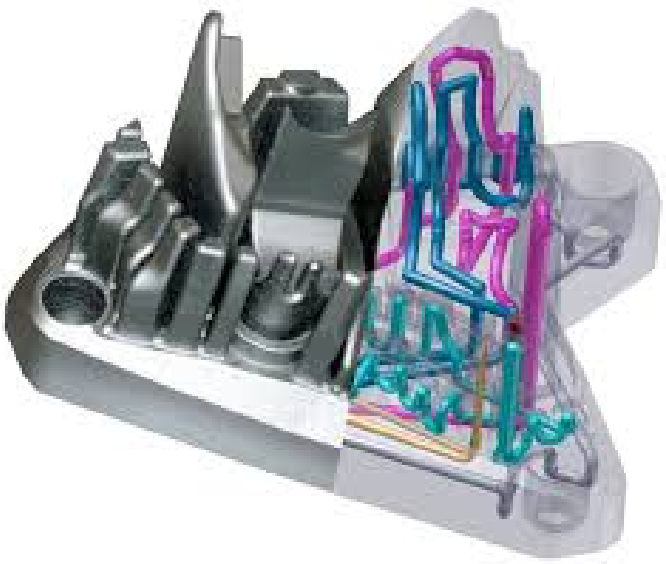

Figure 1.26: An example of RHCM mould with conformal cooling channels

as close as possible to the surface of the mould to increase the heat absorption away from the molten plastic Figure 1.26.

The RHCM technique with electric heating and coolant cooling is the most widely used system in the injection moulding industry. For RHCM, the heating and cooling system design of the electric-heating moulds are of great importance because they have a decisive influence on the moulding cycle and the part quality [52–54]. Figure 1.27 gives the schematic cavity structure of a typical electric-heating mould. For the cooling system, the diameter, Dc , of the cooling channel is about 6–8 mm. Considering the factors of the mould strength and the cooling efficiency, the distance, Hc , from the centre of the cooling channel to the cavity surface and the pitch, Pc , between adjacent cooling channels are, respectively, 3–4.5 times and 2.5–3.5 times of the diameter of the cooling channel. For the heating system, the diameter, Dr , of the heating rod is about 4.5–6.5 mm. The distance, Hr , from the centre of the heating rod to the cavity surface and the pitch, Pr , between adjacent heating rods are, respectively, about 1–1.5 times and 2.5–3.5 times of the diameter of the heating rod. During the heating process, the empty cooling channels can improve the heating efficiency by retarding the heat loss. Before heating, the remaining water in the cooling channels of the mould must be drained out. In order to achieve a good heating effect, the clearance between the heating rod and the wall of the mounting hole in the cavity or core should be smaller than 0.05 mm. Xi-Ping Li et al. [55], proposed a strategy for optimizing the distances between the neighbour heating channels in order to achieve a uniform temperature distribution on the cavity surface.

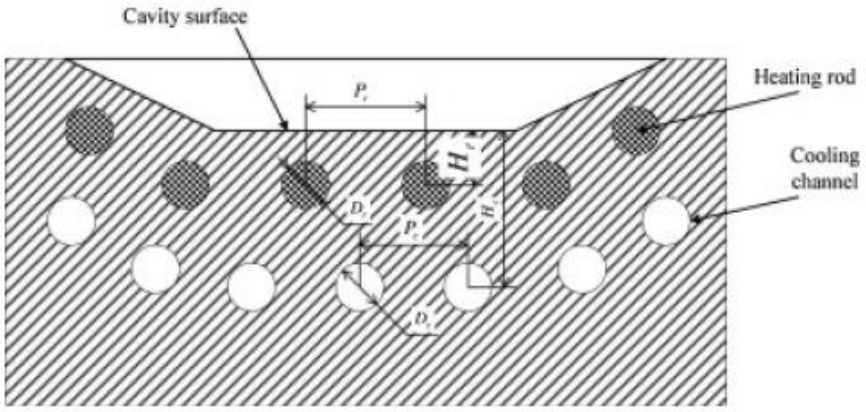

Figure 1.27: The schematic cavity structure of a typical electric-heating mould

However. the temperature profiles of conventional channels show local differences, which cannot be avoided. This problem has been solved with the new ball-filled (BF) mould, developed by the Kunststoff-Institut Lüdensheid, Germany. Figure 1.28 shows the schematic structure of the innovative ball-filled mould. It utilizes the entire area behind the cavity for homogeneous heating and cooling. This provides for efficient flow through the cooling area, thus affecting the cavity's surface very directly. A cooling process fitting closely around the contours with simultaneous high water flow rates can be achieved. Only those parts of the mould that are close to the cavity are heated, which ensures extremely fast and energy-efficient heating and cooling processes. BFMOLD TM ® can be integrated in the mould for a wide range of moulded parts, but can also be used selectively, restricted to critical parts of components. Both conformal channels and ball filling allow rapid and uniform heating of the cavity and provide mechanical support to contrast high injection pressures. However, conformal cooling channels are expensive to produce while ball-filled slots can be realized only for parts with plane geometry.

The BFMold system stems from the idea of locating a wide pocket behind the mold cavity and close to it in order to rapidly heat and cool the mold surface without impairing the mold integrity. However, from the thermal exchange point of view, the balls do not concur to the heating of the cavity, in fact the contact between balls and cavity plane takes place only in the contact areas which are created by the local elastic deformation. Otherwise, they disturb the water flow causing local instabilities depending on the flow rate. Moreover, due to the lowest surface/volume ratio, the balls have an high thermal inertia which is a disadvantages from the energetic point of view. The idea of replacing the balls with a foam aluminum insert was born from Fiorotto et al. [5]. It is very innovative since it satisfies many of the requirements needed for this application. The metallic foams, be-

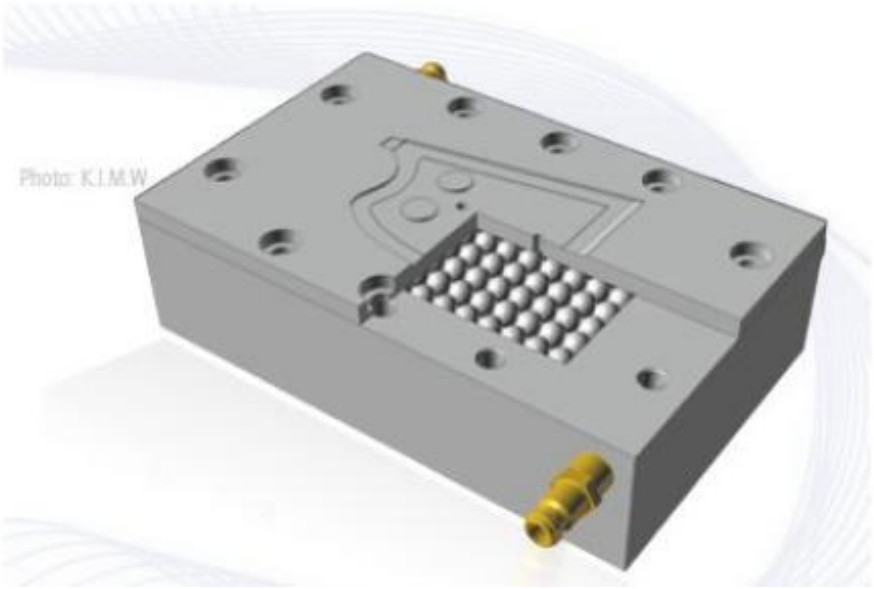

Figure 1.28: Schematic view of the BFMOLD TM technology principle

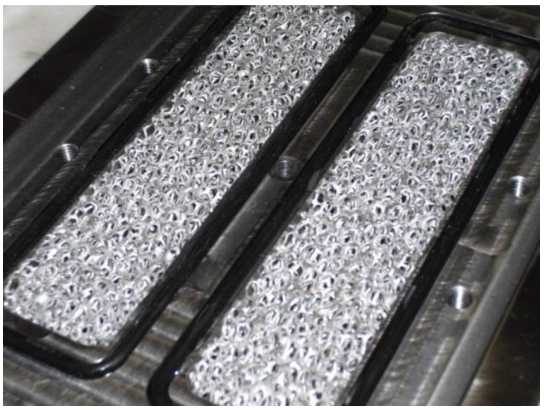

Figure 1.29: Mold with the alluminum foam inserts

sides the advantage of supporting the mold plate, they are involved in the thermal exchange. A further benefit is the low thermal inertia which is approximately negligible. The metallic foam solution has been used widely in aerospace field, where the thermal exchanges have to ensure an high efficiency combined with a low weight. The heating speed obtained was remarkable, considering the limit of this technology. In Figure 1.30 it is possible to see the mold cavity heating profile; in this case the a pressurized water flowed through the aluminum foam at $130^{\circ}C$, with an initial mold temperature of $60^{\circ}C$.

Besides the thermal improvements, the realization of a mold equipped with aluminum foam is also easier. A bulk of metallic foam can be machined by tooling machine in order to obtain a defined shape, therefore, unlike from the BFMold technology, it is possible to use this kind of inserts for any shape, obtaining a conformal and three-dimensional structure. However, for this kind of application, the limit is the me-

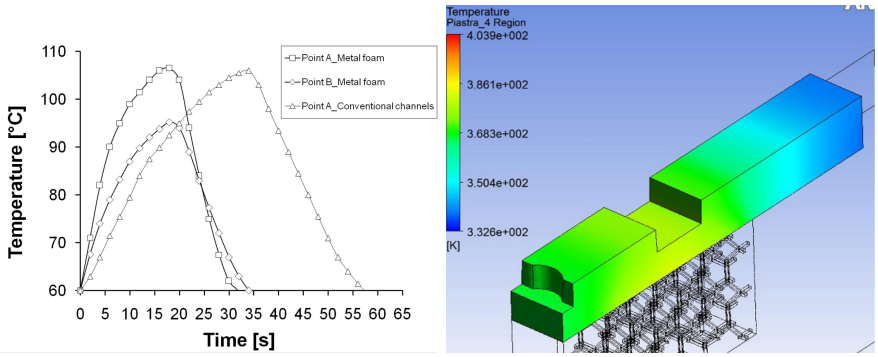

(a) (b)

Figure 1.30: Mold temperature response: (a) temperature profiles (b) temperature distribution

chanical resistance [21]. Their elastic modulus is low and, due to their shape, they have several location of stress concentration. Therefore, it is understandable to expect a low static and dynamic mechanical resistance for this solution.

1.5.9 *RHCM technology summary*

Figure 1.31 summarizes the RHCM technology presented in the previous chapters [11]. In this table are reported the different technology usable nowadays for rapidly heat and cool the molds. A brief analysis has been carried out for each technology, even though the complexity of the system and the applications variability make this rigid classification less useful.

TABLE III
Comparison of Different Methods for Mold Rapid heating Based on Different Performance Criteria

	Heating Uniformity	Maximum Energy	Heating Efficiency	Capability for Heating Complex Mold Shape	Capability for Heating Large Surface Area	Ability of Using Single Metallic Mold	Thermal Stresses	Ability for Active Heating	Complexity in Mold Design and Fabrication	Difficulty for Thermal Measurement
Low-frequency resistive heating	M[a]	H	H	M	M	Nearly impossible	Extremely high	Possible	H	M
Induction heating	M	H	M	M	M	Possible	M/H	Difficult	M/H	H
Proximity heating	L	H	M	L	L	Possible	M/H	Possible	M	H
Infrared radiation heating	M	H	L/M	M	M	Possible	M	Need a transparent mold	M/H	M
Internal oil heating	H	L	M	H	H	Possible	L	Possible	L/M	L
Internal steam heating	H	L	M	H	H	Possible	L	Possible	L/M	L
External hot air heating	M/H	M/H	L/M	M	L/M	Possible	M	Not possible	M	M
Flame heating	M/H	H	L/M	M	M	Possible	M/H	Possible	M/H	M
Passive heating	H	L	H	H	H	Possible	L	Not possible	L	H
Contact conduction heating	L/M	M/H	H	L	M	Possible	L	Difficult	M	M
Thermoelectric heating	M	L	L/M	M	L	Nearly impossible	H	Possible	M	M
Dielectric heating	M	Dependent on molding polymer	Dependent on molding polymer	M	L/M	Possible	L	Possible	L/M	H

[a]H, high; M, medium; L, low.

Figure 1.31: RHCM technology summary

2

INJECTION MOLDING OF FIBER REINFORCED MATERIALS

2.1 MECHANICAL PROPERTIES OF FIBER REINFORCED MATERIALS

Recently, the composite materials have been widely studied both from academic and industrial point of view, due to their advantages such as machinability and high specific mechanical performances combined with low costs. Using fibers, as additive, allow the increasing of mechanical properties such as stiffness and resistance. However, the injection molding process, which is the most used technology for producing composite materials, leads to a significant fiber breakage during the process, impairing the mechanical effect. The fiber reinforced thermoplastic polymer can be classified in two categories, depending on their aspect ratio:

- Short fibers, if the average residual fiber length is lower than 1mm;
- Long fibers, if the average residual fiber length is within the range 1-25mm.

The usage of short fiber reinforced polymer materials hardly become established in industrial applications, due to their low value added compared with the neat materials. To overcome this limitation and to satisfy the market demand, long fiber reinforced thermoplastics (LFT) have been developed. They bridge the gap between the composite materials with short fibers and continuous fibers, obtaining better mechanical properties than the short fiber filled materials but still maintaining the property of being injection molded. However, the fiber breakage which occurs during the injection molding process prejudices the final result. The long glass fibres have an initial length of typically 10-12 mm, but almost all the fibers are broken before their freezing in the final part, among the polymer matrix. Deep studies, concerning the fiber length influence on mechanical performances of fiber reinforced polypropylene, have been carried out by Thomason [56–61]. In particular, in [60] different fillers have been tested from mechanical point of view: short fibers with a diameter of 14 um and 19 um; long fibers with an initial length of 12.5mm and a diameter of 19 um, denominated respectively SF14, SF19, LF19. Besides the fillers type, their concentration was also varied between 10% and 50% of weight. Figure 2.1 shows the results obtained for

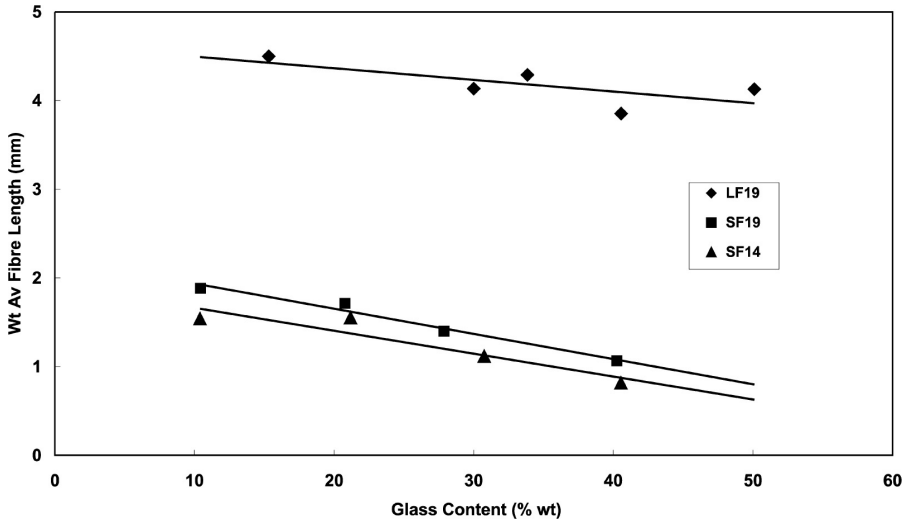

Figure 2.1: Residual fiber length versus fibre content

the residual fibers average length as a function of their concentration. It is evident that the composite LF-PP allow to obtain longer fibers in the final parts, compared with the SF-PP. However, the higher the concentration the lower the residual fiber length, regardless the fibers dimension. This behaviour is due to the higher interaction which occurs for higher concentrations of fibers.

Figure 2.2 describes the results obtained for the elastic modulus, where it is possible to note an approximated linear relation with the fiber concentration. Conversely, only a slight improvement was detected by using long fibers rather than short ones because the tensile elastic modulus is mostly influenced by the fibers and the matrix elastic modulus, the fibers concentration and their orientation rather than their residual length. Concerning the tensile resistance, it is increased for longer fibers, even though the fibers orientation was decreased. These effects give an opposite contribute actually hiding the benefits of longer fibers on mechanical properties. Figure 2.3 shows that the tensile strength has not the same trend of the elastic modulus, otherwise the ultimate tensile stress decreases continuously for higher concentration of fibers. Anyway, the images show that the reinforced material performances are definitely higher than the neat matrix.

As far as the impact resistance is concerned, the notch shape influence on impact resistance seems to be negligible comparing the Izod and the Charpy tests. Analyzing Figure 2.4 and Figure 2.5, it is possible to see that the higher the concentration the higher the impact resistance in particular for long glass fibers.

More recently, some studies of Thomason were focused on relations between structure and performances regarding long fiber composites with a percentage of fibers between 0 and 75% [61, 62]. The main mechanical properties results are reported in Figure 2.6 which shows the composites behavior in terms of elastic modulus, tensile and impact

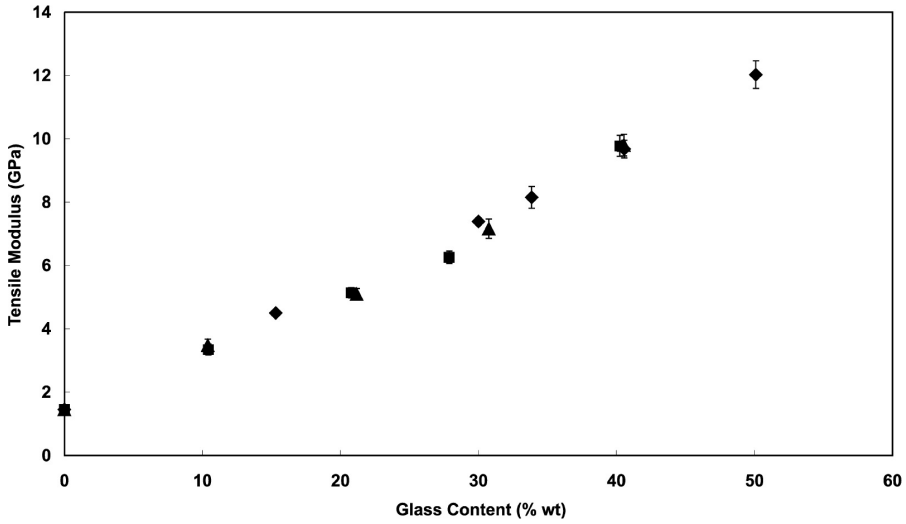

Figure 2.2: Tensile Young's modulus versus fibre content

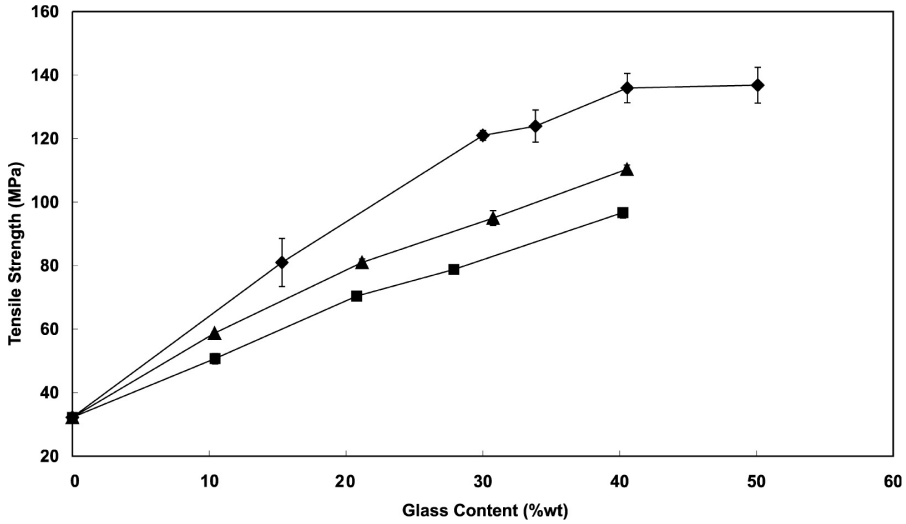

Figure 2.3: Tensile strength versus fibre content

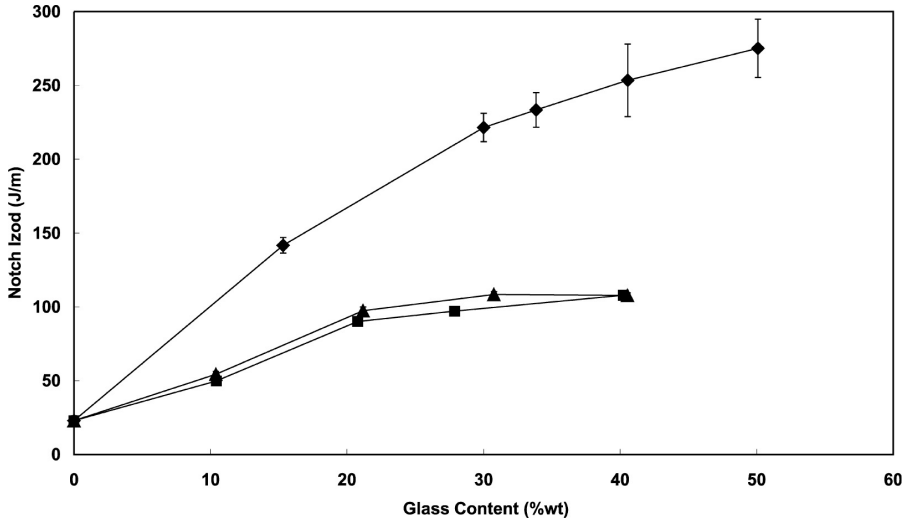

Figure 2.4: Notched Izod impact versus fibre content

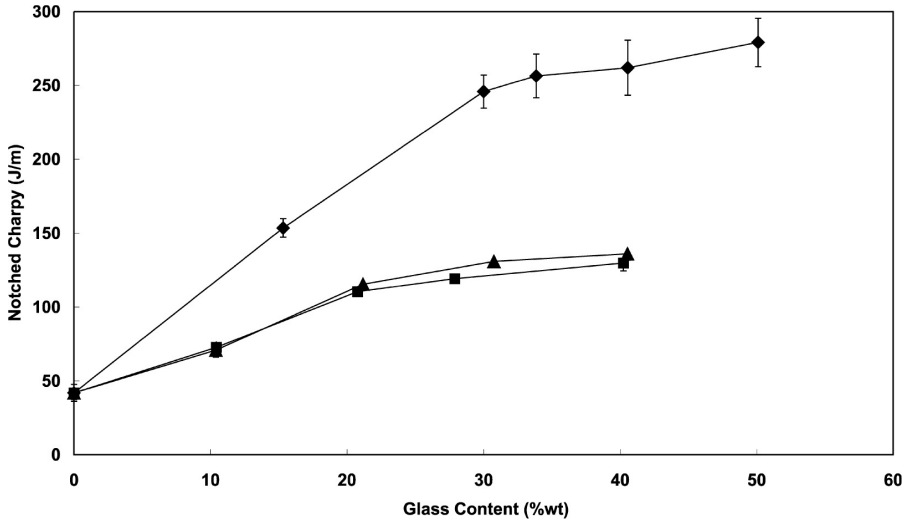

Figure 2.5: Notched Charpy impact versus fibre content

resistance normalized with the neat polypropylene performances. It is possible to understand that, even though the elastic modulus grow up almost linearly with the amount of fibers, the tensile strength and the impact resistance show a maximum in correspondence with a fiber percentage in the range of 40%-50%, whereupon their value decrease almost matching the neat polypropylene performances at the 73% of fiber content.

Plotting the mechanical properties trend as function of the residual fiber length, it is possible to highlight two different plateau in correspondence of short and long fibers. Therefore, above a threshold, a further increasing of fiber length does not lead to an increasing of mechanical properties.

This critical point is different varying the mechanical properties: the composite stiffness reaches 90% of the maximum obtainable load for a fiber length of 1 mm; for the tensile strength, a fibers length of 7 mm are needed to reach the 90% of the maximum obtainable load while in order to maximize the impact strength the fibers should measure at least 16 mm. Therefore, it is allowed to define the concept of critical fiber length, though it depends on the specific mechanical property. One of the main important parameter affecting the mechanical resistance is the interfacial adhesion between fibers and matrix. The development of new additives and materials able to maximize the interfacial resistance has been an interesting topic for many researchers. Indeed, it enables the stress transfer from the matrix to the fibers, enhancing the composite resistance. Moreover, the interaction between fibers and matrix is different considering amorphous or crystalline materials. For the latter, the matrix morphology, the fibers surface properties, the residual stress and the elastic modulus of fibers and matrix play an important role regarding the fiber-matrix interaction which is also influenced by the processing parameters such as

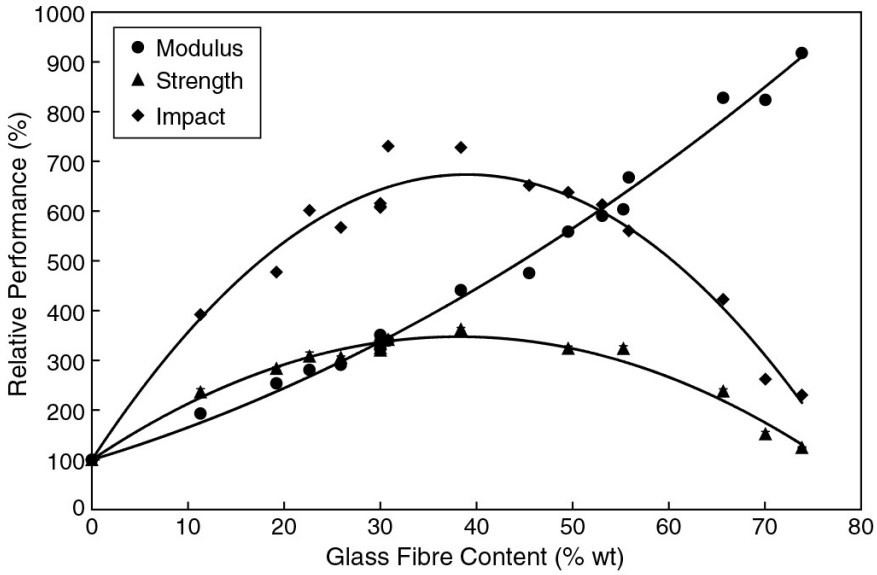

Figure 2.6: Normalized mechanical properties versus fibre content

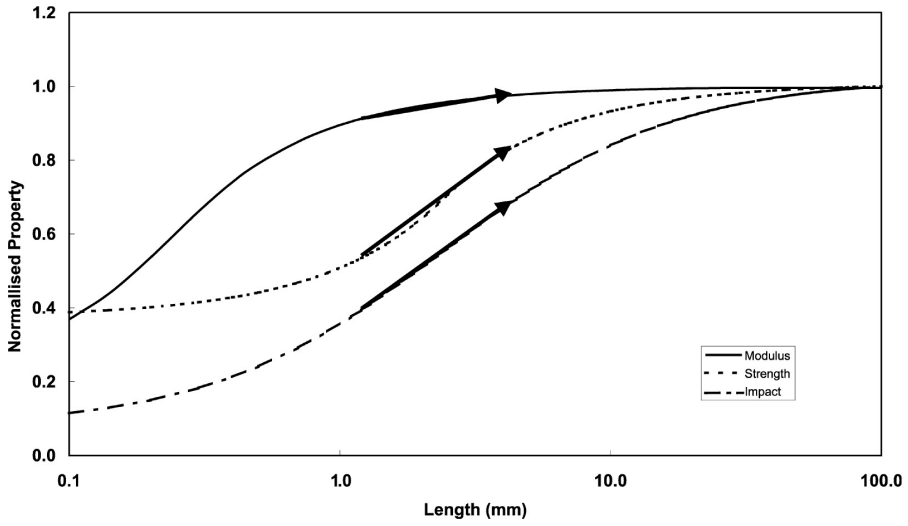

Figure 2.7: Modelling of mechanical performance

melt temperature, injection speed, cooling time, packing pressure and time [63, 64]. Kumar et al. [65] have carried out several studies with the aim of describing the residual fiber length and fiber content influence on mechanical properties of long fiber reinforced polypropylene (LGFP). An additive (Maleic-anhydride grafted polypropylene) has been used to increase the fibers adhesion and its concentration was optimized by performing several tests of fiber pull-out. In this investigation an additive percentage of 2% was detected to be the optimal amount for maximizing the interaction adhesion between glass fibers and polypropylene. An injection molding campaign was carried out in order to investigate the fibers length and the additive presence influence on composite tensile strength. For this purpose, pellets with fibers of different length (3, 6, 9 and 12 mm) have been considered. Even though the composite mechanical properties are affected by the final fiber length, which is lower than the initial pellet length, in this work the correlation between the reinforced material and tensile strength were done considering the initial fiber length. The aim was determining the optimal initial pellet length for the conventional injection molding process. In Figure 2.8 and Figure 2.9 it is plotted respectively the composite tensile strength and the elastic modulus as function of the initial fiber length and the additive presence. It is possible to see that without additive, increasing the fiber length there is not a significant increasing of the tensile strength for the LGFP composite. Whereas, by inserting the additive the longer the fiber length the higher the tensile strength with an initial grow rate of 23%. As far as the elastic modulus results are concerned, the analysis showed that the stiffness is less influenced by the presence of the additive. Conversely, the fiber length affects positively the tensile modulus with an initial grow rate of 10%. To conclude, for the injection molding of glass fiber reinforced polypropylene, an initial fiber length of 9 mm provides the best performances in terms of mechanical properties since a longer fiber would not further increase the resistance due to the deterioration phenomena which occur during the process.

2.1.1 *Fiber degradation*

Residual fiber length and fiber orientation are the main parameters affecting mechanical properties of fiber reinforced injection molded components, therefore a detailed understanding of structure and mechanical properties connection is needed. Concerning the fiber breakage, in scientific literature, several studies are related to the mechanisms which take place in the barrel and inside of the mold during the plastification and the injection phase. In long fiber thermoplastic injection molding, the initial fiber length is 10-13 mm but unlikely it is possible to have fibers with this length in the final part. Even though the fibers can break during any phase of the injection mold-

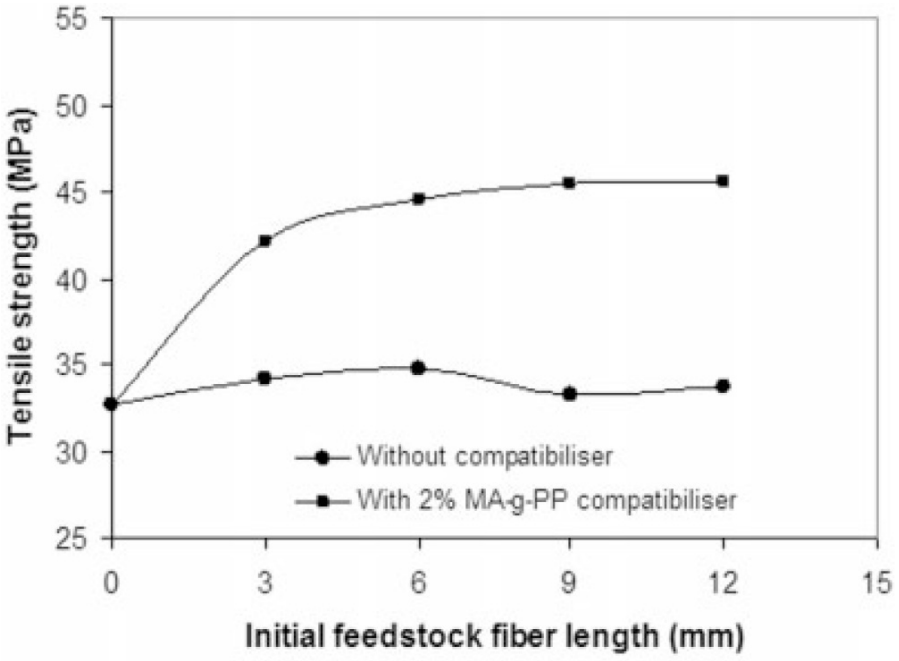

Figure 2.8: Effect of feedstock fiber length on the tensile strength of composite

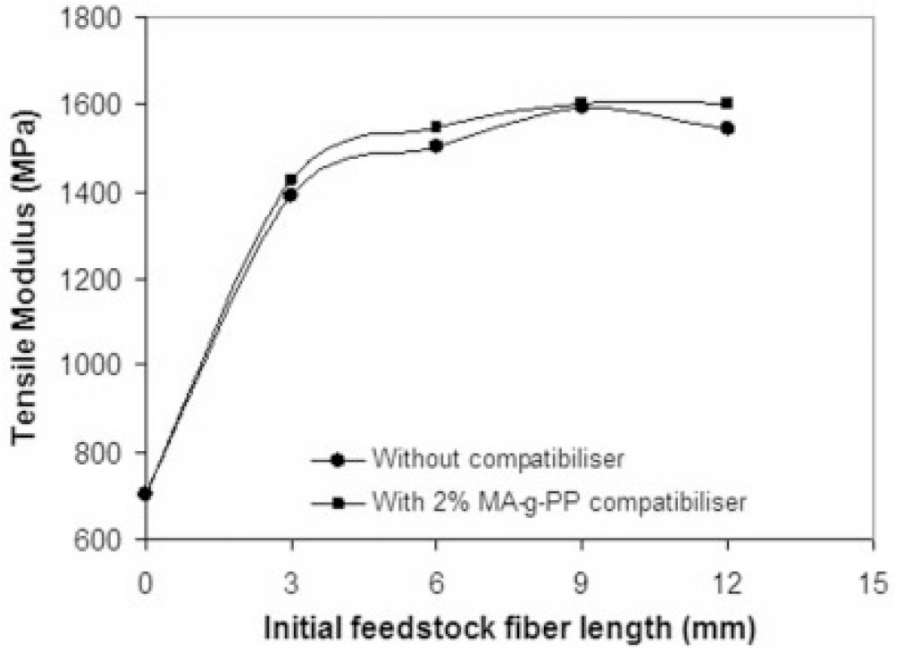

Figure 2.9: Effect of feedstock fiber length on the tensile modulus of composite

ing process, Bailey and Kraft [66] observed that a significant friction take place before the injection phase, specifying that the most of fibers breakage occurs in the nozzle and in the screw. The authors pointed out that fibers with an initial length of 10 mm in a polyamide matrix, are reduced to a length of 1 mm at the end of the injection process, with an average fiber length of 1.6 mm at the nozzle outlet. A residual fiber length of 1 mm in the average, has also been observed by Vu-Khanh et al. [67] where rectangular plates of PBT and PET with a thickness of 6 mm were injection molded. Several works deal with the studying of injection molding parameters influence on fiber breakage such as: screw back-pressure, injection velocity, melt temperature and nozzle design. On the whole, all the parameters which cause a decreasing of the polymer shear stress induce a minor effect on fiber breakage (high melt temperature, low back pressure, ecc.). An exhaustive analysis was carried out by Lafranche et al. [68]. Recently, Chen et al. [69] have proposed an empirical model for reducing the screw effect on fiber deterioration by investigating the screw geometry. That work was focused on the relation between pellets length and screw diameter. However, the studies have also demonstrated that most of the fibers are broken during the melt flow through the cavity and the runner system. O'Regan and Akay [70] and La Franche et al. [68] have studied the residual fiber length injection molding both for a plate and a complex component. In particular, O'Regan and Akay have also evaluated the difference between fibers length in the core and in the skin positions as well as the fiber length degradation along the flow path in the mold cavity which was almost the 30% in some cases. In accordance with the studies of Bailey and Kraft, the fibers length in the core position were longer than those in the skin layer. This phenomenon has been explained considering the high shear stress which affects the skin and the shell layers. The work of Wang et al. [71] was aimed to study the shear stress effect on residual fiber length and orientation for long fiber reinforced polypropylene. A dynamic technique was proposed in order to force an oscillatory shear stress on polymer melt during the packing phase. The results show that, even the fibers were subjected to an higher orientation, the induced shear stress causes a huge fibers breakage. It has also been demonstrated that long fibers are more susceptible to fiber deterioration than short fibers. An example of the relation between residual fiber length and shear rate is shown in Figure 2.10 and Figure 2.11 were the filling of a central gate disk was simulated with the software Moldex3D [72]. It is evident that there is a proportionality between shear rate and fiber length. The average fiber length decreases considerably near to the gate position where the shear stress was the maximum.

Despite the high number of experimental works carried in literature about the fiber breakage, only few publications tackle the ana-

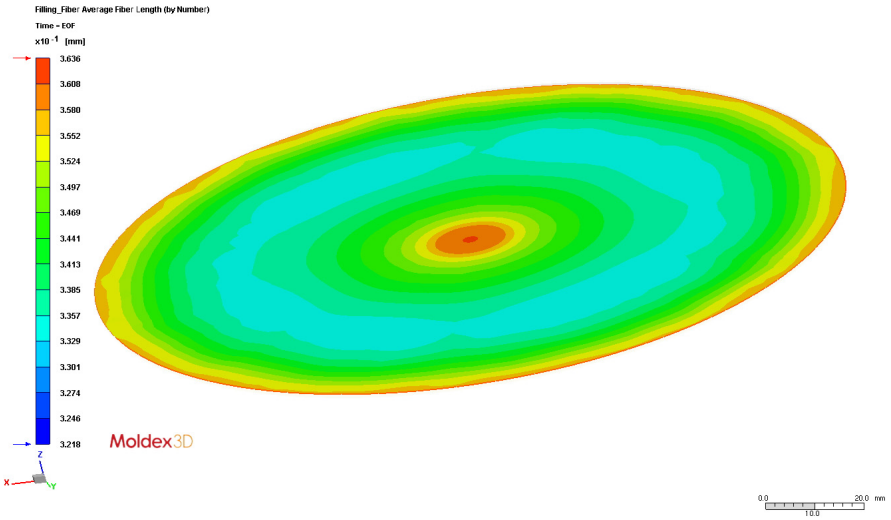

Figure 2.10: Fiber length distribution (number-average fiber length) for molding filling of center-gated disk

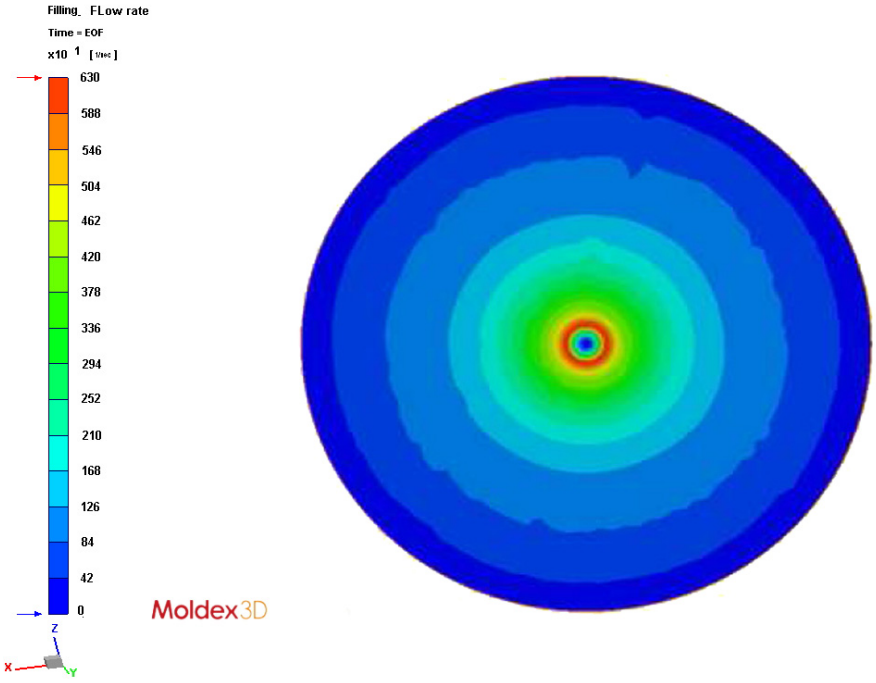

Figure 2.11: Shear rate distribution (number-average fiber length) for molding filling of center-gated disk

lytical modellation of this phenomenon. Phelps and Tucker [73] have developed one of the first quantitative models for predicting the fiber deterioration which occurs in the runners system and subsequently in the mold cavity during the injection phase. A similar model is recently published by Durin et al. [74]. For big parts, where the structural resistance is critical, the residual fiber length simulation is fundamental to understand the variation of fiber length and orientation through the components. The model assumes that a fiber is broken when it is loaded with hydrodynamic forces, causing the fiber buckling. However, during the polymer flow, the fibers are subjected to many other contributes which could lead to their breakage. The contacts between fibers, for example, could promotes the fiber flexure, but also it could lead to the formation of an intertwinement which could preserve the single fibers preventing their breakage. The Tucker and Phelps model rely on the hydrodynamic forces which affects the fibers, in fact it is composed by an equation which describes the fibers total length conservation, combined with a fiber breakage ratio function based on fiber buckling due to the hydrodynamic forces. The microstructure at any position within the flow is described by a discrete approximation of the fiber length distribution. Chosen a finite increment of fiber length $\triangle$l, and let $l_i = i\triangle l$ be a discrete length value, i ranges from 1 to n. The function of fiber length distribution $N_i = N * (l_i, x, t)$ is therefore, proportional to the number of fibers with a length of l_i, per unit of volume, in the position x and at the time t. The fibers length distribution is often summarized by giving an average length value. Here one must be careful to distinguish how the average is computed. The number-average fiber length Ln is

$$L_n = \frac{\sum N_i l_i}{\sum N_i} \tag{2.1}$$

The basic equation that governs the dynamics of the fiber length distribution expresses how N_i changes when fibers break. To write this equation we must define the rate at which parent fibers break, and the corresponding rate at which new, shorter children fibers are formed. The fibers, broken or intact, have to follow a conservation low: balancing the decreasing of fibers with their increasing number due to the generation of shorter fibers it is possible to write the following equation:

$$\frac{dN_i}{dt} = -P_i N_i + \sum_k R_{ik} N_k \tag{2.2}$$

Where N_i is the number of fibers with a length of l_i at the time t, P_i *$\triangle t$ is the probability that a fiber of length l_i is broken between $\triangle t$. $R_{ij}\triangle t$ is the probability that a fiber of length l_j is generated from the breakage of a fiber of length l_i (with l_j<l_i). The new fiber generation rate is determined by assuming that the breakage point was distributed along the fiber with a gaussian profile.

$$R_{ij} = G_{norm}\left(l_i, \frac{l_k}{2}, Sl_k\right) \tag{2.3}$$

Where G_{norm} is the normal Gaussian probability density function for the variable l_i with mean $l_k/2$ and standard deviation Sl_k. The variable S is a dimensionless fitting parameter that control the shape of the Gaussian breakage profile. A small value of S corresponds to a high probability of breakage occurring near the fiber center, while a large S value distributes the probable breakage points more evenly along the fiber length. The subsequent step was the development of a constitutive equation able to provide the breakage rate P_i as function of flow conditions and fiber properties. For a single fiber, the probability of breakage due to hydrodynamic force is expressed by:

$$P_i = C_b \dot{\gamma}_{max}\left\{0, \left[1 - exp\left(1 - \frac{F_i}{F_{crit}}\right)\right]\right\} \tag{2.4}$$

Where C_b is the breakage coefficient, $\dot{\gamma}_{max}$ is the shear rate and the force F is given by the Dinh Armstrong law [75], divided for the fiber buckling critical force. This ratio is the following:

$$\frac{F_i}{F_{crit}} = \frac{8\zeta\eta_m l_i^4}{\pi^3 E_f d_f^4}\left(- \quad \hat{D} : \quad \hat{A}\right) \tag{2.5}$$

Where $\hat{D}$ and $\hat{A}$ are respectively the deformation velocity tensor and the orientation tensor. The other variable are function of the fiber and matrix properties, while ζ is the factor of drag. Considering a model which take into account the total material stress and deformation is important in injection molding where the shear rate profile varies considerably through the thickness. From the mechanical point of view, a model which take into account the distribution of fibers length is important particularly for tensile strength and impact resistance. The model of Phelps and Tucker is employed for the fiber length and orientation prediction in the software Moldflow and it can be implemented in a conventional filling simulation. Figure 2.12 shows the fiber length calculated with the model for a circular cavity with a centered gate. The fiber length distribution in each node has been used for calculating the the average Lw. The obtained values have been utilized to plot the boundaries in the figure. It is visible that the fiber are longer in correspondence of the medium plane of the cavity (z=0) due to the low shear stress and the minor accumulated shear deformation in this zone. Going closer to the cavity surface, the fibers became shorter due to high shear stress and shear deformation accumulation. Finally, for the material adjacent with the mold surface, the fibers there are rather long in fact the material which arrives from the core position in the fountain flow, as soon as it touches the cold surface it freezes almost instantaneously and it is not subjected to high shear anymore.

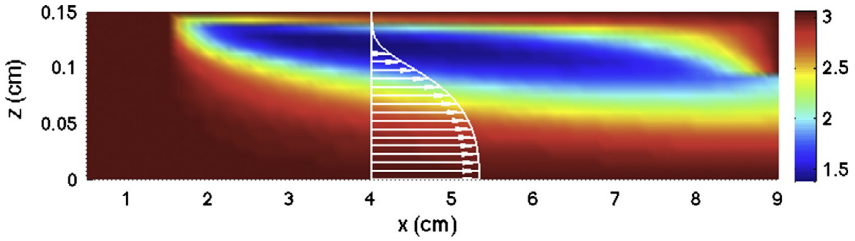

Figure 2.12: Contours of weight-average fiber length Lw versus position in the mold cavity. Colorbar fibers Lw in mm. x measures distance along the flow path, starting just downstream of the gate. z measures distance from the cavity midplane. the arrows indicate the velocity profile at x=4cm

A quantitative comparison between the experiments and the predictions appears in Figure 2.13, which shows the average lengths as a function of distance along the flow path. The predicted curves are flat for x < 1.5 cm, because the fiber length calculations actually start at this location, which is point A. Average fiber length (again, averaged across the part thickness) initially decreases with flow length. This is because fibers farther down the flow path have experienced greater shear strains, and thus have had more opportunity to break. The weight-average length decreases more rapidly than the number-average length, because it is more sensitive to the number of very long fibers, and these fibers are the most likely to break. Closer to the end of the flow path both of the average lengths increase. This is a result of the fountain effect, as discussed in connection with Figure 2.12. The model is quite a good fit for this experimental data, though the changes in average fiber length are fairly modest in this particular example.

The model just described is in good accordance with the experimental data but it has the disadvantage of requiring a great deal of computation. The fiber model tracks a discrete fiber length distribution (FLD) at each spatial node, and approximately 100 variables must be computed at each node. This amount of computation is not practical for a computer-aided engineering tool. To overcome the computational cost issue, Vèlez-Garzia et al. [76] have studied a reduced order model without impairing the simulation accuracy. The results calculated with the new model, have been compared with the experimental data obtained by injection molding a plaque of polyamide charged with 40% of long glass fibers. The critical issue was determining the number of variables to use in the model in order to achieve a reliable residual fiber length prediction. The analysis of results showed that a four variables model was representative for the prediction of the fiber length average through the thickness. However, the local residual fiber length calculation can be carried out appropriately by using eight variables.

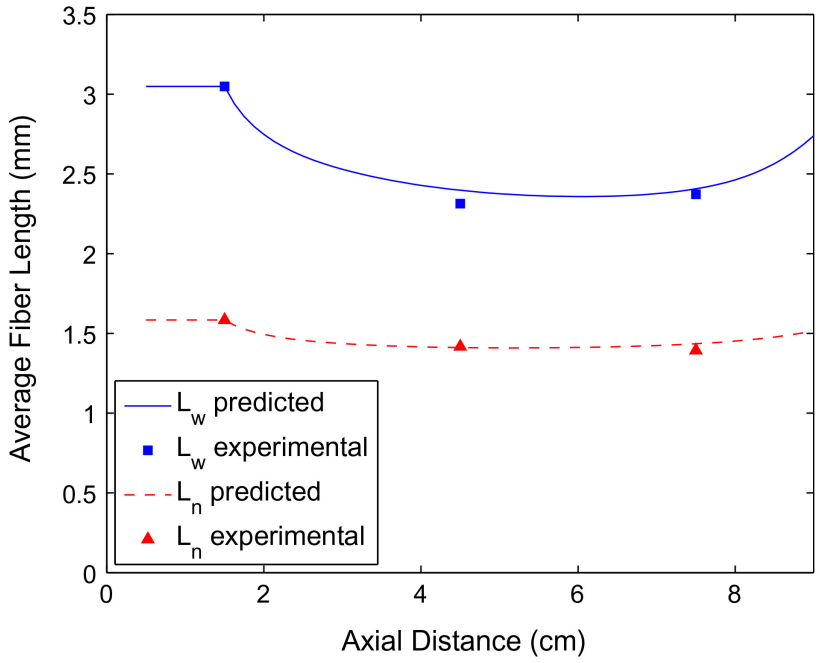

Figure 2.13: Experimental and predicted average fiber lengths as a function of flow distance for sample AF3D. Predictions begin at point A (x = 1.5 cm), using the measured length distribution there as the initial condition

2.1.2 *Fiber orientation*

In injection molding of fiber reinforced thermoplastic, one of the main challenge is the fiber orientation prediction since it directly affects the physical and mechanical properties of the final part. The fiber distribution through the thickness and along the flow path is a function of the mold cavity geometry and the injection molding parameters. Several works in the scientific literature deal with the injection molding parameters optimization for maximizing the performances. Concerning short fiber reinforced thermoplastics, the fiber orientation phenomenon has been widely investigated in literature [77, 78]. The polymer flows through the mold cavity where the fibers are subjected to shear and elongational stresses which cause their orientation inducing the material anisotropy. Regarding the fiber reinforced materials with long fibers, their interaction make difficult the orientation phenomenon since the fibers mobility is reduced and their entanglement prevent the orientation. However, either for long or short fibers, they tend to organize through the thickness with a multilayer structure typically induced by the injection molding process and the fountain flow in particular. The orientation profile is symmetric as visible in Figure 2.14 and it can be divided in the following layers:

- Skin: it is the layer directly in contact with the wall where the fibers have not a preferential orientation. This behaviour can be

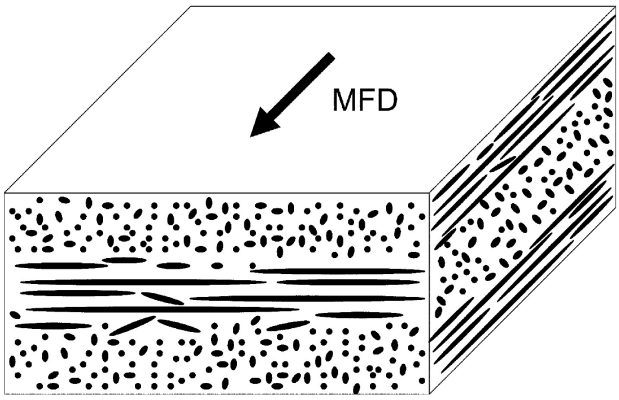

Figure 2.14: Layering configuration of an injection molded plate

attributed to the fountain flow: the fibers close to the flow front are pushed toward the cold surface where they freeze almost instantaneously;

- Shell: here the flow induces a considerable fibers orientation due to the high velocity gradient in the wall proximity;
- Core: in this layer the fibers are oriented perpendicularly with the flow direction. In this position there is a low velocity gradient through the thickness.

In general, the relative thickness of these layers depends on the cavity shape, its thickness and the process parameters. An interesting work of Hine et al. [79] analyzed the fibers distribution (FOD) and mechanical properties of two plaques injection molded varying the processing parameters in order to obtain two different residual fiber length. The plaques were called medium (average residual fiber length= 0.92 mm) and long (2.54 mm). Two different conclusions were drawn from this investigation:

- The main important is that FOD was independent from the residual fiber length but rather from the mold cavity shape and its interaction with the flow front;
- The fibers density was higher in correspondence of the core layer, compared with the shell layer.

In parallel with the experimental approach, several studies are related with the fiber orientation prediction. A general assumption is made in all the model implemented: a composite material can be considered as a mix of particles in suspension within a viscous vehicle and subjected to possible hydrodynamic and mechanical interaction. The suspension can be dilute, semi-concentrated or concentrated depending on the occurring interaction:

- In a dilute suspension the fibre will be never close to each other and there are not interaction;
- In a semi-concentrated the hydrodynamic interactions become significant;
- In a concentrated suspension, the fiber orientation become very complex because there are both mechanical and hydrodynamic forces between the fibers.

Jeffery [80] was the first which modelled the single fiber motion inside of an uncompressible fluid. Its model is applicable only for the suspensions so diluted that any interaction between the fibers is negligible. However, the majority of the composite materials have a fiber percentage in a range of 10% to 50% therefore they are considered concentrated suspensions. Folgar and Tucker [81] have modified the Jeffery model adding an element proportional with the velocity gradient in order to consider the interactions between fiber and fiber in a concentrated suspension. This element, called interaction coefficient and indicated with C_i reduces the orientation degree compared with the Jeffery equation, providing a result in line with the experimental observations. The model of Folgar Tucker (FT) have been widely utilized due to its reliability. The base equation is the following:

$$\frac{Da_{ij}}{Dt} = -\frac{1}{2}\left(\omega_{ik}a_{kj} - a_{kj}\omega_{ik}\right) + \frac{1}{2}\lambda\left(\dot{\gamma}_{lk}a_{kj} + a_{lk}\dot{\gamma}_{kj} - 2a_{ljkl}\dot{\gamma}_{kl}\right) + 2C_l\dot{\gamma}\left(\delta_{ij} - 3a_{ij}\right) \tag{2.6}$$

Where:

- a_{ij} is the fiber orientation tensor;
- ω_{ij} is the velocity tensor and gamma is the deformation velocity tensor;
- λ is a constant which is function of the particles geometry;
- C_l is the interaction coefficient between the fibers, a scalar parameter which is useful for calibrate the model with the experimental data.

More recent researches have nevertheless demonstrated that the fibers orientation in a concentrated suspension evolves slower than that predicted by Folgar-Tucker. To solve this problem a further model called RSC was developed [82]. It is based on the fiber orientation reduction thanks to a scalar factor k, where $K <_1$. The smaller the factor the slower the tensor evolution with the flow. When k=1, the RSC model matches the initial Folgar-Tucker model. Recently Phelps and Tucker [83] have developed a new form of the RSC model (denominated ARD-RSC) which takes into account the interactions

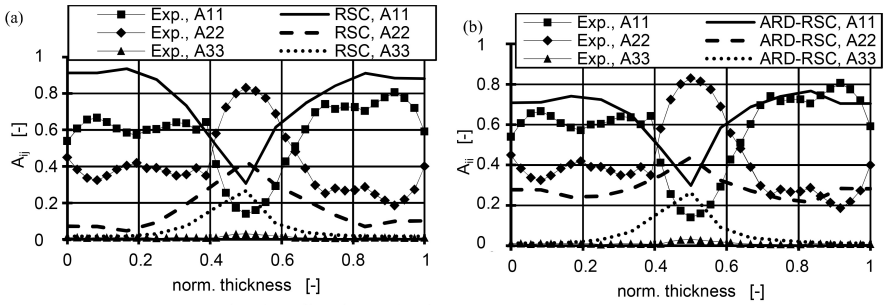

(a) (b)

Figure 2.15: Measured and predicted FOD with the RSC model (a) and the ARD-RSC model (b)

anisotropy and the fiber-fiber interactions using six model coefficients. This model purely phenomenological allows the improvement of the fiber orientation prediction in particular for long fibers. In the Hopmann study et al. [84] the model RSC and ARD-RSC are compared to predict the fiber orientation on specimens made in long fiber reinforced polypropylene. From the experimental point of view, the orientation was measured thanks to a tomographic analysis and subsequently compared with the results obtained from the simulation carried out with the software Moldflow. For the characteristic parameters, the default values were considered. The orientation tensor through the thickness is visible in Figure 2.15. The coordinates are defined as following: 1 for the flow direction, 2 for the trasversal flow direction and 3 for the direction along the thickness. Figure 2.15 (a) and (b) compare the experimental results with the RSC and the ARD-RSC models respectively.

The model ARD-RSC shows a better prediction of the orientation tensor compared with the RSC, mostly concerning the orientation in proximity of the cavity wall where the RSC model overestimates the orientation along the flow direction. As far as the second tensor component is concerned, both the models underestimate the orientation in the flow orthogonal direction. Considering these results, the authors suggest to calibrate the model parameters in function of the utilized material.

2.2 FATIGUE BEHAVIOUR OF FIBER REINFORCED MATERIALS

The long glass fiber thermoplastic (LFT) are often utilized in structural applications where they are subjected to cyclic loads, therefore a fatigue characterization of these materials is becoming fundamental. Several factors govern the fatigue behavior of fiber reinforced materials, however, their influence is not detailed studied yet. In particular, it is fundamental the prediction of the damage mechanisms which are function of the residual fiber length and orientation, the matrix prop-

erties, the fiber-matrix interfacial resistance and the test conditions. The polymer fatigue resistance depends on the testing frequency, the specimen deformation and the polymer matrix visco-elasticity. One of the main issues in fatigue tests is the hysteresis heating due to the viscoelasticity and the low conductivity of the polymer which leads to an increasing of the specimen temperature and consequently to a decreasing of mechanical properties. The hysteresis heating becomes considerable for high loads and high testing frequencies when the equilibrium temperature with the external environment is too high for the material tested [85, 86]. For fiber reinforced materials, a further source of heating during the fatigue tests is the creep between fibers and matrix. Zago and Springer [87] synthesize the effects of the average tensile stress, the frequency, the fibers content and the fiber orientation using a Master curve obtained normalizing the average tensile stress with the static ultimate stress for the same tested material. The load frequency influence on fatigue resistance has been analyzed by Bernasconi and Kulin [87] with a superimposition method based on the correlation between the average stress applied and the average increasing of temperature due to the hysteresis heating and the strain rate [88]. A modification of Gerber equation was proposed by Mallik and Zhou in order to consider the interaction between creep and fatigue resistance by varying the loads; the tests were carried out with a polyamide 66 reinforced with 33% of short glass fibers. Besides the hysteresis effects, the decreasing of the elastic modulus during the fatigue test is also caused by the fiber fracture, the fiber/-matrix debonding, the matrix softening and its cracking [89]. Several techniques have been involved to investigate the damage mechanisms in short glass fiber reinforced materials. Initial works of Horst and Spoormaker [90, 91], have carried out a fractography analysis on the fracture surface of short fiber reinforced polyamide by using a SEM microscope. The investigation pointed out that the damage starts from the fiber ends and it propagates through the fiber-matrix interface. The dynamic modulus variation during the fatigue tests, namely the hysteresis stress-deformation slope, has been considered by many authors by investigating the parameters describing the composite material damage evolution [92–96]. Since the damages on composite materials are thermally activated and it is a dissipative process, a thermographic technique using an infrared thermal images camera has been widely used for investigating the composite damage [97–101]. Moreover, due to the microstructure complexity, and the damages distribution, micro-tomography (LCT) is an efficient instrument for the damage characterization of composite materials subjected to cyclic loads [102–105]. Cosmi and Bernasconi [106] highlighted the LCT advantages and disadvantages for characterizing the damages in short fiber reinforced materials. During the fatigue life, several phenomena occur simultaneously, therefore, a deep analysis of fatigue behaviour

Orientation (°C)	UTS[MPa] (mm/s)	E [MPa] (mm)	A% N/mm^2
0	89.5 ±3.6	4607 ±114	6.47 ±0.73
30	75.6 ±2.2	3229 ±141	9.82 ±0.52
60	58.3 ±2.9	2468 ±70	9.97 ±1.85
90	53.2 ±4.2	2352 ±198	10.98 ±0.44

Table 2.1: Mean values (± standard deviation) of the tensile properties of PA6 GF30 specimens extracted from plates at dfferent orientations

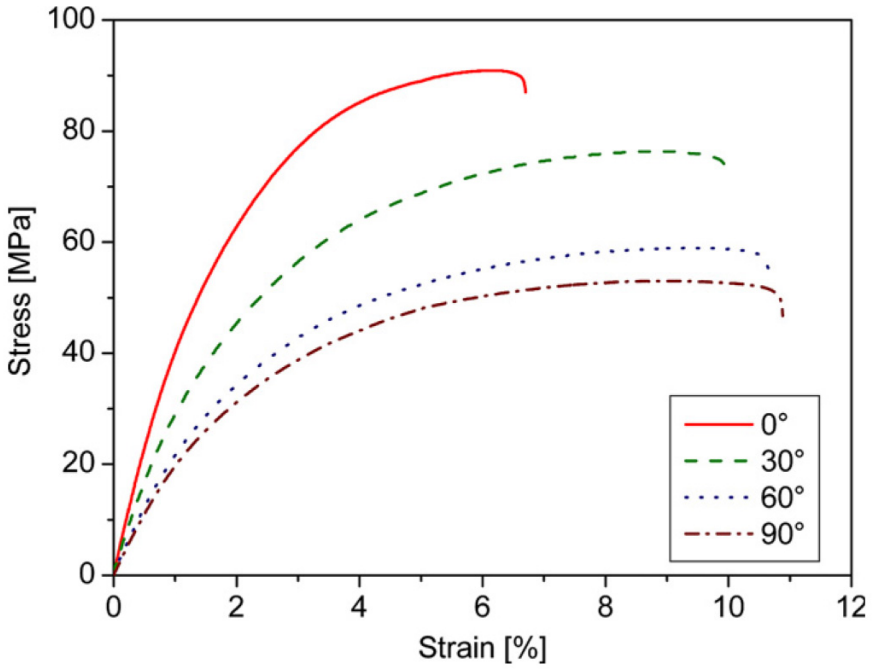

Figure 2.16: Tensile stress–strain curves for dfferent specimen orientations

needs the investigation of the interactions between these effects [88, 89, 107]. Bernasconi et al. [108], carried out a series of fatigue tests on dog bone specimens obtained using a water jet technology for slicing plaques of PA6 GF 30% made by injection molding. The specimens have been cut by varying the angular direction in order to investigate the fiber distribution influence on fatigue life. The tensile test results are plotted in Table 2.1.

From the graph above, it is evident that the higher the orientation angle the lower the ultimate tensile stress and the elastic modulus. The fatigue test results are reported in Table 2.2 and in Figure 2.17.

As occurred for the tensile tests, from the double logarithmic graph, it is understandable that the fatigue life decreases with the increasing of the angle. The interpolation equation used is:

$$\sigma_{max} = \sigma_f N^b \tag{2.7}$$

Orientation	σ_f	b
0	85.5	-0.057
30	66.5	-0.043
60	56	-0.050
90	50.5	-0.045

Table 2.2: Values of the fatigue strength coeffient σ_f and the fatigue strength exponent b of PA6 GF30 specimens extracted from plates at different orientations

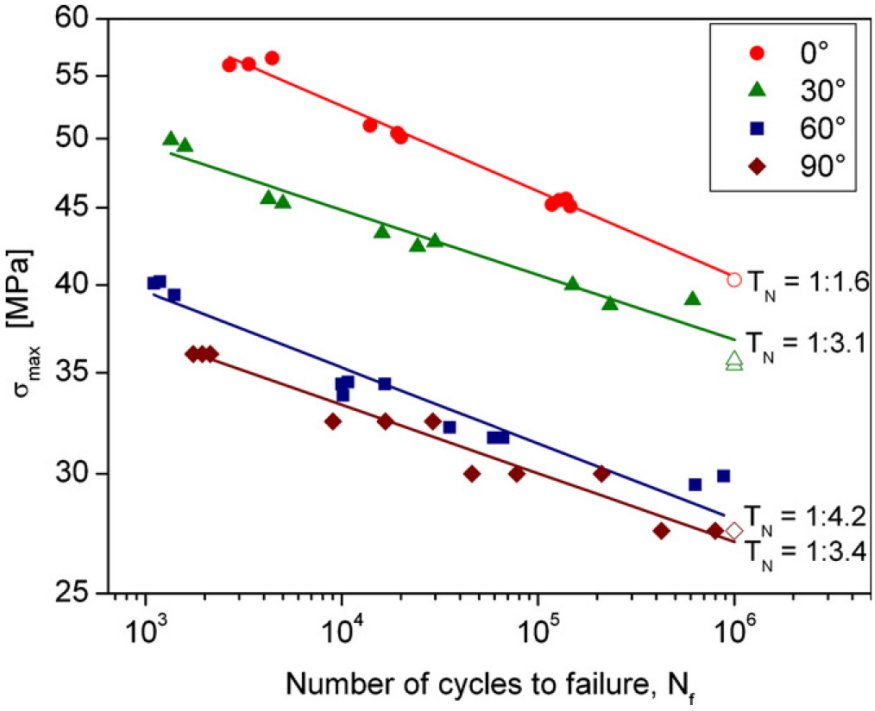

Figure 2.17: S–N curves for different specimen orientations; bright symbols indicate test interrupted at 10^6 cycles (run-outs)

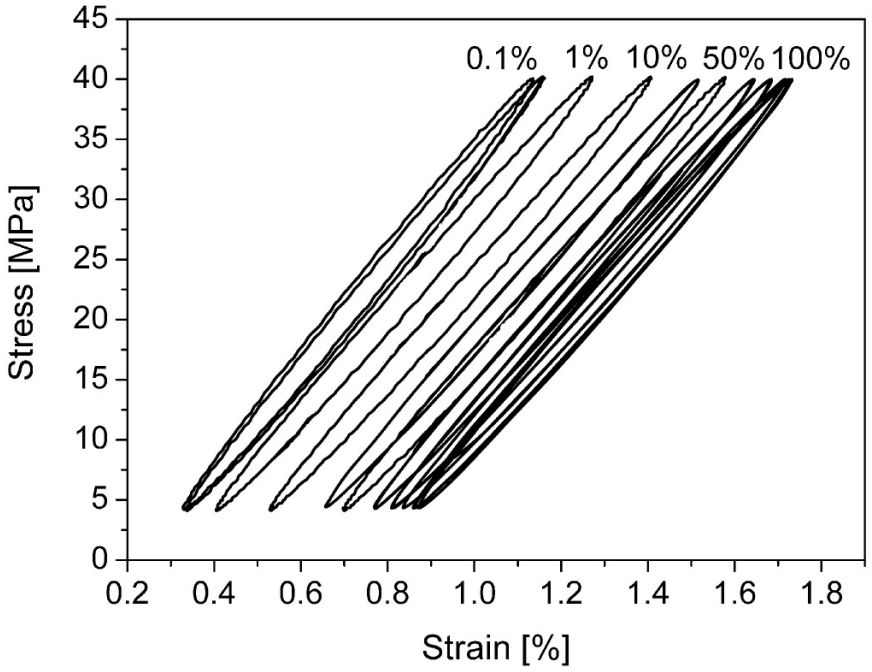

Figure 2.18: Cyclic creep: stress–strain cycles; percent numbers indicate the stage of specimen life at which the full cycles have been recorded, with reference to the number of cycles to failure.

From Table 2.2 it is visible that σ_f decreases with the increasing of the cutting angle following the same trend of the UTS. Conversely, the value of b is almost constant, therefor,e the damage evolution seems to have the same growth rate. During the fatigue tests, the authors have tracked the hysteresis cycles detecting that they progressively move at a constant velocity along the deformation axis during all the fatigue test. The hysteresis cycles dimension and shape as well as the maximum deformation are function of the applied load, the maximum frequency and the environment temperature.

During the fatigue test, the specimen degradation has been associated with the isolated crack nucleation and growing which are interpreted as white lines visible on the surface (Figure 2.20). This phenomenon is a diffuse mechanism of delamination which leads to the global specimen fracture. These considerations are in accordance with the fracture mechanism suggested by Horst [90]. According with the model proposed by Horst, the fatigue failure starts with an initial debonding between matrix and fibers due to the progressive interface yielding which starts at the fibers end where the stress concentration is maximized. When the micro-cavities propagate from the fibers apexes to the interfaces, there is a load transfer from the fiber to the matrix causing a matrix plastic deformation. The micro-cavities propagation is hindered by polymeric chains which work like bridges between the crack surfaces similarly with the crazing formation in the

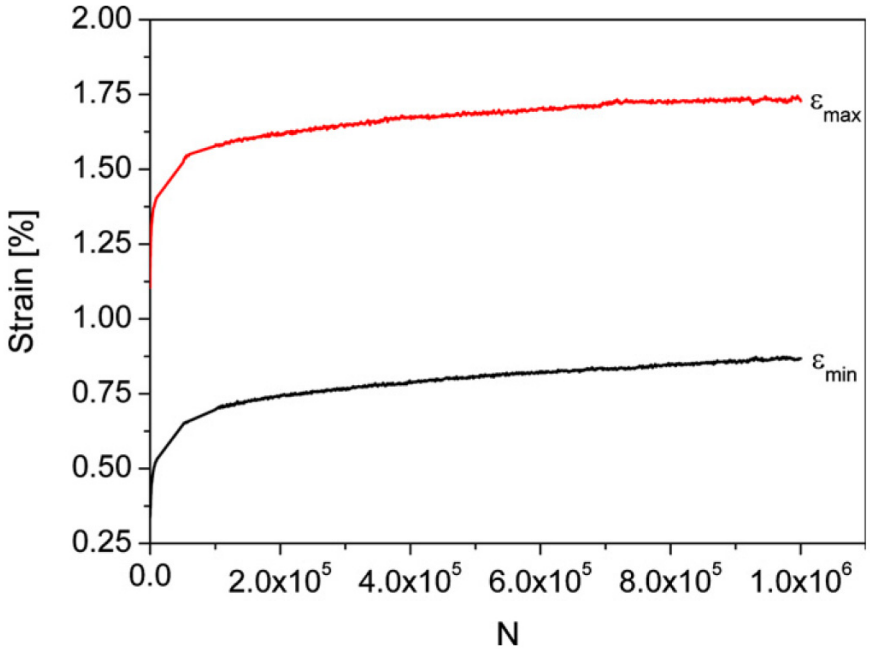

Figure 2.19: Cyclic creep: maximum and minimum strain variation with number of cycles (specimen orientation θ = 0 °; test conditions σ_{max} = 40 MPa, N_f>10^6)

un-filled polymer. The specimen will break in a fragile way when the cracks reach a critical depth.

During the tests, an increasing of temperature has been detected, even though the temperature stabilized after some initial cycles. The utilized frequency was 4 Hz, which is a compromise in order to avoid the thermal failure risk but still performing a fast test. With the aim of interpolating the tensile strength with the average angle of orientation it has been used the quadratic equation of Tsai-Hill [100]. The criterion has been applied assuming an unidirectional fiber orientation even though it is true only in the shell layer. The equation relates the stress applied on normal direction σ_1, with that one in orthogonal direction σ_2 and the stress τ_{12}, with the relative ultimate tensile stress $\sigma_{1,u}$ $\sigma_{2,u}$ and $\sigma_{3,u}$ for all the investigated angles, applying the Equation 2.8.

$$\left(\frac{\sigma_1}{\sigma_{1,u}}\right)^2 + \left(\frac{\sigma_2}{\sigma_{2,u}}\right)^2 - \frac{\sigma_1\sigma_2}{\sigma_{1,u^2}} + \left(\frac{\tau_{12}}{\tau_{12,u}}\right)^2 = 1 \tag{2.8}$$

$$\sigma_u(\theta) = \left[\frac{cos^2(\theta) - \left(cos^2(\theta) - sin^2(\theta)\right)}{\sigma_{1,u^2}} + \frac{sin^4(\theta)}{\sigma_{2,u^2}} + \frac{cos^2(\theta)sin^2(\theta)}{\tau_{12,u^2}}\right]^{-1/2} \tag{2.9}$$

The good accordance between the experimental data and the Tsai-Hill criterion has demonstrated that it is reliable for predicting the ultimate tensile stress varying the angle between fibers and load.

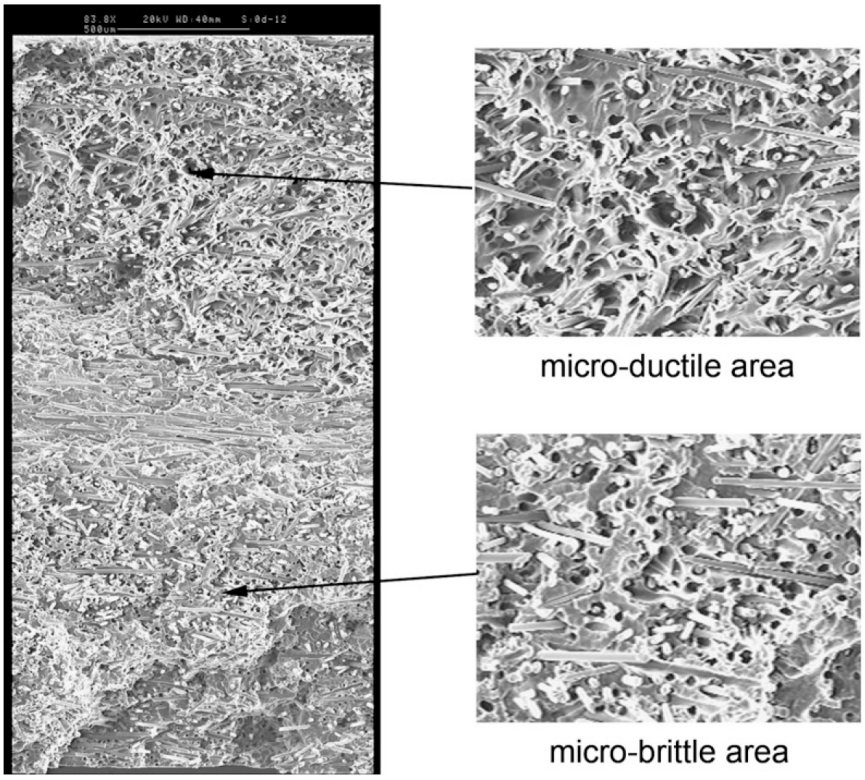

Figure 2.20: SEM micrographs of the fracture surface of a specimen oriented at 0 ° showing the presence of micro-brittle and micro-ductile areas

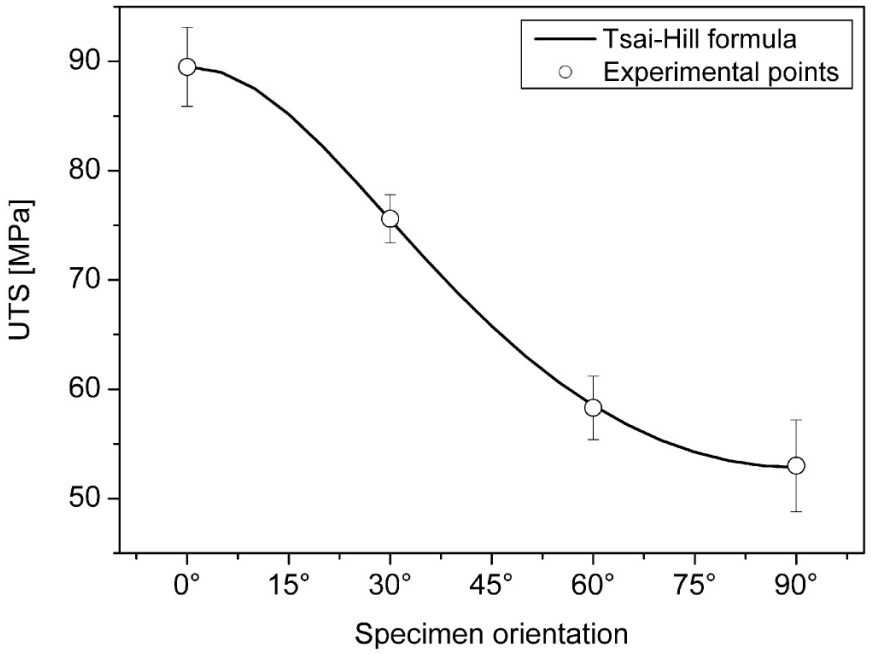

Figure 2.21: Interpolation of the tensile strength values by the Tsai–Hill criterion

$\sigma_{1,u}$ **[MPa]**	$\sigma_{2,u}$ **[MPa]**	$\tau_{12,u}$ **[MPa]**
89.5	53.2	41.9

Table 2.3: Tsai-Hill parameters

σ_f	$\sigma_{1,fat}$	$\sigma_{2,fat}$	$\tau_{12,fat}$
10^4	52.4	33.4	24.5
10^5	45.9	30.1	22.2
10^6	40.3	27.1	20.2

Table 2.4: Tsai-Hill parameters for the fatigue Tsai-Hill formula

The proportionality between fatigue life and UTS suggests a relation among the fatigue resistance and the specimen orientation from the Tsai-Hill criterion. This realyion was proposed by Jen and Lee [109]. The relation has been obtained by modifying the Equation 2.8 and considering the fatigue stress, its cycles number to failure and the orientation angle. For a specific number of cycle breakage N_f it is possible to interpolate the value of fatigue failure with the equation:

$$\left(\frac{\sigma_{1,max}}{\sigma_{1,fat(N)}}\right)^2 + \left(\frac{\sigma_{2,max}}{\sigma_{2,fat(N)}}\right)^2 - \frac{\sigma_{1,max}\sigma_{2max}}{\sigma_{1,fat^2(N)}} + \left(\frac{\tau_{12,max}}{\tau_{12,fat(N)}}\right)^2 = 1 \quad (2.10)$$

Where the maximum loads set in the equation come from the fatigue failure experimental data (N). The values of $\sigma_{1,fat}$ $\sigma_{2,fat}$ and $\sigma_{3,fat}$, as function of the breakage cycles number are reported in the table below. In Figure 2.22 a comparison between experimental data and the Tsai-Hill model is shown.

Despite the good fitting of the Tsai-Hill model with experimental results, the criterion gave a better prediction of the static tensile behaviour compared with the fatigue resistance, due to the higher results variance occurred for the fatigue tests. However, this model cannot be applied linearly for injection molding components because it is very sensible with the layers thicknesses and the fibers orientation degree. The possibility of using this equation is restricted for parts with a constant core thickness and the same relative layers thickness percentage. In order to take into account of the core layer, Bernasconi et al. have proposed a master curve S-N where the stress is normalized with the UTS as visible in Figure 2.23.

This methodology is a general method and it is applicable only if the UTS values are known. The authors concluded that, even though the experimental results were interesting, these method is usable only if the layer distribution is known. Meneghetti et al [110] have studied the fatigue behaviour of fiber reinforced polypropylene under environmental temperature. The material contained also a 42% of calcium carbonate while two different fiber lengths were investigated: a short fiber of 1 mm and a long fiber of 10 mm. The fatigue results could

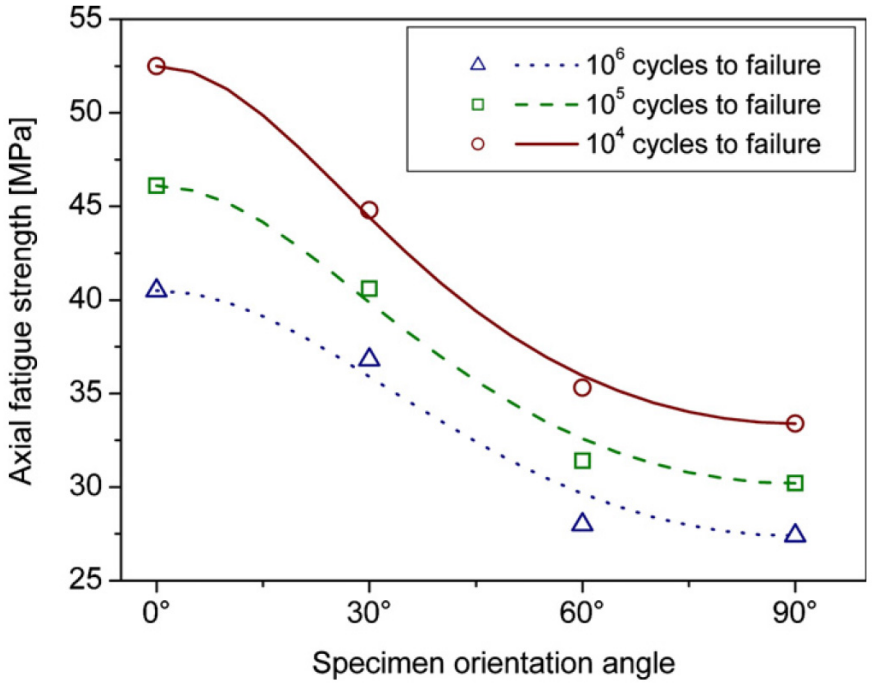

Figure 2.22: Interpolation of the fatigue strength values by the Tsai–Hill criterion

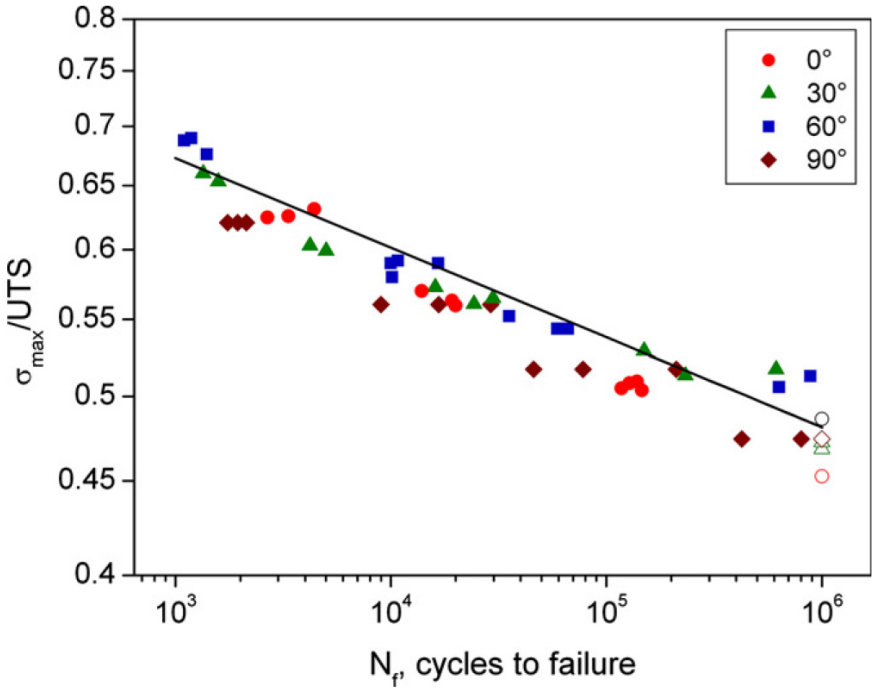

Figure 2.23: Normalized S–N data with superimposed S–N curve of ISO 527 standard specimens

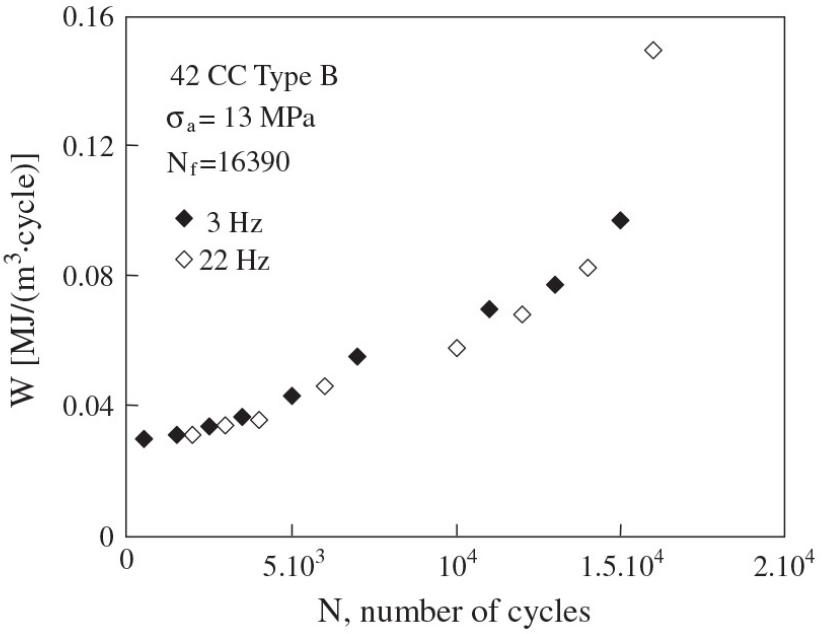

Figure 2.24: Mechanical energy density per cycle vs number of cycles for different test frequencies

be synthesized in a single scatter band by using the mechanical energy expended in a unit of material volume per cycle, W, evaluated from the area of the hysteresis loops measured experimentally. The hysteresis energy was seen to be almost independent on the applied load test frequency in the range of 3–22 Hz as visible in Figure 2.24.

Figure 2.25 shows the hysteresis cycles trend for the investigated materials by varying the load. Figure 2.26 shows the results of the statistical analysis concerning the mechanical energy W varying the materials and the loads conditions.

For metals, Ellyn [111] has highlighted that only a small percentage of the total energy per cycle, W, is stored as internal energy $\triangle U$ and it is the cause of material damage (dislocation movements, cracks nucleation and propagation). The other energy percentage, Q, is thermally dissipated producing the heating of the specimen during the test. Ellyn underlines the difficulty of measuring the thermal dissipation and assumes W, as the damage indicator. This approach has been recently developed by Meneghetti [112] who showed that the dissipated energy in thermal energy, Q, can be used as indicator for the metal damage and short fiber reinforced polypropylene materials [113]. Ellyn and El-Kadi [112] have proposed a criterion for the fatigue failure of composite materials with unidirectional continue fibers based on the elastic deformation density. Starting from the experimental results, an accurate characterization of the composite material is fundamental to understand how the dissipative energy is accumulated during the fatigue life which is divided in: matrix cracking, fiber/matrix delamination at the interface and fibers breakage.

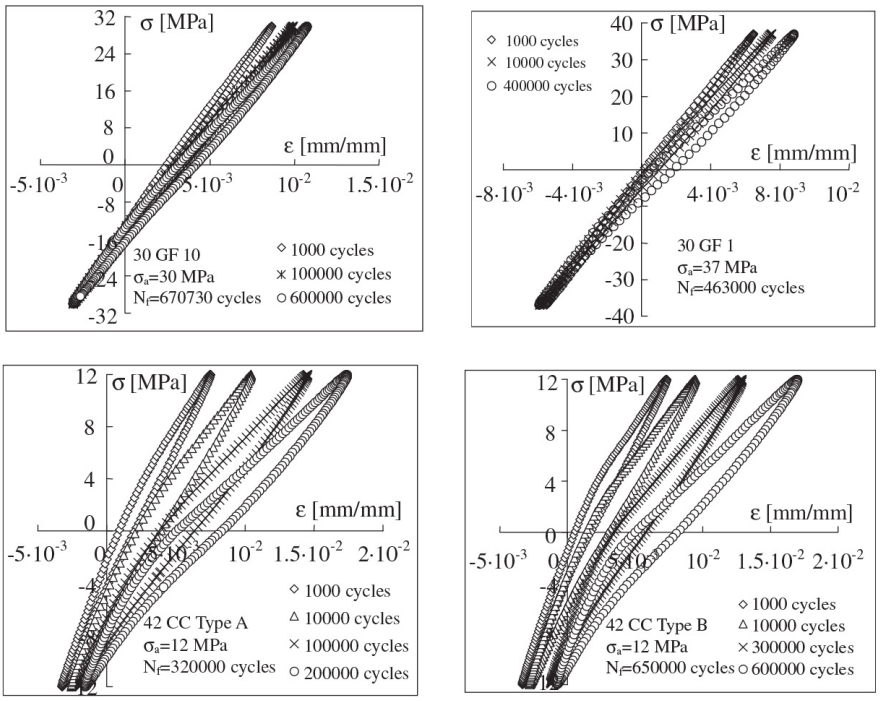

Figure 2.25: Characteristic hysteresis loops measured during the fatigue tests

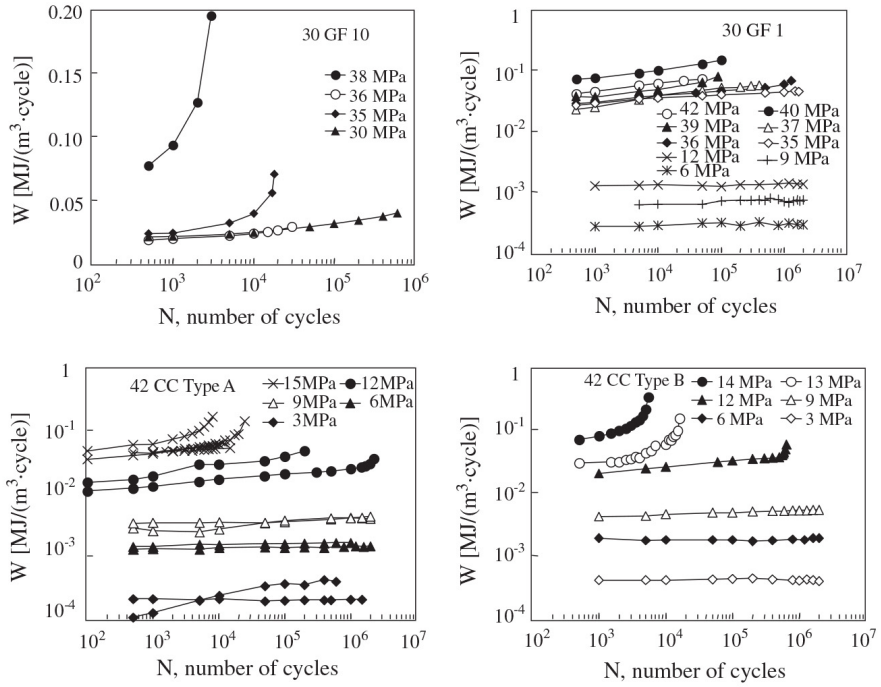

Figure 2.26: Mechanical energy density per cycle versus the number of cycles for tested materials

LFT	UTS [MPa]	Modulo di Young [GPa]
Longitudinal	113.8 ±14.3	6.5 ±1.0
Transversal	68.2 ±10.2	5.0 ±0.5

Table 2.5: Tensile properties of LFT

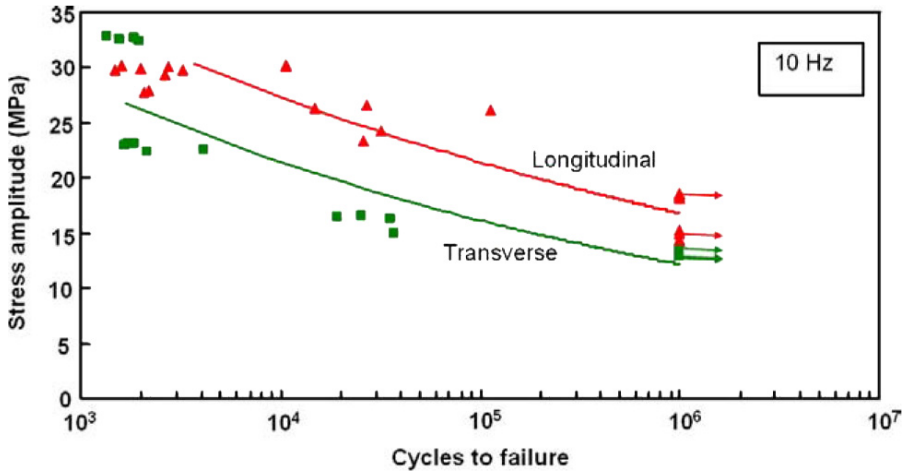

Figure 2.27: S-N curves for the longitudinal and transersal directions

The authors [110] suggested to use the energy deformation density as an index of the whole damage mechanism. In accordance with Ellyn [111], Tao and Xia [114] have considered the deformation dissipated energy and the elastic deformation energy for summarizing the fatigue data obtained from the tests. Goel et al. [115] have studied the fiber distribution and the testing frequency on fatigue behaviour of polypropylene charged with 20% of long fibers. Tensile specimens were made by cutting plaques, in longitudinal and transversal direction, obtained by injection compression molding. The tensile tests are reported in Table 2.5.

The results of the fatigue test, made with the specimens obtained on transversal and longitudinal direction, carried out with a frequency of 10Hz are reported in Figure 2.27.

The specimens cut along the longitudinal direction have an higher fatigue resistance compared with the transversal one. Similar results are obtained with the specimens tested at 15 Hz and 20 Hz. When the curve S-N are normalized with the Young modulus the transversal and the longitudinal fatigue curves are overlapped.

The frequency effect on fatigue life for longitudinal specimens is visible in Figure 2.29. Increasing the testing frequency, the fatigue life decreases independently from the fiber orientation.

The hysteresis thermal heating during the fatigue tests is a critical issue for fiber reinforced polymers due to their low conductivity and the effect of temperature on mechanical properties. The hysteresis energy loss for long fiber reinforced thermoplastics tested at 20 Hz increases rapidly in the initial phase during the test, while it reaches

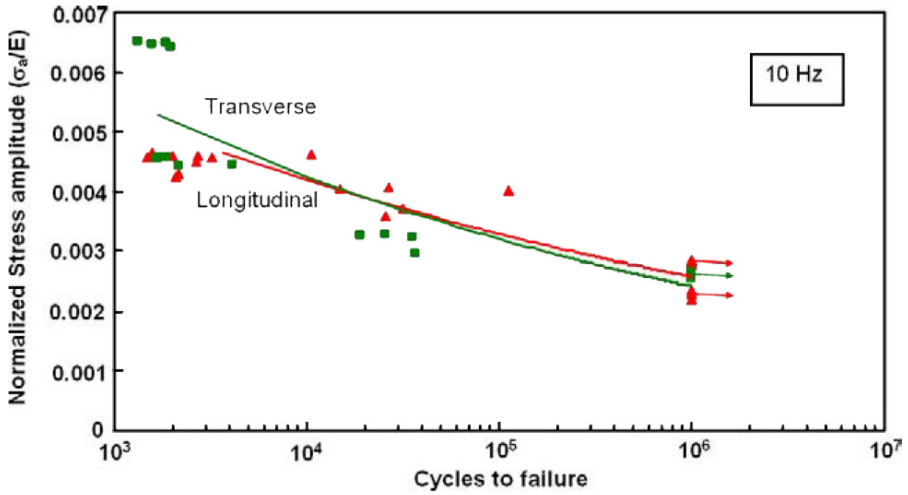

Figure 2.28: S-N curves normalized for the longitudinal and transersal directions

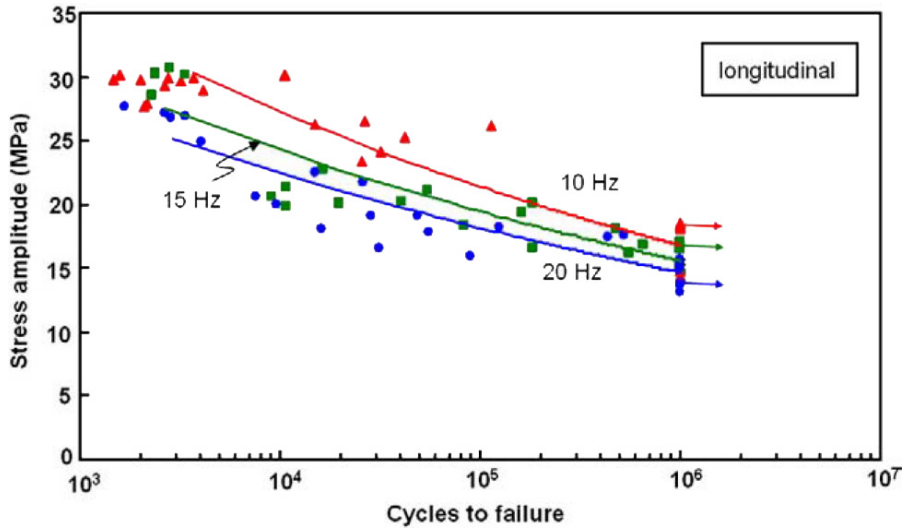

Figure 2.29: S-N curves for the longitudinal and transersal directions, varying the testing frequency

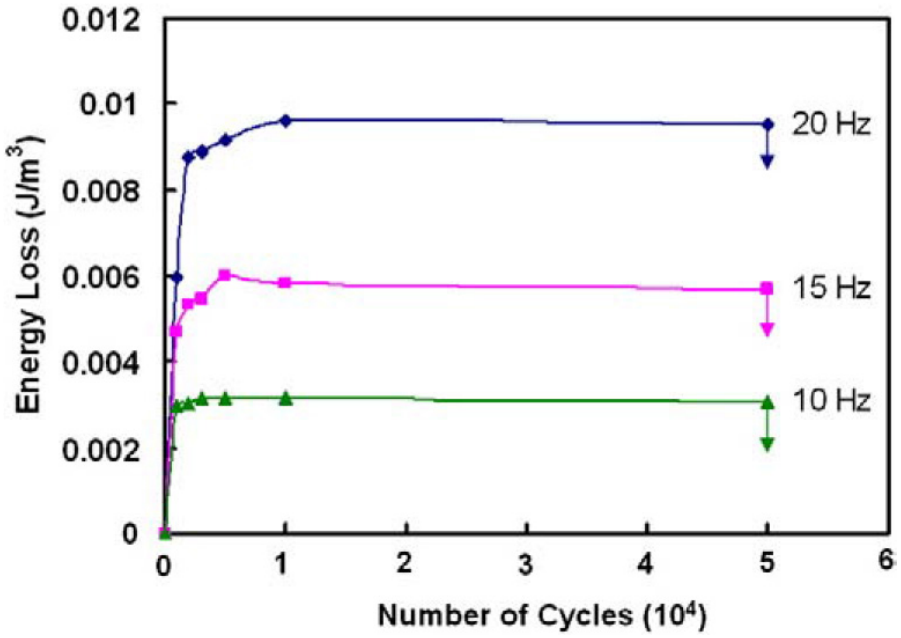

Figure 2.30: Energy loss tested at different frequencies, varying the testing frequency

the stabilization until the final breakage. Figure 2.30 shows the energy loss in function of the cycle number at 20 MPa with a frequency of 10 Hz, 15 Hz and 20 Hz. In general, the higher the frequency the higher the energy loss. The temperature trend of the specimens during the fatigue test has also been investigated. The results show that the heating rate increases for high loads and the same behaviour is shown increasing the frequency. The hysteresis heating leads to a material softening which causes a general decreasing of the elastic modulus.

The fracture surface analyzed with SEM has highlighted the failure mechanisms which are involved in the LFT composite: fiber pullout, fiber fracture and matrix cracking (Figure 2.31). This is mostly true as more as the fibers are oriented along the tensile direction. A similar behavior has been seen for the fracture surfaces obtained from both tensile and fatigue tests.

For fibers longer than the critical value, the fiber breakage is the dominant mechanism [116]. Conversely, the fiber pull out occurs when the interfacial stress overcomes the adhesion between fiber and matrix causing their debonding. The surfaces of most of fibers appear cleaned without particles stuck. An interesting result of Goel et al [115] is the comparison between the fatigue resistance of neat PP with a fiber reinforced PP. From Figure 2.32 it is visible that the specimens made with LFT material tested at 20 Hz have a better performance than the neat PP tested at 1 Hz. From Figure 2.33 it is worth noting that a testing frequency of 1 Hz is enough to induce a material softening in the neat PP while a frequency of 20 Hz do not lead to a material softening for LFT.

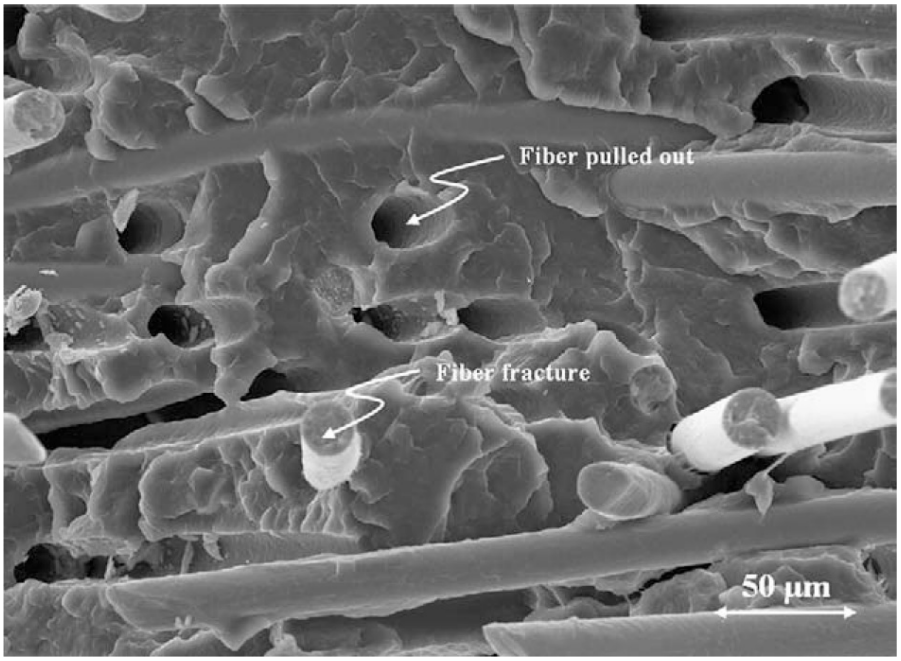

Figure 2.31: Fracture surface of the tensile specimen

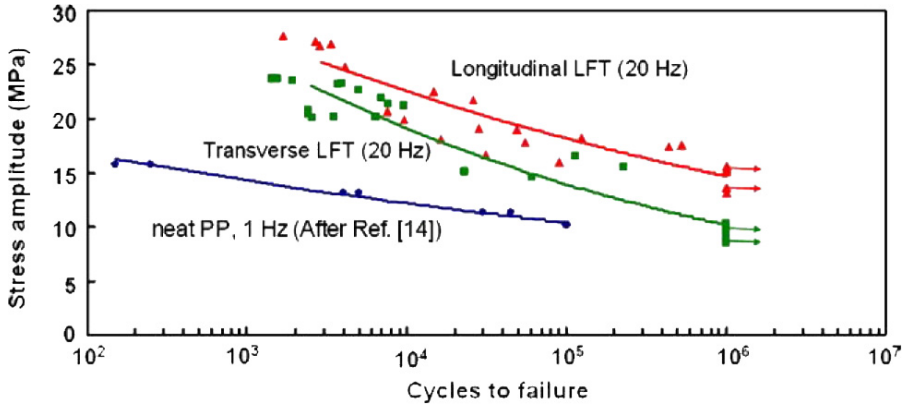

Figure 2.32: A comparison of the fatigue behavior of LFT with unreinforced PP

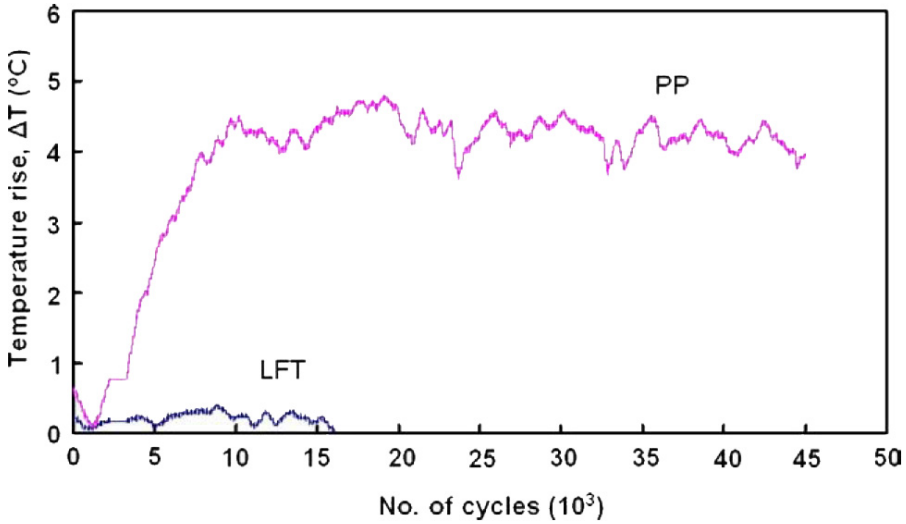

Figure 2.33: Temperature rise in PP and LFT tested at 10 MPa and 20 Hz

There are mainly two causes of specimens heating: hysteresis heating due to the matrix type and frictional heating between fibers and matrix.Figure 2.32 and Figure 2.33 show that the neat PP heats more than LFT-PP meaning that the hysteresis heating is dominated by the matrix viscoelastic heating.

In recent studies, Arif et al [117], have characterized the fatigue behaviour of PA66/GF30 subjected to a mono-axial load with a constant amplitude. They employed a combined analysis of dynamic modulus, cyclic creep, dissipated energy and temperature evolution during the fatigue test. A tomographic analysis has also been carried out to further investigate the failure mechanisms. In order to investigate the anisotropy induced by the injection molding process, the authors have analyzed the specimen morphology with a particular attention for the skin-shell-core layers influence on damage mechanisms (Figure 2.34). The material was a PA66/GF30 and the specimens were made by cutting some plaques obtained by injection molding.

Fatigue test were carried out considering the ratio R=0.1 and a frequency of 3 Hz, an investigated range of $10^3 - 10^6$ cycles, and checking the specimens temperature with an infrared thermal camera. The damage evolution has been qualitatively investigated by performing a tomography at different fatigue life percentages. The longitudinal specimens resistance was twice compared with the transversal specimens. They have also demostrated that the S-N curves have both a linear behaviour as occurred in other publications [108, 118, 119]. In Figure 2.35 the monitored parameters are shown: the dynamic normalized modulus, the maximum deformation and the average temperature for the specimens obtained in longitudinal and transversal directions. The dynamic modulus reduction has been used as an indicator for the damage mechanism evolution [94, 120]. For all the investigated loads in this study, the normalized dynamic modulus shows

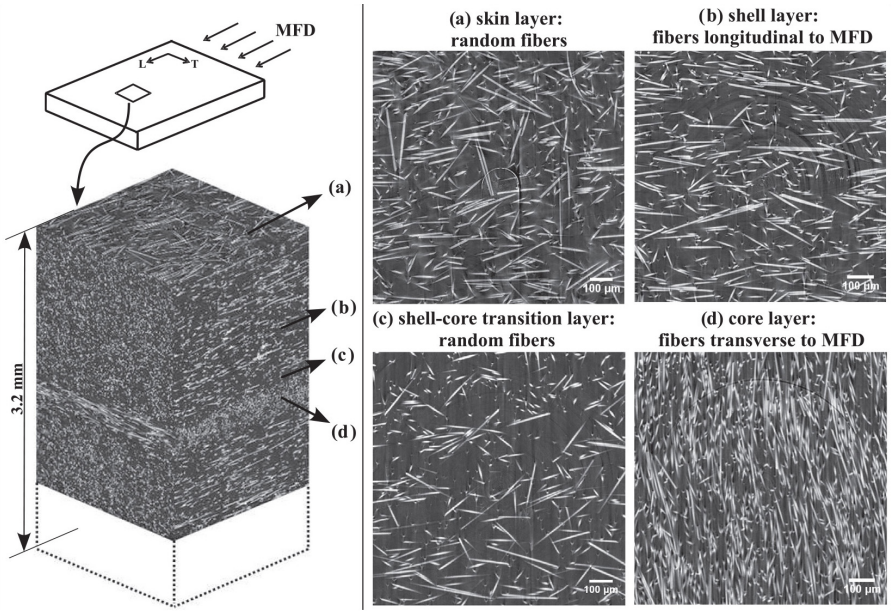

Figure 2.34: Skin–shell–transition–core microstructure formation of PA66/GF30 observed by lCT technique

a stable behaviour until 10^3 cycles whereupon it decreases with a certain velocity, depending on the applied load. Moreover, it is found that the dynamic modulus reduction is directly correlated with the specimens fatigue life. For both the specimens obtained in longitudinal and transversal direction, the temperature evolution shows two phases (Figure 2.35). Initially, the temperature is almost stable in accordance with the dynamic modulus behaviour. In the second phase there is an increasing of the specimens temperature combined with a dynamic modulus decreasing. This behaviour is explained considering that viscous heating is the cause of the temperature increasing in the initial phase while a second cause of heating is added in the second phase due to the damage mechanism.

Focusing on Arif et al. work [117], involving a computed tomography analysis it is possible to evaluate the damage mechanisms directly inside the specimens subjected to cyclic loads. The damages recognition is possible considering the growing up of black portions, in the tomographic images, which correspond to a voids formation. These voids are often observed in correspondence of the fiber/matrix interfaces which can be attributed to the debonding phenomenon. However, it cannot be assessed whether the local damage is adhesive or cohesive from the investigation. Indeed, fiber/matrix interfacial debonding depends on several parameters. Voids at fiber ends are also observed in the loaded fatigue specimens, though it is not necessarily involved in the fiber/matrix interfacial debonding. Few fiber breakages have also been observed but it seems that this damage mechanism is not dominant. This fiber/matrix interfacial debonding

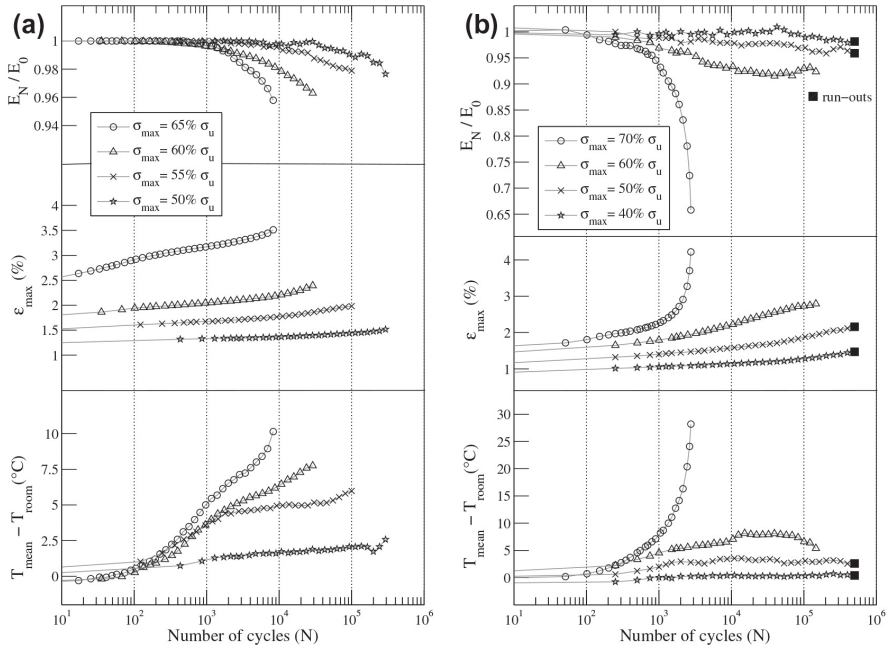

Figure 2.35: Evolution of normalized dynamic modulus ($E_N = E_0$), maximum strain (ϵ_{max}) and mean temperature ($T_{max} - T_{room}$) (a) longitudinal and (b) transverse specimens during fatigue loading of PA66/GF30. σ_u represents the ultimate tensile strength of its respective orientation angles

is frequently observed in the fatigue loaded specimens and can be considered as the main fatigue damage mechanism for PA66/GF30.

3

INJECTION MOLDING OF CRYSTALLINE MATERIALS

3.1 INJECTION MOLDING OF PET THIN WALL BOTTLES PREFORMS

Nowadays, the packaging industry promotes the thicknesses reduction in order to contain the material consumption and the plastic weight of final products. Especially for some electrical connectors, electric component packages and power supply items, manufacturers design even thinner wall sections. These driving forces bring new challenges to the conventional injection molding industry: how can one successfully and economically injection mold long and thin parts? One serious flaw of the conventional injection molding process is that the filling process is coupled with the cooling process [121]. The difficulty in molding ultra-thin wall parts lies in the fact that the ratio of frozen layer thickness to part thickness during filling will drastically increase with the decrease in part thickness. The problem becomes worse, when the frozen layer thickness and the part thickness are comparable. So, it is hard to fill cavities of ultra-thin wall parts under the process conditions of conventional injection molding. It is difficult to select process parameters correctly because there are much more complicated influence factors involved in ultra-thin wall injection molding than that in conventional injection molding [122, 123]. Even the bottles preform industry follows this trend upgrading the development of thin preforms which lead to many problems during the realization process. First of all, the thickness reduction causes an increasing of the injection pressure in fact, considering a preform with a thickness of 2.3 mm, the frozen layer adjacent at the wall has a thickness of approximately 0.25 mm reducing the flow section. Furthermore, if the mold temperature is too low, the material freezes before the complete filling of the cavity, causing an incomplete preform. Other problems can raise when the flow reaches the bottle neck where, due to the small thickness of this part, the rapid increasing of pressure is combined with an high shear stress in that position, which could degrade the material. A common solution regarding the injection molding of thin-wall bottle preforms is the increasing of the injection speed in fact, the higher the injection velocity the lower the front flow cooling. However, it leads to a further increasing of the injection pressure and the material degradation. There are limits to how thin a preform can be made before it becomes impossible or at least economically unfeasible to injection mold [124]. An efficient solution is the using of an injection-compression molding technology,

which overcomes the issue of filling molds with very thin walls, by having the molds slightly open when injection starts, and then closing them as dosing finishes. This means lower injection pressure can be used, lower clamp force is needed (which has the additional benefit of extending mold life), and there is less stress on the melt which means acetaldehyde levels are reduced, and resin intrinsic viscosity falls less. Using an injection compression moulding technology it is possible to make a preform for a 500-mL bottle that weighs just six grams. The system is particularly well suited to produce preforms for bottles up to 1.5 L in volume, but can also be used for bottles up to 2.5 L. On top of all that, the equipment uses lower temperatures and 10% less energy than an injection molding system with the same output and it fits into much less space. However, the injection-compression molding technology can be adopted if the injection machine is provided with the required equipment. In conventional injection molding technology, the most important process parameters that influence the cavity filling are the temperatures of the mould and the melt. In general, with increasing mould or melt temperature, the filling behaviour is favoured and an increasing aspect ratio can be reached. In addition, the using of thermal low conductive mould materials or a dynamic temperature control of the cavity can influence the cooling velocity of the melt. This thermal effect can affects not only the filling of the cavity but also the part morphology (e.g., degree of crystallinity or orientations) and the mechanical properties (e.g., tensile strength) [125]. Therefore, increasing the mold temperature allows the injection molding of thin-wall preforms decreasing the maximum injection pressure. However, being PET a crystalline material, an high mold temperature could lead to the increasing of preforms crystalline degree inducing a possible trouble in the subsequent blow molding process and increasing the bottle opacity. Indeed, one of the desirable characteristics of PET bottles is their transparency. Early crystallization of PET during the injection-blow-molding process may, however, induce haze or render the product opaque. The parameters that keep the crystallization of the PET to a minimum during the manufacturing process therefore must be determined and properly controlled [126]. Thermodynamically, the crystalline phase is in a lower free energy state than the amorphous melt when the temperature is below the equilibrium melting point [127]. The variations of the cold crystallization Hc and the cold crystallization temperature Tc with the mold temperature are presented in Figure 3.1. Hc decreases as the mold temperature increases, indicating an increment of the degree of crystallinity of the moldings.

The increment on Tw results in an increase on the degree of crystallinity of the moldings (revealed by the reduction of the enthalpy of cold crystallization), and in the reduction of the global level of

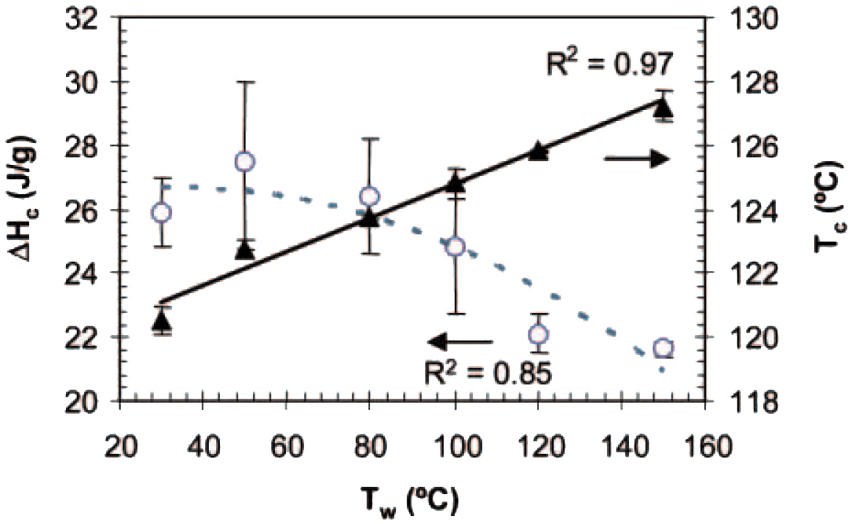

Figure 3.1: Variation of the enthalpy of cold crystallization, $\triangle H_c$ and peak temperature, T_C with the mold temperature, T_w

amorphous molecular orientation (as assessed by the decrease on the percentage of hot recoverable strain) [128].

3.2 PRODUCING OF PLA COMPONENTS: CRYSTALLIZATION AND MECHANICAL PERFORMANCES

Increasing concerns over the environmental impact and sustainability of conventional polymer materials have motivated academia and industry to devote considerable efforts to the development of polymers from renewable resources. Among a few commercially available biobased or partially biobased thermoplastic polymers, Poly(lactic acid) (PLA) has undergone the most investigation [129]. PLA is a versatile polymer made from renewable agricultural raw materials, which are fermented to lactic acid [130]. PLA belong to the family of aliphatic polyesters commonly made from α-hydroxy acids, which include poyglycolic acid or polymandelic acid, and are considered biodegradable and compostable [131]. Homopolymer PLA can be processed into fibers, textiles, films, and molded objects with standard polymer processing equipment. Its initial uses were for medical and dental applications due to its biocompatibility and biodegradability. More recently, however, its usage has extended to packaging materials for food and consumer goods; applications in which the polymer film is typically discarded after use[132]. PLA is an enantiometric polyester including poly(L-lactic acid) and ploy(D-lactic acid). Fully amorphous materials can be made by the inclusion of relatively high D content ($>$ 20%) whereas highly crystalline material is obtained when the D content is low ($<$ 2%) [133]. The amount of D-enantiomer is known to affect the physical properties of PLA, such as melting tem-

perature, degree of crystallinity and mechanical properties. However, for practical applications of PLA, it is required to improve the properties, such as material degradation, flexural properties, heat deflection temperature, gas permeability, impact toughness, etc. [134]. With the aim of improving the mechanical performances of PLA, a particular attention is given to plasticization as well as to impact resistance modification of PLA in the case of (reactive) blending PLA-based systems [135]. A multiphase blends of PLA, ethylene-methyl acrylate-glycidyl methacrylate (EMA-GMA) terpolymer, and a series of renewable poly(ether-b-amide) elastomeric copolymer (PEBA) were fabricated by Zhang et al. through reactive melt blending in an effort to improve the toughness of the PLA [136]. Conversely, excellent stiffness-toughness balance was achieved by ternary of PLA, PHBV and PBS [137]. Saejdlou et al. blended a PDLA in low concentrations with PLLA to produce a stereocomplex and a rheometer test was carried out to simulate melt processing conditions: differences in rheological characteristics of asymmetric PLLA/PDLA blends as compared to neat PLLA were associated to the structural changes happening because of the formation of the stereocomplex [138]. An increase in PLA's total percentage crystallinity can effectively improve HDT, stiffness and chemical resistance. Due to high crystallization half time resulting from the slow crystallization rate of PLA, obtaining an injection molded article with high crystallinity remains a challenge. Therefore, to obtain a molded component with increased crystallinity and maximized mechanical properties and physical performance, Srithep studied the effects of annealing time and temperature on the crystallinity of poly(lactic acid) (PLA) which have been demonstrated to be critical in increasing glass transition temperature and storage modulus [133]. Injection molding parameters were investigated on mechanical performance of impact-modified poly(lactic acid) (PLA): molding with a mold temperature of 30 $^{\circ}C$ versus 90 $^{\circ}C$ the elongation and the impact strength is improved while the polymer becomes very amorphous [139]. The overall crystallization rate and final crystallinity of PLA were controlled adding physical nucleating agents as well as optimizing the injection molding processing conditions. Talc and ethylene bis-stearamide (EBS) nucleating agents both showed dramatic increases in crystallization rate and final crystalline content; isothermal crystallization half-times were found to decrease nearly 65-fold by addition of only 2% talc [132]. Nagarajan et al. investigated the effects of varying the processing parameters and addition of various nucleating agents. With the addition of 1 wt% aromatic sulfonate derivative (Lak-301) as a nucleating agent at a mold temperature of 110 $^{\circ}C$, PLA biocomposites exhibited dramatic reduction in crystallization half time to 1.3 min. Mechanical and thermal properties assessment for these biocomposites revealed a 4-fold increase in impact strength compared to neat PLA. The HDT of PLA biocom-

posites increased to 85 $^{\circ}C$ from 55 $^{\circ}C$ compared to neat PLA [140]. Several other additives have been used in literature with the aim of improving mechanical properties of PLA such as EBH crystal nucleating agents [141], cyclodextrin (CD) and calcium carbonate [142]. Noticiable mechanical improvements were reached mixing PLA with natural fibres such as man-made cellulose and abaca fibres [143], microfibrillated cellulose (MFC)[144, 145]. The progress which has developed recently in the field of nanoscience and nanotechnology has given a unique opportunity to develop revolutionary materials which overcome the typical performance compromises of the conventional materials by benefiting through a synergism occurring between components below certain dimensions [146]. For instance, Zhou and Xanthos had studied the influence of unmodified and organomodified clays at 5 wt% content to the material degradation rate [131]. The effect of clay and chain extender on the nonisothermal, isothermal crystallization kinetics, and morphology of polylactide (PLA) was investigated by Najafi et al. [147].

Part II

AN INNOVATIVE SOLUTION FOR POROUS INSERTS REALIZATION

4

AN INNOVATIVE SOLUTION FOR POROUS INSERTS REALIZATION

In the chapter 1, a first solution was briefly introduced to achieve the molding with rapid variation of temperature in the mold based on the realization of a single circuit, supplied with pressurized water, in which two metal foam inserts were placed behind the mold cavity, with the purpose of increasing the thermal flow and decrease the heating and cooling time. This solution, extensively described in the previous chapter, was the starting point for the development of the present work. The replacement of these inserts, made with metal foams, with a new ones in order to improve the cavity heating rate and the mold stiffness is the base idea of this work. This chapter describes all the activities carried out from the formulation of the problem up to the definition of the prototype geometry. The optimization procedure has required an intensive use of advanced simulation tools, to obtain a reliable result from the thermo-fluid-dynamic and the mechanical simulations. The modeling strategy adopted was based essentially on two stages. A first one aimed to define a mold geometric configuration based on a simplified numerical model with the goal of making a first prototype with optimized performances. The second step involved the definition of a detailed model. The fluid dynamic model, in particular, has been scheduled in order to allow the rapid variation of numerous parameters concerning the materials thermal properties, the boundary and the initial conditions. This procedure allowed the experimental model validation by calibrating the model parameters, creating a reliable tool for the thermal simulation of the mold heating and cooling.

4.1 MOLD WITH METAL FOAM

The mold provided with metal foam inserts is visible in Figure 4.1. The inserts are placed as close as possible to the mold cavity with the aim of reducing the thermal inertia between the cavity surface and the circulating fluid. The disadvantage of this solution is the fact that the inserts are subjected to an high compression loads caused by the injection pressure.

In the work carried out by Fiorotto et al. [4], the mold has been structurally verified for the stress due to the injection of ABS, the clamping force of the machine and especially the temperature gradients induced by the thermal cycle imposed. In doing this, the metal foam insert was considered as continuous, homogeneous and

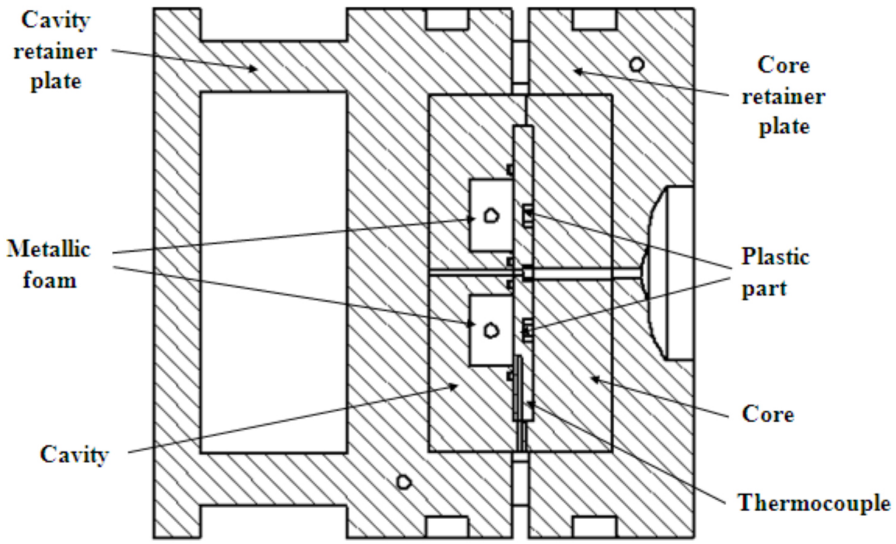

Figure 4.1: Schematic structure of the RHCM mould with metallic foams

isotropic solid. It is believed that this result is not reliable, due to excessive approximation that is committed to consider the foam as a continuous. This choice might be acceptable for the global deformation point of view, however it is inaccurate regarding the local stress. Considering the structure of metal foams, there is a substantial localized stress concentrations when a compression load, even constant, is applied from the outside. Since the stress is a local variable by definition, the value obtained by this simulation is therefore meaningless as well as inaccurate for the structural verification. There are numerous examples in scientific literature that demonstrate the need of considering a smaller scale in the calculation of cell type structures Figure 4.2 to correctly predict the structure failure [21, 148, 149].

In any case, even assuming reliable the result, the development of a new mold with higher rigidity is needed. Furthermore, it has to be considered that the width of the insert in the mold is quite small therefore, the most load percentage is supported by the cavity plate (Figure 4.1), due to the low stiffness of the foam. If the geometry of the object was more extended, the load supported by the foam insert would increase. Even though the structural resistance of metal foam inserts is unsatisfactory, their heat exchange efficacy has been proven in several domains. As regards the injection molding with rapid variation of temperature, it is documented in [4] the result of heating simulations starting from a mold temperature of 60 $^{\circ}C$ with the hot water at a temperature of 130 $^{\circ}C$, compared with the experimental data carried out with the same conditions. The results, visible in Figure 4.3, show a certain discrepancy between the heating curves, especially in the initial section.

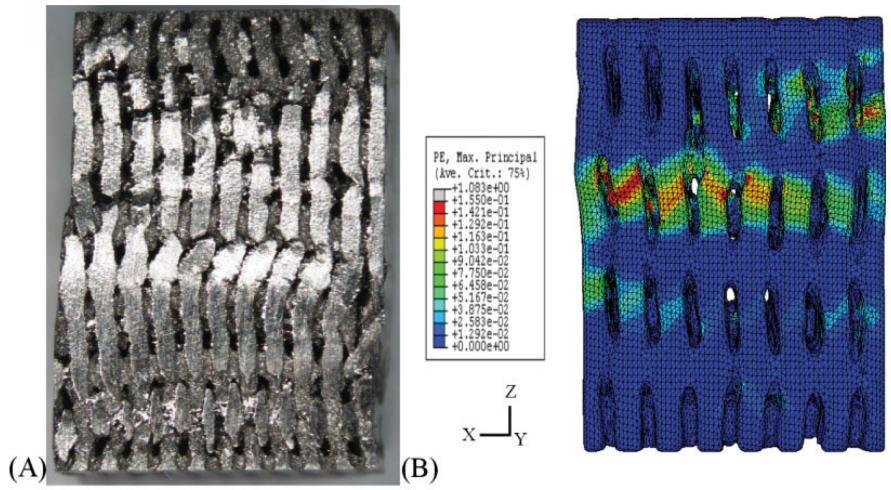

Figure 4.2: Titanium scaffolds following experimental testing and corresponding FEA results

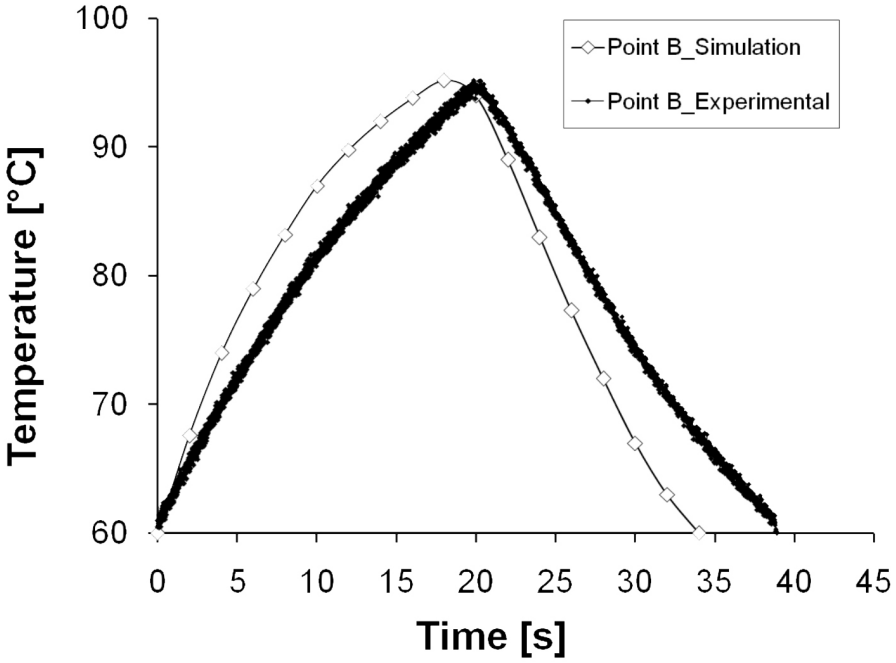

Figure 4.3: Aluminum foam inserts: comparison of the temperature history between experimental data and simulation results

The average experimental heating rate in the first 10 seconds is 2 $^{\circ}C/s$. Which is a rather low value when compared with other RHCM technologies.

4.2 OBJECTIVES DEFINITION

The objective of this work was the development of a new porous insert solution with a defined geometry (non-stochastic) in order to achieve the requested stiffness resistance and further enhance the thermal exchange between the mold cavity and the circulating fluid. To achieve a comparable result with the previous solution, it was decided to work on the same mold used by Ing. M.Fiorotto [4]. The only variation concerns the realization of a new plate for the molding of testing specimens as described in the following sections.

4.3 POROUS INSERTS WITH A LABYRINTH GEOMETRY

4.3.1 *Formulation of the idea*

The greatest benefit of metal foams is undoubtedly the high surface/volume ratio, which allows to supply an high thermal power with a negligible iniertia. However, the metal foam has a relevant problem concerning the contact area between with the mold plate which is extremely reduced. The thermal flow, removed by the metal foam inserts from the water, is limited by the high thermal contact resistance with the cavity plate. Consequently, the overall exchange coefficient between the water and the cavity surface is heavily penalized. In proposing a new solution the following goals are proposed:

- Increasing contact area between the insert and the plate to be heated;
- Maintain an high surface/volume ratio;
- Increased exchange surface between water and insert;
- High stiffness and resistance to compression loads;
- Feasible technological solution.

The idea proposed here is born looking for an alternative technology for the realization of the insert. The porous inserts manufacturing method consists in realizing a geometry labyrinth by overlapping metal sheets with square holes made by laser cutting. Arranging the metal sheets it is possible to obtain a labyrinth structure of channels through which circulate the pressurized water as visible in Figure 4.4

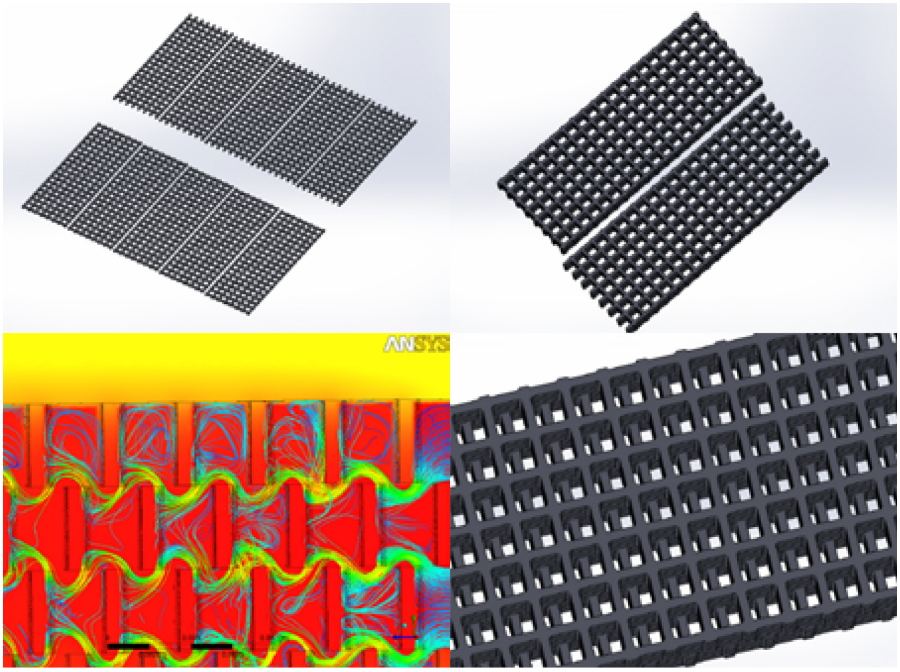

Figure 4.4: Labyrinth porous inserts generation

SOLUTION POTENTIALITY The realization of the insert, overlapping few metal sheets, allows a greater geometric freedom compared with other technological solutions. In fact, there are numerous degrees of freedom that can be handle: the shape and size of the holes, the thickness of the sheets and the reciprocal arrangement of the different layers. Even though additive manufacturing technology would be the best solution from this point of view, managing appropriately all these parameters, it becomes possible to realize a high number of different geometries. The insert can be designed in order to obtain a high surface-volume ratio without impairing the stiffness, to manage the contact surface between the insert and the mold plate and create an efficient water path through the mold. Moreover, this method of producing porous inserts is fast and cheap. The time needed for the realization of an insert with a selective laser melting is much longer than that one needed to obtain the metal sheet by laser cutting reducing also the purchase costs.

POSSIBLE ISSUES TO TAKE INTO ACCOUNT Besides the numerous benefits of this solution, there are some weak points which have to be taken into account, both from the technological and the functional point of view.

Regarding the first aspect, there are some geometric constraints which arise from the sheets manufacturing by laser cutting. Considering Figure 4.5 it is reasonable to believe that there is a minimum distance between the holes beyond which the part overheating could occur due to the passage of the laser beam. There is also a limit on the

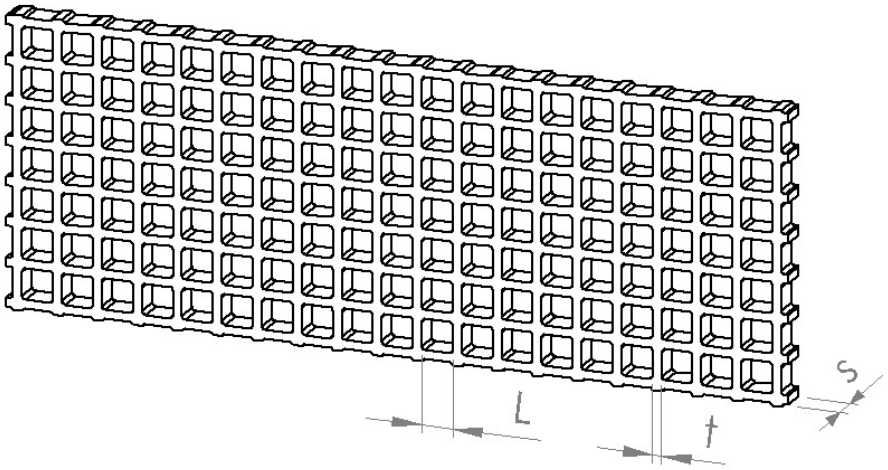

Figure 4.5: Geometry of a single metal sheet

sheet maximum thickness, still related to the overheating caused by the laser beam. With regard to the functional aspect, the main issue concerns the reduction in heat exchange power because of the thermal contact resistance between the various laminates and the mold plate.

4.3.2 *Design strategy definition*

MOLD CONSTRAINS The design strategy is based on the initial mold constrains. The porous inserts, for example, have to be collocated in place of the metal foam, therefore their overall dimensions were already defined. In particular, the insert is a parallelepiped with the base dimensions of 33 x 90 mm and height of 20 mm. The temperature control unit available was a Wittmann Tempro Plus 180 D Vario, a thermoregulator with double circuit equipped with a pneumatic valve group. The pressure drop and the flow rate were function of the pump characteristic curve therefore there was a limitation concerning the maximum flow rate available. Concerning, the geometry of the cavity plates, the whole thickness of the cavity plate was 9 mm while the part thickness was 4 mm. Therefore the distance between the inserts and the cavity was 5 mm. The determined variables were:

- Shape and dimensions of the new cavity;
- Dimensions of the new porous inserts, particularly the metallic sheet thickness and their hole geometry;
- Porous inserts and plates materials;
- Positioning of the thermocouples for controlling the mold temperature.

PROJECT METHODOLOGY Due to the fact that some important parameters of the problem, including the water flow rate, which depends on the inserts geometry, were unknown initially, it was decided to divide the work two distinct phases. In the first one a series of fluid-dynamic simulations were performed considering a simple model of the system. The geometric parameters were varied within a reasonable range of values with the aim of obtaining a first response surface in terms of cavity mold heating rate. This initial analysis allowed the definition of the best porous inserts geometry, among the investigated range, which maximized the mold heating. Once the prototype was made, the second step took place. The goal of this phase was the validation of the numerical model through a detailed comparison with the experimental tests.

4.3.3 *First phase: porous inserts geometry optimization and mold designing*

MOLD GEOMETRY GENERATION The first aspect regards the cavity shape, indeed once the mold was made, it has been used for a subsequent experimental campaign which will be explained in the chapter 5. For this purpose a mirror finishing was obtained for mold surface. The mold cavity was made by overlapping two plates. The first, with a thickness of 5 mm, has been mirror-polished on both faces, while on the second plate, with a thickness of 4 mm, two rectangular pockets have been obtained by laser cutting for obtaining the mold cavities as visible in Figure 4.7.

MESH GENERATION As mentioned above, the model mesh was calculated using ICEM CFD. The need to perform the calculation of the mesh for each design point has suggested the use of an automatic algorithm that can be applied to generate the mesh of each geometry. The input parameters settings for the mesh generation were evaluated through some preliminary analysis in order to understand the model sensibility with the mesh size. Once that a reliable mesh size was defined, the mesh was generated as visible in Figure 4.6.

POROUS INSERTS GEOMETRY SELECTION As already advanced before, the porous inserts are made by overlapping two different metal sheets. Both the metal sheets are designed with a series of square holes "L". The two types of metal sheets have the same holes geometry but they are assembled misaligned along the water flow direction by a distance equal to half of the square hole. Doing so a labyrinth shape was obtained by overlapping alternatively these two metal sheets. The dimension parameters considered as design variables and their ranges are:

- The side holes (from 2.5 mm to 5 mm);

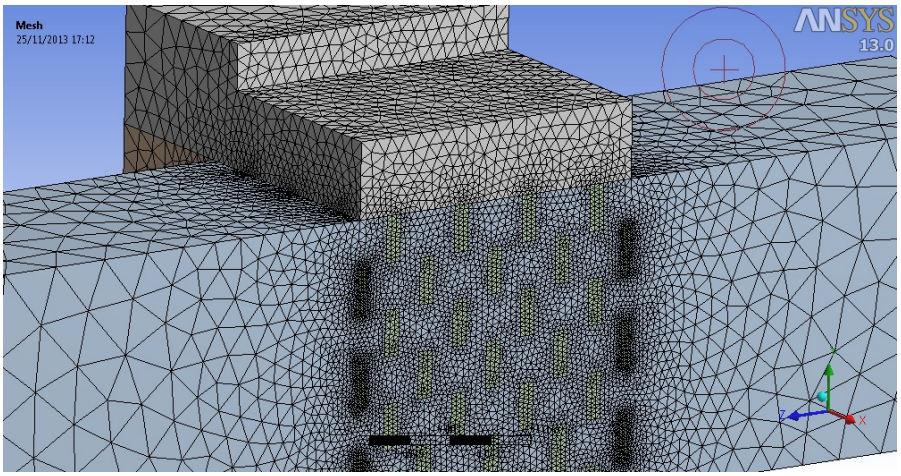

Figure 4.6: solids meshing for CFD simulation

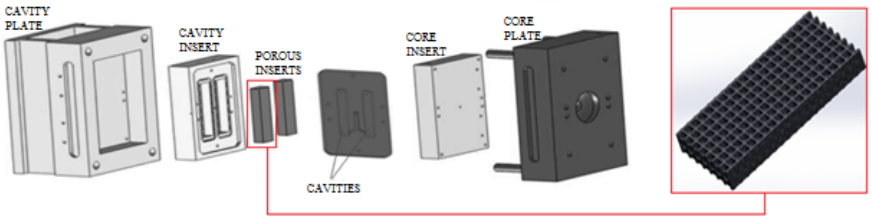

Figure 4.7: The RHCM mold assembly

- Sheet thickness S (from 1 mm to 5 mm).

The minimum distance between the holes "t" was assumed as constant and fixed to 1 mm in order to allow the laser cutting of contiguous holes. As regards the model assumptions, they are summarized below:

- The porous inserts were considered as a bonded solid, neglecting the thermal contact resistance between the overlapped sheets;
- The water flow was assumed turbulent;
- In order to reduce the mesh computation it was needed to consider the solid as symmetric;
- For the same reason, only a section of 20 mm was chosen to carry out the simulation as shown in Figure 4.8

CFX MODEL SETTING The simulation conducted for each type of geometry lasts a transitional period of 2 s in which the flowing water temperature was 420 $°K$, with an initial mold temperature of 295 $°K$. The fluid domain, in the inlet and outlet regions, has been extended in order to remove the influence of the porous inserts shape on the

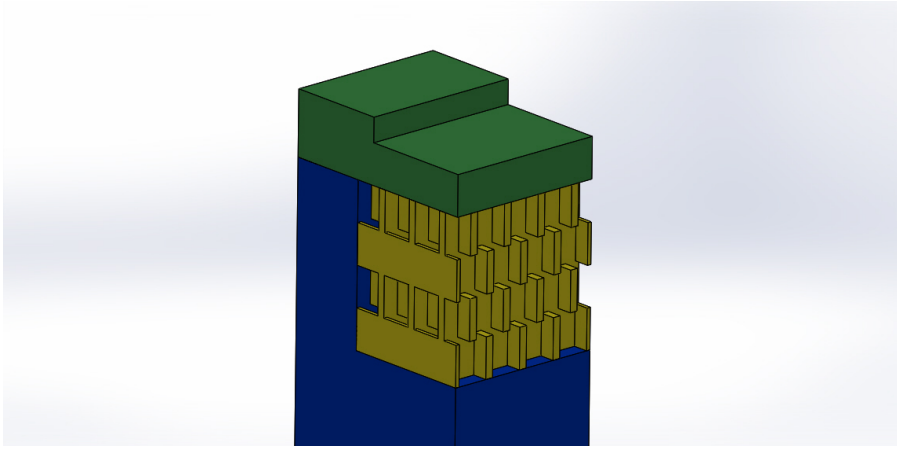

Figure 4.8: Solid domain considered in the first simulations campaign

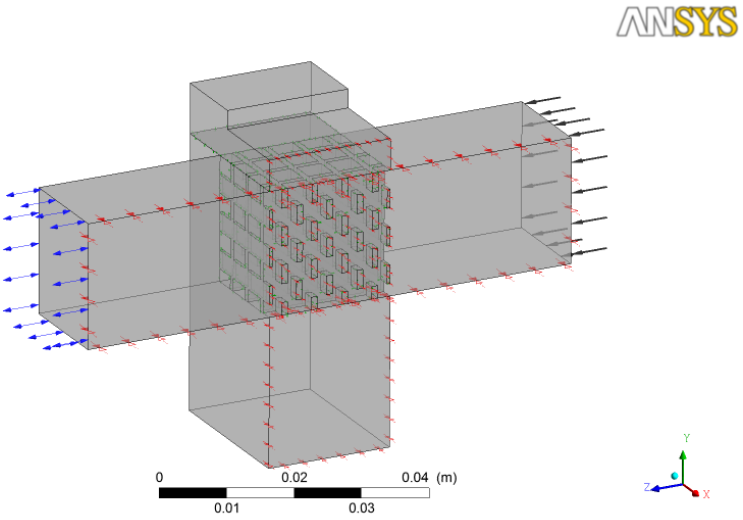

Figure 4.9: Model boundary conditions

DOMAIN: WATER		
Inlet	Inlet	$Q_m = 0.05Kg/s; T = 420K$
Exit	Opening	p= 400000 Pa
DOMAIN: Mold		
Environment	Wall	HTC $K = 10Wm^2K^{-1}$; Tenv=295K

Table 4.1: Model boundary conditions

DOMAIN	INITIAL CONDITIONS
WATER	T=420 $^\circ K$; p=400000Pa; U,V,W=0m/s
MOLD	295 $^\circ K$

Table 4.2: Model initial conditions

local flow condition which could result in a lower simulation accuracy (Figure 4.9).

The walls of the extended domain have been imposed adiabatic and frictionless, so as to ensure on one hand the constancy of the water temperature until the mold inlet and on the other hand an uniform flow distribution through the section. Symmetric conditions were applied in all the surfaces lying in the introduced plane of symmetry. The main initial and boundary conditions imposed on the model are shown in Table 4.1.

It is also notable that the domains initialization has been made neglecting the real phenomena description, in fact, it has been considered that the water instantaneously fill the porous insert and the real mold temperature distribution has not been considered. However, this choice was not influent concerning the porous inserts geometry optimization because it deals a relative comparison between the results. Moreover matching the initial conditions in each geometry analyzed, ensure a reliable results understanding.

ANALYSIS OF RESULTS AND POROUS INSERTS GEOMETRY DEFINITION Thanks to the CFX software interface it has been possible to determine the temperature distribution along the mold surface at the end of the transitional time. The response variable chosen to thermally compare the different porous inserts geometries solutions is the maximum temperature in the cavity reached after 2 seconds. The results are shown in Table 4.3

The results can be summarized with the response surface visible in Figure 4.10 where it is shown the maximum mold cavity temperature trend for the investigated porous inserts geometries.

It is visible that, for the parameter "S", the highest cavity temperature is achieved in correspondence of his upper value within the investigated range. Therefore, higher values of this parameter could be investigated to further increase the mold thermal performance. However, considering that the width "t" of the sheets was only 1 mm and

		SQUARE SIDE LENGTH "L" (mm)				
		3	3.5	4	4.5	5
Thickness "S" (mm)	3	368.2	366.2	362.6	359.2	359.8
	4	368.7	369.9	367.1	363.6	364.4
	5	371.1	374.1	372.3	363.4	364.9

Table 4.3: Maximum cavity temperature (°C) after 2 seconds varying the inserts geometry parameters

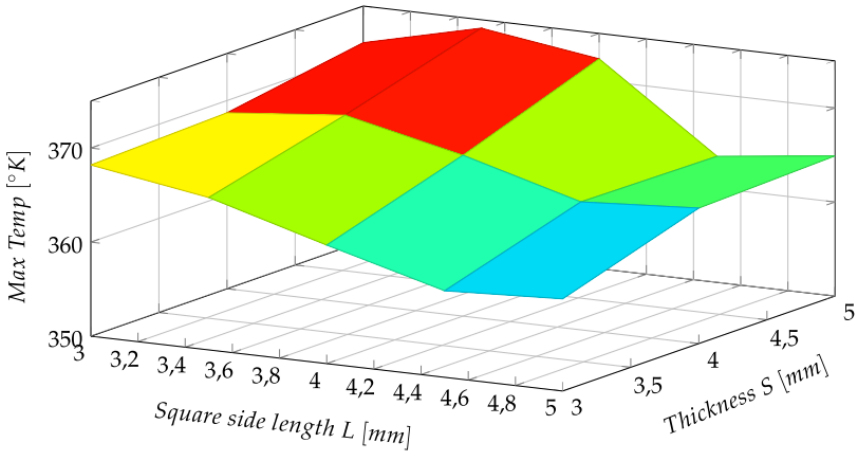

Figure 4.10: Simulation response surface

the inserts were subjected to an high compression loads, it was decided to not exceed the value of 5 mm for the parameter "S" in order to avoid undesired structure buckling. Therefore, the porous inserts geometry which ensure the highest thermal exchange between cavity surface and the circulating fluid has the following geometry:

- Square hole side L = 3.5 mm;
- Thickness S = 5 mm;
- Minimum distance between holes t = 1 mm.

4.3.4 *Second phase: detailed fluid-dynamic model generation*

MATERIAL SELECTION AND POROUS INSERTS MANUFACTURING

The preliminary simulation has suggested the design of the porous inserts made by overlapping metal sheets with a thickness of 5mm and a square hole side of 3.5mm. The best solution for obtaining precisely this type of dimensions would be the cutting water jet technology, however, because it is an expensive and time consuming process it was decided to produce the metal sheets by laser cutting. Concerning the choice of material, the best solution would be make the insert with a copper-beryllium alloy, which is a material already used to mold inserts with a high thermal conductivity. This type of alloys

have a thermal conductivity of about 100 W/mK, combined with a rather high yield strength, especially after heat treatment. However, because this first prototype has the purpose of validating the CFD model and executing some molding tests, the high thermal conductivity is not of primary importance. It has therefore been chosen to realize the insert in stainless steel AISI 304; material having a rather low thermal conductivity (16 W/mK at 25 °C), but easily workable by laser cutting. A further advantage of this material compared to other steels is the inoxidizability. The insert material in fact, is immersed in stagnant water for many hours therefore, in such environment, a carbon steel would eventually corrode, and the oxide formed would be carried from the water during the subsequent operation may hindering the water flow.

CONTACT THERMAL RESISTANCE Considering the porous inserts as a pack of few metal sheets. The contact thermal resistance is defined as :

$$\mathbb{R}_c = \frac{1}{h_c} = \frac{Q/A}{\triangle T} \tag{4.1}$$

The main factors that affect the contact thermal resistance are:

- Roughness, waviness and flatness of the surfaces;
- Fluids and inpurities at the interfaces;
- Contact pressure;
- Thermal properties and mechanical properties of materials in contact.

In general it can be said that for a given material the resistance increases with increasing roughness, whereas decreases with increasing the contact pressure. This fact suggested two important practical considerations, namely the need to polish the metal sheets to reduce the surface roughness and to impose an interference pre-load during the metal sheets assembly. The interfacial resistance was taken into account in the following simulation.

DEVELOPMENT OF A DETAILED THERMO-FLUID-DYNAMIC MODEL The purpose of this second model is in one hand the understanding of the phenomena that occur in the new inserts and in the other hand is the generation of a reliable tool for predicting the mold thermal behaviour for further future projects. For these reasons it is necessary that the numerical model:

- Would be able to describe the reality in detail;
- Would be suitable to be validated experimentally.

DOMAIN: WATER	
Density	935 Kgm^{-3}
Thermal conductivity	0.688 $Wm^{-1}K^{-1}$
Thermal heat capacity	4270 $JKg^{-1}K^{-1}$
Dynamic viscosity	0.212 $10^{-3}Pas$
DOMAIN: Mold	
Density	7900 Kgm^{-3}
Thermal conductivity	16 $Wm^{-1}K^{-1}$
Thermal heat capacity	500 $JKg^{-1}K^{-1}$

Table 4.4: Domains properties

The first point involves the need to eliminate simplifying assumptions, such as the neglecting of thermal resistances and the usage of unsuitable symmetric boundary condition in Table 4.1. The second point, however, entails the need of knowing all the material properties as well as the real initial and boundary conditions. Once that all these parameters were known, it was possible to perform a calibration of the model by planning experimental tests carried out with the physical prototype. Only through a validated numerical model it is possible to perform a qualitative predictions of the effect of any changes in the system, such as: using a different material for the insert, modify the mold geometry, setting a different water temperature etc. With this regard, the first goal of the model experimental calibration was to compare the accuracy of using a turbulence model for the fluid domain or a laminar flow model.

MODEL GEOMETRY The geometry of the model is shown in Figure 4.11. As visible it was considered the entire mold while the computational domain was reduced to a portion of the system with a thickness of 13.5 mm, obtained by cutting the model with two parallel planes. In order to adopt a finer mesh, the symmetry properties of the mold was exploited.

The choice was made for the need to have a computational domain reduced enough to permit the simulation performing in an acceptable time and with the available hardware.

FLUID-DYNAMIC MODEL SETTINGS Thanks to the platform Workbench, the model parameters can be managed from the main window in order to ease the evaluation of the input parameters sensitivity on final results. Concerning the fluid and solid domains, they have the properties listed in Table 4.4.

Both the input and the output parameters are set to "Opening" condition with the assignment pressure value, in order to accurately represent the flow conditions with a complete developed speed. The adoption of this type of boundary condition required the calculation

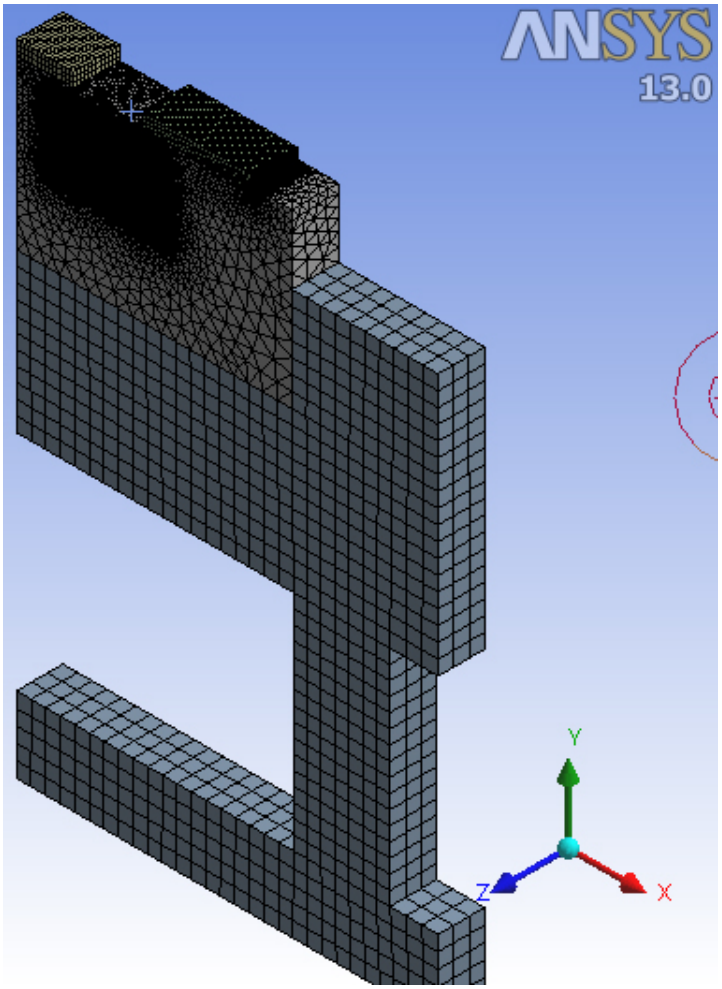

Figure 4.11: Meshing of the detailed CFD model

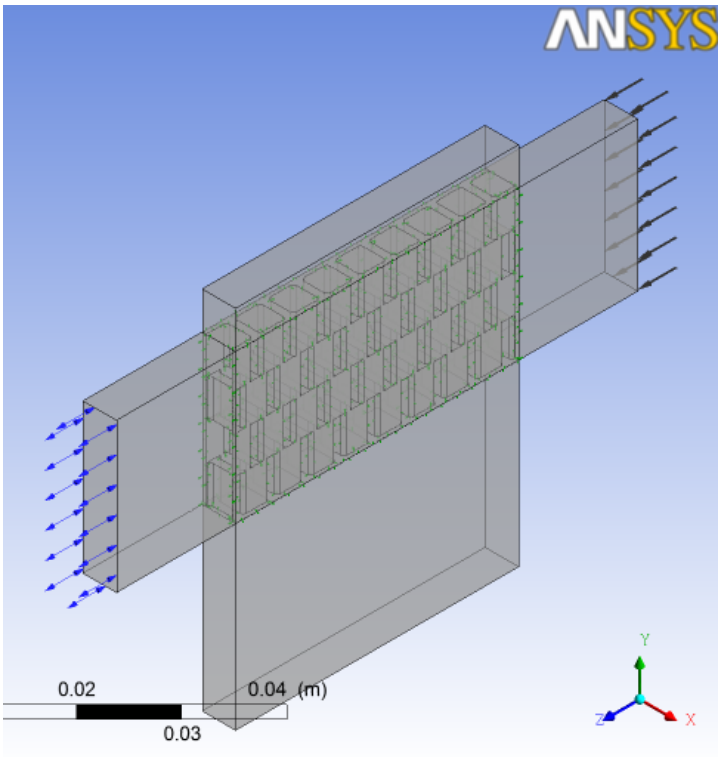

Figure 4.12: Model utilized to determine the pressure drop

of the correct pressure drop between inlet and outlet of the simulated model. The steps employed for calculating the pressure drop are the following:

- Execution of an experimental test with the phisical prototype in order to determine the pressure drop imposed by the thermoregulator pump. The pressure value was supplied by the same temperature control unit and is equal to: $\triangle P = 5bar$;
- Using the characteristic curve of the pump, it was determined the flow rate of circulating water in the mold, equal to: Q= 10 l/min The volume circulating in the single insert is therefore equal to: 5 l/min;
- Performing of a fluid-dynamic simulation to determine the pressure drop per unit length through the insert. To do this a simplified numerical model was created, which actually simulated the flow through a single channel of the porous inserts labyrinth. Doing so, it is assumed that in each "channel" of the porous inserts the pressure drop would be constant. The geometry of such a model is visible in Figure 4.12.

The flow rate through a single channel of the porous insert was calculated by dividing the flow rate by the number of channels. Thanks to this simulation the pressure drop was determined: $\frac{\partial P}{\partial x} = 530300 \frac{Pa}{s}$ Assuming a linear relationship between pressure drop and insert

DOMAIN: WATER		
Inlet	Inlet	$p = 500000Pa; T = 130°C$
Exit	Opening	p= 492840 Pa
DOMAIN: Mold		
Environment	Wall	HTC $K = 10Wm^2K^{-1}$; Tenv=15 $°C$

Table 4.5: Model boundary conditions for the transient simulation

length, the calculated pressure drop between the input and the output of the model visible in Figure 4.11 is:

AP = 7160 Pa

A further issue regards the modeling of the thermal contact resistance. A rigorous modeling of the contact resistance would be extremely complex, since besides its dependence on material properties it also depends on the contact pressure, which varies because of the differential thermal expansion. It has been chosen to consider a fixed value of contact resistance regardless its dependence from other variables. The first attempt value was assigned equal to:

$R_c = 2.7 * 10^{-4} \frac{m^2K}{W}$

It is considered important at this point a clarification concerning the fluid model choice. The Reynolds number was calculated for the labyrinth geometry, taking as reference a single rectangular sections as visible in Figure 4.12. Considering the flow conditions explained above and a water temperature of 130 $°C$, the hydraulic diameter was calculated as 4A/P where A is the flow section and P the wet perimeter. In this case the Reynolds number was 7345. From literature it is learned that for the flow through rectangular mini-channels the transition from laminar to turbulent flow occurs for Reynolds numbers between 2200 and 2500, depending on the relationship between the height h and the base b. It was therefore decided to set up a turbulence fluid domain model, namely the k-epsilon model. In this case, however, the choice was made not without several unknowns, concerning the fact that the data reported in the literature usually refer to constant cross section, while in the present case the section is greatly variable along the fluid path. The consequences of the rapid changes in the flow section are not easily predictable. Considering the boundary conditions listed in Table 4.5, the complete simulation was performed in two steps:

- Stationary analysis with the circulating water at 60 $°C$;
- Transient heating analysis with an inlet water temperature of 130 $°C$, for a duration of 30 seconds.

They were then applied the boundary conditions as visible in

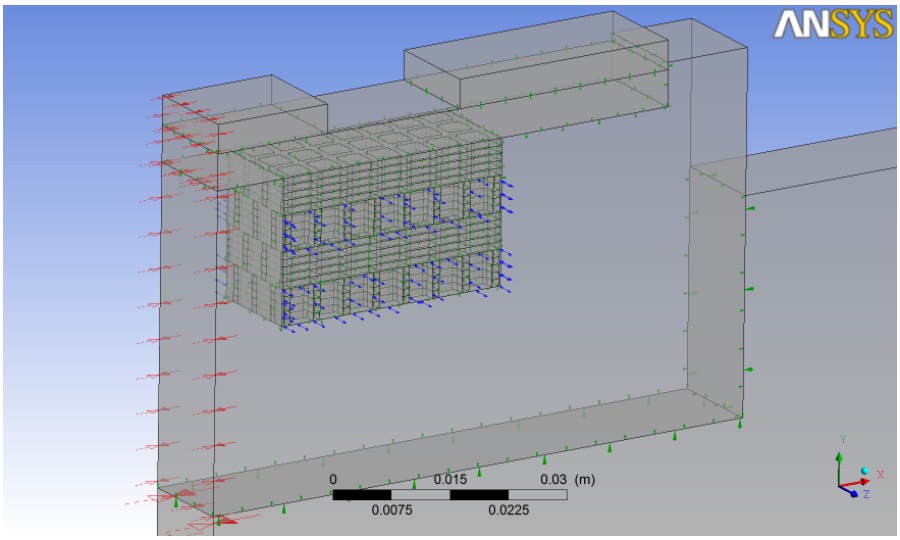

Figure 4.13: Boundary conditions for the transient simulation

SIMULATION RESULTS A first qualitative evaluation can be made by observing the evolution of the temperature field, represented with a color map in Figure 4.14.

It is observed that the lack of an isolation layer between the insert and the internal mold causes the heating of the entire area surrounding the insert. Despite this waste of energy it is still visible that the temperature increases rapidly on the surface cavity, because of the reduced thickness of the plate. The placement of the insert as close as possible to the cavity, results in a reduction of the heating time due to the fact that the conductive thermal resistance and the thermal inertia of the interposed material is reduced. Another important aspect is the fact that after 1 second the insert had already almost the same temperature of the water, highlighting the fact that the bottleneck of the heating phase was the plate thermal inertia. It is also reasonable to believe that a higher insert conductivity would lead to a lower heating time. From a quantitative point of view, it is possible to observe the graph in Figure 4.15, which represents the trend of the maximum temperature in the cavity, the average temperature and the temperature at the point corresponding to the position of a thermocouple installed in the phisical prototype (as discussed below).

These graphs allow the calculation of the heating rate:

$HS_{T_{av},(8s)} = \frac{T_{av}(8s) - T_{av}(0)}{8} = 5.87 \frac{^\circ C}{s}$

Where $HS_{T_{av},(8s)}$ is the heating rate calculated for the cavity surface average temperature considering the initial 8 seconds of the transient heating. In correspondence of the thermocouple point the heating rate was:

$HS_{TCT,(8s)} = 5.38 \frac{^\circ C}{s}$

where TCT refers to the temperature in the point where the thermocouple was placed.

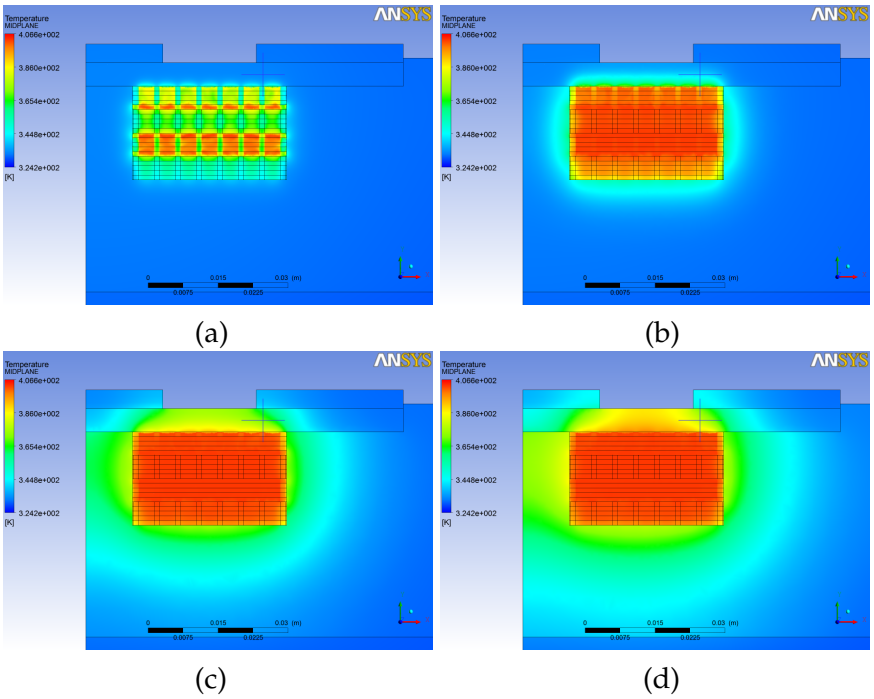

Figure 4.14: Mold section temperature distribution after 0.1 seconds(a) after 2 seconds (b) after 6 seconds (c) and after 10 seconds (d)

4.3.5 *Mold structural verification*

LOADS CONDITIONS A mold structural simulation was carried out to calculate the stress field caused by the injection polymer pressure in the cavity and the thermal load due to the rapid heating. To determine the injection molding pressure a filling and packing analysis was carried out with the software Autodesk MoldFlow 2013, while the load caused by the mold thermal expansion was obtained thanks to the transient thermal simulation.

PERFORMING OF THE INJECTION MOLDING SIMULATION This simulation aimed to determine the cavity pressure distribution caused by the pressure developed by the plastic during injection phase. The injection molding parameters were chosen considering the usage of a fiber reinforced polypropylene (Celstran PP50% lgf) with standard conditions (Table 4.6).

In Figure 4.16 it is reported the cavity pressure profile along the polymer flow direction. As visible in the same image, the mold was designed with two cavities while the molded part was a small plate. The maximum injection pressure, reached in correspondence of the main runner, was 40MPa. Through this simulation, the load distribution was determined and it could be inserted as boundary condition in the subsequent structural simulation. However, in order to simplify the simulation set up and for safety motivations, it has been consid-

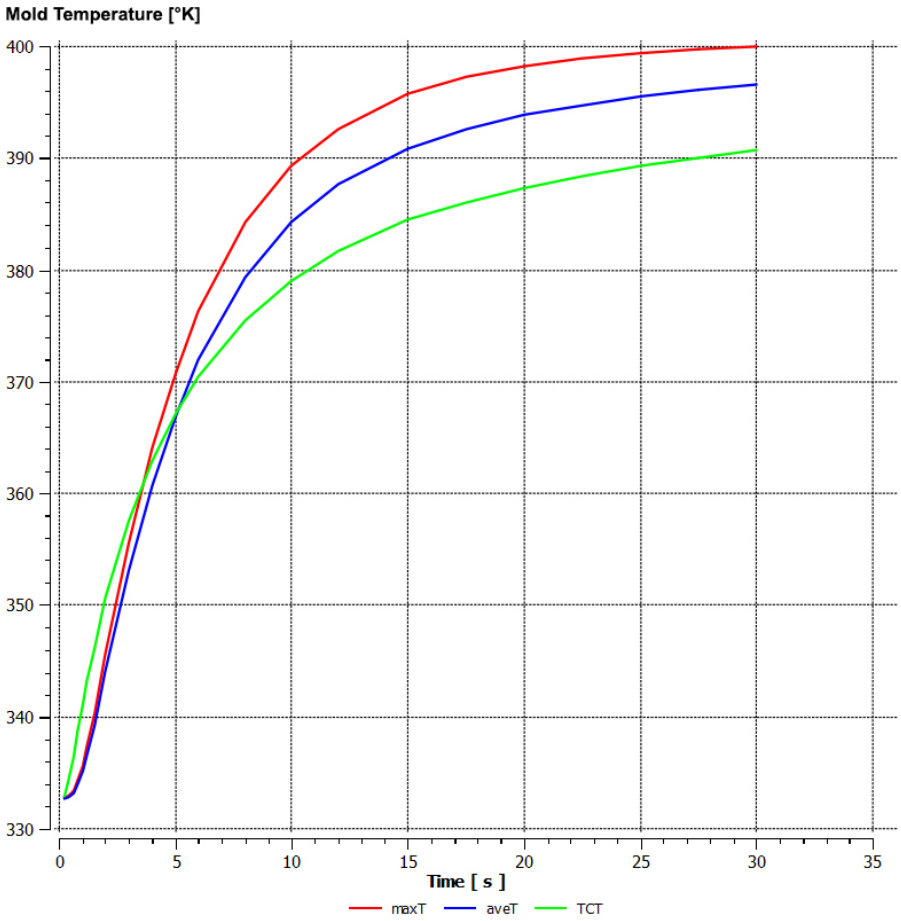

Figure 4.15: Heating profiles obtained for a cavity central point (red), for the average temperature of the cavity mold (blu) and for the thermocouple point (green)

Process parameters	
Melt temperature	240 °C
Mold temperature	50 °C
Injection molding time	1 s
Switch over	99% of the total filled volume
Packing pressure	40 MPa
Packing pressure time	10 s

Table 4.6: Injection molding simulation parameters

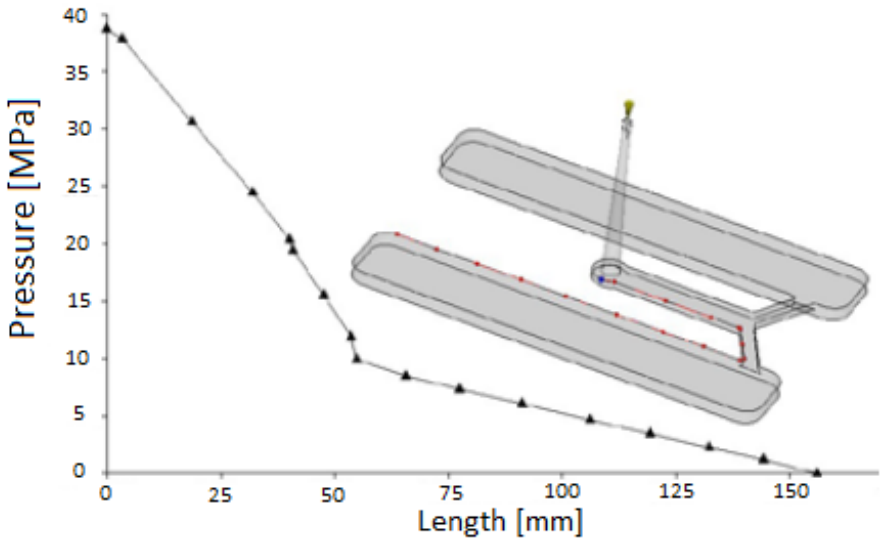

Figure 4.16: Mold cavity pressure profile

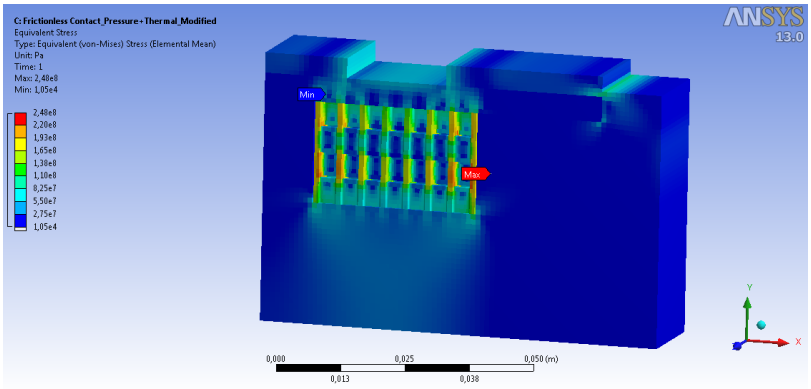

Figure 4.17: Mechanical simulation stress results

ered a constant pressure of 40MPa applied to all the surface cavity, even though this value was reached only in the central position.

STRUCTURAL SIMULATION ANALYSIS In the structural simulation, the material elastic modulus and the yield material stress were fixed to E=190 GPa and σy=270 MPa respectively. The stress caused by the thermal expansion was also taken into account.

In Figure 4.17, the mechanical simulation result shoes a maximum equivalent Von Mises stress of 248 MPa, which is below the yield material stress. The mold vertical deformation is visible inFigure 4.18. The latter figure highlight that the cavity deformation is dominated by the effect of the insert thermal expansion, rather than by the pressure in the cavity. Indeed, the maximum deformation along the axis z, orthogonal to the surface of the cavity, is equal to 0.00724mm and it is positive. This is the effect of the insert thermal expansion which prevails over the cavity pressure. The stiffness of the insert is there-

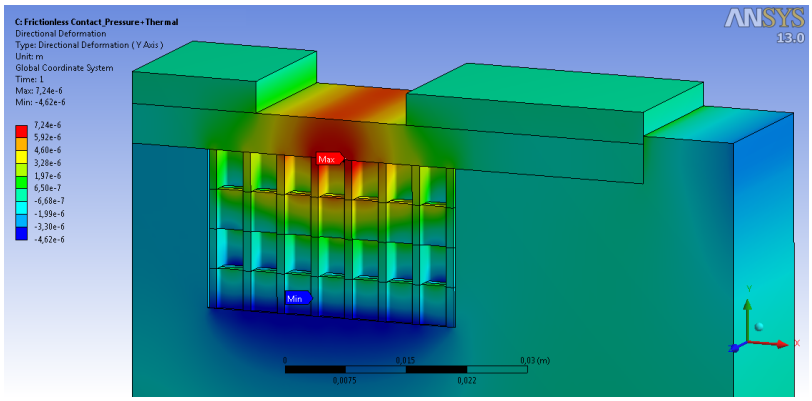

Figure 4.18: Mechanical simulation deformation results

fore rather high, when compared for example with metal foams. The chain of fluid-dynamic, thermal, injection molding and structural simulations has permitted the development of an optimized mold which will be used in the following chapter for validating the model of the fluid dynamic simulation and subsequently for an experimental campaign with the aim of investigating the RHCM influence on fiber reinforced and crystalline materials.

4.4 MOLD MANUFACTURING AND FLUID-DYNAMIC MODEL VALIDATION

In the first part of this chapter it was presented the procedure used to define the size and the shape of the porous insert for the rapid variation of mold temperature, using mainly simulation tools. This chapter summarizes the essential aspects of the experimental campaign conducted on the physical prototype to experimentally measure the cavity heating trend, varying the operating conditions. The experimental apparatus will be discussed in this chapter. A comparison between the simulation and the experimental results will be carried out. It will be highlighted that the assumptions made during the design phase have led to an overestimation of the heating rate. To conclude, a fluid model validation will be carried out.

4.4.1 *Materials and methods*

The metal sheets, made with AISI 304 (austenitic stainless steel), were obtained by laser cutting. The mold plates were also obtained for laser cutting of semi-finished laminates in AISI 304. Both the plates were then processed with a CNC machining center 3-axis. The varioterm cycle was performed with a Tempro D Vario Plus 180 thermoregulator, provided by Wittmann-Battenfeld. The alternative flowing of hot and cold water through the mold was ensured by six pneumatic valves, controlled by a PLC, that manages the phases duration

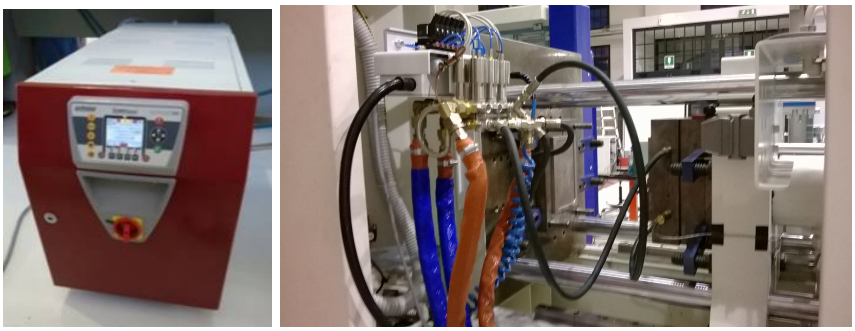

(a) (b)

Figure 4.19: (a) Thermoregulator system (b) Pneumatic valves system

(a) (b)

Figure 4.20: (a) Thermocouple placed in the mold water inlet (b) Thermocouple placed in the mold cavity

and the trigger signals. In Figure 4.19 is visible the thermoregulator and the valves system.

The experimental mold characterization was made by acquiring the water temperature at the mold inlet and the temperature of the cavity mold. For doing this, two thermocouples were used as visible in Figure 4.20. The temperature signals are digitized by means of a data logger (NI) and acquired through a program created with LabView (National Instruments).

4.4.2 *Model validation*

The model validation was carried out by comparing the thermal simulation with the experimental results. By means of the thermocouple placed in contact with the water inlet, it was possible to detect a small difference between the effective temperature of the water which enters into the mold, and that one set with the temperature control unit. There is also a further aspect, it should be noted that when the valves unit switches from the cooling phase to the heating one, the cold water still inside of the mold channels and the connecting pipes will be added to the hot circuit. To further investigate this aspect two heating tests were conducted using pipes of different lengths, respectively

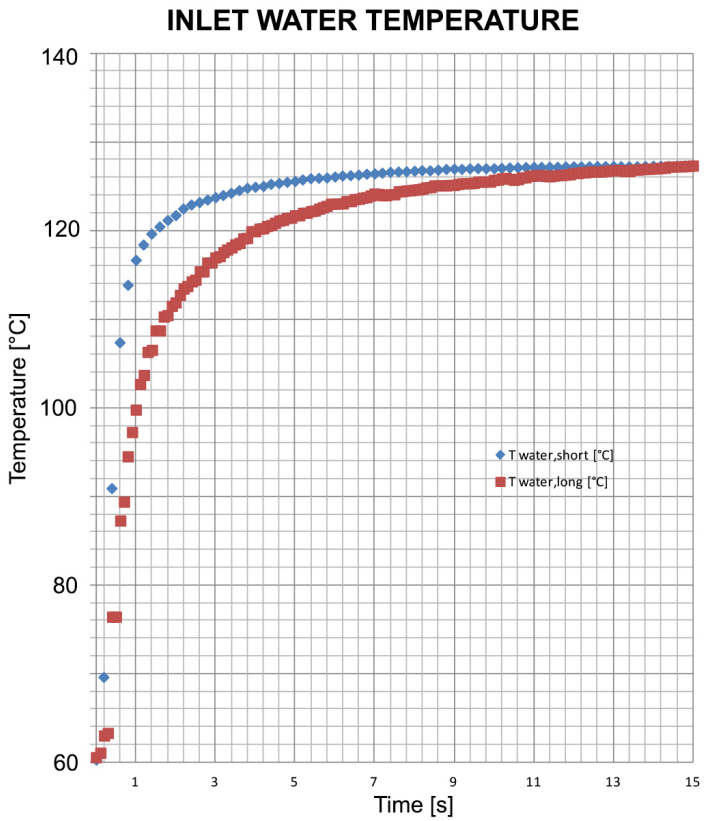

Figure 4.21: Comparison between the inlet water temperature using long channels (red line) or short channels (blue line)

700mm and 2500mm, to connect the valve station with the mold. It is seen that longer tubes determines two phenomena. The first, obviously, it is a delay of the mold heating, due to the fact that the hot water takes more time to reach the mold. The second, less obvious, is the increasing of the time needed for the termoregulator to heat the water up to the set value. This time is enhanced reducing the heating power of the thermoregulator. Therefore, the solution could be use shorter tubes or at least increase the thermoregulator power.

The effective water temperature was considered as inlet boundary condition in the model. The pressure drop between inlet and outlet was given directly from the thermoregulator pressure trasducers. The coefficient of thermal exchange between mold and environment was set to $10 Wm^{-2}K^{-1}$ where the external temperature was 15 $°C$. In Figure 4.22, a comparison between the simulated and the experimental heating profiles is shown; in this example, the inflow water temperature was 130 $°C$. The red line and the green one describe the simulated heating profiles considering a turbulent and a laminar flow model respectively. The black line represent the experimental heating profile measured with the thermocouple placed directly in the mold cavity. Comparing the heating profiles calculated by the numerical simulations and the experimental one, it is possible to conclude that the

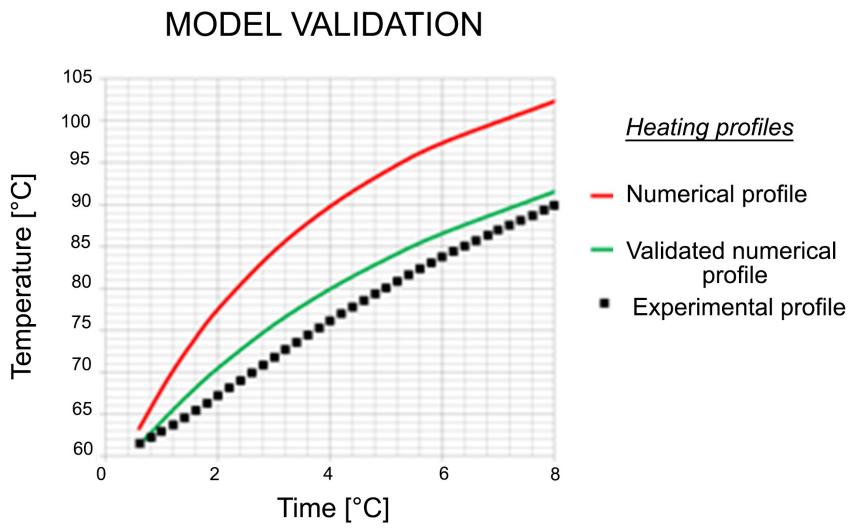

Figure 4.22: Numerical and experimental comparison between the heating profiles

laminar model gives a better prediction of the real heating profile. The maximum error was 6, 5%.

In Figure 4.23, several heating cycles were acquired at different water temperatures, with an initial mold temperature of 60 $^{\circ}C$. These heating profiles are relative to the temperature detected by the termocouple placed just behind the cavity surface. They have been useful to predict the time needed to achieve a specific mold cavity temperature. The maximum heating rate obtained was 7 $^{\circ}C/s$ with a circulating hot water of 175 $^{\circ}C$.

4.5 DISCUSSIONS

The experimental campaign conducted with the physical prototype has provided many important informations regarding the proposed technology performances. Regarding the cavity heating, the technology based on the labyrinth insert has been seen to be competitive with the best technologies that use the fluid convection for mold heating, in particular for the steam heating. The maximum heating rate obtained is about 7 $^{\circ}C/s$, using pressurized water at 175 $^{\circ}C$ and starting from a temperature of 30 $^{\circ}C$. The comparison with the technology based on the foam metal insert has sanctioned an increasing of 59% of the heating rate for the same conditions. Moreover, it is shown experimentally that the channels length influences the inlet water temperature in the mold and consequently the heating of the same. The greater the length of the connection pipe, the greater the heating delay and the lower the heating rate. This fact suggests to place the valve unit as close as possible to the mold, including the possibility of installing a dedicated control directly in the half-mold. Concerning the

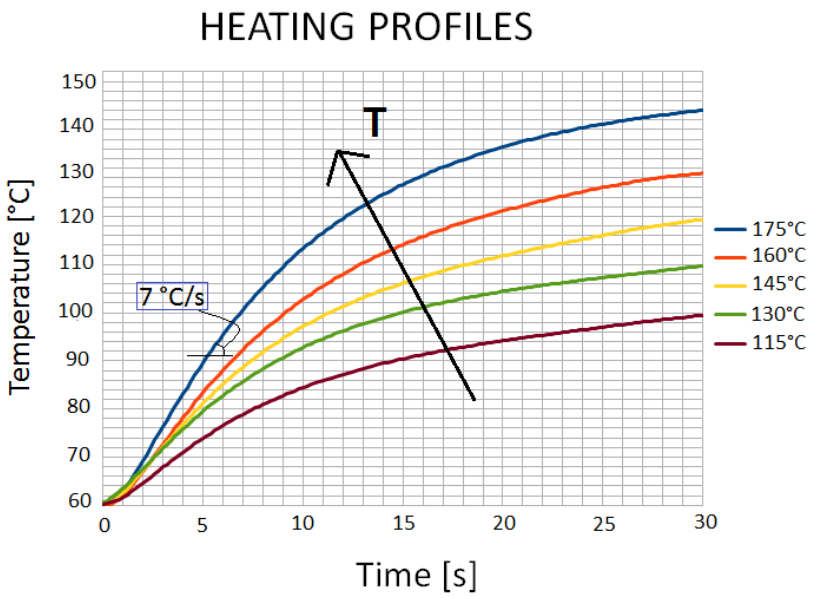

Figure 4.23: Heating profiles for different water temperatures

porous inserts design, the investigation of other manufacturing methods or materials could be very useful to further increase the mold thermal response. For example, the employment of an SLM technology would increase the number of available geometries which can be used as porous inserts. Another interesting aspect concerns the materials choice. In this paper the main purpose was the development of a new method to design cooling channels and validate the CFD model. For this reason the materials choice was made paying attention to the requirements of ease of processing and cost, giving little weight to the thermal properties, which are rather low in this case. Therefore, it is reasonable to expect remarkable improvements using materials with higher thermal diffusivity, such as copper alloys or aluminum alloys. Each solution will have to take into account the both the structural and differential thermal expansion issues.

Part III

STUDYING OF THE RAPID HEAT CYCLE MOLDING INFLUENCE ON APPEARANCE AND MECHANICAL PROPERTIES OF FIBER REINFORCED MATERIALS

5

INFLUENCE OF PROCESS PARAMETERS ON SURFACE APPEARANCE OF FIBER REINFORCED INJECTION MOLDED PARTS WITH A RAPID HEAT CYCLE MOLDING TECHNOLOGY

Thermoplastic long-fiber bridge the gap between the thermoplastic composite short fibers and those in continuous fibers, providing better mechanical properties than those in short fibers but retaining the ability to be injection molded. This technology is the most widespread for the production of these materials, since it allows the production of components of large size and complex geometries with reduced cycle times. It is therefore possible to produce articles with high performance at low cost. However, a typical goal in fiber reinforced polymer injection molding, is the achievement of high aesthetic quality surfaces. In particular, due to the low mold temperature, the fibers which reach the cavity wall freeze instantaneously resulting in a high surface roughness and a poor quality in general. Some results of recent research about the mold temperature influence on surface roughness and gloss are highlighted in chapter 1. In this work it is studied the mold temperature, the injection rate and the packing pressure effects on surface topography. The molded part was a small plate made with PP reinforced with 50% of long glass fibers. To statistically investigate the experimental results, the experiment was conducted using the method of Design of Experiments (DOE).

5.1 MATERIAL AND METHODS

This experiment was conducted to evaluate the effect of the rapid heat cycle molding on molded part surface roughness of polypropylene charged with 50% of long glass fibers. This topic was already studied in literature but only considering the effect of mold temperature actually neglecting the interaction with the others injection molding parameters. Besides mold temperature the most influential parameters on surface topography are the injection rate and packing pressure. These three parameters are therefore the factors considered in this analysis. The response parameter was the root main square Sq, defined as:

$$S_q = \sqrt{\frac{1}{A} \int \int x^2(x,y) dx dy} \tag{5.1}$$

where z (x, y) is the function that expresses the topography of the surface with respect to its middle plane, acquired with an optical pro-

RANGES OF FACTORS	
Mold temperature [°C]	70-110
Injection speed [mm/s]	70-150
Packing pressure [MPa]	20-40

Table 5.1: Design of experiments

Figure 5.1: Optical microscope Sensofar

filometer. The material used was Celstran PP 50% lgf, a polypropylene charged with 50% long glass fibers. The initial fiber length was about 10 mm. The definition of the factorial plane requires firstly the choice of the investigated factors ranges. The intervals considered in this case are:

Therefore, the full factorial design relies in 8 combinations of parameters. For each combination 5 replications were carried out.

5.2 EXPERIMENTAL APPARATUS AND MEASURING SYSTEM

The injection molding machine (Battenfeld HM 110 / 525H / 210S) has a clamping force of 110 tons, with hydraulic drives for both the closure unit and the injection unit. The system used for the rapid variation of mold temperature is that one equipped with porous inserts, described in the chapter 4. Concerning the mold temperature control, it has been used the same system explained in the chapter before, composed with two thermocouples interfaced with the LabView software. The surface topography characterization was carried out with the optical profilometer Sensofar (Figure 5.1), using the optics in the confocal mode. The supplied software is capable of providing directly the value of the roughness Sq. The specimens surface has been scanned with an optical of 20 x, which is a suitable resolution for our purpose.

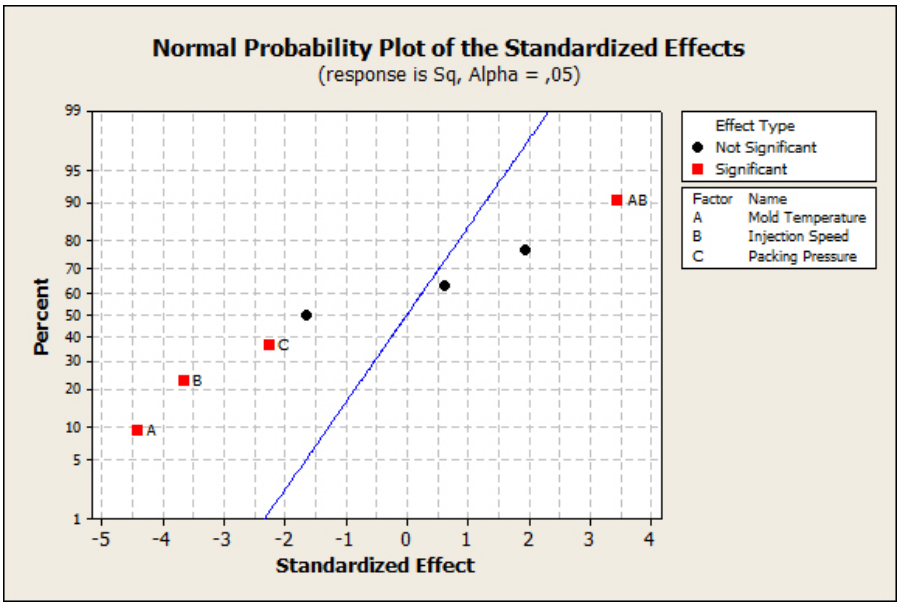

Figure 5.2: Normal probability plot of the standardized effects

5.3 RESULTS AND DISCUSSIONS

The statistical analysis was carried out by adopting a confidence interval of 95%. The results of the experiment show that, among the intervals chosen for the factors, all the main effects are significant and it is also significant the interaction between the temperature of the mold and the injection speed, as shown in the graph of normal probability in Figure 5.2.

Concerning the main effects plots, the experiment shows, in agreement with the other results reported in literature, that using an high mold temperature leads to the specimens roughness reduction Figure 5.3. This is because the material close to the cavity wall is kept at high mold temperature, allowing the migration of the matrix towards the surface, avoiding the fibers surfacing. The difference is also qualitatively visible by comparing the following images Figure 5.5, acquired with the optical microscope, representing the surface of two specimens obtained at different mold temperatures. Regarding the effect of the packing pressure, similarly with the conventional molding, there is a reduction of the surface roughness increasing the pressure. The increasing of injection speed determines a lower roughness; this behavior could be explained in one hand considering the lower material viscosity at high shear rate due to the shear thinning phenomenon and on the one hand, at high injection speed the packing phase occurs in advance giving less time for the melt freezing. To conclude, the experiment highlights a very interesting aspect, which relates to the interaction between mold temperature and injection speed. In Figure 5.4 it is seen that increasing mold temperature, the injection speed becomes almost irrelevant for the surface roughness. This fact

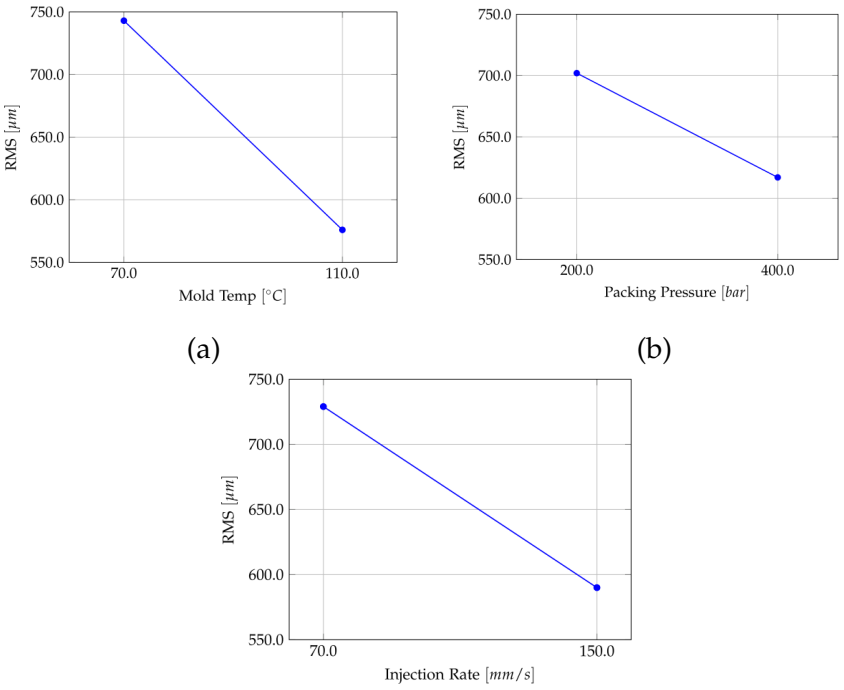

Figure 5.3: Main effects plot: (a) Mold temperature (b) Packing pressure (c) Injection Rate

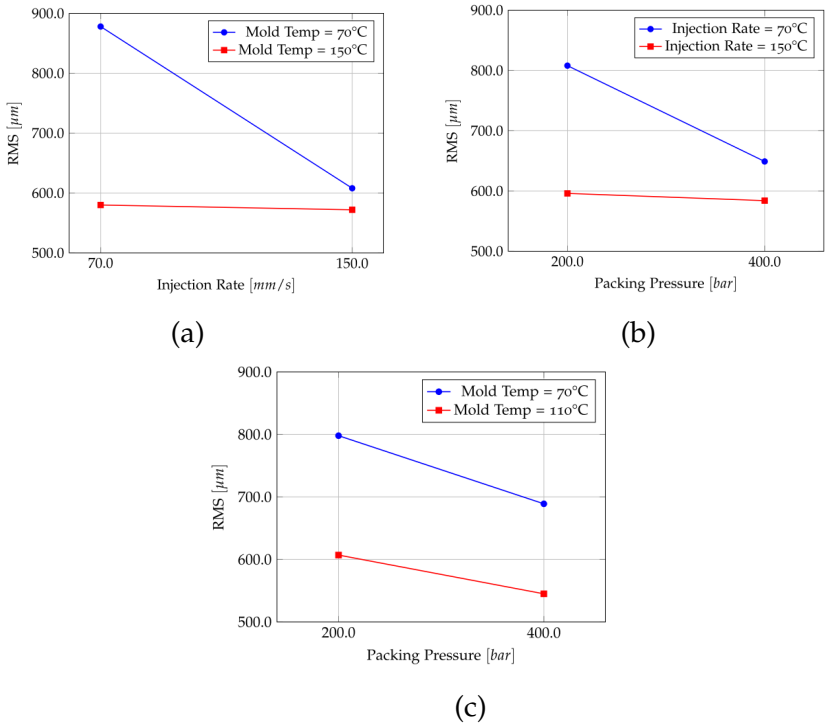

Figure 5.4: Interaction plots: (a) Mold temperature-Injection rate (b) Packing pressure-Injection Rate (c) Mold temperature-Packing pressure

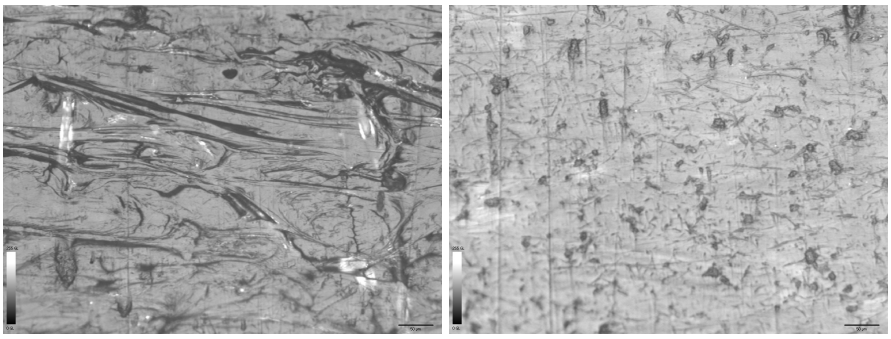

Figure 5.5: Surface topography for the specimens molded with a mold temperature of 70 $^{\circ}C$(a) and 110 $^{\circ}C$ (b)

has an important implications regarding the advantages of using a rapid heat cycle molding technology for fiber reinforced materials. Indeed, it is possible to obtain an high quality surface finishing even with a low injection speed. This consideration means that at high mold temperature it is possible to reach a good quality surface also with a low injection velocity meaning lower fiber deterioration and fibers orientation anisotropy reduction.

6

RAPID HEAT CYCLE MOLDING TECHNOLOGY INFLUENCE ON STATIC MECHANICAL BEHAVIOR OF FIBER REINFORCED POLYMER MATERIALS

The employment of reinforcing fibers can improve the materials mechanical properties such as tensile strength, stiffness and impact resistance. In general, the longer the fibers length the higher the mechanical properties at least up to a critical fiber length where a further increasing of the reinforcement length would not lead to an increasing of mechanical properties. Long glass fibers, which are the most used for injection molding applications, have an initial length of 10-12 mm. However, during the entire process, the fibers are subjected to mechanical stresses which cause their breakage, thus reducing the length. The shear stress was identified as the most influential parameter on fiber breakage and orientation. In particular, from chapter 5 it is seen that increasing mold temperature, it is possible to obtain an high quality surface finishing even with a low injection speed. This consideration means that at high mold temperature it is possible to reach a good quality surface even with a low injection speed reducing the fiber deterioration during process. This work stem from the challenge of optimizing the injection molding process in order to improve at the same time surface appearance and mechanical properties of fiber reinforced polymers. In particular, a Design of Experiments analysis (DOE) was considered for experimentally study the influence of main injection molding process parameters on residual fiber length, fiber morphology and mechanical properties. A new methodology was developed for measuring the residual fibers length. The procedure involved the using of a professional scanner and a specific software able to automatically measure the fibers length. Compared with the traditional technique where the fibers were measured individually, this new measuring system allows the evaluation of a greater number of fibers at the same time. The internal molded part morphology was investigated with an X-ray tomography system which allowed the reconstruction of the internal part micro-structure without impairing the material integrity. The analysis involved the fibers orientation and the specimens porosity evaluation. Tensile tests were conducted to investigate the influence of processing parameters on the specimens ultimate tensile stress. The results were interpreted by analyzing the correlation between residual length and fibers orientation with the mechanical results.

6.1 MATERIAL AND METHODS

Even in this experimental tests, the injection molding machine was Battenfeld HM 110 / 525H / 210S. The mold was that one developed in the chapter 4 , equipped with the porous inserts. To analyze the influence of the molded parts geometry on fiber breakage and orientation, three plates with a different cavity thickness were made in C45 steel. The cavity thicknesses considered in this experiment were 4 mm, 2.5 mm and 1 mm. The specimens cavity was a type 1A dog bone specimen, according to ISO 527. Semi-finished products were obtained for laser cutting while the following activities where carried out subsequently with a CNC machining center in three axes:

- Milling of the runner system and the specimen cavity;
- Drilling operation dor the thermocouple placement;
- Drilling operation for the ejectors guides.

The technical drawing of the plate with a cavity thickness of 1 mm is shown in Figure 6.1.

The thermoregulator employed is the Tempro Plus 180 D Vario, produced by Wittmann-Battenfeld. It is equipped with two separated circuits, one for the low temperature water and the other for the high temperature; it is able to achieve temperatures up to 180 $^{\circ}C$. The mold temperature control was made by placing a thermocouple near to the cavity edge (Figure 6.2) allowing the sincronization between the thermoregulator and the injection molding machine cycles.

The material used in this experimentation was polypropylene filled with 30% of long glass fibers.

6.2 MECHANICAL TEST SETUP

Tensile strength tests were carried out at a deformation rate of 5 mm/s according to ISO R527 standard. For each combination of process parameters considered, five tests were made to statistically analyze the specimens mechanical behavior.

6.3 SYSTEM COMPUTED MICROTOMOGRAPHY

The commonly 2D techniques used to determine the fibers orientation of fiber-reinforced materials (ex. 2D X-rays or section microanalysis) have limitations in extrapolating the three-dimensional fibers distribution from two-dimensional images (X-rays or micrographs of sections). Conversely, the X-ray computed microtomography (CT) is a not destructive method which allows to obtain a complete three-dimensional reconstruction of the piece permitting, in our case, the

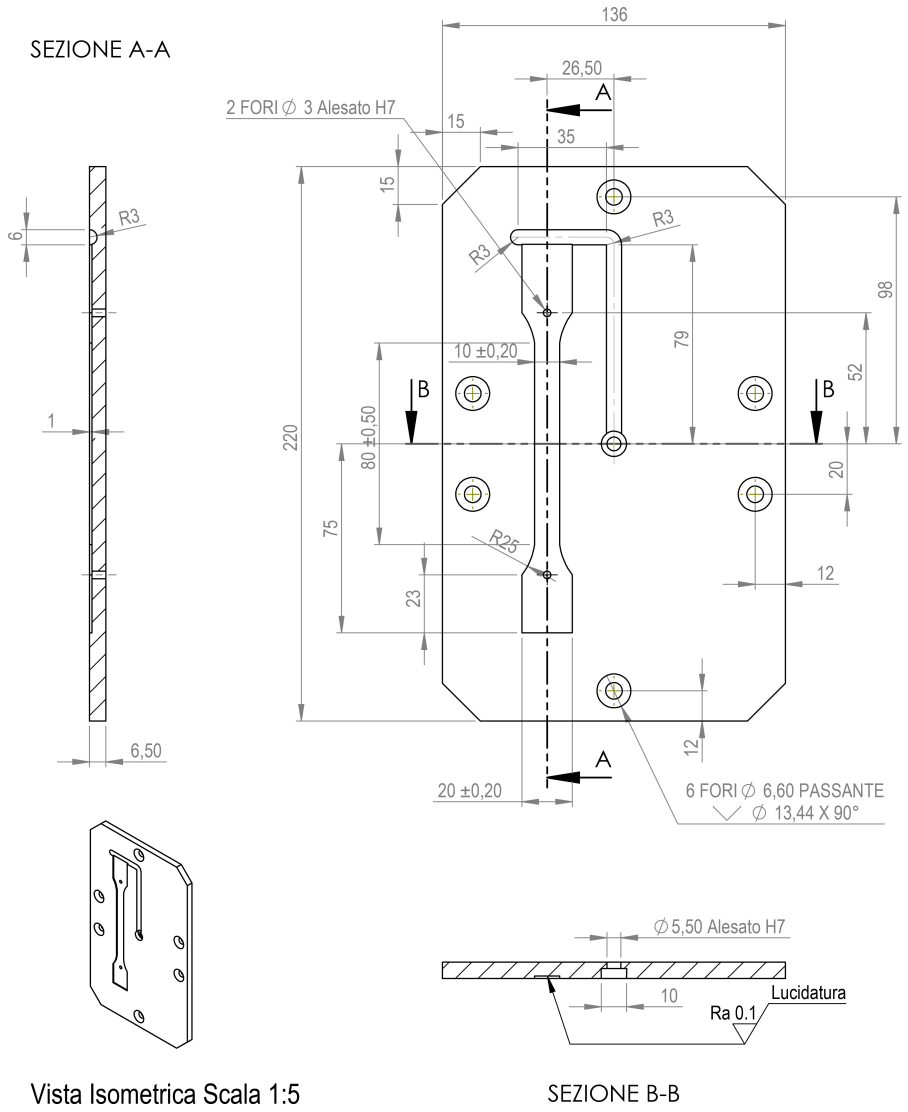

Figure 6.1: Technical drawing of the plate with a thickness of 1 mm

Figure 6.2: Thermocouple position for checking the mold cavity temperature

display of the spatial distribution of the fibers within the matrix. For the images acquisition, a source emits a cone beam of X-rays that invests the sample placed on a rotary table. The emitted radiation are attenuated, partly absorbed from the material and partially dispersed. This attenuation is determined by the thickness that is crossed, by the composition, the material density and the energy of the X-ray. The residual radiation which crosses the piece is measured by a X-ray detector (detector): what is obtained is a radiograph (two-dimensional projection). A high number of projections taken at different angular positions of the sample allows, thanks to a mathematics reconstruction, to obtain a volumetric model composed of voxels (equivalent volumetric pixel). The information that is obtained, consequently, is not limited to one surface of the object, but also about its internal characteristics, allowing, for example, to directly observe the fibers orientation of composite materials. A more detailed discussion of this technique, and a summary of the state of the art can be found in [150], while for an overview of its numerous industrial applications, see [151]. In this study the measurements were made using the system computed microtomography Metrology Nikon Metrology XTEK MCT225, at the Te.Si. laboratory Figure 6.3.

6.4 RESIDUAL FIBER LENGTH MEASUREMENT PROCEDURE

6.4.1 *Traditional procedure for measuring the residual fibers length*

The fibers breakage analysis is important because the residual fiber length is correlated with the injection molding process parameters as

Figure 6.3: CT System Nikon Metrology XTEK MCT225

well as with the workpiece mechanical properties. There are many methods available for determining the fibre length distribution. The most widely used involves several operations (including pyrolysis and ultrasonic system) performed to obtain a series of photographs of the fibres from which information about their length are extrapolated by means of software for image analysis. The micrographs should be large enough to accommodate even longer fibres, but this is not always possible especially in the cases of thermoplastics reinforced with long fibres, whose length can be even longer than the field of view of the vision tool. The inability to measure the longer fibres leads to an underestimation of the average fibre length and thus the correlation between the process parameters and the fibre damage is impaired. Therefore the traditional technique, which is limited by the field of view of the optical CMM used, has been improved to make it suitable for measuring even longer fibres by Berton [152]. For this purpose the image mosaic technique has been applied to merge different images, in order to overcome the limit imposed by the instrument. The new technique has been then applied to a test case, with the aim of analyzing the influence of the process parameters on residual fibres length during injection moulding. In summary, the advantages brought by the technique of Image Mosaic are:

- Ability to measure all the fibers in the sample;
- Need to make a single calibration.

Despite these advantages, however, it remains the major limitation of being a technique not-automated, in which the fibers are extracted manually one by one from the image. Therefore, it is also a time consuming operation.

6.4.2 *Innovative procedure for measuring the residual fibers length*

In this work it was developed a new method which introduces the following features:

- A scanner was employed in order to solve the limitation of the field view, allowing the acquisition of images much larger than those with the CMM machine;
- Automatic measurement of fibers within the acquired image: the use of a specific software for this purpose (described in more detail hereafter) avoids the problem of having to measure the fibers one by one.

With these improvements it was possible to analyze the length of a much larger number of fibers (about 2000 per each sample) in a short time. However it was necessary to spend time for the procedure development, particularly concerning the optimization of the scanner parameters and the calibration of the software used for recognizing the fiber length. In summary, the process for measuring the fiber is divided schematically in the following points:

- Pyrolysis of a portion of the specimen to obtain the fibers from the polymer matrix;
- Removal of a small amount of fibers from the sample using tweezers;
- Dispersion of fibers on a thin glass sheet;
- Use of an high resolution scanner for the acquisition of the fibers sample image;
- Subdivision of the original image into a series of smaller images with an optimal size for the subsequent analysis;
- Image analysis with software ctFIRE which recognizes the fibers and measures their length in pixels;
- Conversion of fibers length from pixels to millimeters by calibrating a few sample fibers with the CMM machine in order to determine the Num.Pixel/millimiters ratio;
- Calculation of the average residual fiber length.

The various steps are described in more detail below.

Figure 6.4: The utilized oven for burning the polymer matrix

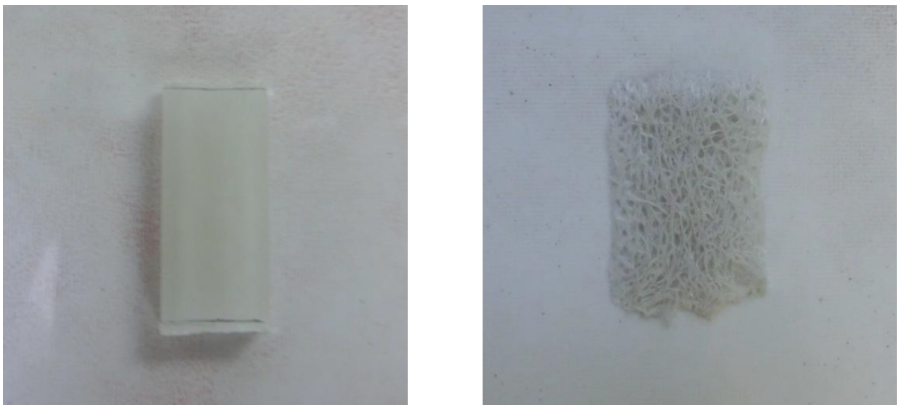

Figure 6.5: Sample obtained from the specimen before and after pyrolysis

PYROLYSIS To make a direct measurement of residual fibers length it is necessary to delete the polymer matrix from the specimen. For each specimen investigated, a small samples of material long 30 mm , has been cut in the central position of the specimens. Taking advantage of the fibers resistance at high temperatures, the separation between fibers and polymer matrix was carried out by heating the samples with an oven in order to burn the matrix Figure 6.4.

The test specimens are placed on a refractory stone which is inserted into the the oven cavity once the temperature reaches about 700 °C. The complete pyrolysis of matrix requires about one hours, after which the plate with the fibers is picked up from the oven and cool at the room temperature. The difference between the initial sample and the burned one is visible in Figure 6.5.

In these conditions it is not possible to directly measure the fibers length, since the plot is a three dimensional structure that does not allow to distinguish the individual fibers. It is therefore necessary to take a small amount of fiber from the sample with tweezers, trying to

Figure 6.6: Grid placed above the scanner glass; the fibers were dispersed in all the visible square holes

avoid the areas adjacent to the cut, since the fibers in this area could be further damaged.

IMAGE ACQUISITION The procedure used to measure the residual fibers length regards the analysis of the images obtained with an high resolution scanner. After isolating a portion of fibers from the burned sample using tweezers, it was dispersed on a glass plate of the same dimensions of the scanner glass. The fibers were spread within 35 square holes of 971x971 pixels as visible in Figure 6.6. This special grid was created because the CTfire software was not able to analyze the entire image acquired with the scanner therefore the image division would result in a fibers cut with the consequence of considering the cut fibers in the analysis. In order to avoid this problem each grid square hole had the same dimension of the image which can be analyzed with the CTfire software. Great attention was paid for the separation of fibers, so that they were easily recognizable and measurable.

The acquired image with the scanner had a resolution of 800 dpi. The scanning conditions were kept constant for all the acquisition carried out. To limit the light reflection a black box of 30 mm thickness was made and placed in order to cover the scanner glass. Each scan enabled the measurement of about 2000 fibers.

IMAGE ANALYSIS In this step the 35 acquired images are imported in the ctFIRE analysis software, developed by Loci: Laboratory for Optical and Computational Instrumentation and available free. The purpose of this independent package MATLAB is the automatic extraction of fibers from an image to analyze their characteristics such as length, thickness or curvature. The program reads the file input images and recognizes the individual fibers by removing the noise from

Figure 6.7: (a) Image acquired with the high resolution scanner (b) Fibers recognition with ctFire (b)

the image and measuring the length of the fibers, with the algorithm FIRE. The fibers recognition is visible in Figure 6.7.

The next step was the conversion of fiber length in pixels to millimeters. For this purpose different fibers were measured with a coordinate-measuring machine optical Werth Video-Check IP 400 CNC. The same reference fiber were then scanned and measured by the program ctFIRE in pixels: in this way it was possible to associate the fiber length measured in pixels, obtained with the image analysis software, with that one measured in millimeters, obtained with the CMM. Therefore, the obtained scale factor was used for converting the output of the ctFire analysis in units of length.

CALCULATION OF THE AVERAGE LENGTH The fibers length measurement was carried out to analyze the investigated injection molding parameters influence on residual fibers length. The ctFire output is the length of thousands measured fibers. Therefore, a mean value is needed to compare the residual fiber length in order to summarize the entire distribution in only one parameter. To characterize the fibers average length it may be used a numerical averageEquation 6.1 or a weighted average Equation 6.2:

$$L_n = \frac{\sum N_i L_i}{\sum N_i L_i} \tag{6.1}$$

$$L_w = \sqrt{\frac{\sum N_i L_i^2}{\sum N_i L_i}} \tag{6.2}$$

where N_i is the number of fibers long L_i. From studies conducted to evaluate the ability of different types of averages to represent the relationship between residual fiber length and mechanical properties of injection molded parts it is seen that the Equation 6.1 and Equation 6.2 consider the fibers lengths with the same weight. Therefore they do not provide a correct representation of the mechanical behavior, in fact, the contribute of longer fibers to the mechanical resistance of fiber reinforced materials is more significant compared with short

fibers. A new approach, proposed by Huq and Azaiez, is based on a mathematical model used to determine the contribution of fibers on the total stress. Therefore the model of Huq and Azaiez was employed in this analysis [153]:

$$L_{Huq} = \sqrt{\frac{\sum N_i L_i^3}{\sum N_i L_i}} \tag{6.3}$$

CRITICAL ASPECTS OF THE MEASUREMENT PROCEDURE The achievement of accurate results and the errors reduction during the measuring process is obtained only taking care of the measuring steps described above. The main issues are related to:

- The tweezers used to take the sample of fibers can cause their breakage, it also operates as a filter by grasping more easily longer fibers;
- Depending on the point where the portion of fibers is extracted it is possible to obtain different length distributions, since the fbers length varies through the thickness;
- Presence of noises in the scanned image due to scratches, blemishes and dust which is unavoidably positioned on the scanner glass;
- Especially in areas with greater concentration of fibers the software hardly distinguishes the fibers overlapped each other.

The solution adopted to minimize these errors has been to pick up a fiber sample through all the specimen thickness and taking care of avoiding fibers overlapping during the images acquisition.

6.5 DESIGN OF EXPERIMENTS

The purpose of this study is to analyze the RHCM technology influence on fiber orientation, residual fiber length and tensile strength of fiber reinforced materials. Thanks to this analysis, it will be identified the most suitable injection molding parameters that can be used to preserve the fibers length and consequently the mechanical properties of molded components. The injection molding parameters investigated in this analysis have been chosen in order to obtain as many results as possible from the experimental campaign. The mold temperature will be the most interesting parameters since it affects the cavity thermal distribution during the injection phase causing the variation of the melt viscosity and the melt flow. A further parameter, which directly influence the material morphology and consequently the mechanical properties of the final part, is the injection molding velocity. Besides mold temperature and injection speed the molded part

Factors	Low level	High level
Mold temperature [$^{\circ}C$]	60	120
Injection speed [mm/s]	10	100
Specimen thickness [mm]	1	4

Table 6.1: Design of experiments

Injection molding parameters	
Melt temperature [$^{\circ}C$]	245
Back pressure [bar]	50
Ejection temperature [$^{\circ}C$]	60
Post-pressure [bar]	80% of max injection pressure

Table 6.2: Design of experiments

geometry is critical because it affects both the melt flow rate through the cavity and the thermal distribution. An experimental campaign was therefore planned taking into account three factors:

- Mold temperature;
- Injection speed;
- Specimen thickness.

Once selected the factors of interest, the next step was choosing the factors levels, which are summarized in the following table:

The temperature range of the mold was chosen considering that the minimum temperature is that one recommended for the material for a conventional injection molding process while the maximum temperature has been set in order to be slightly higher than the glass transition temperature of the material. Regarding the injection speed the lower investigated speed was that one which ensure a complete filling of the mold cavity in the worst injection molding conditions, namely with the smallest specimen thickness and the lower mold temperature. The maximum value for the injection speed was set as the maximum achievable by the injection molding machine. Finally, concerning the specimen thickness, it was decided to investigate a range sufficiently large to cover the most common thicknesses used in injection molding applications. The injection molding set up is reported in Table 6.2:

In figure Figure 6.8 it is visible the porous insert mold with the molded specimen. Once that the processing parameters were set, the picking up of the investigated specimens was done only after that the mold thermal distribution and the injection molding process was stabilized. A pressure piezo-electric trasducer was also utilized in order to check the injection molding pressure profile during the injection phase. Therefore, the statistical criterion of Chauvenet was used to

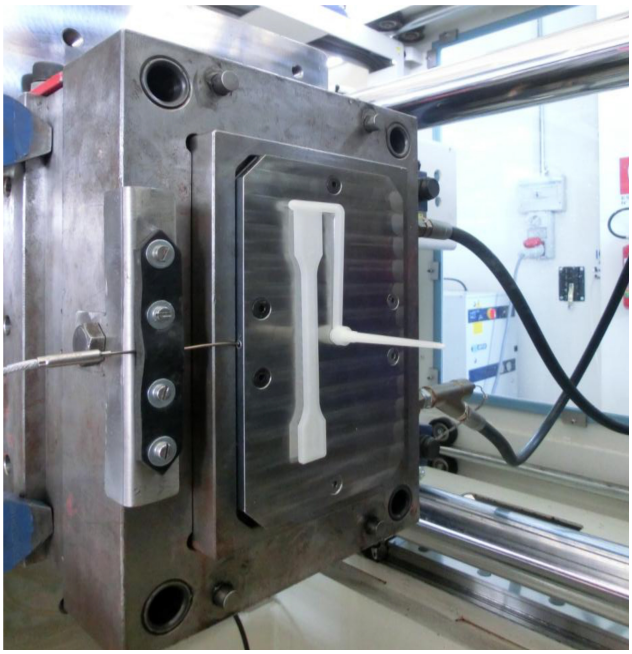

Figure 6.8: The molded specimen

separate any specimen whose pressure profile was out of this criteria. Even though the mold thermal cycle was accurately controlled with the thermocoupled placed close to the cavity wall, this kind of specimens selection was needed due to the variability of the RHCM process caused by the thermal fluctuations.

6.6 RESIDUAL FIBER LENGTH ANALYSIS

In the chapters before it was already advanced the phenomenon of fiber breakage during the injection molding process of fiber reinforced materials. In particular, during the injection phase, fibers are subjected to high stresses: the polymer flow through the nozzle of the machine, abrupt variation of the mold geometry and high shear stresses are the main phenomena which induce fibers breakage. The results of the experimental tests are reported in Figure 6.9, where the average length was calculated according to the Huq and Azaiez equations (Equation 6.3).

The most significant parameter is the specimen thickness. This is due to the high interaction between fibers and cavity walls during the injection phase as well as the increasing of flow rate which occur decreasing the specimens thickness. Indeed, assuming that the shear stress is the main cause of fiber breakage during the injection phase, an high flow rate leads to an increasing of the fiber degradation. This supposition is well supported by the literature[73], and the results achieved in this experiment are in accordance with this supposition since inFigure 6.9 it is shown that increasing the injection

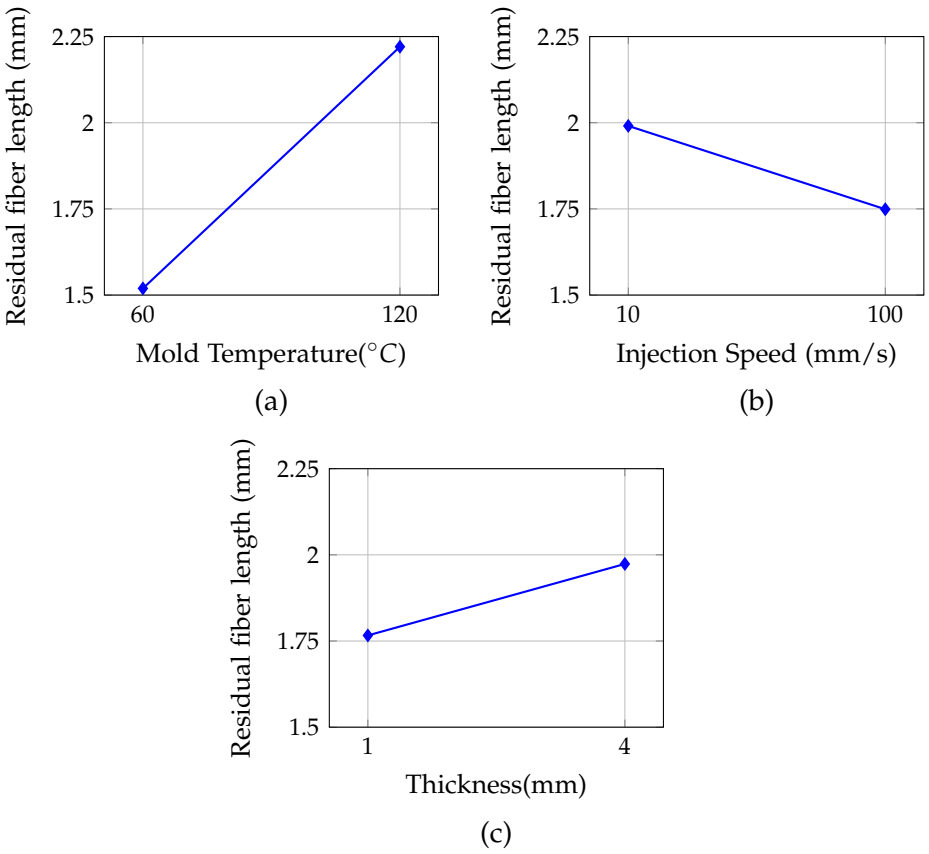

Figure 6.9: Influence of injection molding parameters on residual fibers length: main effects

speed and consequently the shear stress, a negative effect on residual fiber length is denoted. As far as the mold temperature parameter is concerned, the main effects plot shows that an high mold temperature causes an increasing of the average fiber length. This is in accordance with the hypothesis of this work which expected an higher residual fibers length by using a rapid heat cycle molding technology. Hereafter, it will also confirmed the residual fiber length dependence from the shear stress. Indeed, considering the specimen section as a slit die, for an isotherm flow the shear stress equation is governed by the Equation 6.4:

$$\tau_w = \eta * \frac{6Q}{W * H^2} * \frac{1}{3} * (\frac{2n+1}{n}) \tag{6.4}$$

In Equation 6.4 the shear stress is increased by a lower slit die thickness, high flow rate and viscosity. This is the same for the injection molding parameters investigated, in fact, correlating the cavity thickness with the parameter "H", the injection speed with the flow rate "Q" and the mold temperature with the reciprocal of viscosity, Figure 6.9 can be summarized by the Equation 6.4. Concerning the interaction plots, the only significant interaction between the investigated parameters regards that one between mold temperature and mold thickness. It is visible that the smaller the cavity thickness the higher the benefit led by using high mold temperatures. It is a reasonable behavior since as long as the thickness is small, it is more influenced by the mold temperature. Indeed, the skin layer, which occurs at the first contact between cavity wall and melt polymer and which grows during all the injection phase, is a relevant percentage of the total cavity thickness. Still regarding Figure 6.10, it is possible to understand the slope of the plotted lines by considering Equation 6.4 and in particular the term of shear rate within the square bracket in Equation 6.5:

$$\tau_w = \eta * \left[\frac{6Q}{W * H^2} * \frac{1}{3} * (\frac{2n+1}{n})\right] \tag{6.5}$$

From Equation 6.5 the higher the shear rate the more influential the mold temperature effect. In fact, the mold temperature affects the melt viscosity as more as the thickness is decreased and the flow rate is increased.

6.7 FIBER ORIENTATION ANALYSIS

The reinforcing effect provided by the fibers consists in an increasing of stiffness and mechanical resistance, which depends on both the residual fiber length and orientation along the flow direction. The X-ray computed microtomography (CT) is a non-destructive method that allows the three-dimensional reconstruction of the investigated

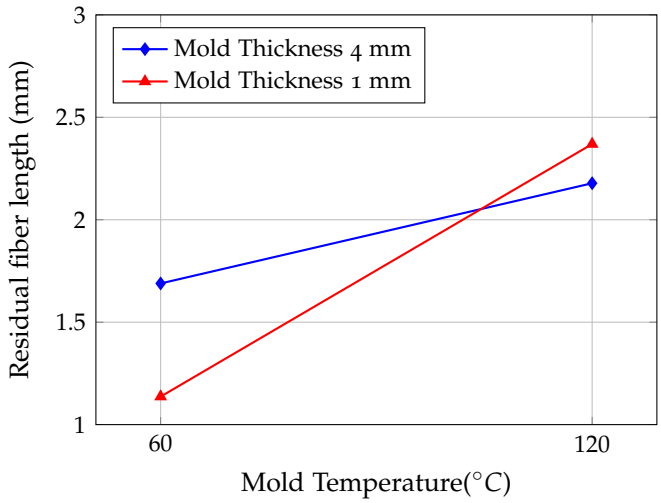

Figure 6.10: Influence of injection molding parameters on residual fibers length: Interaction plots

part. The microstructure of the material obtained is visible in Figure 6.11.

The typical micro-structure induced by the injection molding process can be noted, characterized by a skin-shell-core distribution visible in Figure 6.12.

This configuration results from the fountain flow which occurs when the polymer melt flows through a small gap between two parallel walls. The velocity gradient is the maximum in correspondence of the mold wall and it reaches the minimum in the central position. This behavior causes the parallel orientation of fibers in the layer where the shear rate is the maximum, the so-called shell layer, while the fibers are oriented perpendicularly to the flow direction in the core layer. In addition, a layer of thin skin in which the fibers do not present a preferential direction is formed due to the direct contact of the polymer melt with the cold walls of the mold.

6.7.1 *A qualitative analysis of fiber orientation*

The fiber orientation trend was analyzed using the tensor orientation representation proposed by Advani and Tucker [154]. This method is widely used to characterize the fibers orientation due to its efficiency, simplicity and short computational time required. In particular, the fibers orientation distribution through the specimen thickness was calculated thanks to the software VG Studio Max 2.2 (Volume Graphic GmbH). As illustrated in Figure 6.13, the specimens were fixed inside the ct instrument cabin and it has been scanned in a central portion, for a length of 13 mm and with resolution of 7.4 microns.

The acquisition parameters are listed in Table 6.3.

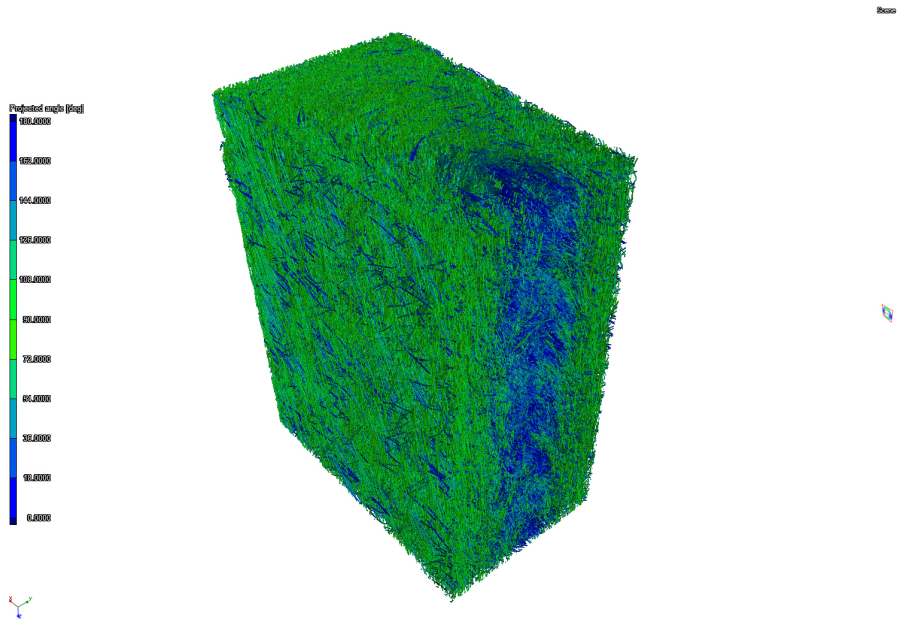

Figure 6.11: Portion of the specimen scanned with micro-tomography

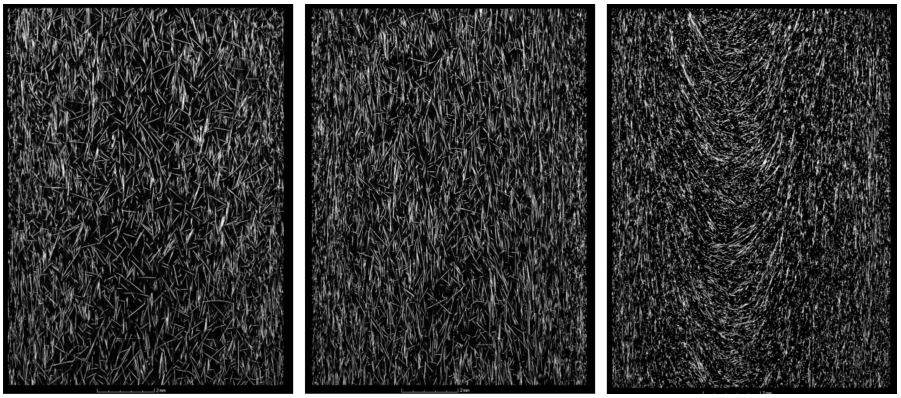

(a) (b) (c)

Figure 6.12: Different fiber distribution by layering the specimen through the thickness: skin layer (a), shell layer (b), core layer (c)

Parameter	Value
Voltage [kV]	80
Current [uA]	6.16
Power [W]	20-40
Exposure time [s]	4
Voxel size [mm^3]	0.0074
Number of projections	1500

Table 6.3: CT acquisition parameters

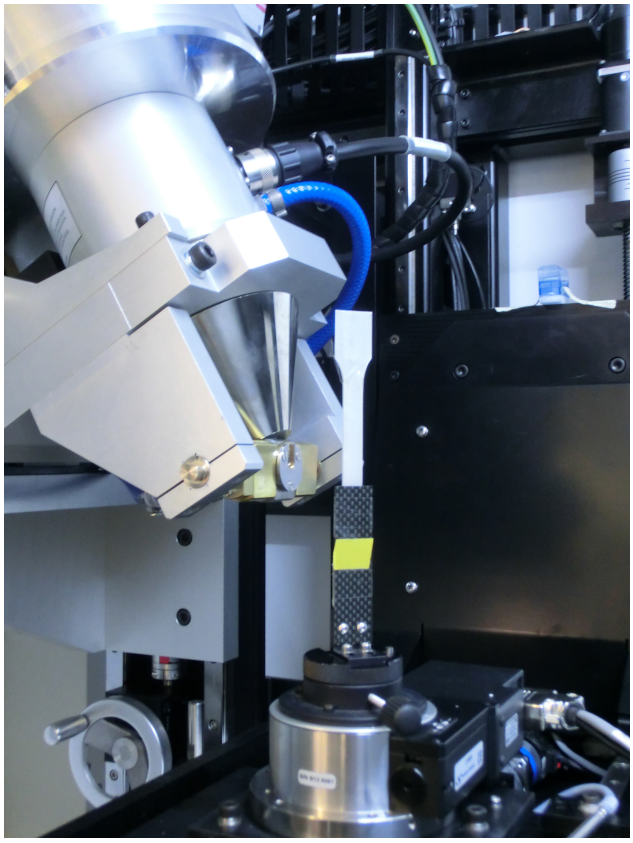

Figure 6.13: The specimen fixed on the micro-ct rotating table

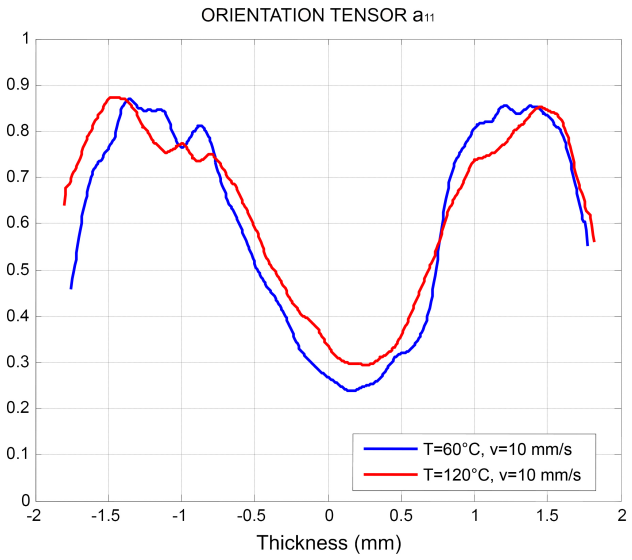

Figure 6.14: FOD through the sample thickness for the specimen molded at injection speed of 10mm/s

The response variable investigated was the fibers tensor orientation a_{11} along the flow direction, calculated through the specimen thickness. An high value of a_{11} indicates a great percentage of fibers orientated parallel to this direction. Conversely, a low value of a_{11} indicates that the fibers are oriented transversely to the flow direction. Due to the high variability of fiber orientation detected for the specimens with a thickness of 1 mm, the following analysis will tackle the fiber orientation results for the specimens with a thickness of 4 mm. In particular, Figure 6.14 and Figure 6.15 show the influence of the mold temperature on fibers orientation for the specimens molded with an injection speed of 10 mm/s and 100 mm/s respectively. The data were filtered with the software Matlab by using a moving average filter in order to remove noises and smooth the fluctuations of data, outlining a more regular and understandable result. The blue and the red lines represent the calculated fiber orientation distribution with a mold temperature of 60 $°C$ and 120 $°C$ respectively. The Figures show the shear-core orientation distribution while the skin layer was too thin to be evaluated because of the specimens surface irregularity.

Considering the shear layer, the FOD analysis shows that the lower the mold temperature the higher the fiber orientation. This behavior was predictable because of the minor shear stress involved increasing the mold temperature and consequently reducing the melt viscosity. In order to further investigate the fiber orientation phenomenon, an injection molding simulation was also performed. It showed that, molding at high mold temperature, the shear stress is also decreased by lower shear rate. Focusing on the specimens with a thickness of 4 mm, in Figure 6.16 it is plotted the shear rate trend through the speci-

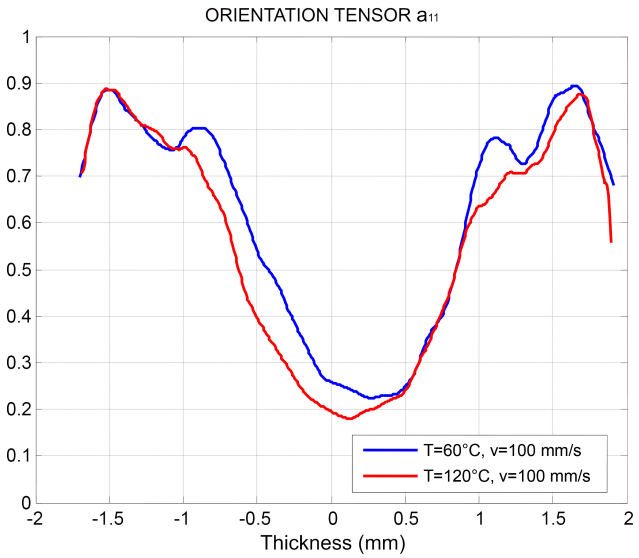

Figure 6.15: FOD through the sample thickness for the specimen molded at injection speed of 100 mm/s

Mold Temperature [°C]	**60**	**120**	**60**	**120**
Injection Speed [mm/s]	**10**	**10**	**100**	**100**
Total thickness [mm]	3.54	3.66	3.65	3.71
Sheel layer [mm]	56%	62%	52%	56%
Core layer [mm]	44%	38%	48%	44%

Table 6.4: Specimens thickness and layers percentage distribution

men thickness obtained with an injection molding simulation carried out with the software Autodesk Moldflow. The graph shows that, except for an initial portion, the shear rate is increased by molding at low mold temperature, promoting the orientation phenomenon.

The specimens morphology has been further investigated. The RHCM influence on the skin-shear-core layers distribution through the thickness was analyzed. However, the skin layer thickness was not detectable with a sufficient accuracy so it was not considered in this analysis. Even so, the relative percentages of the shear-core layers are listed in Table 6.4.

A first evaluation concerning the specimens thickness indicates that the cavity shape is better replicated increasing the mold temperature and the injection velocity. This trend is explainable considering that the post-pressure is more efficient if the bulk freezes at low cooling rate. The distribution of the specimens layers seems to be affected by the mold temperature in fact the parts molded at high mold temperature showed an increasing of the shell-core ratio. This difference is more evident for low injection velocities. A further interesting investigation, tackled in this work, is the analysis of porosity. This evaluation has been limited to the specimens with a thickness of 4

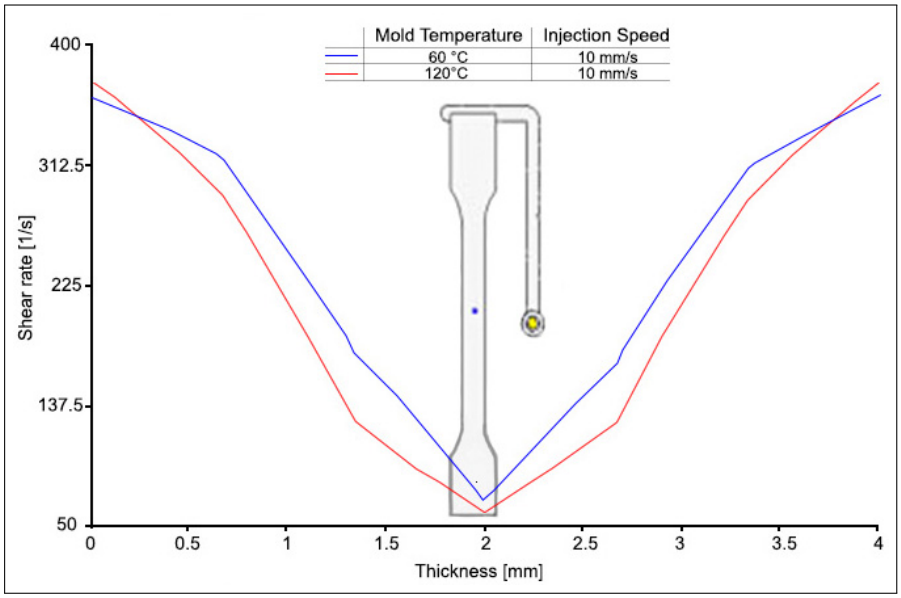

Figure 6.16: Shear rate profile in function of the specimen thickness at 10mm/s injection speed and mold temperature of 60 °C and 120 °C respectively

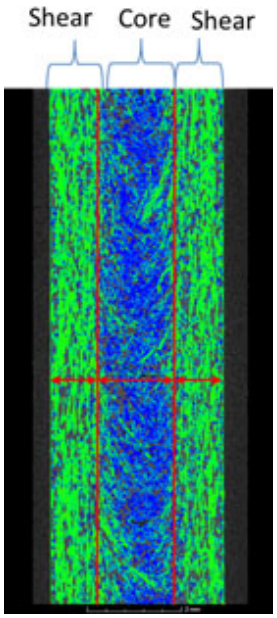

Figure 6.17: FOD distribution through the samples

mm because of their high attitude to be affected by this problem. Table 6.5 shows that the porosity percentage is decreased by high mold temperature. This is due to:

- The better Post-Pressure efficacy on the shrinkage phenomenon;
- An high mold temperature allows an uniform bulk shrinkage, decreasing the skin layer which occur when the polymer come in contact with the mold cavity during the injection phase;
- Considering that the fibers aligned in the thickness direction prevent the matrix shrinkage causing the growing of empty spaces, this phenomenon is reduced for the specimens molded with RHCM because of its high shear-core ratio detected in the previous analysis.

Analysis of porosity		
	T=60 $^{\circ}C$	**T=**120 $^{\circ}C$
Injection Speed=10**mm/s**	3.38%	2.66%
Injection Speed=100**mm/s**	3.18%	1.75%

Table 6.5: Specimens porosity at different molding conditions

6.7.2 *A quantitative analysis of fiber orientation*

In order to quantitatively understand the processing parameters influence on fiber orientation a further analysis was carried out. In particular, the area of the specimens section taken in the middle position was considered and it was divided following a $3x3$ grid for the specimens of 4 mm and a $1x3$ grid for the specimens of 1 mm, due to the small area. The grids division is visible in Figure 6.18 and Figure 6.19. Since the tomographic scans are time consuming operations, it was necessary to decrease the number of scans, therefore in this case the injection speed was kept at the lower value of 10 mm/s. In this condition the influence of mold temperature and cavity thickness, which are the main interesting parameters in this analysis, on fiber orientation was more evident.

The software calculates the fiber orientation for each combination of mold temperature and thickness. In the Figure 6.20 the fiber orientation distribution has been represented with a contour plot. The images show that for higher mold temperature, the fiber orientation is globally decreased through the specimen section.

It is interesting to note that for high mold temperature the fiber distribution shows an asymmetric behavior. This is probably due to the different mold temperature between the moving half mold and the fixed one. Indeed, the porous inserts are placed only in one half

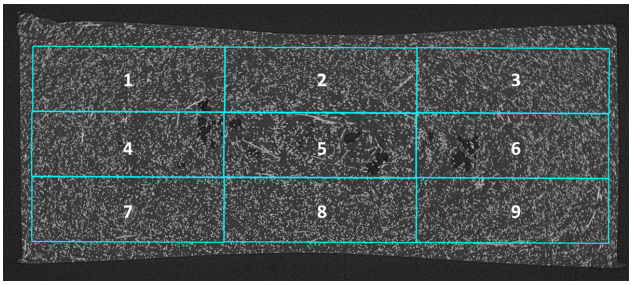

Figure 6.18: Specimen central section subdivision for those ones with a thickness of 4 mm

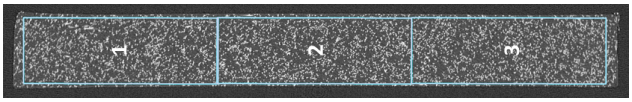

Figure 6.19: Specimen central section subdivision for those ones with a thickness of 1 mm

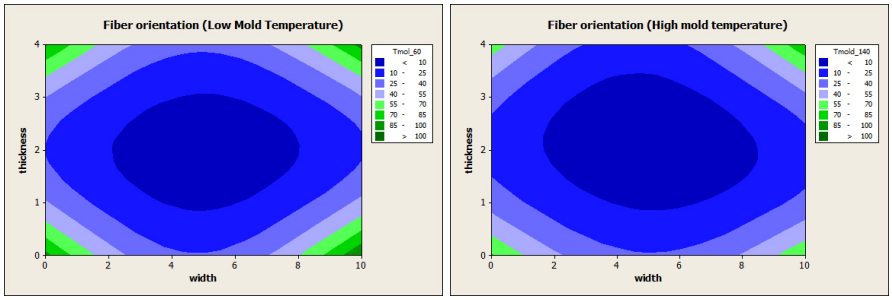

(a) (b)

Figure 6.20: FOD distribution plot for the specimens with a thickness of 4 mm, an injection speed of 10mm/s and injection molded respectively at low mold temperature (a) and high mold temperature (b)

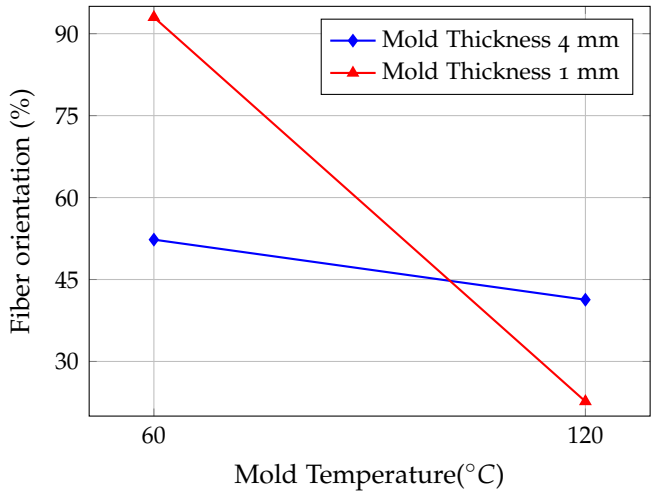

Figure 6.21: Influence of mold temperature and cavity thickness on fiber orientation

mold therefore, the unavoidable cavity thermal variation through the thickness has induced this flow unbalancing. A further consideration was carried out to summarize the effects of mold temperature and mold thickness on fibers orientation. Considering that mechanical properties are affected by the fibers orientation through all the specimens section, the global average of the orientation tensor through the specimen area has been calculated. Moreover, this average value has been considered to compare the fiber orientation percentage for the specimens obtained with different mold temperature and cavity thickness. Figure 6.21 shows that mold temperature affects negatively the fiber orientation as well as the lower the mold cavity thickness the higher the influence of mold temperature on fiber orientation.

6.8 TENSILE STRENGTH RESULTS

In Figure 6.22, it is shown the trend of the main effects, all the parameters were significant. Decreasing injection speed the mechanical resistance is enhanced. Conversely, the tensile strength is increased by an high mold cavity thickness. Concerning the mold temperature, form Figure 6.22 seems that the higher the mold temperature the lower the UTS.

In order to better understand the mold temperature influence on tensile strength it is useful to have a look of the interaction between factors. In particular the interaction between mold temperature and cavity thickness. Considering Figure 6.23 the result is interesting in fact, the mold temperature effect on tensile strength is the opposite varying the mold cavity thickness from a specimen of 1 mm to 4 mm. In particular the RHCM technology influences positively the ultimate

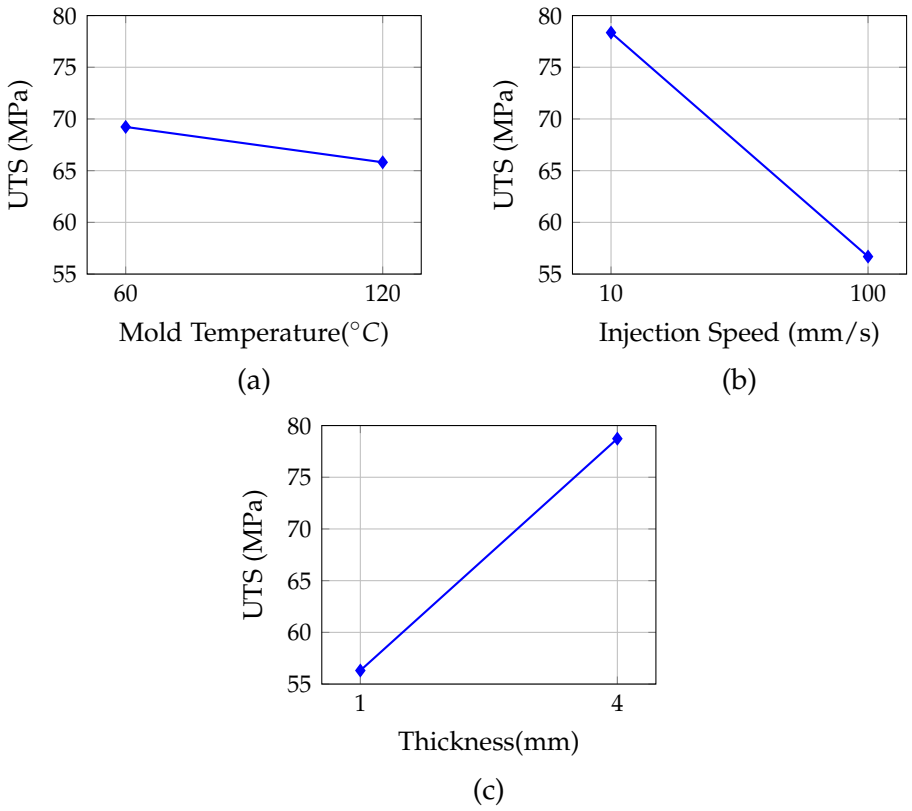

Figure 6.22: Influence of injection molding parameters on tensile strength: main effects

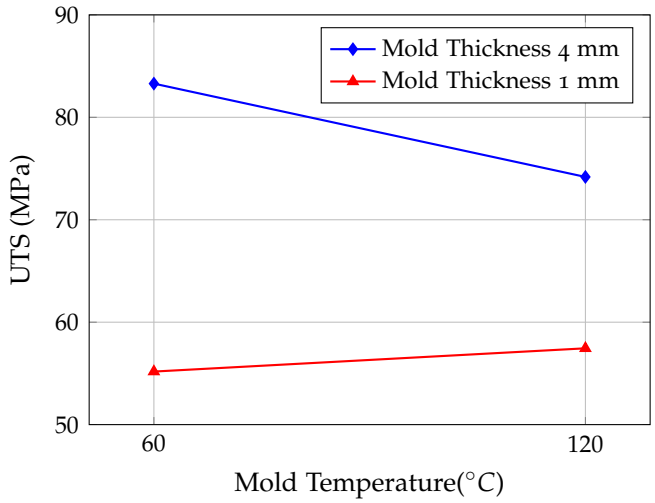

Figure 6.23: Influence of injection molding parameters on tensile strength: interaction plot between mold temperature and specimen thickness

tensile strength for a small specimen thickness while it affects negatively the specimen with a thickness of 4 mm.

6.9 DISCUSSIONS

The residual fiber length analysis has shown that the injection speed, the cavity thickness and the mold temperature, affects the fibers breakage phenomenon. The mold temperature influences positively the residual fiber length while it affects negatively the fibers orientation. Therefore, considering that the tensile strength of composite materials is increased by longer and more oriented fibers, it is understandable that there is not a linear behavior between mold temperature and tensile strength. In Figure 6.24 it is plotted at the same time the residual fiber length, the fiber orientation and the tensile strength analysis. It is visible that fiber orientation and residual fiber length have an opposite trend by varying the mold temperature. Moreover, the effect of part thickness on mold temperature is similar for both the investigated parameters. Therefore, it would be predictable that the UTS behavior were not affected by the mold temperature due to the balancing of the two effects plotted in Figure 6.24. Even so, the interaction plot between mold temperature and cavity thickness was significant concerning the UTS analysis. Moreover, it is also pointed out that, in terms of specimens tensile strength, it is worth using high mold temperature as long as the specimens thickness is small. This behavior can be explained by considering that the effect of the residual fiber length is dominant for small part thicknesses while fiber orientation becomes dominant increasing the part thickness. Understanding the reason of this phenomenon is complicated because the specimen mor-

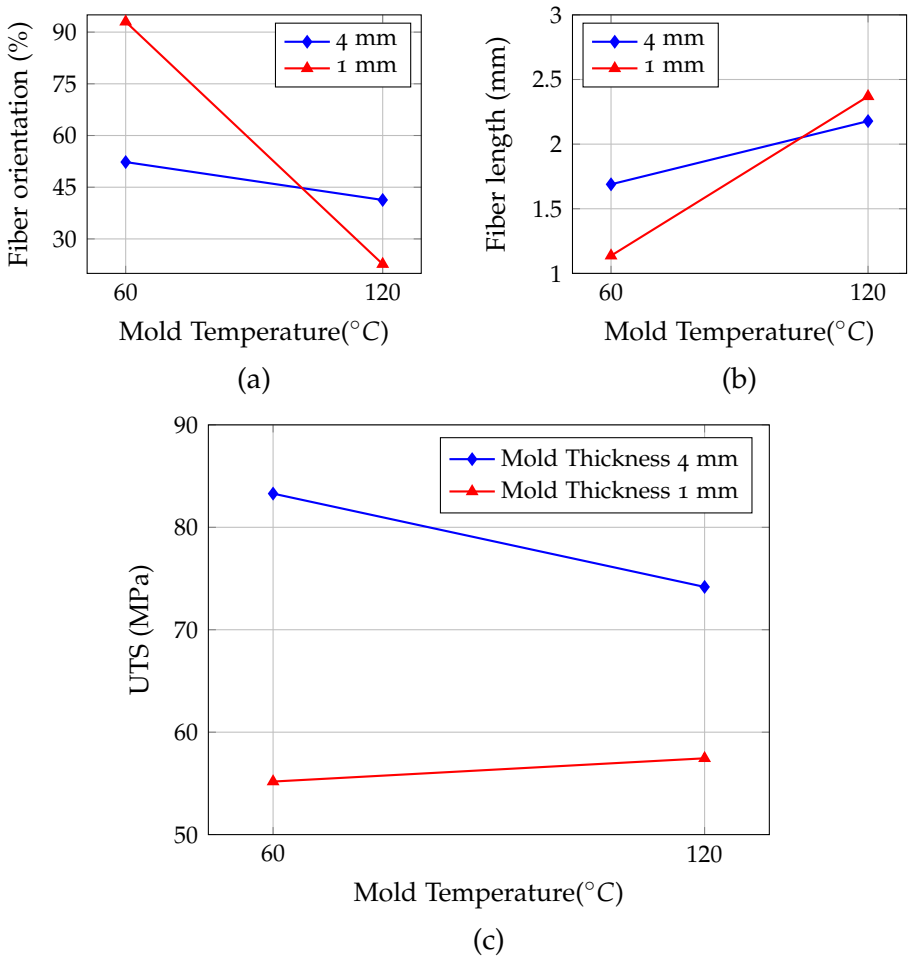

Figure 6.24: (a) Fibers orientation, (b) Mold temperature, (c) Tensile strength

phology is directly connected with the melt flow through the specimen. However, a possible reason could be the fact that, for the specimen with a thickness of 4 mm, even though the mold temperature is decreased causing an increasing of the skin layer and the shear stress, the flow section is still big enough to ensure the melt flow without causing the increasing of fiber breakage. For the specimens with a thickness of 1 mm the decreasing of mold temperature would result in a substantial decreasing of the melt flow section causing a relevant fibers breakage. Therefore, in this case, the effect of higher fiber orientation, caused by the low mold temperature, is impaired by the too small residual fiber length.

7

RAPID HEAT CYCLE MOLDING TECHNOLOGY INFLUENCE ON FATIGUE RESISTANCE OF FIBER REINFORCED POLYMER MATERIALS

Glass fiber reinforced composite materials, as an alternative to traditional materials like metals, now have been widely used for aerospace components, sporting goods, structural applications in automobiles, ships, aircraft, etc., in view of their beneficial characteristics, such as stability, high specific strength, stiffness and good chemical resistance. In fact, structural components are usually subjected to complex fatigue loadings, which is one of the main forms of failure in mechanic and structural catastrophe. Thus, it is important to investigate and determine the fatigue characteristics of long glass fiber reinforced composites for application as the primary structural member in various fields. The aim of this work is to investigate the mold temperature influence on fatigue life of fiber reinforced polymers as well as study the damage mechanisms which occur during the cyclic tests. The correlation between static and dynamic failure of the specimens will be investigated in order to evaluate how the sample morphology affects fatigue life.

7.1 EXPERIMENTAL PLAN

In order to analyze the process conditions influence on fatigue life of fiber reinforced injection molded parts with a RHCM technology, a further experimental test was carried out. A1 dog bone specimens were injection molded by varying the mold temperature in the range of 60 °C and 140 °C. The injection molding equipment employed was the same of the previous experimental campaign concerning the tensile strength analysis. The experiments were made following the next steps:

- Tensile tests were conducted for subsequently correlate tensile strength and fatigue resistance. The tests were carried out at a deformation rate of 5 mm/s according to ISO R527 standard. For each combination of process parameters considered, five tests were made;
- Fatigue tests were conducted to investigate the influence of mold temperature on the fatigue behavior of fiber-reinforced material.
- A fatigue fractional test was carried out in order to evaluate the influence of specimens porosity on fatigue behavior.

Tensile test machine EA010	
Maximum force [KN]	85
Stroke [mm]	300
Position resolution [μm]	1.75
Positioning repeatability [μm]	$\pm$8

Table 7.1: Design of experiments

The decision of using for this analysis the specimens with a thickness of 4 mm was taken considering the low data dispersion shown during the tensile test previously carried out in the fatigue test. Fatigue tests were conducted with the tensile test machine EA010, having the characteristics reported in the Table 7.1.

The cycle ratio R = $\sigma_{min}/\sigma_{max}$ was set to 0.1 in order to avoid compression loads and the risk of structure buckling. The frequency was set to 5 Hz, the maximum allowed by the machine, however it was a suitable value in order to carry out the tests in a reasonable time but still avoiding the risk of thermal failure. Indeed, the specimen heating by hysteresis is a significant problem during the fatigue tests because of the visco-elastic behavior of the polymers materials. The temperature was monitored at regular intervals with the thermometer HASCO Z251/2 in order to exclude the temperature influence on the tests results. The porosity influence on fatigue behavior of molded specimens was also investigated by conducting a fatigue test interrupted at several percentages of the life. After each interruption, the specimen was analyzed by micro-tomography in order to evaluate the damage evolution during the fatigue test. The idea of doing a such investigation stems from the porosity results pointed out in the tomographic analysis in the chapter 6 where a lower porosity was detected injection molding at higher mold temperature. With this fractional test we would be able to understand on one hand if the tomographic analysis is able to appreciate the damages mechanisms caused by cyclic tests and on the other hand if the material porosity affects the fatigue resistance, varying its magnitude during the test. Indeed, from technical literature it is pointed out that the mechanism of fatigue failure starts from the micro-voids located to the fibers apex leading to the interfacial debonding that progressively cause the part failure.

7.2 RESULTS AND DISCUSSIONS

7.2.1 *Fatigue resistance analysis*

The Wohler curve is visible in Figure 7.1:

The equation used to describe the relationship between the fatigue stress and the failure number of cycles is visible in the Equation 7.1.

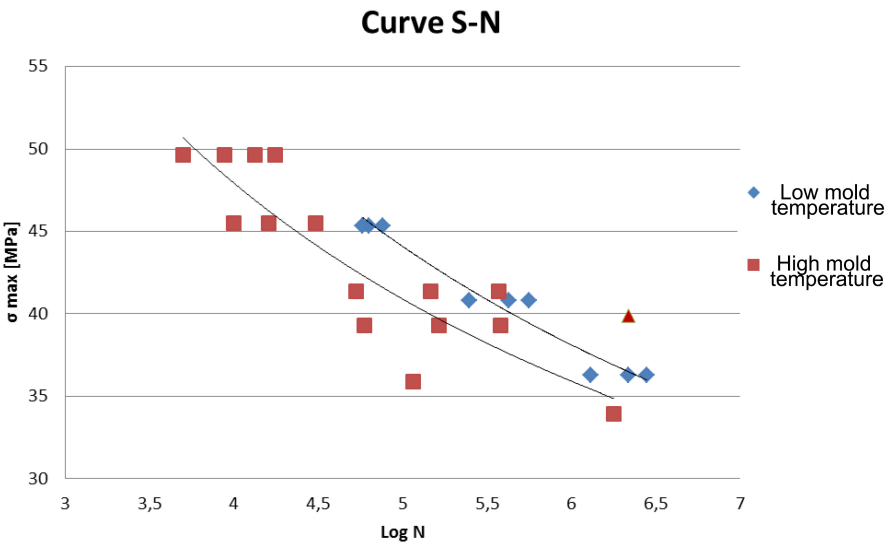

Figure 7.1: S-N curve

Mold Temperature	σ_r	b
Low mold temperature	90.947	-0.063
High mold temperature	71.782	-0.049

Table 7.2: Fatigue curves fitting parameters

$$\sigma_{max} = \sigma_f N^b \tag{7.1}$$

The values of σ_f and b are shown in Table 7.2 for the curves obtained with the specimens injection molding at low and high mold temperature.

From the above data it is possible to see that the curves are nearly parallel and slightly shifted. To confirm this behavior the tensile strength resistance is taken into account. In Figure 7.2 it is reported the static specimens resistance behavior varying the mold temperature between 60 $^{\circ}C$ and 140 $^{\circ}C$.

It seems that the mold temperature influence on fatigue resistance and static tensile strength follows the same behavior. By normalizing the fatigue stress with the UTS, of the specimens injection molded with the same processing conditions, it is possible to plot a series of normalized fatigue curves which fall on the same Mastercurve as suggested by Bernasconi et al. [88]. The results are shown in Figure 7.3.

7.2.2 *Fractional fatigue test*

The fractional fatigue test was carried out on the specimen with a thickness of 4 mm and injection molded at low mold temperature due to its lower data variability. The adopted procedure was the following:

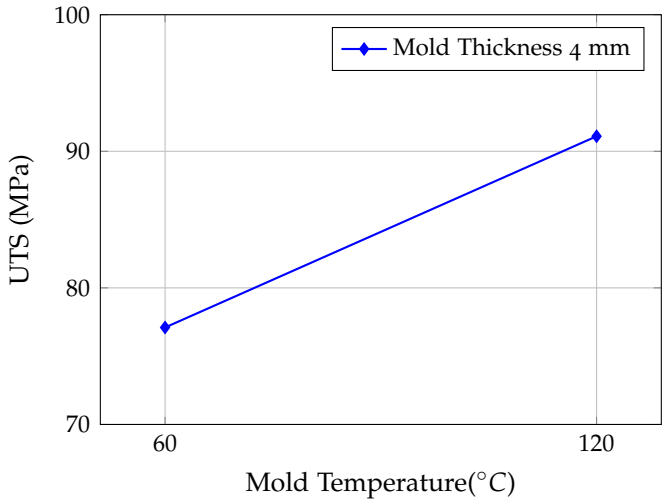

Figure 7.2: Variation of the UTS with the mold temperature

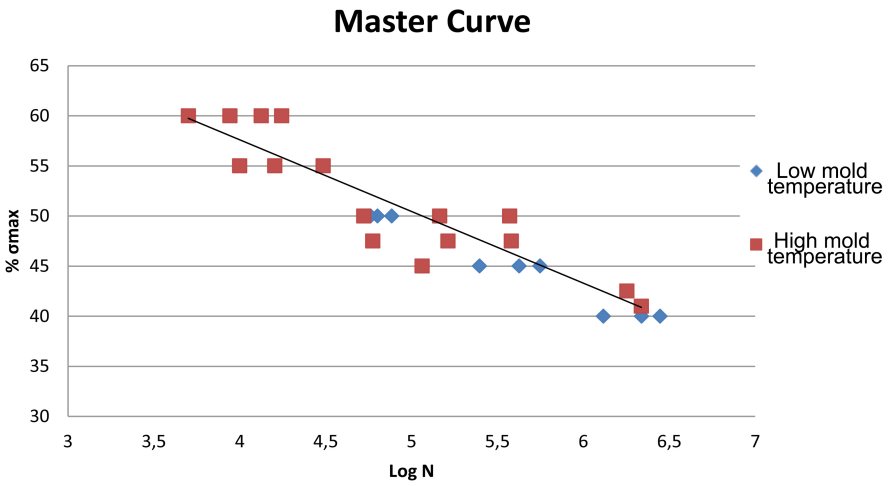

Figure 7.3: Mastercurve enclosing all fatigue data normalized by the UTS

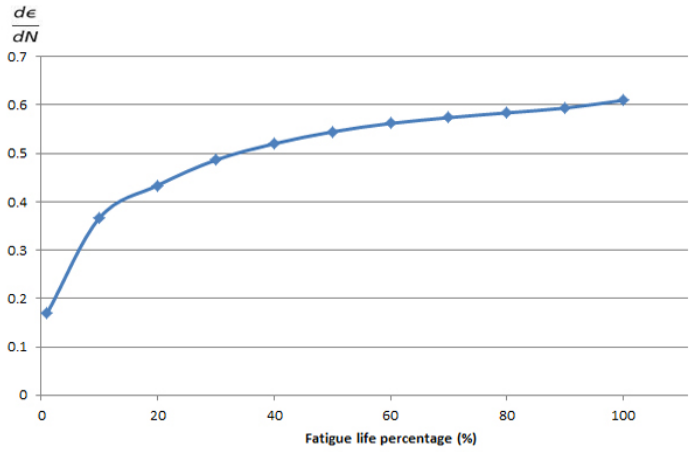

Figure 7.4: Specimen plastic elongation evolution during the fatigue life

- Understanding of the predicted fatigue life of the investigated specimen by using the S-N curve drawn above;
- Performing of an initial ct scan of the undamaged specimen;
- Studying of the plastic specimen elongation evolution (creep) during the test an considering this parameter as an indicator for understanding the number of cycles at which interrupt the fatigue test for the tomographic analysis;
- Fatigue test performing interrupting the test for the tomographic analysis.

Analyzing the S-N curve, the 45% of the ultimate tensile stress was considered for carrying out the fractional fatigue test, due to its low data dispersion. As advanced before, the dynamic modulus was considered in order to evaluate the appropriate number of cycle in which interrupting the fatigue tests. The results obtained are shown in the following figures.

In literature (chapter 2), the variation of the dynamic modulus is chosen as an indicator of the material damage during the fatigue life. However, no variations of the dynamic modulus were detected during the fatigue life of the investigated specimens. Thus, it was decided to consider the plastic specimen elongation variation as the parameter which summarize the damage mechanisms evolution. This assumption is reasonable considering that during the test, the sample is subjected to a progressive plastic elongation and the elongation rate is function of the damage mechanisms evolution. From the upper figure it is seen that the plastic elongation increases rapidly until the 20% of the fatigue life, whereupon its variation is almost linear up to almost the 50% of the fatigue life as visible in Figure 7.4. Therefore the fatigue test interruption was done at the 20% of the predicted specimen life, at 50% and at the specimen breakage. In Figure 7.5 it is

compared the porosity evolution between the undamaged specimen and the broken one. As visible from the images, there is no difference in the voids position or size.

The porosity analysis carried out in the undamaged specimen and in the broken one shows that the porosity percentage increased from 1.71% to 1.92% which is a difference close to the same order of measure uncertainty. Therefore, it seems that the porosity due to the injection molding process, do not influence the fatigue behavior of the material. Thus, the mechanism of material damage involves a smaller scale compared with the tomographic resolution.

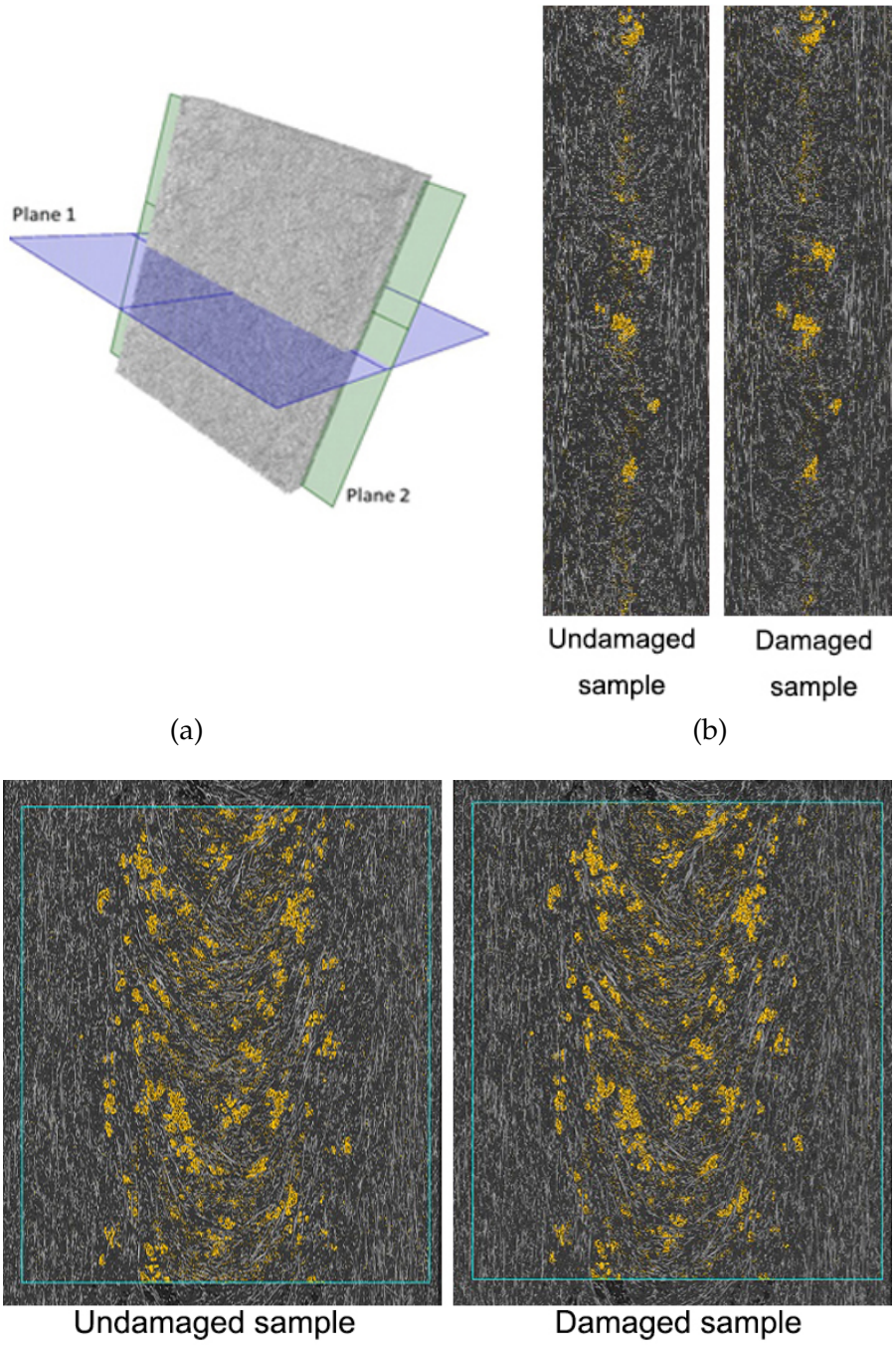

Figure 7.5: Micr-voids variation during the fatigue test. (a) Scheme of the cutting plane; (b) Voids evolution along the plane 1; (c) Voids evolution along the plane 2

Part IV

STUDYING OF THE RAPID HEAT CYCLE MOLDING INFLUENCE ON CRYSTALLINE MATERIALS

8

INJECTION MOLDING OF PET BOTTLE PREFORMS WITH A RHCM TECHNOLOGY

Nowadays the industry of packaging promotes more and more a reduction in the parts thickness. This is also done in the production of bottles by encouraging the use of preforms with a thickness becoming thinner with the origin of several problems related to the process. The thickness reduction in fact involves a substantial increasing in the maximum injection pressure: for a preform of 2.3 mm thickness for example, the frozen layer is about 0.25 mm, which means that the channel in which flow the material will be reduced to 2.05 mm. Furthermore, if the cooling rate is too high, the material solidifies before that it filled the entire cavity leading to a problem of incomplete filling. Other problems may be encountered when the flow reaches the neck of the future bottle: because of the decreasing in the flow section, the melt speed increases causing a more than linear increasing of injection pressure leading to an overload and thus to a material degradation. Finally, a further problem, relating to the molding of thin preforms, regards the injection speed in fact, for preforms with high length-to-thickness ratio it is necessary to increase the injection velocity to decrease the cooling flow front causing the increasing of the cavity pressure, and the degradation of the material. A solution for these problems can be the usage of high mold temperatures since such a process condition allows to obtain greater flow lengths with the same injection pressure. In this work, a Rapid Heat Cycle Molding technology has been involved with the aim of decreasing the injection molding pressure of thin-wall preforms. An high mold temperature allows to diminish both the skin effect and the cooling of the melt flow front. The purpose of the present work is therefore to investigate the possibility of applying the technology RHCM, taking advantage of the high mold temperature, without increase the final part crystallinity. Therefore, it will be taken to account the problem of crystallization which may results from a too slow preform cooling rate. Initially a rheological and thermal material characterization will be carried out. Subsequently the injection molding simulation was calibrated by optimizing the coefficient of heat exchange and the glass transition temperature. This calibration was performed by minimizing the errors resulting from the comparison between the simulated injection pressure peak and real pressure peak at the same boundary conditions. In particular, the injection pressure was acquired by placing a piezoelectric pressure sensor directly inside of the mold cavity. Once that the simulation was calibrated, several simulations were

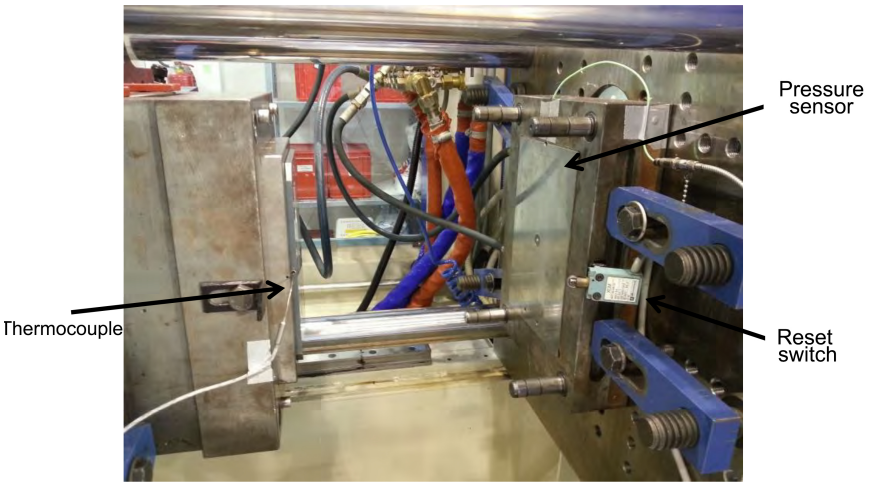

Figure 8.1: Mold Equipment

performed in order to numerically investigate the effects of using a RHCM technology on injection pressure and crystallinity degree of bottle preforms. It will be demonstrated that the RHCM technology reduces the injection, maintaining a reasonable cycle times and an adeguate level of crystallization(less than 10% of the total volume).

8.1 MATERIALS AND METHODS

8.1.1 *Mold equipment*

The injection molding machine employed for this experimental campaign was a Battenfeld HM 110. The mold was composed by:

- The fixed half mold in which there was placed the piezo-electric sensor for the injection pressure acquisition;
- The movable half mold in which an A1 dog bone specimen (ISO 527-2) cavity was manufactured, and a thermocouple for the temperature acquisition was positioned.

The pressure acquisition system was composed by a piezoelectric sensor Kistler with a diameter of 2.5 mm and a pressure range of 0-2000 bar, the sensitivity was 9.4 pC/bar. It was placed in the fixed half mold where a pressure reset switch was also inserted.

The sensor is connected to the computer where the LabVIEW system was involved to acquire the injection molding pressure with an high frequency.

8.1.2 *Material characterization*

The rheological characterization of PET (Eastapak 9663) was carried out with the capillary and the rotational rheometers. A Cross-WLF

Figure 8.2: Pressure acquisition system

model was involved for the rheological material modellation. The Cross interpolation is the following:

$$\eta(\dot{\gamma}) = \frac{\eta_0}{1 + \left(\frac{\eta_0 \dot{\gamma}}{\tau^*}\right)^{1-n}} \tag{8.1}$$

where $\eta(\dot{\gamma})$ is the melt viscosity varying $\dot{\gamma}$ and η_0. τ^* and n are the coefficient shown in Figure 8.3.

The obtained coefficients which allow the best fitting of the experimental data where n= 0.4 and τ^*=3857.18. The viscosity η_0 was obtained by the William Landel Ferry model described in the following equation:

$$\eta_0 = D_1 exp\left[\frac{-A_1(T - T^*)}{A_2 + (T - T^*)}\right] \tag{8.2}$$

$T^* = D_2 + D_3 p$ $A_2 = \widetilde{A_2} + D_3 p$

where T^* is the material transition temperature and D_1 D_2 D_3 A_1 and $\widetilde{A_2}$ are coefficients which allow the best experimental data fitting. The obtained parameters were: $T^* = 80°C$ $D_1 = 4.2 * 10^{12}$ $A_1 = 37.8517$ $A_2 = 94.429$ $D_3 = 0$

The experimental data fitting with the Cross-WLF model is visible in Figure 8.4.

In order to carry out the thermal characterization of PET, a DSC test was performed heating a small sample of material with an heating rate of $5°C$ from $30°C$ to $300°C$. A transition temperature of $80°C$ and a melting temperature of $250°C$ were detected from the test.

8.1.3 *software calibration*

The calibration can be defined as the set of activities to make the FEM model as close as possible to reality. There are several items that can be subjected to a calibration activity:

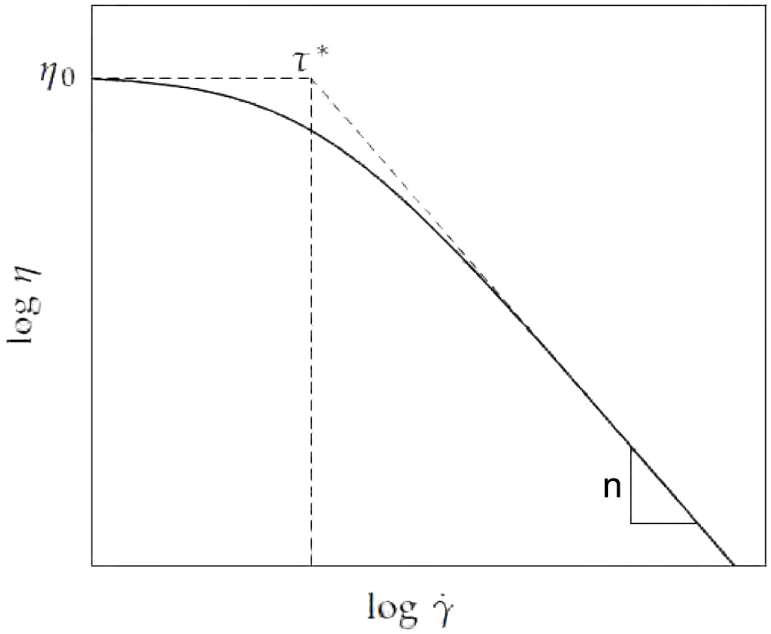

Figure 8.3: Cross model parameters

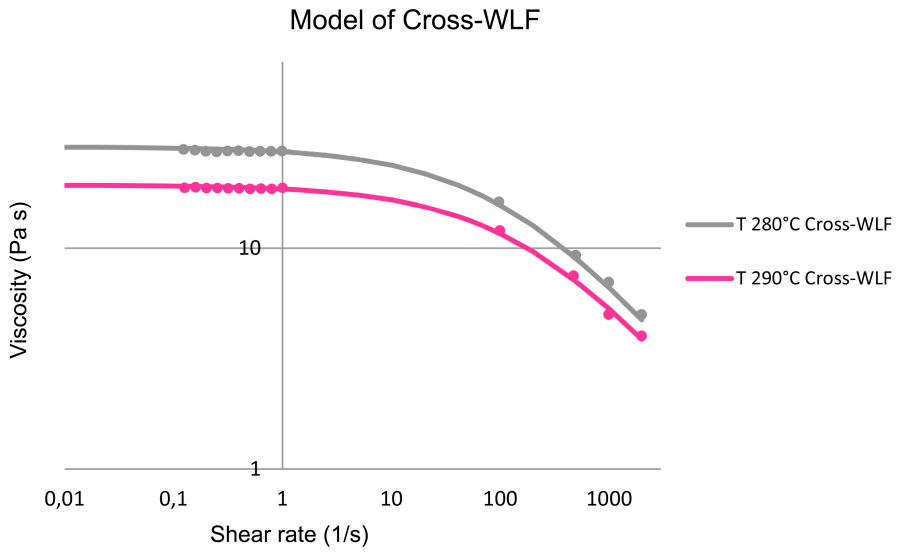

Figure 8.4: Material modellation with a Cross-WLF model

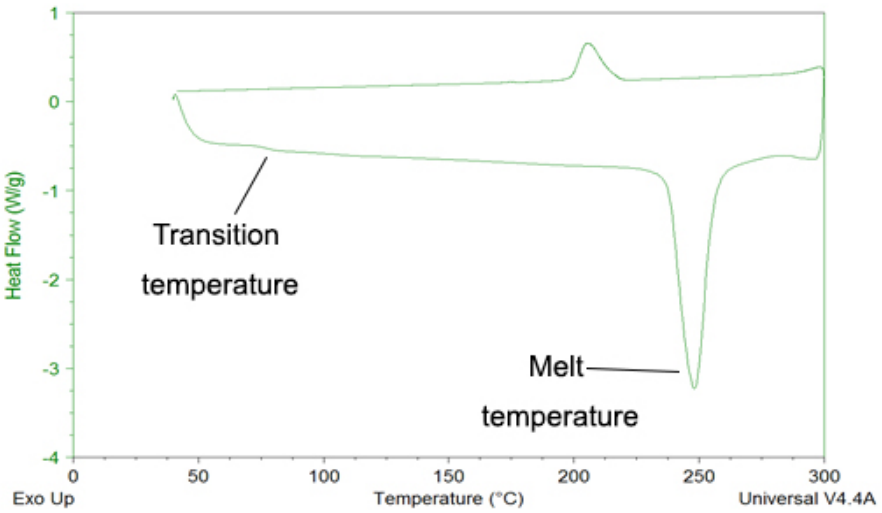

Figure 8.5: Thermal characterization of PET

Mold temperature	30 °C	50 °C
Specimen thickness	1mm	2.5mm
Injection speed	50mm/s	70mm/s

Table 8.1: Design of experiments

- The geometry of the system components;
- The material model;
- The boundary conditions: the coefficient of thermal exchange between the polymer melt and the mold wall and the glass transition temperature;
- The mesh and the solver parameters.

To perform the numerical model calibration, it was chosen a method based on the comparison between the cavity pressure profile acquired in the piezo-electric position and the pressure profile obtained with the numerical simulation in the same point. The process parameters were defined equally in the injection molding machine and in the simulation model. In order to perform a model calibration for a wide range of injection molding conditions, it was made by varying three processing parameters within two levels each one. A full factorial design was considered for the experimental campaign and the parameters are listed in Table 8.1.

For each of the eight conditions, the pressure curve was acquired with the pressure sensor and the acquisition system Labview. An example of the obtained pressure curve is visible in Figure 8.6.

The simulation model was calibrated by optimizing the parameters of HTC (Heat transmission coefficient) and the transition temperature

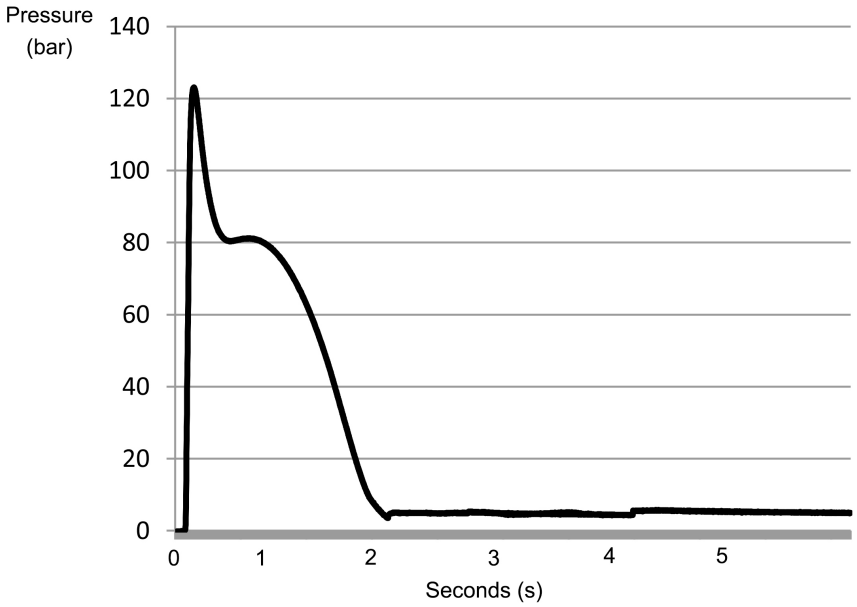

Figure 8.6: An example of an acquired injection pressure profile with a mold temperature of 30 $^{\circ}C$, an injection speed of 70 mm/s and the specimen thickness of 1mm

Tg. The analysis involved the variation of HTC within a range between $1000W/m^2K$ and $5000W/m^2K$ and the transition temperature between $40^{\circ}C$ and $110^{\circ}C$. Every injection molding produced a short shot specimen as visible in Figure 8.7. The peak of pressure acquired during the melt polymer injection was set as input in the correspondent injection molding simulation. Subsequently the difference between the simulated and the real short shot length was considered as the error variable which has been minimized by varying HTC and Tg. For each combination of HTC and Tg investigated it was calculated the error between the virtual and the real short shot length. Considering a combination of HTC and Tg, a global error was calculated by summing the single errors obtained by varying the processing parameters following the Table 8.1. For each combination of HTC and Tg investigated a global error was calculated. Therefore, the simulation model was optimized for that combination of HTC and Tg which minimized the global error.

8.1.4 *Numerical simulation of PET preforms with a RHCM technology*

With the calibrated model, a series of numerical simulations were carried out with the aim of comparing the conventional injection molding of bottles preforms with a RHCM technology. For the RHCM application it was set a flow rate of 20 liter/min, a hot water inlet temperature of $180^{\circ}C$ and a cold water temperature of $20^{\circ}C$. A a spiral channel design was created from the outside of the bottle preform

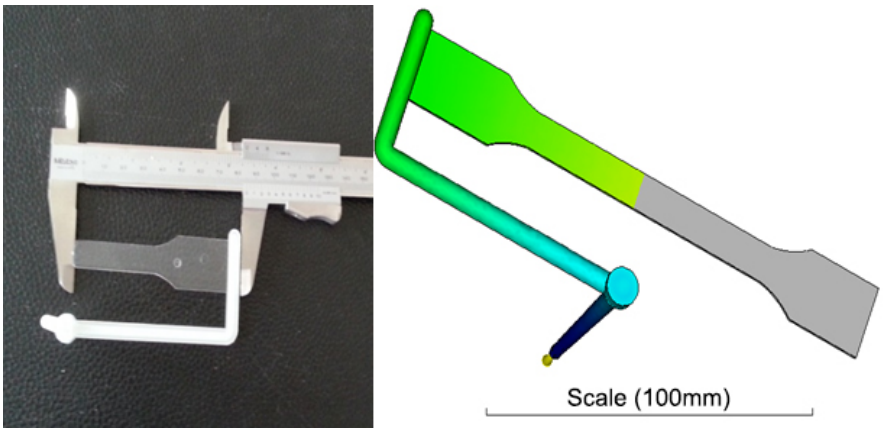

Figure 8.7: Physical and virtual measurement of the short shot length

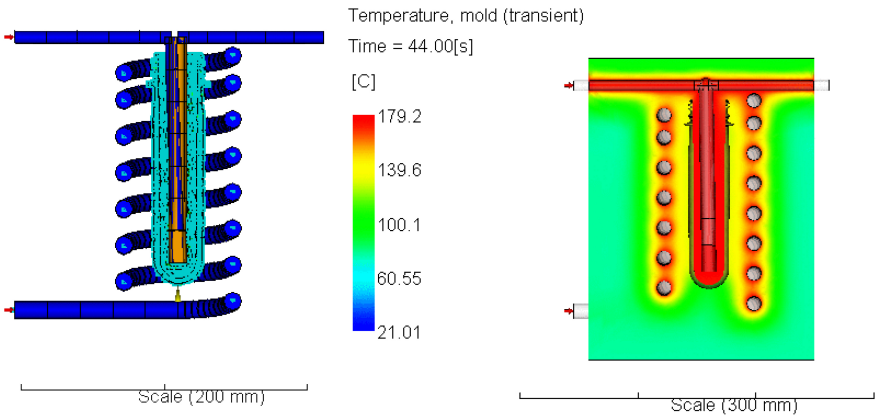

(a) (b)

Figure 8.8: Channels simulation model (a) and the simulated heating phase (b)

while a bubble was design inside of the preform. The geometrical model and an example of the heating phase is shown in Figure 8.8.

The injection molding parameters are the following listed in Table 8.2.

8.2 RESULTS AND DISCUSSIONS

For each combination of HTC and Tg the global error was calculated and the results are summarized with the response surface visible in Figure 8.9.

The absolute error was minimized by using an HTC of $4000 W/m^2K$ whereas the transition temperature had a negligible effect on model calibration. With the optimized values of HTC and Tg a series of numerical simulation were carried out to evaluate the influence of a RHCM technology on the injection pressure, crystallization degree and cycle time. The chart in Figure 8.10 summarizes the simulation

Mold temperature	285°C
Packing time	2 s
Packing pressure	80% of inj. pressure
Injection time	2 s
HTC	4000 W/m^2K
Tg	80 °C

Table 8.2: Injection molding parameters

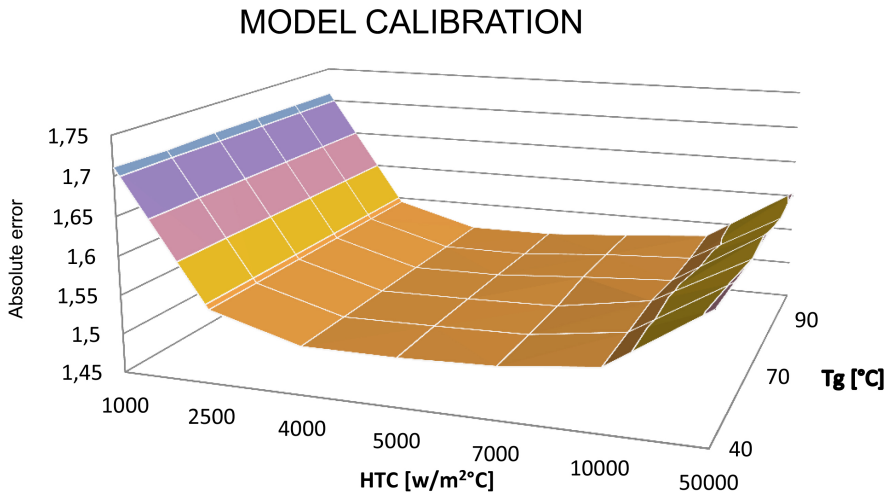

Figure 8.9: Model calibration response surface

results concerning the usage of a CIM or RHCM processes. Analyzing the results it is possible to see that a RHCM technology allow the reduction of the injection pressure of almost 37% with only a slightly increasing of the cycle time. Finally, concerning the crystallization degree, it increases almost linearly with the mold temperature, even though its value do not exceeds the critical degree within the investigated mold temperature range. It is interesting to note that the injection pressure reduction takes place varying the mold temperature between 23°C and 100°C, whereupon it do not further decrease. Therefore, a slightly increasing of mold temperature compared with the CIM process could lead to a benefit in terms of preform filling without compromise the cycle time and the preforms crystallization degree.

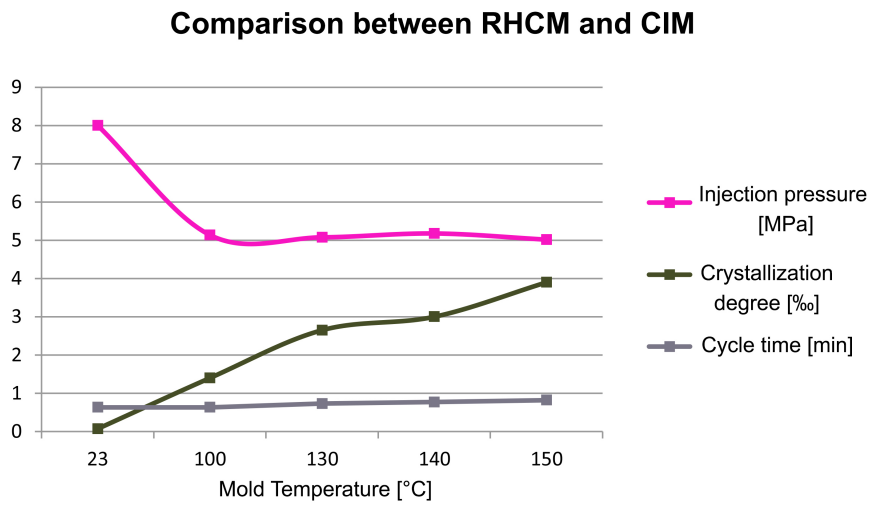

Figure 8.10: Model calibration response surface

9

EXPERIMENTAL INVESTIGATION OF THE RHCM INFLUENCE ON PLA CRYSTALLINITY AND MECHANICAL PROPERTIES

Polylactic acid or polylactide (PLA, Poly) is a biodegradable thermoplastic aliphatic polyester derived from renewable resources. PLA has a glass transition temperature 60–65 °C, a melting temperature 173–178 °C and a tensile modulus 2.7–16 GPa. PLA can be processed by extrusion, injection molding, film and sheet casting, 3d printing, and spinning, providing access to a wide range of materials. Being able to degrade into innocuous lactic acid, PLA is used as medical implants in the form of anchors, screws, plates, pins, rods, and as a mesh. Depending on the exact type used, it breaks down inside the body within 6 months to 2 years. This gradual degradation is desirable for a support structure, because it gradually transfers the load to the body (e.g. the bone) as that area heals. The polymer's crystallinity plays a significant role in the material performance. For example, an increase in overall crystallinity leads to improvements in stiffness, strength, heat deflection temperature, and chemical resistance. However, as advanced in the chapter 3, the PLA crystallization hardly takes place for the conventional conditions of injection molding. In this study, the degree of crystallinity in injection molded PLA specimens under different mold temperature and annealing time was investigated. In this case a RHCM technology was involved in order to heat the mold after the injection phase in order to promote the material crystallization inside of the mold. The annealing time was also varied to allow the specimen heating an consequently the material crystallization. The crystallization degree was investigated with a polarized optical microscope and the DSC. The mechanical performances were studied by measuring the specimens surface Shore hardness. This project has been carried out at the University of Leoben within a collaborative research activity program.

9.1 EXPERIMENTS

9.1.1 *sample preparation*

The injection molded part in this work is an A1 dog bone ISO 527-2 specimen of PLA. The material investigated was a Natural Works "Ingeo Biopolymer 3251D" The injection molding parameters were the following listed in Table 9.1.

Melt temperature	200°C
Mold temperature	25°C
Back pressure	50 bar
Injection speed	50 mm/s
Packing pressure	80% of the inj. pressure

Table 9.1: Injection molding parameters

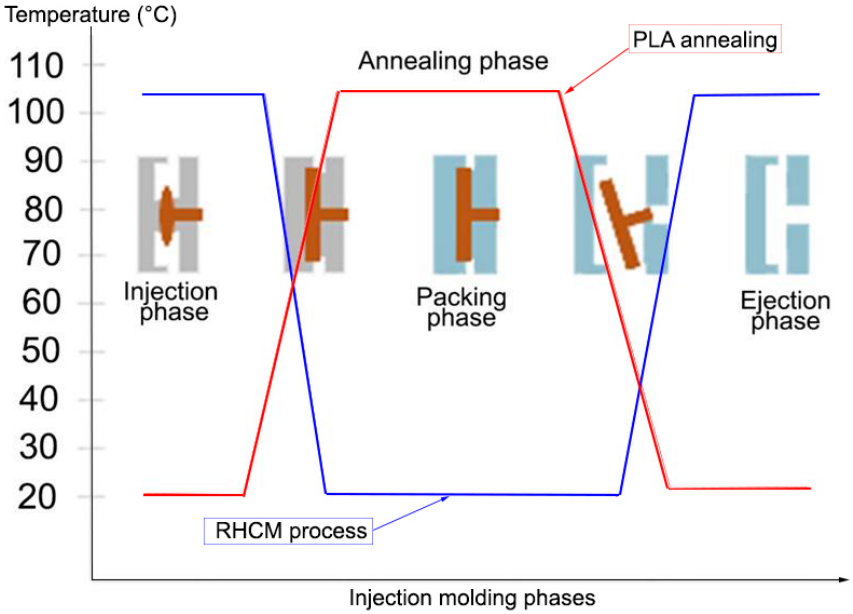

Figure 9.1: Thermal cycle for the PLA specimens injection molding

Conversely, from a typical rapid heat cycle molding, the mold heating do not occurs after the part ejection whereas just after the injection phase in order to induce the material crystallization. The thermal cycle is shown in Figure 9.1.

The investigated mold temperature were 100°C 120°C and 140°C while the annealing time tested were: 10s, 30s, 60s, 120s, 240s and 480s. The injection molding machine used was a Battenfeld HM 110 while the mold is visible in Figure 9.2. The mold heating was performed, in the moving half mold, with a ceramic heater placed behind the mold cavity with a dimension of 30x30 mm. The ceramic heaters were positioned in correspondence of the middle of the specimen cavity therefore, the mold was heated only in correspondence of the specimen center for a width of 30 mm only from one side. Indeed, the fixed mold half was kept at 25°C.

9.1.2 *Differential scanning calorimetry*

The PLA crystallinity degree was studied with the differential scanning calorimeter TA Q2000. In this procedure, a small sample of the

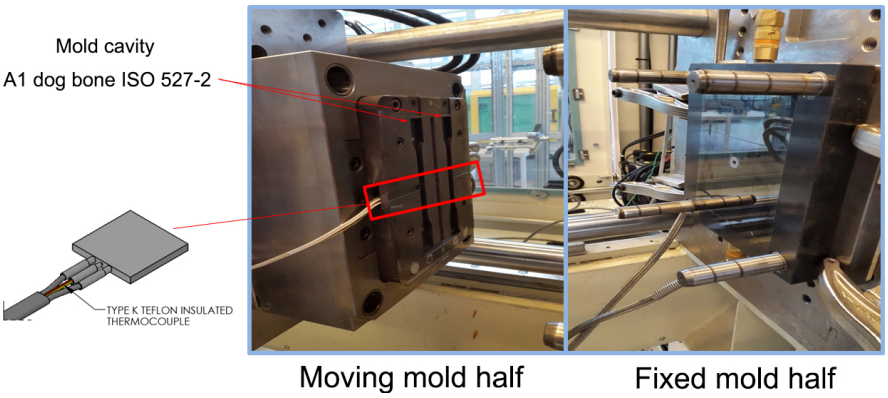

Figure 9.2: The mold for injection molding of PLA

Tip stroke:	0-2.5 mm
Test range	0-100 HD
Available test range	20-90 HD
Tip dimension	SR 0.1 mm
Dimension: 115x60x25 mm	
Net weight: 0.5 Kg	

Table 9.2: Shore hardness instrument specifications

investigated specimen was cut from the crystallized side. The sample was heated from 25°C to 200°C with an heating rate of 10 K/min. The melting temperature (T_m), apparent melting enthalpy ($\triangle H_f$), and enthalpy of cold crystallization ($\triangle H_{cc}$) were determined from DSC thermograms. The absolute degree of crystallinity (χ_c) of the molded and annealed PLA was calculated by:

$$\chi_c(\%) = \frac{\triangle H_f(PLA) - \triangle H_{cc}(PLA)}{\triangle H^{\circ}(PLA)} x100 \tag{9.1}$$

where the cold crystallization enthalpy $\triangle H_{cc}(PLA)$ was subtracted from the total enthalpy $\triangle H_f(PLA)$. The term $\triangle H^{\circ}(PLA)$ is the ideal melting enthalpy per gram of 100% crystallinity (93 J/g).

9.1.3 *Shore hardness test*

Shore D is an instrument for testing vulcanized rubber and plastic products, it carries out the international standard ISO 7619. The instrument specifications were:

The test was carried out at room temperature in the range of 10°C 30°C, the relatively umidity was less than 85% and the testing surface was sooth and without defects. The hardness test was made to the specimens from the crystallized side in order to quantitatively compare the relation between crystallization degree and mechanical properties.

9.2 ANALYSIS OF RESULTS

9.2.1 *DSC Data*

The DSC scans of the sample cut in the middle of the injection-molded PLA specimens with a mold temperature of 100°C, 120°C and 140°C are presented in Figure 9.3

The curves are described by four thermal characteristics: a glass transition temperature near 60°C(Tg), the cold crystallization peak near 100°C, the recrystallization peak around 155°C-160°C and the melt temperature near 170°C. In each image the curves are plot from the top to the bottom by increasing the annealing time. Due to the high cooling rate which affects the material during the injection molding process the material hardly crystallize without a subsequent annealing phase. This behavior is confirmed by the presence of the cold crystallization peaks which are visible in all the DSC curves except for the sample obtained from the specimens which were subjected to the annealing for 480 seconds with a local mold temperature of 120°C or 140°C. It is interesting to note that the enthalpy of the cold crystallization peaks decreased with increasing the annealing time. This confirms that the high mold temperature induced a material crystallization directly inside the mold and this behavior is promoted by the annealing time. Concerning the thermal characteristics, it seems that they occur almost at the same temperature therefore, they are not affected by the variation of annealing time or mold temperature. The recrystallization peak could be the result of the reconstruction of already existed crystals. In Figure 9.4 it is plotted the crystallization degree calculated with the Equation 9.1, varying the mold temperature and the annealing time. The results show that the higher the annealing time and the mold temperature the higher the crystallinity degree. In correspondence of a crystallization degree of 0,45%, the trend seems to reach a stabilization which is achieved for lower annealing time increasing the mold temperature.

9.2.2 *Hardness test*

The results of the hardness tests, made on the central position of the specimens injection molded and annealed directly in the mold, are shown in Figure 9.5.

The specimens surface hardness follow almost the same trend of the crystallinty degree in fact, the higher the mold temperature and the annealing time the higher the surface hardness. It is interesting to note that similarly with the crystallization degree trend, even the hardness behavior shows a stabilization which occurs for lower values of annealing time, compared with the cristallinity degree trend.

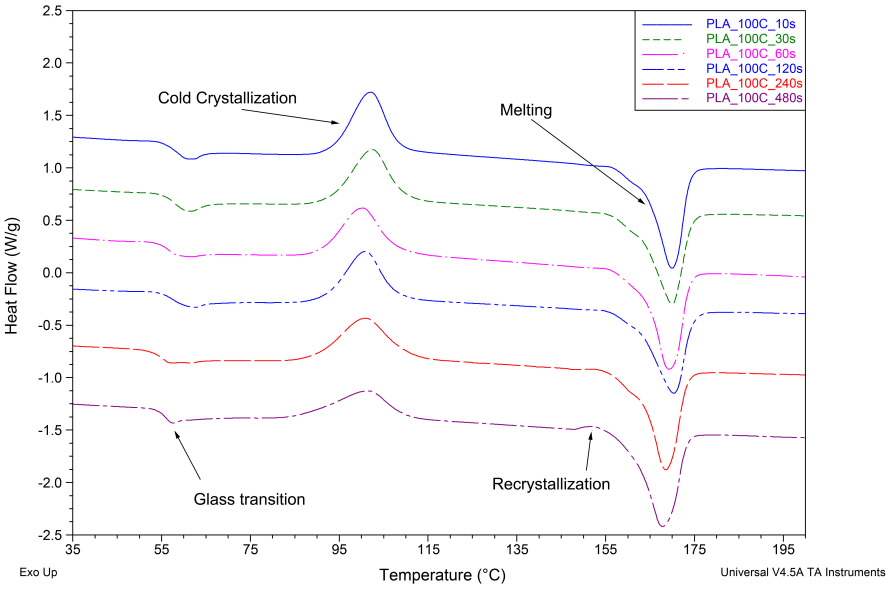

(a)

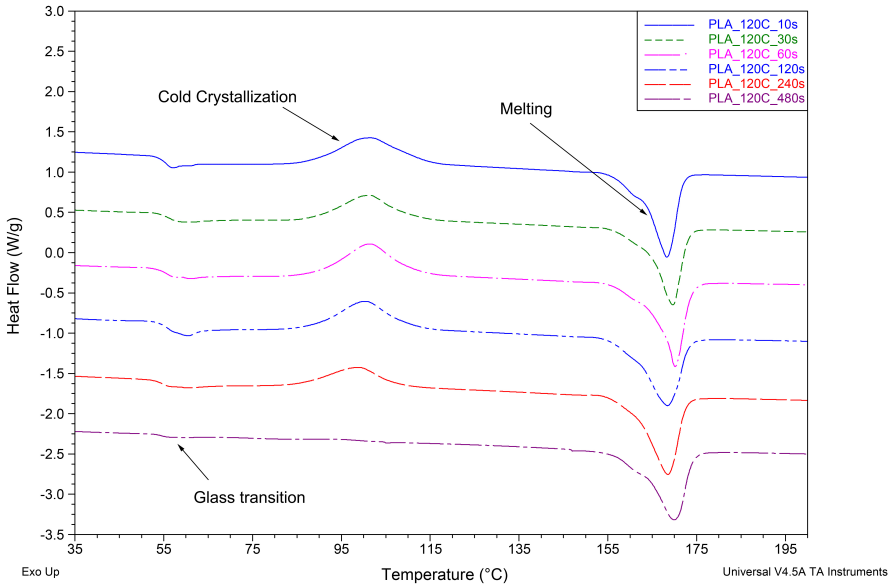

(a)

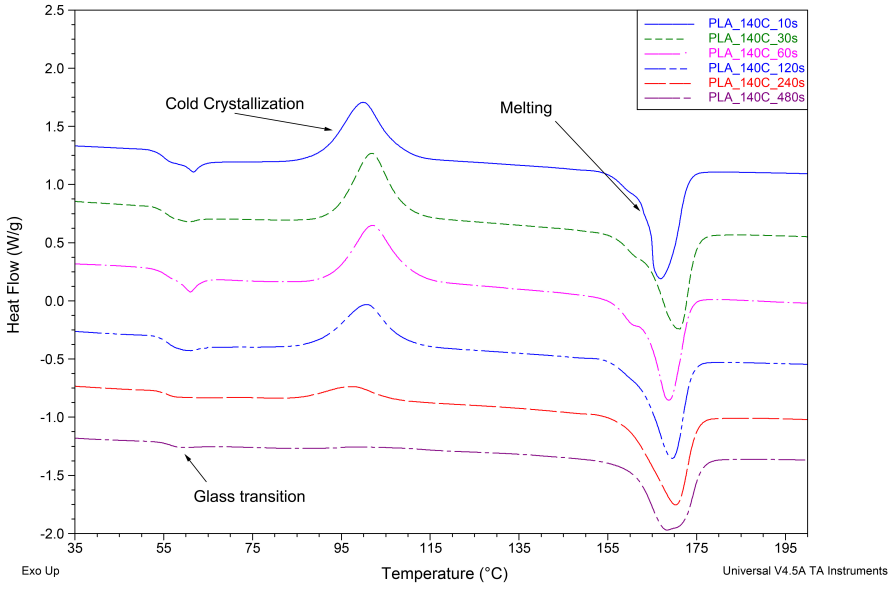

(a)

Figure 9.3: DSC scans of the sample cut in the middle of the specimens annealed with a mold temperature of 100°C(a), 120°C (b) and 140°C (c)

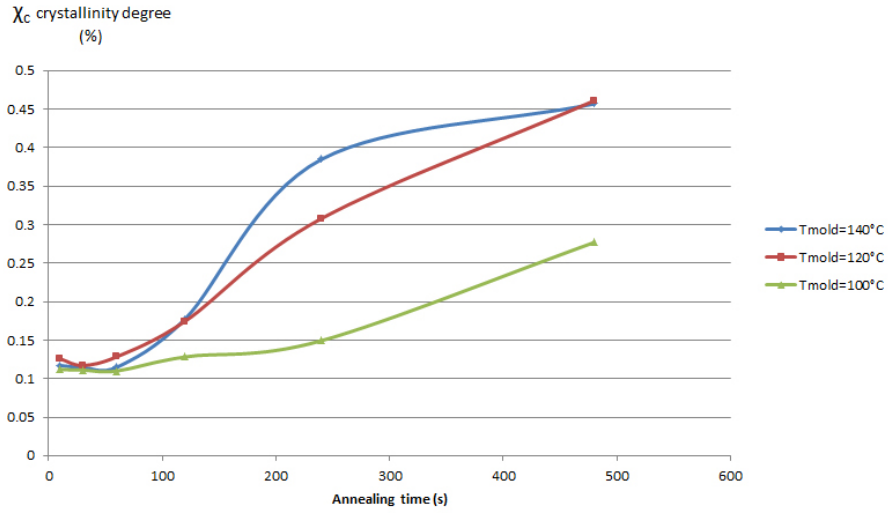

Figure 9.4: The crystallization degree trend varying the mold temperature and the annealing time

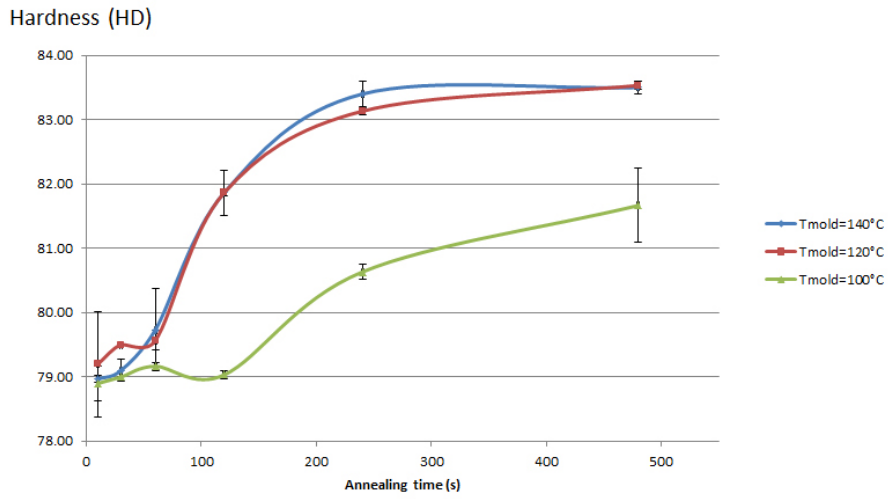

Figure 9.5: The samples hardness trend varying the mold temperature and the annealing time

9.3 DISCUSSIONS

The idea of using a RHCM technology in order to anneal the PLA material directly inside of the mold has been proved as a valid alternative for increasing crystallinity. In general the PLA components were first of all made by injection molding, whereupon they were annealed in a specific oven at a certain temperature. However, the contact between the injection molded part and the mold cavity wall seems to allow a faster heating of the specimens and consequently an increasing of the crystallization rate. Indeed, the global coefficient of thermal conduction between the specimen and the mold wall is substantially higher than that one between specimen and air in the oven. In particular, comparing the results obtained in literature [133], a similar crystallization degree obtained annealing a PLA specimen in a high temperature oven for a few hours, can be achieved already after few minutes by annealing the specimens directly inside the mold. Moreover, because of the cavity shape and the mold thermal distribution, the injection molding of a good quality specimen was possible only by filling the mold at low mold temperature and starting the annealing phase just after the injection phase. Therefore it is predictable that the crystallization rate could be further enhanced by design a suitable mold capable of molding a good quality specimen even starting the heating of the mold before the injection phase. It is worth noting that the surface hardness follows almost the same trend of the crystallinity degree confirming the link between these properties. The images acquired with the polarized optical microscope confirmed the results obtained with DSC. In Figure 9.6 on the right side of each image there is the sample edge. Therefore, the conductive thermal heating gradient goes from the right to the left of the same images.

It is visible that the annealing time and mold temperature affects the nucleation density and the crystals grow rate. It is interesting to note, in particular in the image representing the sample annealed for 60 seconds with a mold temperature of 140°C, that the crystals nucleation does not start exactly from the edge where the sample temperature is the maximum. Conversely, the first nucleation takes place almost 0.25 mm from the sample edge. Considering the typical layer distribution of injection molded parts, this zone could correspond to the finishing of the skin layer and the starting of the shell layer. Considering that the shell layer is characterized by a strong macro-molecular orientation which facilitates the crystal nucleation, it could be possible that the combination of temperature profile and the sample layering causes the first nucleation in the position where the temperature is not the maximum.

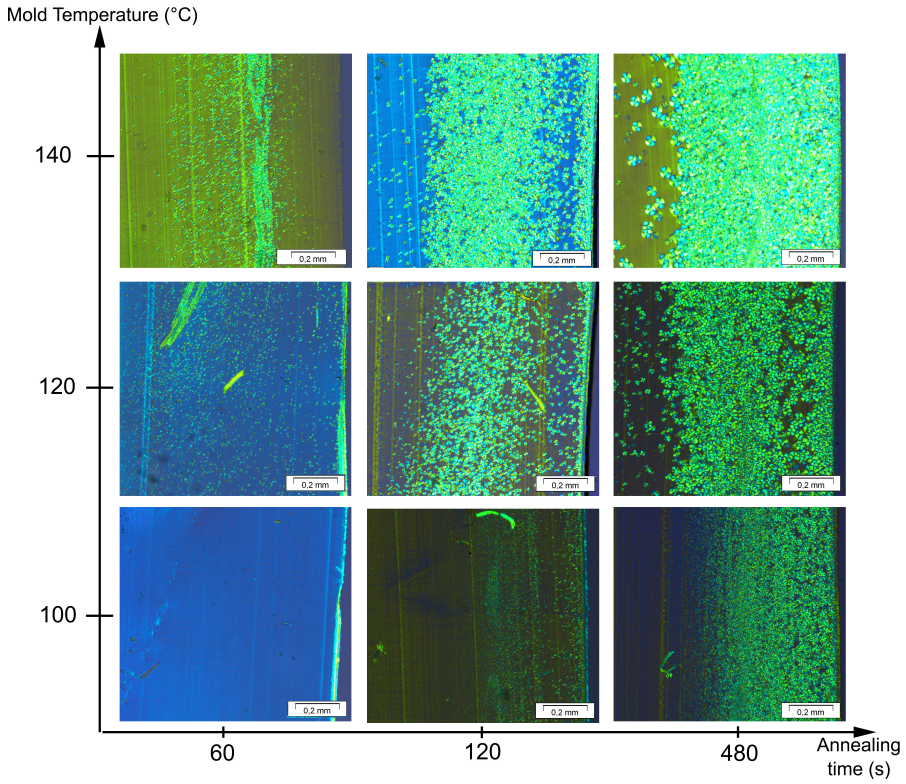

Figure 9.6: The crystals analysis with the polarized optical microscope

Part V

CONCLUSIONS

10

CONCLUSIONS

In this work, a new solution to rapidly control the mold temperature was developed. This technology has been employed for injection molding fiber reinforced materials, taking advantage of the longer achievable flow length and the better surface quality, in order to increase the residual fiber length and consequently the mechanical properties of the molded composites. A final task regarded the usage of a RHCM technology for improving the filling behavior as well as the mechanical properties of injection molded crystalline materials. The main results of this work are the following:

- An innovative RHCM system has been developed replacing the traditional cooling channels with numerically optimized porous inserts placed behind the mold cavity surface. The maximum heating rate was $7°C/s$, but further improvements are needed to overcome this value, particularly concerning the materials selection and the mold insulating properties. An higher performance would be reached insulating the porous inserts from the whole mold excepting for the cavity surface.

- An experimental analysis was carried out in order to investigate the effects of injection molding parameters on appearance and mechanical properties of fiber reinforced materials. The surface roughness analysis confirmed the hypothesis concerning the benefits in using high mold temperature in order to increase the molded parts surface appearance. However, the main interesting result regards the interaction between mold temperature and injection rate. The latter becomes negligible increasing the mold temperature. This consideration means that at high mold temperature it is possible to reach a good quality surface even with low injection velocity meaning lower fiber deterioration and fibers orientation anisotropy reduction.

- The latter becomes negligible increasing the mold temperature. This consideration means that at high mold temperature it is possible to reach a good quality surface even with low injection velocity meaning lower fiber deterioration and fibers orientation anisotropy reduction. Tensile strength tests were performed to study the effect of injection molding process parameters on the samples mechanical resistance. The experimental approach involved a fiber length analysis and an X-ray computed tomography (CT) measuring technique which allowed

the direct observation of fibers orientation in the molded components and the specimens morphology. Dog bone shaped specimens were molded at different molding conditions. In particular, the effects of mold temperature, injection speed and part thickness were investigated. The results showed that specimens morphology is affected by processing parameters. In particular the higher the mold temperature the longer the residual fibers and the higher the fiber orientation. Combining the results of fiber orientation and fiber length it is possible to explain the analysis of mechanical properties which are maximized by high part thickness, low mold temperature and injection velocity. In particular, as far as mold temperature is concerned, the interaction plot between mold temperature and part thickness has shown that the mold temperature influences positively the tensile strength for a small cavity thickness. Conversely, an higher mold temperature have a negative effect on tensile strength for thick specimens. Therefore, it is worth using a RHCM technology as long as the specimen thickness is small. This is a further improvement concerning the injection molding of fiber reinforced thin wall components where, besides the good appearance, the decreasing of the melt cooling during the injection phase and the injection pressure reducing, the tensile strength is also enhanced by using a RHCM technology.

- Fatigue tests were also carried out for the specimens of 4 mm in order to evaluate the mold temperature influence on tensile cyclic loads. The analysis of results highlighted that for the same testing conditions, the specimens injection molded at high mold temperature have shown a shorter cycle time compared with those ones molded at low temperature. In the Wohler fatigue plot, the curve related to the specimens molded at high mold temperature is parallel but shifted beneath the other curve. This trend is due to the lower fiber orientation detected for the specimens injection molded with a RHCM technology. An interesting result regards the drawing of a master-curve where, in the Wohler graph, in place of the fatigue stress, it was plotted the ratio between the fatigue stress and the correspondent value of UTS. Doing so, the curves related to the specimens injection molded at different mold temperature were almost overlapped meaning that the causes of breakage for the tensile strength are the same for the fatigue resistance. Therefore, it is possible to assume that, at least for the specimens of 4 mm, the tensile strength tests can predict the behavior of the fatigue resistance for fiber reinforced molded specimens.

- A fatigue fractioned test was done by carrying out a single fatigue test, stopping the execution for a few percentages of its

life and performing a tomographic scan each time. The purpose of this work was the studying of the damage evolution during the application of a cyclic tensile load. In particular, the evolution of the micro-voids caused by the material shrinkage during the cooling phase in injection molding was the main investigated effect. The results showed that the specimen porosity did not changed during the fatigue test therefore it seems that the micro-voids do not influence the fatigue behavior of the material. Thus, the mechanism of material damage involves a smaller scale compared with the tomographic resolution.

- As far as the crystalline materials are concerned, a numerical approach was involved in order to investigate the influence of RHCM technology on injection pressure, cycle time and crystallization degree in injection molding of PET thin wall bottle preforms. For this purpose an experimental campaign was also carried out for the numerical model calibration in order to perform the simulations with an high accuracy. The calibration was performed by minimizing the errors resulting from the comparison between the peak pressure resulted form the injection molding simulated and the real pressure peak obtained with a pressure transducer. The heat transfer coefficient (HTC) and the material transition temperature were the optimized numerical parameters. The results shown that the error between real pressure peak and the simulated one was minimized by using an HTC equal to $4000 W/m^2K$, while the glass transition temperature had no influence on pressure peak. A series of injection molding simulations were performed for comparing the CIM with a RHCM technology by varying the mold temperature. Ranging from a mold temperature of $23°C/s$ to $150°C/s$ the maximum injection pressure decreases of 37.5% without involving a substantial increasing of the cycle time. Furthermore, in spite of the higher mold cooling rate, crystallization degree did not increased over the value allowed for the subsequent blow molding phase.

- A rapid heat cycle molding technology was employed in order to control the mold temperature during the injection molding of PLA, promoting the crystals nucleation and consequently the mechanical properties of the molded parts. The analysis pointed out that conducing the annealing phase directly in the mold can substantially reduce the whole manufacturing time. The crystallization analysis made with DSC and the hardness tests, made on the injection molded-annealed parts, shown that the higher the annealing time and the mold temperature the higher the crystallization degree and the specimen hardness. Plotting the crystallization degree and the surface hardness as

function of mold temperature and annealing time, it is interesting to note that both the investigated properties show a trend stabilization in correspondence of 45% for the crystallization degree and 83.5 HD for the hardness test. Furthermore, the surface hardness follows almost the same trend of the crystallization degree confirming the link between these properties. The analysis of results have also highlighted the dependence of material crystallization on the amount of strain experienced during flow. Indeed, the first nucleation took place almost 0.25 mm from the sample edge, where the temperature was the maximum. This means that the crystallization is not only promoted by the temperature but also increasing the macro-molecular orientation.

To conclude, the achievements obtained by controlling the mold temperature are many, since it affects directly the morphology of the injection molded part. It has been shown that a RHCM technology is an interesting solution for the injection molding of thin wall components. In particular, besides the advantages of the lower injection pressure and the high quality appearance, the use of high mold temperature can further improve the mechanical properties of fiber reinforced parts. The reduction of the injection pressure in injection molding of thin wall bottle preforms is an interesting result. The possibility of molding preforms with an high length/thickness ratio allows an uniform stretching of the preforms during the blow molding process, decreasing the material costs and enhancing the bottles quality. It has been seen that a precise control of the mold temperature can affect the injection molded part morphology. Therefore, it is clear that the possibility of controlling the mold temperature during the injection molding process is critical for varying the molded part morphology. The presented solution, for rapidly heat and cool the molds, has shown interesting results as well as it has pointed out a new approach for designing thermally optimized molds. To this extent, this work provides a contribution to overcome one of the main challenges, concerning the employment of a RHCM process in a wide industrial scale. In details, it concurs to the development of a technological solution which could be at the same time able to rapidly heat and cool the cavity mold surface, environmental friendly, completely safety for the operators and economically convenient.

BIBLIOGRAPHY

[1] G. Wang, G. Zhao, X. Wang, *The International Journal of Advanced Manufacturing Technology* **2013**, *68*, 1293–1310.

[2] G. Wang, G. Zhao, X. Wang, *Materials & Design* **2013**, *44*, 509–520.

[3] G. Wang, G. Zhao, X. Wang, *Materials & Design* **2013**, *46*, 457–472.

[4] M. Fiorotto, **2012**.

[5] G Lucchetta, M Fiorotto, P. Bariani, *CIRP Annals-Manufacturing Technology* **2012**, *61*, 539–542.

[6] F. Pisciotti, A. Boldizar, M. Rigdahl, I. Ariño, *Polymer Engineering & Science* **2005**, *45*, 1557–1567.

[7] E. Dawkins, K. Horton, P. Engelmann, *Coloring Technology for Plastics* **1999**, 149.

[8] M. Oliveira, A. Brito, M. Costa, M. Costa, *Polymer Engineering & Science* **2006**, *46*, 1394–1401.

[9] X. Wang, G. Zhao, G. Wang, *Materials & Design* **2013**, *47*, 779–792.

[10] B. H. Kim, R. R. Wadhwa, *Polymer-Plastics Technology and Engineering* **1987**, *26*, 1–22.

[11] D. Yao, S.-C. Chen, B. H. Kim, *Advances in Polymer Technology* **2008**, *27*, 233–255.

[12] K. Jansen, A. Flaman, *Polymer Engineering & Science* **1994**, *34*, 894–897.

[13] S.-C. Chen, W.-R. Jong, J.-A. Chang, *Journal of Applied Polymer Science* **2006**, *101*, 1174–1180.

[14] D. Yao, B. Kim, *Polymer Engineering & Science* **2002**, *42*, 2471–2481.

[15] D. Yao, T. E. Kimerling, B. Kim, *Polymer Engineering and Science* **2006**, *46*, 938.

[16] R. X. Xu, E. Sachs, *Polymer Engineering & Science* **2009**, *49*, 305–316.

[17] X. Xu, **1999**.

[18] K. Au, K. Yu, *The International Journal of Advanced Manufacturing Technology* **2007**, *34*, 496–515.

[19] D. Dimla, M Camilotto, F Miani, *Journal of Materials Processing Technology* **2005**, *164*, 1294–1300.

[20] S.-C. Chen, Y. Chang, T.-H. Chang, R.-D. Chien, *International Communications in Heat and Mass Transfer* **2008**, *35*, 130–138.

[21] M Smith, Z Guan, W. Cantwell, *International Journal of Mechanical Sciences* **2013**, *67*, 28–41.

[22] B. H. Kim, N. P. Suh, *Polymer-Plastics Technology and Engineering* **1986**, *25*, 73–93.

[23] M. J. Liou, N. P. Suh, *Polymer Engineering & Science* **1989**, *29*, 441–447.

[24] H Kataoka, H Yamaki, Y Umei, I Katou, *JAPANESE JOURNAL OF POLYMER SCIENCE AND TECHNOLOGY* **1998**, *55*, 671–676.

[25] Y. Kim, K. Seong, S. Kang, *Optical Engineering* **2002**, *41*, 2276–2281.

[26] J.-S. Lee, K.-W. Park, S.-W. Lee, J.-H. Kim, S. Kim, *Optical Data Storage* **2003**, 228–30.

[27] K. Inoue, K. Hayashi, Y. Kawasaki, E. Ohno, *Japanese journal of applied physics* **2003**, *42*, 774.

[28] Y. Kim, J. Bae, H. Kim, S. Kang, *Journal of Physics D: Applied Physics* **2004**, *37*, 1319.

[29] D. Hatch, D. Kazmer, B. Fan, *SPE ANTEC Tech. Papers* **2001**, *47*, 428–432.

[30] W Schintlmeister, W Wallgram, J Kanz, K Gigl, *Wear* **1984**, *100*, 153–169.

[31] D. Yao, B. Kim, *Applied thermal engineering* **2003**, *23*, 341–352.

[32] S.-C. Chen, W.-R. Jong, Y.-J. Chang, J.-A. Chang, J.-C. Cin, *Journal of Micromechanics and Microengineering* **2006**, *16*, 1783.

[33] S. Kim, C.-S. Shiau, B. H. Kim, D. Yao, *Polymer-Plastics Technology and Engineering* **2007**, *46*, 1031–1037.

[34] K. Park, S. Choi, S.-J. Lee, Y.-S. Kim, *Transactions of the Korean Society of Mechanical Engineers A* **2008**, 481–487.

[35] G. H. Brown, C. N. Hoyler, R. A. Bierwirth, et al., *Theory and application of radio-frequency heating* **1947**.

[36] L. Erwin, N. P. Suh, *Polymer Engineering & Science* **1976**, *16*, 841–846.

[37] S.-K. Byon, Apparatus for heating a mold for an injection molding system, US Patent 5,762,972, **1998**.

[38] R. L. Akopyan, Dielectric mold for uniform heating and molding of polymers and composites in microwave ovens, US Patent 6,984,352, **2006**.

[39] B. Whiteside, M. Martyn, P. Coates, P. Allan, P. Hornsby, G Greenway, *Plastics rubber and composites* **2003**, *32*, 231–239.

[40] S Kim, R Trichur, G Beaucage, C. Ahn, B. Kim in Proceedings of the 10th solid-state sensor, actuator and microsystems workshop, **2002**, pp. 206–209.

[41] Y Kurosaki, I Satoh, T Saito in Proceeding of the ASPE Spring Topical Meeting on Precision fabrication and Replication, *Vol. 19*, **1999**, pp. 46–49.

[42] T. Saito, I. Satoh, Y. Kurosaki, *Polymer Engineering & Science* **2002**, *42*, 2418–2429.

[43] P.-C. Chang, S.-J. Hwang, *Journal of applied polymer science* **2006**, *102*, 3704–3713.

[44] P.-C. Chang, S.-J. Hwang, *International Journal of Heat and Mass Transfer* **2006**, *49*, 3846–3854.

[45] P. C. Chang, S. J. Hwang in Materials science forum, *Vol. 505*, Trans Tech Publ, **2006**, pp. 1261–1266.

[46] M.-C. Yu, W.-B. Young, P.-M. Hsu, *Materials Science and Engineering: A* **2007**, *460*, 288–295.

[47] D. Yao, P. Nagarajan, L. Li, Y. Y. Allen, *Journal of manufacturing science and engineering* **2006**, *128*, 837–843.

[48] H. Stumpf, K. Schulte, Molds, cycle times, US Patent 5,824,237, **1998**.

[49] N. Lee, J. Han, J. Lim, M. Choi, Y. Han, J. Hong, S. Kang, *Japanese Journal of Applied Physics* **2008**, *47*, 1803.

[50] H Iwami, M Fukuoka, Y Ohno, H Kanayama, H Hamada in ANTEC 2003 Conference Proceedings, **2003**, pp. 468–472.

[51] C Kukla, H Loibl, H Detter, *Kunststoffe-Plast Europe* **1998**, *88*, 1331–1334.

[52] G. Zhao, G. Wang, Y. Guan, H. Li, *Polymers for Advanced Technologies* **2011**, *22*, 476–487.

[53] G. Wang, G. Zhao, H. Li, Y. Guan, *Materials & Design* **2010**, *31*, 382–395.

[54] W. Guilong, Z. Guoqun, L. Huiping, G. Yanjin, *Materials & Design* **2010**, *31*, 3426–3441.

[55] X.-P. Li, G.-Q. Zhao, Y.-J. Guan, M.-X. Ma, *Materials & Design* **2009**, *30*, 4317–4323.

[56] J. Thomason, M. Vlug, *Composites Part A: Applied science and manufacturing* **1996**, *27*, 477–484.

[57] J. Thomason, W. Groenewoud, *Composites Part A: Applied Science and Manufacturing* **1996**, *27*, 555–565.

[58] J. Thomason, M. Vlug, G Schipper, H. Krikor, *Composites Part A: Applied Science and Manufacturing* **1996**, *27*, 1075–1084.

[59] J. Thomason, M. Vlug, *Composites Part A: Applied Science and Manufacturing* **1997**, *28*, 277–288.

[60] J. Thomason, *Composites Part A: Applied Science and Manufacturing* **2002**, *33*, 1641–1652.

[61] J. Thomason, *Composites Part A: Applied Science and Manufacturing* **2005**, *36*, 995–1003.

[62] J. Thomason, *Composites Part A: Applied Science and Manufacturing* **2007**, *38*, 210–216.

[63] S Mukhopadhyay, B. Deopura, R Alagiruswamy, *Journal of Thermoplastic Composite Materials* **2003**, *16*, 479–495.

[64] J. Thomason, *Composites Part A: Applied Science and Manufacturing* **2002**, *33*, 1283–1288.

[65] K. S. Kumar, A. K. Ghosh, N. Bhatnagar, *Polymer Composites* **2007**, *28*, 259–266.

[66] R Bailey, H Kraft, *International Polymer Processing* **1987**, *2*, 94–101.

[67] T. Vu-Khanh, J Denault, P Habib, A Low, *Composites Science and Technology* **1991**, *40*, 423–435.

[68] E. Lafranche, P. Krawczak, J.-P. Ciolczyk, J. Maugey, *Advances in Polymer Technology* **2005**, *24*, 114–131.

[69] H. Chen, M. Cieslinski, D. G. Baird in PROCEEDINGS OF PPS-30: The 30th International Conference of the Polymer Processing Society–Conference Papers, *Vol. 1664*, AIP Publishing, **2014**, pp. 478–482.

[70] D O'Regan, M Akay, *Journal of materials processing technology* **1996**, *56*, 282–291.

[71] J. Wang, C. Geng, F. Luo, Y. Liu, K. Wang, Q. Fu, B. He, *Materials Science and Engineering: A* **2011**, *528*, 3169–3176.

[72] T. Huan-Chang, C. Yuan-Jung, H. Chia-Hsiang, C. Rong-Yeu in PROCEEDINGS OF PPS-30: The 30th International Conference of the Polymer Processing Society–Conference Papers, *Vol. 1664*, PPS Society, **2014**, pp. 1149–1153.

[73] J. H. Phelps, A. I. A. El-Rahman, V. Kunc, C. L. Tucker, *Composites Part A: Applied Science and Manufacturing* **2013**, *51*, 11–21.

[74] A. Durin, P. De Micheli, J. Ville, F. Inceoglu, R. Valette, B. Vergnes, *Composites Part A: Applied Science and Manufacturing* **2013**, *48*, 47–56.

[75] S. M. Dinh, R. C. Armstrong, *Journal of Rheology (1978-present)* **1984**, *28*, 207–227.

[76] V.-G. Gregorio M., T. I. Charles L. in PROCEEDINGS OF PPS-30: The 30th International Conference of the Polymer Processing Society–Conference Papers, *Vol. 1664*, PPS Society, **2014**, pp. 609–613.

[77] K. J. Meyer, J. T. Hofmann, D. G. Baird, *Composites Part A: Applied Science and Manufacturing* **2014**, *62*, 77–86.

[78] T. B. N. Thi, M. Morioka, A. Yokoyama, S. Hamanaka, K. Yamashita, C. Nonomura in PROCEEDINGS OF PPS-30: The 30th International Conference of the Polymer Processing Society–Conference Papers, *Vol. 1664*, AIP Publishing, **2015**, p. 110011.

[79] P. Hine, B. Parveen, D. Brands, F. Caton-Rose, *Composites Part A: Applied Science and Manufacturing* **2014**, *64*, 70–78.

[80] G. B. Jeffery in Proceedings of the Royal Society of London A: Mathematical, Physical and Engineering Sciences, *Vol. 102*, The Royal Society, **1922**, pp. 161–179.

[81] F. Folgar, C. L. Tucker, *Journal of Reinforced Plastics and Composites* **1984**, *3*, 98–119.

[82] J. Wang, J. F. O'Gara, C. L. Tucker III, *Journal of Rheology (1978-present)* **2008**, *52*, 1179–1200.

[83] J. H. Phelps, C. L. Tucker, *Journal of Non-Newtonian Fluid Mechanics* **2009**, *156*, 165–176.

[84] C. Hopmann, M Weber, J van Haag, M Schöngart in PROCEEDINGS OF PPS-30: The 30th International Conference of the Polymer Processing Society–Conference Papers, *Vol. 1664*, AIP Publishing, **2015**, p. 050008.

[85] R. Hertzberg, M. Skibo, J. Manson, *Fatigue Mechanisms* **1979**, 471.

[86] S. Kultural, I. Eryurek, *Materials & design* **2007**, *28*, 816–823.

[87] A. Zago, G. S. Springer, *Journal of reinforced plastics and composites* **2001**, *20*, 564–595.

[88] A. Bernasconi, R. M. Kulin, *Polymer Composites* **2009**, *30*, 154–161.

[89] S. Hitchen, S. Ogin, *Composites science and technology* **1993**, *47*, 239–244.

[90] J. Horst, J. Spoormaker, *Polymer Engineering & Science* **1996**, *36*, 2718–2726.

[91] J. Horst, J. Spoormaker, *Journal of materials science* **1997**, *32*, 3641–3651.

[92] A. B. C. Larbi, H Sidhom, K Sai, D Baptiste, *Journal of materials engineering and performance* **2006**, *15*, 575–580.

[93] L. Toubal, M. Karama, B. Lorrain, *International journal of Fatigue* **2006**, *28*, 1867–1872.

[94] H Nouri, F Meraghni, P Lory, *International Journal of fatigue* **2009**, *31*, 934–942.

[95] F Meraghni, H Nouri, N Bourgeois, C Czarnota, P Lory, *Procedia Engineering* **2011**, *10*, 2110–2116.

[96] F Meraghni, H Nouri, N Bourgeois, C Czarnota, P Lory, *Procedia Engineering* **2011**, *10*, 2110–2116.

[97] R Steinberger, T. V. Leitão, E Ladstätter, G Pinter, W Billinger, R. Lang, *International Journal of Fatigue* **2006**, *28*, 1340–1347.

[98] A Ghorbel, N Saintier, A Dhiab, *Procedia Engineering* **2011**, *10*, 2123–2128.

[99] B Esmaeillou, J Fitoussi, A Lucas, A Tcharkhtchi, *Procedia Engineering* **2011**, *10*, 2117–2122.

[100] B Esmaeillou, P Ferreira, V Bellenger, A Tcharkhtchi, *Polymer Composites* **2012**, *33*, 540–547.

[101] B Esmaeillou, P Fereirra, V Bellenger, A Tcharkhtchi, *Journal of Applied Polymer Science* **2012**, *125*, 4007–4014.

[102] J. Montesano, Z. Fawaz, H. Bougherara, *Composite structures* **2013**, *97*, 76–83.

[103] E Bayraktar, S Antolonovich, C Bathias, *International Journal of Fatigue* **2006**, *28*, 1322–1333.

[104] J Lambert, A. Chambers, I Sinclair, S. Spearing, *Composites Science and Technology* **2012**, *72*, 337–343.

[105] P. J. Withers, M. Preuss, *Annual Review of Materials Research* **2012**, *42*, 81–103.

[106] F Cosmi, A Bernasconi, *Composites Science and Technology* **2013**, *79*, 70–76.

[107] P. Mallick, Y. Zhou, *International journal of fatigue* **2004**, *26*, 941–946.

[108] A Bernasconi, P Davoli, A Basile, A Filippi, *International Journal of Fatigue* **2007**, *29*, 199–208.

[109] M.-H. R. Jen, C.-H. Lee, *International Journal of Fatigue* **1998**, *20*, 617–629.

[110] G Meneghetti, M Ricotta, G Lucchetta, S Carmignato, *Composites Part B: Engineering* **2014**, *65*, 17–25.

[111] F. Ellyin, *Fatigue damage, crack growth and life prediction*, Springer Science & Business Media, **2012**.

[112] G Meneghetti, *International journal of fatigue* **2007**, *29*, 81–94.

[113] G. Meneghetti, M. Quaresimin, *Composites Part B: Engineering* **2011**, *42*, 217–225.

[114] G. Tao, Z. Xia, *International journal of fatigue* **2007**, *29*, 2180–2190.

[115] A Goel, K. Chawla, U. Vaidya, N Chawla, M Koopman, *Materials characterization* **2009**, *60*, 537–544.

[116] K. K. Chawla, *Composite materials: science and engineering*, Springer Science & Business Media, **2012**.

[117] M. F. Arif, N. Saintier, F. Meraghni, J. Fitoussi, Y. Chemisky, G. Robert, *Composites Part B: Engineering* **2014**, *61*, 55–65.

[118] M De Monte, E Moosbrugger, M. Quaresimin, *Composites Part A: Applied Science and Manufacturing* **2010**, *41*, 1368–1379.

[119] Y. Zhou, P. Mallick, *Polymer composites* **2006**, *27*, 230–237.

[120] P. Ladeveze, E LeDantec, *Composites Science and Technology* **1992**, *43*, 257–267.

[121] D Yao, B Kim in ANTEC 2003 Conference Proceedings, **2003**, pp. 521–525.

[122] M. Song, Z Liu, M. Wang, T. Yu, D. Zhao, *Journal of Materials Processing Technology* **2007**, *187*, 668–671.

[123] M. Otsuka, A. Oyabe, H. Ito.

[124] O. Brandau, *Bottles, Preforms and Closures: A Design Guide for PET Packaging*, William Andrew, **2012**.

[125] S. Meister, D. Drummer, *The Scientific World Journal* **2013**, *2013*.

[126] D.-M. Fann, S. K. Huang, J.-Y. Lee, *Polymer Engineering & Science* **1998**, *38*, 265–273.

[127] R Zheng, P. Kennedy, *Journal of Rheology (1978-present)* **2004**, *48*, 823–842.

[128] J. C. Viana, N. M. Alves, J. F. Mano, *Polymer Engineering & Science* **2004**, *44*, 2174–2184.

[129] H. Liu, J. Zhang, *Journal of polymer science part B: Polymer Physics* **2011**, *49*, 1051–1083.

[130] A. P. Mathew, K. Oksman, M. Sain, *Journal of Applied Polymer Science* **2006**, *101*, 300–310.

[131] Q Zhou, M Xanthos, *Polymer degradation and stability* **2008**, *93*, 1450–1459.

[132] A. M. Harris, E. C. Lee, *Journal of applied polymer science* **2008**, *107*, 2246–2255.

[133] Y. Srithep, P. Nealey, L.-S. Turng, *Polymer Engineering & Science* **2013**, *53*, 580–588.

[134] M. Panigrahi, N. K. Singh, R. K. Gautam, R. M. Banik, P. Maiti, *Composite Interfaces* **2010**, *17*, 143–158.

[135] G. Kfoury, J.-M. Raquez, F. Hassouna, J. Odent, V. Toniazzo, D. Ruch, P. Dubois, *Frontiers in chemistry* **2013**, *1*.

[136] K. Zhang, V. Nagarajan, M. Misra, A. K. Mohanty, *ACS applied materials & interfaces* **2014**, *6*, 12436–12448.

[137] K. Zhang, A. K. Mohanty, M. Misra, *ACS applied materials & interfaces* **2012**, *4*, 3091–3101.

[138] S. Saeidlou, M. A. Huneault, H. Li, C. B. Park, *Journal of Applied Polymer Science* **2014**, *131*.

[139] Y. Srithep, P. Nealey, L.-S. Turng, *Polymer Engineering & Science* **2013**, *53*, 580–588.

[140] V. Nagarajan, K. Zhang, M. Misra, A. K. Mohanty, *ACS applied materials & interfaces* **2015**.

[141] B Suksut, C Deeprasertkul, *Journal of Polymers and the Environment* **2011**, *19*, 288–296.

[142] B Suksut, C Deeprasertkul, *Journal of Polymers and the Environment* **2011**, *19*, 288–296.

[143] A. K. Bledzki, A. Jaszkiewicz, D. Scherzer, *Composites Part A: Applied science and manufacturing* **2009**, *40*, 404–412.

[144] M. Huda, L. Drzal, A. Mohanty, M Misra, *Composites Part B: Engineering* **2007**, *38*, 367–379.

[145] L. Suryanegara, A. N. Nakagaito, H. Yano, *Cellulose* **2010**, *17*, 771–778.

[146] S. Molinaro, M. C. Romero, M. Boaro, A. Sensidoni, C. Lagazio, M. Morris, J. Kerry, *Journal of Food Engineering* **2013**, *117*, 113–123.

[147] N Najafi, M. Heuzey, P. Carreau, *Polymer Engineering & Science* **2013**, *53*, 1053–1064.

[148] G. Ryan, P. McGarry, A. Pandit, D. Apatsidis, *Journal of Biomedical Materials Research Part B: Applied Biomaterials* **2009**, *90*, 894–906.

[149] M Vesenjak, C Veyhl, T Fiedler, *Materials Science and Engineering: A* **2012**, *541*, 105–109.

[150] J.-P. Kruth, M Bartscher, S Carmignato, R Schmitt, L. De Chiffre, A Weckenmann, *CIRP Annals-Manufacturing Technology* **2011**, *60*, 821–842.

[151] L. De Chiffre, S Carmignato, J.-P. Kruth, R Schmitt, A Weckenmann, *CIRP Annals-Manufacturing Technology* **2014**, *63*, 655–677.

[152] M Berton, A Cellere, G Lucchetta, *International Journal of Material Forming* **2010**, *3*, 671–674.

[153] A. Huq, J Azaiez, *Polymer Engineering & Science* **2005**, *45*, 1357–1368.

[154] S. G. Advani, C. L. Tucker III, *Journal of Rheology (1978-present)* **1987**, *31*, 751–784.

[155] P. C. Painter, M. M. Coleman, *Fundamentals of polymer science: an introductory text*, Technomic Lancaster, PA, **1997**.

[156] T. A. Osswald, *Understanding polymer processing: processes and governing equations*, Hanser, **2011**.

[157] I. Arino, U. Kleist, L. Mattsson, M. Rigdahl, *Polymer Engineering & Science* **2005**, *45*, 1343–1356.

[158] I. Arino, U. Kleist, M. Rigdahl, *Polymer Engineering & Science* **2005**, *45*, 733–744.

[159] F. B. Leloup, G. Obein, M. R. Pointer, P. Hanselaer, *Color Research & Application* **2014**, *39*, 559–570.

[160] R. S. Hunter, *METHODS* **1937**.

[161] S.-C. Chen, P. S. Minh, J.-A. Chang, S.-W. Huang, C.-H. Huang, *International Communications in Heat and Mass Transfer* **2012**, *39*, 216–223.

[162] A. Agazzi, V. Sobotka, R. LeGoff, Y. Jarny, *Applied Thermal Engineering* **2013**, *52*, 170–178.

[163] G. Wang, G. Zhao, H. Li, Y. Guan, *Expert Systems with Applications* **2011**, *38*, 6705–6719.

[164] H. HT., *Fatigue of composites*, Delware Composites Design Encyclopedia, **1990**.

[165] P.-A. Eriksson, A.-C. Albertsson, P Boydell, K Eriksson, J.-A. Månson, *Polymer composites* **1996**, *17*, 823–829.

[166] P.-A. Eriksson, A.-C. Albertsson, P Boydell, G Prautzsch, J.-A. Månson, *Polymer composites* **1996**, *17*, 830–839.

[167] S.-Y. Fu, B Lauke, E Mäder, C.-Y. Yue, X Hu, *Composites Part A: Applied Science and Manufacturing* **2000**, *31*, 1117–1125.

[168] S. Hitchen, S. Ogin, P. Smith, *Composites* **1995**, *26*, 303–308.

[169] H. Huang, R. Talreja, *Composites science and technology* **2006**, *66*, 2743–2757.

[170] P. Mallick, Y. Zhou, *International journal of fatigue* **2004**, *26*, 941–946.

[171] W. B. Nelson, *Accelerated testing: statistical models, test plans, and data analysis*, *Vol. 344*, John Wiley & Sons, **2009**.

[172] V. Azzi, S. Tsai, *Experimental mechanics* **1965**, *5*, 283–288.

[173] F Ellyin, H El-Kadi, *Composite Structures* **1990**, *15*, 61–74.

[174] I. Carrascal, J. Casado, S Diego, J. Polanco, F GUTIÉRREZ-SOLANA, *Fatigue & Fracture of Engineering Materials & Structures* **2012**, *35*, 683–691.

[175] N. G. McCrum, C. Buckley, C. B. Bucknall, *Principles of polymer engineering*, Oxford University Press, **1997**.

[176] N Chawla, C Andres, J. Jones, J. Allison, *Scripta materialia* **1998**, *38*, 1595–1600.

[177] B Mlekusch, *Composites Science and Technology* **1999**, *59*, 547–560.

[178] C. Eberhardt, A. Clarke, *Composites Science and Technology* **2001**, *61*, 1389–1400.

[179] Y. Lee, S. Lee, J. Youn, K. Chung, T. Kang, *Materials Research Innovations* **2002**, *6*, 65–72.

[180] S.-Y. Fu, Y.-W. Mai, E. C.-Y. Ching, R. K. Li, *Composites Part A: Applied Science and Manufacturing* **2002**, *33*, 1549–1555.